Two Stroke Diesel Engines for Large Ship Propulsion

Haider, Sajjad; Meyer, Knud Erik; Schramm, Jesper

Publication date:
2011

Document Version
Publisher's PDF, also known as Version of record

Experimental and Numerical Study of Swirling Flow in Scavenging Process for 2-Stroke Marine Diesel Engines

By:

Sajjad Haider

A dissertation submitted in partial fulfillment of Degree of
Doctor of Philosophy

Supervisors:

Assoc. Professor Knud Erik Meyer
Assoc. Professor Jesper Schramm

Abstract

In low speed large two-stroke marine diesel engines, uniflow scavenging is used to remove the exhaust gases from the cylinder and fill the cylinder with fresh air charge for the next cycle. The swirl enhances the mixing of fuel with air and improves combustion efficiency. The thesis focuses on characterizing the confined swirling flow during the scavenging process. A simplified experimental model of an engine cylinder is developed. Smoke visualization results show that at fully open intake port there is a well-defined vortex core. The core size increases in a hollow conical shape along the flow downstream. As the port closes, the mixing of smoke particles in the core with surrounding regions is enhanced. The hollow conical smoke pattern disappears and resembles to a jet. Laser Doppler Anemometry measurements are conducted in the swirl generator and at the entrance to the test cylinder. The results show that the incylinder swirling flow has a precessing vortex core. The precession frequency is found to be linearly dependent on the volumetric flow rate at a given swirl number.

The stereoscopic particle image velocimetry (SPIV) measurements are conducted for two sets of experiments. In the first experiment, the intake port is kept fully open and three different cylinder lengths are investigated. The results indicate that the incylinder flow is a concentrated vortex decaying downstream due to wall friction. The mean axial velocity has a wake-like profile. The radial velocity is very small compared to tangential and axial components. No reverse flow is observed in the vortex core. The initially confined vorticity in the vortex core region is distributed to outer regions along the flow. Turbulent kinetic energy is high in the vortex core and near wall regions. The incylinder flow is majorly governed by the flow conditions at the cylinder inlet and the increased length of cylinder provides further decay of the swirl. The profiles of velocity components remain the same for a given cross-sectional plane common in different cylinder lengths. The mean position of the vortex center is not aligned with the cylinder axis at all measuring position and follows a helical path along the cylinder length. For cylinder length of eight diameters, the mean vortex path does not complete one revolution and instead re-twists at one side of the cylinder axis.

In the second SPIV experiment, the measurements are conducted to characterize the effect of piston position on the in-cylinder swirling flow. The piston is positioned to cover the cylinder intake port by 0%, 25%, 50% and 75%. For increasing port closures the tangential velocity profile changes to a

forced vortex and the axial velocity changes correspondingly from a wake-like to a jet-like. This change, however, starts at cross-sectional planes close to cylinder outlet and moves to upstream positions. At 50% port closure, the mean axial velocity in the whole cylinder attains a jet like profile. The tangential velocity resembles more to a wall-jet than a forced vortex profile. With 75% port closure, the jet-like axial velocity profile at cross-sectional plane close to intake port changes back to wake-like at the adjacent cross-sectional plane and downstream. This indicates a vortex breakdown like characteristic. The tangential velocity then has forced vortex profile throughout the cylinder. The non-dimensional profiles of velocity components have no significant variation with the variation in Reynolds number.

Numerical simulations are conducted only for the fully open intake port case. The turbulence models include RNG $k-\varepsilon$ and Reynolds stress models. The simulation results, however, do not show satisfactory agreement with the experimental data. The models predicted a larger vortex core size with a reverse flow. The downstream decay in the swirl is predicted to be lower than observed from experimental results. However, there are some qualitative features like distribution of modeled Reynolds stress components that, to some extent, have reasonable agreements. The factors affecting the performance of the CFD models possibly lie both in the treatment of turbulence and the numerical aspects.

Resumé

For store langsomtgående totakts diesel-motorer, anvendes uniflow-skylning til at fjerne udstødningsgasserne fra cylinderen og fylde cylinderen med frisk luft til den næste cyklus. Swirl øger blanding af brændstof med luft og forbedrer forbrændingseffektiviteten. Afhandlingen fokuserer på karakterisering af de indesluttede roterende strømning under skylningen. En forenklet eksperimentel model af en motorcylinder er udviklet. Røgvisualisering viser, at der for helt åbne indtagsporte, er en veldefineret vortex kerne. Kernen bliver større nedstrøms og får en hul kegleform. Når porten lukker, forøges opblandingen mellem røgpartikler i kernen og de omkringliggende regioner. Den hule koniske form forsvinder og kommer til at ligne en jet. Laser Doppler anemometri målinger er foretaget i swirlgeneratoren og ved indgangen til testcylinderen. Indtagporten holdes helt åben. Resultaterne viser, at strømningen i cylinderen har en hvirvelkerne med præcession. Præcessionsfrekvensen er lineært afhængig af den volumetriske strømningsrate for et givent swirl nummer.

Stereoskopisk "Particle Image Velocimetry" (SPIV) målinger er udført for to forsøg. I det første, er indtagsporten holdt helt åben, og tre forskellige cylinderlængder er undersøgt. Resultaterne indikerer, at strømningen I cylinderen er en koncentreret hvirvel, der henfalder nedstrøms på grund af vægfriktionen. Den gennemsnitlige aksialhastighed har et kølvandslignende profil. Den radiale hastighed er meget lille i forhold til de tangentielle og aksiale komponenter. Ingen tilbagestrømning er observeret i hvivelkernen. Vorticiteten er først begrænset til hvirvelkernen, men bliver nedstrøms fordelt til de ydre regioner. Turbulent kinetiske energi er høj i vortex kernen og i nærheden af vægregionerne. Strømningen I cylinderen styres hovedsagligt af strømningsforholdene ved indtagsportene, og den øgede længde af cylinderen giver yderligere henfald af rotationen. Profilerne af hastighedskomponenterne forbliver de samme for et givent tværsnit ved forskellige cylinder længder. Den gennemsnitlige placering af hvirvelcenteret følger ikke cylinderaksen, men er istedet spiralformet. For en cylinderlængde på otte diametre fuldfører det gennemsnitlige hvirvelcenter ikke en hel omdrejning, men vrider sig I stedet tilbage på den ene side af cylinderaksen.

I det andet SPIV eksperiment karakteriseres effekten af stemplets position på strømningen I cylinderen. Stemplet er positioneret til at dække cylinderens indtagsport med 0%, 25%, 50% og 75%. Ved forøgning af porttildækningen ændres den tangentielle hastighedsprofil til en tvungen vortex og den aksielle hastighed ændres tilsvarende fra en kølvands- til et jet-lignende profil. Denne

ændring begynder dog ved tværsnit tæt på cylinderudløbet, og flytter til opstrømspositioner. Ved 50% porttildækning, antager den gennemsnitlige aksiale hastighed i hele cylinderen en jet-lignende profil. Den tangentiale hastighed ligner mere en væg-jet end et tvungent hvirvelprofil. Ved 75% porttildækning, ændres den jet-lignende aksielle hastighedsprofil ved tværsnittet tæt på indtagsporten tilbage til et slipstrømslignende profil ved det tilstødende tværsnit og videre nedstrøms. Dette indikerer en strømning som ligner et "vortex breakdown" Den tangentielle hastighed har derefter tvungent hvirvelprofil. De ikke-dimensionelle profiler af hastighedskomponenterne har ingen betydelig ændring med variationen i Reynolds tal.

Numeriske simuleringer udføres kun for de tilfælde hvor indtagsportene er helt åbne. Turbulensmodellerne inkluderer RNG $k-\varepsilon$ og Reynolds stress modeller. Resultaterne af simulationerne viser dog ikke tilfredsstillende overenstemmelse med de eksperimentelle data. Simuleringerne viser en større hvirvel kerne størrelse for en tilbagestrømning. Henfaldet af rotation nedstrøms er mindre end hvad der blev observeret eksperimentelt. Men der er nogle kvalitative egenskaber såsom distribution af modelberegnede Reynolds stress komponenter, der til en vis grad, stemmer overens. De faktorer, der påvirker resultaterne af CFD modellerne ligger muligvis både i behandlingen af turbulens og de numeriske aspekter.

Preface

This dissertation is submitted in partial fulfillment of the requirement for the degree of Doctor of Philosophy in Mechanical Engineering. The dissertation is based on the research work carried out during the period from 2006 to 2010 at the Technical University of Denmark (DTU). The work was carried out under the supervision of Associate Professor Knud Erik Meyer, Associate Professor Jesper Schramm and Assistant Professor Dalibor Cavar along with useful suggestions from Professor Valery Okulov and PhD Stefan Mayer Manager Basic Research at MAN Diesel & Turbo.

The dissertation consists of six chapters excluding the conclusions and appendices. Bibliography is given after the summary and conclusions. Chapter 1 gives and introduction to the scavenging process in two stroke marine diesel engines and identifies the scope of the work. Chapter 2 provides a brief overview of swirling flows based on theoretical and experimental work from scientific literature. Chapter 3 gives a description of the experimental test model used in this research work. Chapter 4 presents the results of the first stereoscopic PIV experiment where the length of the cylinder is changed. Chapter 5 gives the results from second experiment where the measurements are conducted at different intake port closures while keeping the cylinder length constant. Chapter 6 provides the description and results of the numerical simulations carried out. Finally the Summary and conclusions will summarize the results of the research work and point out the potential future work. Due to limited space, all the results from the experiments in Chapter 4 & 5 could not be given in the respective chapters and are instead given in Appendix A & B respectively. Appendix C includes the manuscript of the article ready to be submitted to a related scientific journal.

Acknowledgment

Regarding this thesis, the acknowledgment goes to many people who have been directly or indirectly giving their support and help.

At first I am very thankful to DTU, MAN Diesel and Turbo and Danish Centre for Maritime Technology (DCMT) for funding the project and giving me the opportunity to work on a very challenging and interesting topic.

At the university, among teachers I am thankful to V. Okulov, J. H. Walther, D. Cavar, J. Schramm and especially my supervisor K. E. Meyer for their guidance and suggestions throughout. Many thanks go to colleagues, Clara Velte, Anas Obeidat, Kristian Ingvorsen and Teis Schnipper for many fruitful discussions. I should especially thank Morten from workshop at MEK without whom setting up the experimental test rig was not possible.

I am also thankful to students Lauritz Andersen, Morten Plum and Flavio Pergolesi for their work and help in the development of the experimental setup while carrying their thesis works.

Finally I am very thankful to my family for their love and affection without which those times of being tired and work stressed would not be over easily.

To my Parents for their love and support in their lives and after.

Nomenclature

A	Area
A_{in}	Inlet area
A_i	Total area of inlet to the cylinder/ nozzle area
D	Internal diameter of cylinder or vortex chamber
D_o	External diameter of cylinder or vortex chamber
D_e	Internal diameter of outlet pipe
d_c	Diameter of conditional circle
I	Turbulence intensity
k	Turbulent kinetic energy
L	Length of cylinder or vortex chamber
L_e	Length of outlet pipe
l	Length scale representing size of largest eddy
l	Helix pitch
p	Pressure
Q	Inlet volume flow rate
Q_{in}	Inlet volume flow rate
r	Radial distance from the center of vortex
r_a	Radial distance from vortex center to location with maximum tangential velocity
R	Radius of the cylinder/ vortex chamber
Re	Reynolds number
S	Swirl number/ parameter
S_o	Initial swirl intensity
S_c	Characteristic swirl number
V_{av}	Average velocity
V_θ	Normalized tangential velocity
V_r	Normalized radial velocity
V_z	Normalized axial velocity
v_θ	Tangential velocity
v_r	Radial velocity
v_a	Axial velocity

$\overline{v_i' v_j'}$	Reynolds stress components
$\overline{v_i' v_j'}$	Normalized Reynolds Stress components in polar coordinates
$\overline{u_i' u_j'}$	Normalized Reynolds Stress components in Cartesian coordinates
X	X-axis based on its origin at axis of the test cylinder
X_v	X-axis based on its origin at mean vortex center
x	X-axis based on its origin at axis of the test cylinder computational mesh and for experimental data it represents X_v.

Greek Symbols and Notations

Ω	Angular Velocity
Γ	Circulation around the vortex core
δ	Length scale representing the effective size of vortex core
ρ	Density
ε	Energy dissipation
θ	Angle between radial and tangential velocity components
ϕ	Diameter of the circle having blade curvature as an arc
γ	Angle between cylinder radius and direction of nozzle/ inlet Energy dissipation
ψ	Streamline angle
β	Rate of swirl decay
μ_t	Turbulent viscosity
μ_{t_0}	Turbulent viscosity without swirl
α_s	Model swirl constant
ω_z	Mean axial vorticity
ω_θ	Mean tangential vorticity

Subscripts

i, j	Vector components in Cartesian and Polar coordinates
m	Model quantity

Abbreviations

BDC	Bottom Dead Center
CFD	Computational Fluid Dynamics
IMO	International Marine Organization
LSE	Low Speed Engine

LDV/ LDA	Laser Doppler Velocimetry/ Anemometry
NO_x	Oxides of Nitrogen NO and NO_2 (air pollutants)
PVC	Precessing vortex core
SPIV	Stereoscopic Particle Image Velocimetry
TDC	Top Dead Center
T.I	Turbulence Intensity
TKE	Turbulent Kinetic Energy

Table of Contents

1 Introduction 1

1.1 Large Two-Stroke Marine Diesel Engine 1
1.1.1 Two-Stroke Diesel Engine Cycle 2
1.2 Significance of Scavenging Process 3
1.3 Types of Scavenging Systems 5
1.3.1 Cross Scavenging 5
1.3.2 Loop Scavenging 5
1.3.3 Uniflow Scavenging 6
1.4 Comparison of Scavenging Types and Ideal Engine Scavenging Process 6
1.5 Swirling Flow during Uniflow Scavenging Process 7
1.6 Scope of thesis 9
1.7 Thesis Layout 10

2 Swirling Flows 11

2.1 Classification of Confined Swirling Flows 12
2.2 Methods of Swirl Generation 16
2.3 Some Aspects of Swirling Flows 18
2.3.1 Stream line Curvature 18
2.3.2 Radial Equilibrium 19
2.3.3 Swirl Intensity and Decay 20
2.3.4 Upstream influence 22
2.3.5 Instabilities Vortex Breakdown in swirling Flows 23

2.3.6 Helical Vortex Structures 24
2.4 CFD Modeling Challenges 28

3 Experimental Setup 31

3.1 Scavenging Flow Test Model 31
3.1.1 Cylinder 32
3.1.2 Inlet Section (Swirl Generator) 32
3.1.3 Outlet Section 33
3.2 Experimental Setup 34
3.3 Differences between Test Model and Real Engine Scavenging process 35
3.4 Smoke Visualization 36
3.5 Stereoscopic PIV Setup 40
3.5.1 Alignment and Calibration 42
3.5.2 Seeding Setup 43
3.5.3 Data Acquisition and Processing 44
3.6 LDA Setup 44

4 Swirling Flow in a Pipe 47

4.1 LDA Measurements (Inlet Section) 49
4.2 PIV Experimental Results (L3) 54
4.2.1 Mean Velocity Field 54
4.2.2 Tangential Velocity Profile 57
4.2.3 Axial Velocity Profile 58
4.2.4 Mean Axial Vorticity 59
4.2.5 Reynolds Normal Stresses 63
4.2.6 Reynolds Shear Stresses 75
4.2.7 Average Turbulent Kinetic Energy 84
4.3 Effect of Cylinder Length 87
4.3.1 Tangential Velocity Profile 88

4.3.2 Axial Velocity Profile 90
4.3.3 Radial Velocity Profile 92
4.3.4 Swirl Parameter 93
4.3.5 Mean Axial Vorticity 95
4.3.6 Mean Vortex Core Position 95
4.4 Cylinder Wall Pressure Measurements 98
4.5 Discussion 100

5 Effect of Piston Position 107

5.1 Results and Discussion 108
5.1.1 Tangential and Axial Velocity Profiles 109
5.1.2 Mean Velocity Field 118
5.1.3 Reynolds Normal Stresses 122
5.1.4 Reynolds Shear Stresses 132
5.1.5 Mean Axial Vorticity 140
5.2 Cylinder Wall Pressure Measurements 142
5.3 Discussion 144

6 Numerical Modelling 147

6.1 Computational Details 148
6.1.1 Turbulence Models 148
6.1.2 Boundary Conditions 149
6.1.3 Near Wall Treatment 151
6.1.4 Solution Methods 151
6.2 Results 151
6.2.1 Tangential Velocity 151
6.2.2 Axial Velocity 154
6.2.3 Velocity Magnitude 157
6.2.4 Normalized Reynolds Normal Stresses 158

6.2.5 Normalized Reynolds Shear Stresses 160
6.3 Discussion 161

Conclusions 164
References 173
Appendix A A-1
Appendix B B-1
Appendix C C-1

When theoretical results are presented,
no one seems to believe in them, except
the one who did the analysis.

When experimental results are presented,
everyone seems to believe in them, except
the one who did the experiments.

From webpage of Professor Atle Jensen
Mechanics Division
Department of Mathematics
University of Oslo

Introduction

In this chapter a background of the motivation for the current study is given. Working principle of two-stroke marine diesel engines is described. A description of different types of the scavenging process is given and significance of scavenging process and the need for more efficient uniflow scavenging process is discussed. The chapter introduces the scope of the problem studied in this project and gives a layout of the current thesis.

After its invention by Sir Dugald Clerk at the end of 19th century (Blair, 1990), the two stroke cycle engine has evolved in different type/ designs. Today their applications vary from Lawn movers to large container ship propulsion. The most successful of all the two stroke cycle engines are the marine diesel propulsion units with their thermal efficiency being more than 50% (Blair, 1990).

Low Speed Marine diesel engines mostly use very low grade diesel fuel. The combustion of such fuels and their large consumption result in production of large amount of environmental pollutants like CO_2, NO_x, Sulphur Oxides, Soot and different other particulate matters etc. With the increase in global trade, the marine transportation/ traffic has also increased. Considering a potential threat to air and marine environment, different governments and international legislative bodies acted and an international agreement on emission regulations was obtained in 1997 (Dam, 2007). Today, International Marine Organization (IMO) which is a United Nations Agency with 169 member states, develops and maintains the comprehensive regulatory framework for emission control from shipping industry as one of its mandates (Wikipedia, 2010). The IMO regulation 'Annex IV of Marpol 73/78-Regarding the prevention of air pollution from ships', ratified in 2005, has made the marine engine producers to develop more fuel efficient and environmentally benign technologies (Dam, 2007). The current study is also one of the many research projects by MAN Diesel A/S with goal of developing future marine diesel engines.

Before discussing the scope of this study a short description and working cycle of large two stroke marine diesel engine is given.

1.1 Large Two-Stroke Marine Diesel Engine

A schematic picture of large two stroke marine diesel engine is given in figure 1.1 which shows cold air entering from the scavenging box to cylinder via scavenging ports and removing the exhaust gases through cylinder

exhaust valve. A detail description of all the engine components and their respective working is not given here and interested reader should see (Woodyard, 2009) and (McGeorge, 1999) for further details.

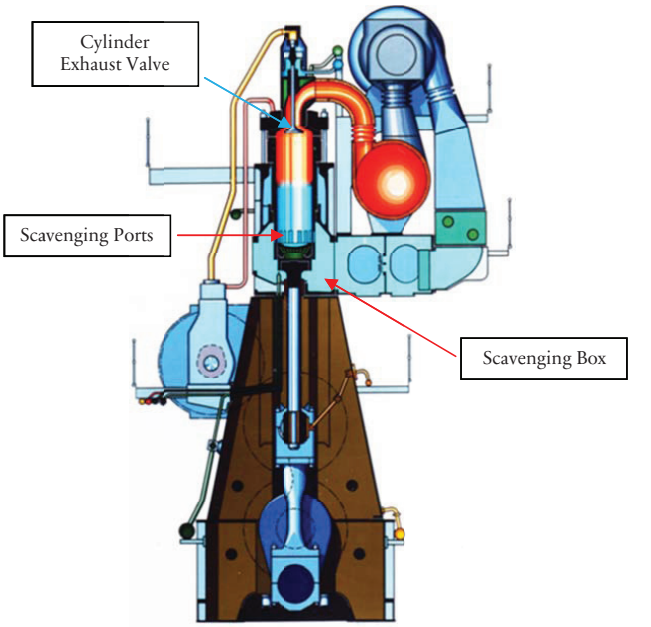

Figure 1.1:

Schematic Picture of Large Two-Stroke Marine Diesel Engine with Uniflow Scavenging (piston is at BDC). (http://sites.google.com).

1.1.1 *Two-Stroke Diesel Engine Cycle*

The schematic pictures given in figure 1.2 demonstrate different stages during the two stroke diesel engine cycle. Each stage is discussed separately below as:

(a) The piston is at the bottom dead centre (BDC). Both the cylinder exhaust and scavenging ports are open. The fresh cold air is entering into the cylinder from scavenging ports and the exhaust gases are being scavenged from the cylinder through the exhaust valve. The scavenging ports are located above the BDC.

(b) The piston moves towards the top dead centre (TDC) by first blocking the scavenging ports. The exhaust valve then closes and the fresh air

inside the cylinder is compressed in to a small volume attaining very high pressure and temperature.

(c) The diesel fuel is injected in the compressed air pocket a little before top-dead-center (TDC). The fuel evaporates and gets mixed with the air and combustion starts by self-ignition. In 4T50ME-X test engine, at MAN Diesel A/S, has three fuel injection nozzles mounted on the cylinder head in a circle with a spacing of 120° between each nozzle. However, there exist different nozzle mounting configurations depending on different engine designs.

(d) Due to combustion high temperature and pressure is generated inside the cylinder causing the piston to move downward towards the bottom dead centre. The piston force is transferred to the crankshaft. This is called the 'Power Stroke'.

(e) When piston reaches very close to scavenging ports, the exhaust valve opens before the scavenge ports and some exhaust gases leaves the cylinder through that (Blowdown). Then piston gradually uncovers the scavenging ports and fresh air enters the cylinder and removes the remaining exhaust gases as the piston moves up again.

Thus it can be understood that the complete scavenging process begins at the end of power stroke and ends in the start of compression stroke. Engine's Turbocharger is used to derive the scavenging system.

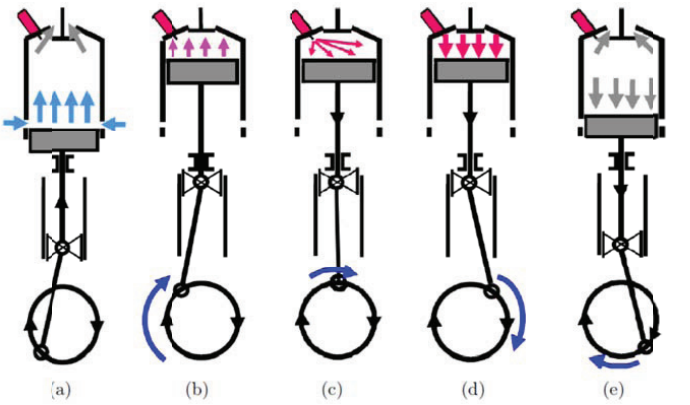

Figure 1.2:

Schematic Picture of Two-Stroke Diesel Engine Cycle with Uniflow Scavenging. (Dam, 2007).

1.2 Significance of Scavenging Process

Compared to four-Stroke engines where the scavenging is carried in one complete piston stroke, in two stroke engines there is a short time available

for the scavenging process. Moreover, it not only serves to scavenge the cylinder exhaust gases but also as to fill the cylinder with fresh air charge for the next cycle which, in case of four stroke engine, is also accomplished in a separate piston stroke. This makes scavenging process very important for engine performance and efficiency both in terms of fuel and emissions. This is because scavenging process not only removes exhaust gases and provides fresh air to the engine but also provides the necessary and initial swirl to the fresh air in which the diesel fuel is to be injected. As diesel combustion is a mixing enhanced combustion process, a proper and good mixing of fuel with air ensures better/ complete combustion of the fuel injected. Further, the resulting heat release defines the production of different pollutants like NOx and Soot etc. The heat release during combustion also defines the temperature distribution in the cylinder fluid mixture (injected fuel, fresh air, combustion products) and heat transfer through cylinder walls, cylinder head and piston. This in turn defines the distribution thermal stresses generated in the aforementioned solid materials and the requirement of their cooling.

From the point of view of engine research and development, for example in computational modeling of in-cylinder diesel combustion, an initial flow field is to be defined in the compressed air pocket in which the diesel fuel is to be injected. This flow field then governs the simulation of fuel evaporation and mixing, consequent combustion and pollutant formation and heat generation and transfer through the cylinder enclosure walls. An improper definition of this flow field gives erroneous simulation results and hinders the efforts for understanding the overall process and identifying the key aspects required to be improved in order to develop the so called future engines. The knowledge about the initial flow field can only be understood by understanding the scavenging process. During the compression stroke, when the piston closes the scavenging ports, the in-cylinder flow field at that moment is the initial condition for the final piston-compressed flow field in which the fuel is to be injected.

Practically, in the current marine diesel engines, the amount of air supplied during the scavenging process is more than what is required. This makes some amount of fresh air to enter and leave the cylinder through exhaust valve. This is called as Short Circuiting (Pulkrabek, 2003). In addition to having not well understanding of the in-cylinder fluid dynamics during scavenging process (flow field and interaction of fresh air with exhaust gases), another aspect of supplying more air is cooling the exhaust valve.

Efficient scavenging improves the combustion performance of the 2-stroke diesel engines. Thus understanding, optimizing and developing an efficient scavenging process is one of the key aspects of developing efficient and environmentally friendlier marine diesel engines.

1.3 *Types of Scavenging Systems*

There are mainly three types of scavenging systems used in two stroke marine diesel engines (Figure 1.3) (Heywood, 1988).

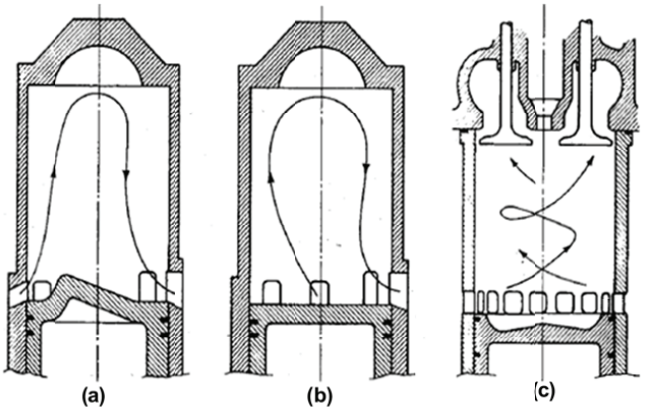

Figure 1.3:

Schematic Pictures of types of Scavenging (a) Cross Scavenging (b) Loop Scavenging (c) Uniflow Scavenging. (Heywood, 1988).

1.3.1 *Cross Scavenging*

In this type of scavenging, the scavenge/ air intake port is at one side of the cylinder near the bottom dead centre (BDC) and the cylinder exhaust port is on the other side of the cylinder (Figure 1.3a). Both the intake and exhaust ports are opened and closed by piston during its motion. The exhaust port opens before the intake port and some portion of exhaust gases, being at higher pressure than atmospheric, leaves the cylinder. Then piston uncovers the intake port. The piston is given a special shape which directs the fresh air up towards the cylinder head and then air flows down to exhaust port and removes the exhaust gases.

1.3.2 *Loop Scavenging*

In loop scavenging, both the exhaust and intake ports are on the same side of the cylinder. The piston does not have a special profile as in case of cross scavenging. Similar to cross scavenging, the piston opens the exhaust port first and then the intake ports. The incoming air enters the cylinder and flows in loop as shown in figure 1.3b. For both cross and loop scavenging types there exists no exhaust valve.

1.3.3 *Uniflow Scavenging*

The uniflow scavenging is shown in figure 1.3c. The air intake ports are located near the bottom dead centre (BDC). The exhaust port is located in the cylinder head. An exhaust valve is used to open and close the exhaust port whereas the intake ports are controlled by piston motion. As discussed in section 1.1.1, the fresh air enters the cylinder near the bottom dead centre and flows upward and removes the exhaust gases though the exhaust port at the cylinder head. Since the scavenging air flows from bottom to top inside the cylinder, this type of scavenging is called as uniflow scavenging. Most of marine diesel engines with uniflow scavenging have a single exhaust port.

1.4 Comparison of Scavenging Types and Ideal Engine Scavenging Process

The engines equipped with cross and loop scavenging have simple construction due to less moving parts i.e. no exhaust valve. This results in simpler cylinder cover design, less stressed cam shaft and also prevents the problem of thermal stressing due to exhaust valve heating-up (Raunek, 2009). From scavenging point of view, the main disadvantage of these two types of scavenging is that the scavenging air cannot completely remove all the exhaust gases from the cylinder.

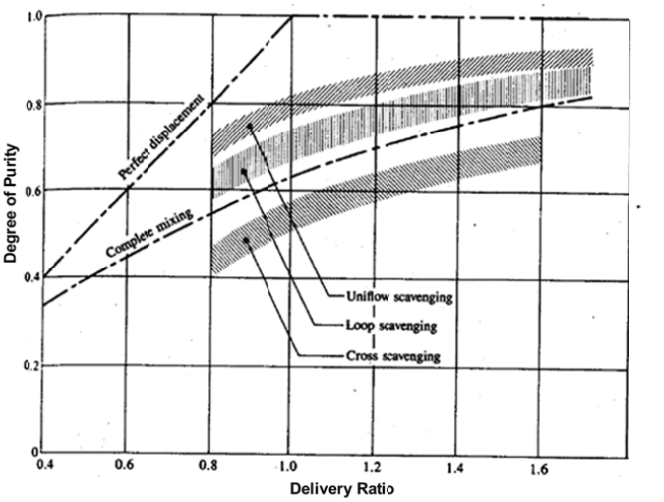

Figure 1.4:

Purity as a function of Delivery Ratio for different types of large marine Two-stroke Diesel Engines. (Heywood, 1988).

Figure 1.4 gives a comparison of scavenging performance of different aforementioned scavenging types based on two parameters (Heywood, 1988):

$$\text{Delivery Ratio} = \frac{\text{Mass of delivered air (or mixture) per cycle}}{\text{Reference (exhuast gas) mass}}$$

$$\text{Purity} = \frac{\text{Mass of air in trapped cylinder charge}}{\text{mass of trapped cylinder charge}}$$

(Schweitzer P. H., 1949) describes the ideal engine scavenging process as:

"*The ideal engine scavenges the cylinder of all residual products of combustion, fills it with uncontaminated fresh air, and in so doing wastes no fresh air through the exhaust.*"

This is also defined as 'perfect displacement scavenging process' by Hopkinson (1914). In the perfect displacement scavenging process all fresh air charge entering the cylinder is retained and perfectly displaces the exhaust gases (Blair, 1990). In actually engine scavenging processes there always occurs mixing of fresh air charge with the exhaust gases. However, the level of mixing depends on the type of scavenging. In ideal scavenging, the scavenge air acts like a piston and pushes the exhaust gases out of cylinder without mixing with them (Schweitzer, 1949). From figure 1.4 it can be seen that the uniflow scavenging type is most efficient one. Uniflow flow scavenging is the most efficient scavenging system but require added cost of exhaust valve system (Pulkrabek, 2003). Also it accounts for higher engine thermal efficiency due to better air/ gas exchange (Pevzner, 1998). Today almost all of the modern large marine diesel engines use uniflow scavenging (Raunek, 2009). Earlier measurements conducted on some marine diesel engines, manufactured by MAN Diesel A/S, resulted in 98% of purity at a delivery ratio of 1.5 (MAN Diesel, 2010). This shows that the uniflow scavenging in that engine has better performance than the one given in figure 1.4. However, optimization of the amount of air used during the scavenging process is still a challenging and potential task in order to improve the overall engine system efficiency and also to reduce cost due to scavenging system delivering excess amount of air than is actually needed.

1.5 Swirling Flow during Uniflow Scavenging Process

As discussed in section 1.2, in addition to exhaust gas scavenging as the main criteria, the design of uniflow scavenging process also considers to provide a 'mixing favorable' flow field to the injected diesel fuel at the end of compression stroke. Introducing swirl in the flow has a wide spread use in many engineering applications for enhancement of mixing process. Swirl in the in-cylinder flow is introduced by making the intake ports at an angle to

the cylinder radius (Figure 1.5 & 1.6). The scavenging ports, depending on different engine designs, are at an angle with the cylinder radius to impart tangential velocities producing a swirling air column. The resulting in-cylinder confined swirling flow removes the exhaust gases from cylinder, provides fresh air charge for the next cycle and introduces swirl to enhance mixing of injected fuel and its consequent combustion. Moreover, it also has a cooling effect on the cylinder liner and exhaust valve. In case of a non-axis symmetric swirl, an uneven temperature distribution at the walls can be resulted. Thus investigation of in-cylinder confined swirling flow is a key step forward in optimization of scavenging process and development of more efficient uniflow scavenging process.

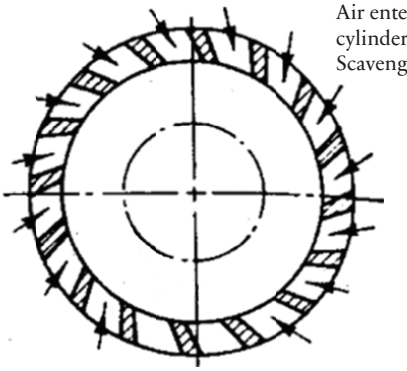

Figure 1.5:

Intake Port arrangement for Uniflow Scavenging System. (Heywood J. B., 1988).

Figure 1.6:

Cylinder liner with scavenging ports. (www.brighthub.com).

Experimental results available in scientific literature, focused on studying the uniflow scavenging process in large low speed marine diesel engines, are very few compared to scavenging in other (smaller and high speed) two stroke

diesel engines. Nishimoto et al. (1984) obtained the shape of the front surface of the scavenging air using thermocouple in a uniflow model engine. The model engine used hot air for scavenging the cylinder filled with air at room temperature. It was observed that with the increase in the engine rpm (rotations per minute) and port angle, the scavenging air front surface profile changes from jet like to a wake like profile analogous to vortex breakdown in an axial flow vortex chamber. A method was also proposed to obtain a flat profile front surface at an arbitrary Reynolds number for maximum scavenging efficiency. Laser Doppler Velocimetry (LDV) experiment was conducted on a model test engine by Dedeoglu (1988). The measurements involved using a single liquid and cylinder liner with different intake port configurations. Result show that the in-cylinder flow consists of a rotational flow in the cylinder axis region and a potential flow in the near wall region. Nakagawa et al. (1990) used 2-component LDV measurements on a model of large, low speed engine with large bore acrylic cylinder and using air. The tangential/ swirl velocity profile for piston at TDC is found to be governed by the scavenging port angle. Larger port angles resulted in a larger axial velocity drop in the central region of the cylinder thus occasionally resulting in a reverse flow. Litke (1999) studied the influence of the scavenging port angles on the scavenging efficiency by using liquids on a 1:4 scaled engine model instead of gases. It was observed that the highest scavenging efficiency is obtained with an inlet scavenging port angle of 20°. The results also indicated a better performance of using scavenging ports with combination of different angles compared to the ports with uniform angle.

1.6 Scope of thesis

Large physical size and high in-cylinder pressure for LSE makes experimental investigations in the engine very expensive to conduct and difficult to get optical access. The scavenging process is transient and complex in nature thus making statistics difficult. In terms of variation in geometry of the flow domain, piston is in continuous motion during the scavenging process thus changing the cylinder length and also the effective shape of air intake ports. Such complex inlet flow conditions make it difficult to distinguish between inlet effects and swirling flow effects. Regarding the flow physics, mixing and stratification of exhaust gases with fresh air charge occurs while in-cylinder mass flow rate changes between opening and closing of the scavenging ports. This simultaneous variation in flow domain and flow physics consequently affects the in-cylinder swirl characteristics and the type of the vortex generated by the swirl.

Considering the complex nature of the real engine scavenging process, a detailed understanding of the incylinder scavenging process requires isolation and consequent study of each flow phenomenon in a simplified form. The complex physics can then be better analyzed by gradually adding different flow effects.

The goal of this study is to study and develop a simplified steady state and isothermal case of in-cylinder swirling flow. The focus is to

- Characterize the in-cylinder confined swirling flow in the test setup.
- Obtain experimental data.
- Study the capability and performance of different turbulence models.
- Identify key design aspects to develop future test models.

1.7 Thesis Layout

This thesis has been divided into three major sections.

(1) ***Introduction and Theory of Swirl Flows***: introduce the background of the problem studied and provide a theoretical basis for the analysis of experimental and Numerical results.
(2) ***Experimental Section***: describes the experimental setup design and presents and analyses the experimental results.
(3) ***Numerical Section***: gives the results of computational fluid dynamics (CFD) models and compares them with experimental results and discusses the performance of different turbulence models for predicting the in-cylinder swirling flow.

Swirling Flows

This chapter gives a brief overview of flows having swirling motion. A general classification of different swirling flow regimes have been given based on the tangential velocity profile. Different swirl generation methods have also been presented. Aspects of swirling flows related to current study have been discussed based on experimental results available in the scientific literature. Some of the challenges regarding the numerical modeling of swirling flows with focus on RANS based models are also discussed.

According to American Heritage Dictionary of English Language, the word 'swirl' means "to move with a twisting or whirling motion". In fluid mechanics the term 'swirling flow' can in general be defined as a class of different flow types that involve an 'overall' twisting or whirling motion because in many flows localized twisting or whirling motion of fluid exist as a result of mixing or turbulence is observed yet they are not considered as swirling flows. The main characteristic of swirling flows as defined by Baker et al. (1974) and Ito et al. (1986) is that the flow has a combination of tangential/ vortical and axial motions. Thus the presence of 'vortex' is an important characteristic of swirling flows. Vanyo (1993) defines a vortex as a mass of fluid whose elements are moving in nearly circular path lines about a common axis. Care must be taken in distinguishing a vortex from vorticity because vorticity is the rotation of infinitesimal fluid elements (Vanyo, 1993). Greitzer et al. (2004) has further characterized the swirling flow as can be having a large variation in static pressure through the vortex core compared to an essentially uniform static pressure across a thin shear layer or boundary layer in a non-swirling flow.

In nature, swirling flows can be observed in case of cyclones, dust devils, whirlpools and tornados etc. In engineering applications, the swirling flows exist in many engineering applications both as confined (cyclone separators and swirl tubes, rotary kilns, co-axially rotating cylinders, hydraulic turbine draft tubes etc.) and un-confined (swirling jets in combustors and tornado like flow upstream of the intake of a gas turbine etc.) (Escudier et al. 2006, Lam, 1993). Swirl in the flow enhances heat transfer in heat exchangers, homogenizes mixtures in casting and reactants in chemical industry, and in combustion processes breaks fuel droplets and stabilizes the flame (Cazan et al., 2009). Contrarily, the swirl/ vortices generated in some engineering applications e.g. at the intakes of liquid pumps, draft tubes of hydraulic turbines, weirs and draining of reservoirs etc. are by-product of the fluid motion and can severely affect the main function of the equipment (Lam, 1993). Therefore, swirl and its effect on the flow field containing it is very important to be studied. As discussed in Chapter 1, the in-cylinder flow during scavenging process of large two-stroke diesel engine is also a confined

swirling flow. Thus the focus in this chapter is on the theoretical aspects of confined swirling flows.

2.1 Classification of Confined Swirling Flows

Swirl flows mostly are classified based on their tangential velocity profile (Vanyo 1993, Steenbergen et al. 1998, Hoffmann et al. 2002). Moene (2003) has given a rough classification of different tangential velocity profiles (Figure 2.1).

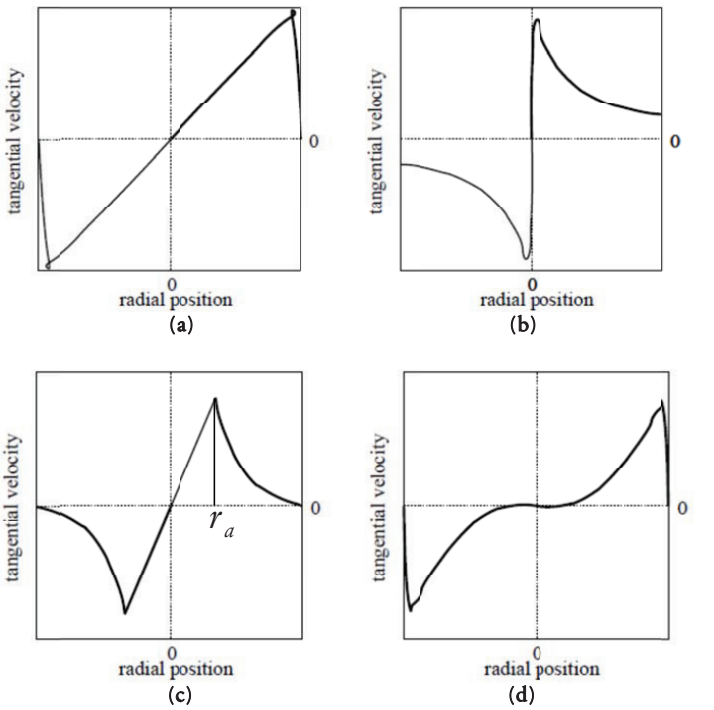

Figure 2.1:

Classification of Swirl Types (Moene, 2003).

(a) ***Forced Vortex***: Flow essentially has a solid body rotation i.e. the linear (tangential in this case) velocity increases with the increase in the distance from the vortex center (Figure 2.1a). In case of a confined swirling flow, the tangential velocity increases with radius until it reaches the wall boundary layer where it decreases to zero at the wall.

The flow in a forced vortex is rotational. The tangential velocity is given by

$$v_\theta = r\ \Omega \tag{2.1}$$

Where Ω is the angular velocity and r is the radial distance from the center of the vortex. The fluid is without shear and has a vorticity of 2Ω at each position in the vortex (Wikipedia, 2010).

(b) ***Free Vortex***: Also named as 'line' or 'potential' vortex (Figure 2.1b). The tangential velocity decreases as the distance from the vortex center increases. Vorticity is zero at all positions in the vortex except for a singularity in the vortex core center line. The flow is therefore irrotational. The tangential velocity is given a:

$$v_\theta = \frac{\text{constant}}{r} \tag{2.2}$$

(c) ***Rankine Vortex***: It is a combination of forced and free vortex type (Figure 2.1c). The tangential velocity in the inner core region has a forced vortex profile and the outer flow region has a free vortex profile. The flow in the forced vortex is rotational and irrotational outside it. The tangential velocity profile has a sharp peak at some arbitrary radial position 'r_a' where the inner forced vortex profile meets the outer free vortex. This is an approximation to Burgers vortex discussed later.

(d) ***Wall Jet***: The type of swirling flow in figure 2.1d can be understood by considering plane wall jets. In case of plane jets, a wall-jet is defined as a fluid jet that is issued tangentially to and grows on a wall (Pani et al., 1976). Due to velocity discontinuity, a shear layer develops on the fluid side and on the wall side a boundary layer is developed (Rajaratnam, 1976). For confined swirling flows with tangential wall-jet like profile, analogous to plane wall jets, a tangential velocity jet is issued to the cylinder walls. Maximum tangential velocity is observed at a radial distance from curved wall where the shear layer meets the wall boundary layer and minimum tangential velocity is observed in the vortex center.

The above mentioned profiles represent the tangential velocity field in ideal fluids i.e. without the effect of wall friction and intermolecular friction due to viscosity. In real, for example, in some swirling flows the solid body rotation is found only in some part of the flow cross-section. In case of 'Rankine vortex', there exists no sharp peak at the interface of inner forced and outer free vortices. Instead a smooth curve in indicates a smooth transition between the two vortex regions. This profile is called a 'Burgers Vortex' profile which is axis-symmetry, accounts for fluid viscosity and is an exact solution of the Navier-Stokes equations (Figure 2.2) (Alekseenko 2007).

The tangential velocity profile for the Burgers vortex is given in equation (2.3) (Escudier et al., 1982).

$$v_\theta = \frac{\Gamma}{2\pi r}\left[1 - \exp\left(-r^2/\delta^2\right)\right] \tag{2.3}$$

Where Γ is the circulation around the vortex core and δ is a length scale representing the effective size of the vortex core.

Very close to the wall there is also a steep gradient in the velocity profile due to no slip condition at the wall. This modified shape of Rankine/ Burgers vortex profile is classified by Steenbergen et al. (1998) as a 'Concentrated Vortex' (Figure 2.3). However, there is no accurate definition of a concentrated vortex and for an ideal fluid it is rigorously defined as a space-localized zone with non-zero vorticity surrounded by a potential flow (Alekseenko et al., 2007). In other words, the vorticity is concentrated in a small tubular region near the vortex center, decaying rapidly outward in radial direction (Lam, 1993). Depending on the similarity with the aforementioned definition of concentrated vortex, a great variety of vortex flows in nature and engineering can be interpreted as concentrated vortices; most commonly are columnar or filament-type vortex (whirlpool in liquid flowing out of a container, tornado and vortices in flow over delta wing under a high attack angle etc.) (Alekseenko et al., 2007). In case of highly turbulent swirling flows, the instantaneous velocity field is very complex and it is the mean tangential velocity profile that is used to identify the type of the vortex.

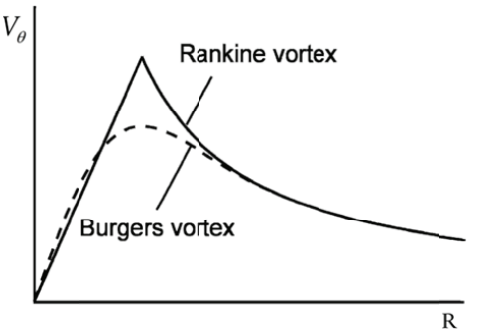

Figure 2.2:

Tangential Velocity Profiles for Rankine and Burgers Vortex (Alekseenko et al., 2007).

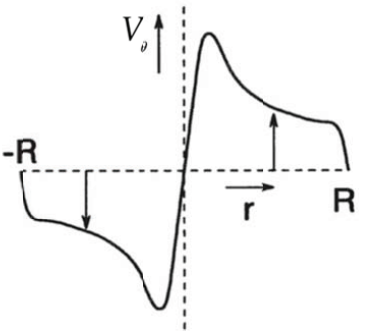

Figure 2.3:

Tangential Velocity Profile for a Concentrated (Steenbergen et al., 1998).

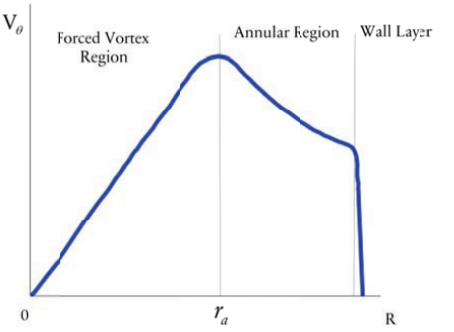

Figure 2.4:

Schematic of Different Regions in Tangential Velocity Profile for a Concentrated Vortex. Modification of illustration by (Islek A.A., 2004).

Figure 2.4 gives a description of different regions in the tangential velocity profile of a concentrated vortex. As discussed earlier in case of Rankine vortex, the vortex core has a forced vortex profile until a radial distance 'r_a' where the maximum tangential velocity is observed. In real swirling flows, the radial position 'r_a' in figure 2.4 is determined by tangential velocities, viscosity, turbulence, and/or the introduction of non-rotating fluid at the vortex center (Vanyo, 1993). The 'wall layer' has very large gradients and flow in this region, in cylindrical enclosures, is probably influenced by Görtler vortices (Escudier et al., 2006). Görtler vortices are secondary flows that appear in a boundary layer flow along a concave wall *see* Saric (1994) for details. Further, in the near wall region, vorticity is generated due to skin friction factor acting as an external force to a very thin fluid layer attached to the wall (Ebrahimi et al., 2007). The region in between the forced vortex and wall layer is 'Annular region'. The flow in this region should ideally be irrotational (based on description of Rankine vortex). However, in real flows this region has a very low vorticity. The visualization results by Escudier et al. (1982) show ring-like large vortices in the outer region and appear to be of Taylor-Görtler type; distorted by the axial flow and also responsible for uniformly distributing the small amount of vorticity from highly vortical vortex core. Alekseenko et al. (1999) also found out that the experimental

data for V_θ profile in a vortex chamber did not agree to the empirical formula by Escudier et al. (1982) in the annular region.

2.2 Methods of Swirl Generation

Swirl in the flow is generated by imparting tangential velocities in to the flow. In the experimental setups the flow passes through the swirl generator before entering into the main cylinder/ pipe/ tube or chamber where the measurements are due to be taken. Different types of swirl generation are shown in figure 2.5.

There are basically two categories of swirl generators as described below:

(1) The flow, after passing through the swirl generator, enters the main chamber with a combination of tangential and radial component. These types of swirl generators are mostly employed with guide vanes that are fixed at a certain angle(s) to obtain a desired swirl and in some cases the inlet is fitted in a tangential direction to the vortex chamber (Figure 2.5 a and b). Another way is that the flow enters the main chamber through nozzles fitted or ports grooved (as in Large Two Stroke Diesel Engines) on the periphery of the chamber walls. These nozzles or ports are at an angle with the radius of the chamber.

(2) The second category contains devices that are axially aligned with the main chamber. The flow enters the swirl generator in axial direction and the swirl is introduced by a twisted tape or a propeller or an externally rotated honeycomb (Figure 2.5 c and d).

The physical design of the swirl generator and the way swirl is introduced in the pipe/ cylinder plays a very significant role in the resulting confined swirling flow. For example, in experiments where the swirl is generated by a rotating honeycomb section fitted axially with the test cylinder/ pipe, the tangential velocity peak is always observed at larger distance from the cylinder axis see (Pashtrapanska et al. 2006, Marliani et al., 2003) etc. The vortex core will be large in size and the size of the annular region will be small. The reason for this profile is due to the solid body rotation of the honey-comb section and the flow passing through it following the same profile. Due to the presence of wall boundary layer the location of peak tangential velocity is observed at a small distance from the wall. The size of the vortex is also influenced by the magnitude of radial velocity and in the case of rotating honeycomb, swirl is introduced in a non-swirling axially flowing fluid a larger vortex core should be expected. In the experiments where the swirl is generated by a propeller (Parchen et al. 1998, Algifri et al. 1988) or twisted tape (Young et al. 1978) etc., also mounted axially with the pipe axis, the tangential velocity profile and the vortex core size depend on the physical profile of the twisted tape and propeller blades. In case of swirl generators with guide vanes and a conical shaped center body (Sarpkaya 1974, Faler et al. 1977, Kitoh 1991) etc. the size of the vortex core is

determined by the thickness of the boundary layer shed by the center body and decreases with an increase in Reynolds number (Leibovich, 1984).

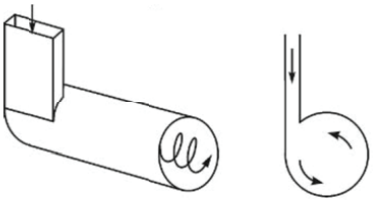

(a) Tangential Inlet (Source: Alekseenko et al., 2007)

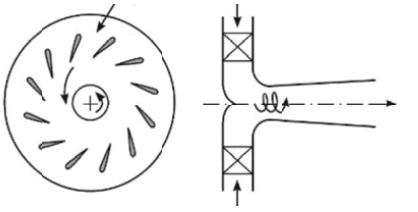

(b) Vane Type (Source: Alekseenko et al., 2007)

Figure 2.5:

Different Methods of Swirl Generation.

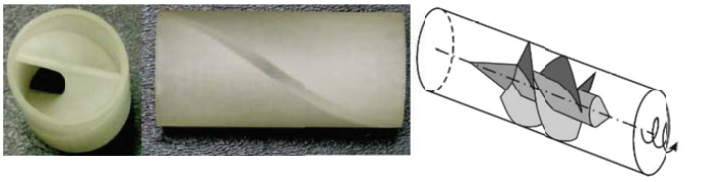

(c) Twisted Tape (Cazan et al., 2009) and Screw Type (Source: Alekseenko et al., 2007)

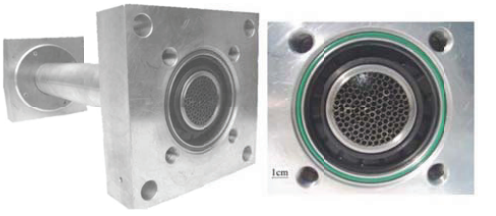

(d) Rotating pipe having Honeycomb (Source: Pashtrapanska, 2006)

There have been a lot of experimental studies on characteristics of turbulent swirling flows in straight pipe/ vortex chamber where swirl is generated using propeller (Algifri et al., 1988) (Parchen et al., 1998), tangential injection (nozzle or holes drilled in tangential direction) (Martemianov et al., 2004) and (Zhang et al. 2006), twisted tape (young et al. 1978) (Islek A. A., 2004) and (Cazan et al., 2009), rotating tube bundle or honeycomb (Marliani et al., 2003 and Pashtrapanska et al, 2006) and fixed vanes (Kitoh, 1991) (Sarpkaya, 1971) (Leibovich et al, 1978) etc. The aforementioned works are very few in a very large amount of experimental measurements available in the scientific literature and a detailed account is beyond the scope of this thesis.

The measurement techniques used also vary and include swirl vortex meters, pitot tubes, hot wire anemometry, Laser Doppler Velocimetry and Particle Image Velocimetry etc. For example Kreith et al. (1965) etc. used swirl vortex meters, (Lam H. C., 1993) etc. used five hole pitot tube, Algifri et al. (1988) and Kitoh (1991) etc. conducted measurements using hot wire anemometry, laser Doppler Velocimetry (LDV) (Parchen et al., 1998) (Marliani et al., 2003) etc. and particle image Velocimetry (PIV) (Zhang et al. 2006) etc.

2.3 *Some Aspects of Swirling Flows*

Swirling flows have different distinct aspects compared to non-swirling flows. In this section only some of the aspects are briefly discussed and for a detailed account see (Alekseenko et al. 2007, Gupta et al. 1984, Saffman 1995, Greitzer et al. 2004, Wu et al., 2006) etc. Effects of Coriolis forces are beyond the scope of this thesis and thus are not discussed.

2.3.1 *Stream line Curvature*

In swirling flows with pure rotation i.e. no bulk flow in axial direction, the streamlines are curved as shown in figure 2.6a. With the addition of axial velocity, the streamline pattern resembles to a spring/ axially stretched spiral object (Figure 2.6b). The spiral shape of the streamlines depends on the type of the swirling flow, axial velocity profile, swirl decay, symmetric or asymmetric swirl, wall curvature in case of cylindrical vortex chamber etc. Figure 2.6c gives a sketch of the streamlines in idealized case of decaying solid-body rotation with uniform axial velocity.

Figure 2.6:

Sketch of Streamlines for Rotating Flows (Moene A.F., 2003).

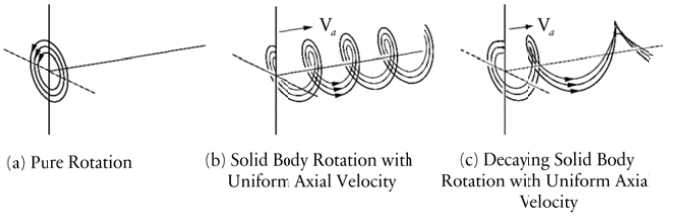

In real turbulent flows the presence of any or a combination of aforementioned factors will give a very complex picture of streamlines and consequently change the overall structure of the turbulent flow field. This topic is discussed in detail in section 2.6 for Numerical modeling of Turbulent Swirling Flows.

2.3.2 *Radial Equilibrium*

A swirling flow with radial equilibrium is the simplest class of swirling flows which is steady, axisymmetric, has radial velocity zero everywhere and consequently has axial velocity, tangential velocity and pressure as a function of radial distance from the vortex center (Greitzer et al., 2004). In such a flow the continuity, axial and circumferential momentum equations are satisfied except the radial momentum. In such a flow the tangential/ circumferential motion generates centrifugal forces which balance or become in equilibrium with the radial pressure gradient (Sloan et al., 1986). This strong coupling between swirl and the pressure field has made the modeling of swirling flows very complex (Ansys Fluent 12.1 user guide).

$$\frac{1}{\rho}\frac{dp}{dr} = \frac{v_\theta^2}{r} \tag{2.4}$$

In experimental results of real turbulent swirling flows, the radial velocity is not zero but very small in magnitude compared to axial and tangential velocity components (Kitoh, 1991) etc. In case of asymmetric swirling flows the radial pressure gradient will not be same in all radial directions due to asymmetric distribution of tangential velocity.

2.3.3 *Swirl Intensity and Decay*

In order to quantify the amount or degree of swirl in a given swirling flow, the most commonly used non-dimensional parameter is the 'Swirl Parameter/ Number' denoted by a symbol 'S'. However, there is no universal definition/ equation to calculate this. There are many definitions

that have been used by the scientific community and this often makes it difficult to compare the results of one case of swirling flow with the other. In its simplest definition, the swirl parameter is defined as 'the ratio of maximum tangential velocity to the maximum axial velocity' (Alekseenko et al., 2007). Greitzer et al. (2004) has adopted the definition as the ratio of tangential to axial velocity. The definition by Gupta et al (1984) defines swirl number as 'the ratio of axial flux of angular momentum to axial flux of axial momentum times the size L (which in case of cylindrical vortex chamber is the internal radius R of the chamber)' (Alekseenko et al., 2007).

$$S = \frac{F_{mm}}{F_m L} \tag{2.5}$$

Where

$$F_{mm} = \int_A \left(\rho v_\theta v_a + \rho \overline{v'_\theta v'_z} \right) r \, dA \tag{2.6}$$

is the angular momentum flux taking into account the component of the Reynolds shear stress tensor and

$$F_m = \int_A \left(\rho v_a^2 + \rho \overline{v'^2_a} + \left(p - p_\infty \right) \right) \, dA \tag{2.7}$$

is the momentum flux in axial direction taking in to account the normal component of Reynolds stress tensor in axial direction. The pressure represents the axial thrust (Khanna V. K., 2001).

The calculation of swirl number based on above equations (2.5-2.7) is often very difficult because the velocity fields are usually unknown a priori (Alekseenko et al., 2007). The above equations are also simplified by dropping the shear stress and pressure terms. In case of experimental results, the use of above equations requires a complete knowledge of the velocity field for both axial and tangential components for a given cross-sectional plane. Consequently, for experiments where measurements are conducted for a part of the cross-sectional plane, the aforementioned equations cannot be used to estimate the degree of swirl.

Another estimate of the swirl parameter is based on the geometrical parameters of the vortex chamber called as 'design swirl parameter' (Alekseenko et al., 2007):

$$S = \frac{D d_c}{A_i} \tag{2.8}$$

$$d_c = \mathrm{D}\tan\gamma \tag{2.9}$$

Where D is the internal diameter of the cylindrical chamber, γ is the angle between cylinder radius and direction of nozzle/ inlet, d_c is the diameter of the conditional circle (an imaginary circle to which the nozzle/ inlet direction makes a tangent) and A_t is the total area of nozzles/ inlets (Figure 2.6).

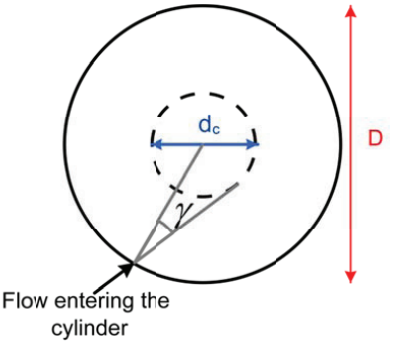

Figure 2.7:

Illustration of design swirl parameter.

Estimation of swirl intensity can also be based on streamline angle equation (2.10) evaluated at some position in the cross-section. However, an axial change in the swirl angle can also be due to axial changes in the axial flow field and near the wall the swirl angle is a function of rate of decay rather than to swirl intensity itself (Steenbergen et al., 1998).

$$\psi = \tan^{-1}\frac{\mathrm{V}_\theta}{\mathrm{V}_a} \tag{2.10}$$

The swirl parameter though important is not the only parameter to characterize the swirling flows. There can be swirl flows having same Reynolds number and the swirl intensity but having quite different flow structures due to different boundary conditions (Alekseenko et al., 2007). Parameters like swirl distribution, distribution of stagnation pressure and vorticity are also important to characterize a given swirling flow yet none of the mentioned parameters can independently characterize a given swirling flow (Greitzer et al., 2004).

The decay of the swirl is caused by the transport of angular momentum to the vortex chamber wall (wall friction) and is a function of streamwise position z . Steenbergen et al. (1998) reports that in most observed references with low swirl intensities the decay in the swirl is exponential and can be

fitted with exponential decay functions (Equation 2.11). However, for high swirl number flows this function is an approximation (Steenbergen et al., 1998).

$$S(z) = S_o \, e^{-\beta \frac{z}{D}} \tag{2.11}$$

Where S_o is the initial swirl intensity. β is the rate of decay and is a function of friction factor for fully developed pipe flow.

2.3.4 *Upstream influence*

Swirling flows, at certain swirl number, begin to exhibit an influence on the upstream velocity profile at high swirl numbers. Escudier et al. (1985) conducted LDA experimentation on a model of swirl combustor with water as the fluid and no combustion involved. Figure 2.8 shows the streamline plots at Re=10,600 derived from the LDA measurements, on the effect of exit contraction on the upstream flow inside the aforementioned experimental test setup. Figures 2.7a & b are for a given low swirl number and figures 2.8c,d are for a high swirl number flow. It can be seen that at the given low swirl number the upstream effect of an exit contraction is very small but at a higher swirl number there is a significant change in the upstream streamline profiles. This upstream influence is often defined as the criticality of the flow where downstream information travels upstream and the swirling flow is called to be subcritical. The flows below the critical swirl number exhibit small or no upstream influence are defined to be in supercritical regime.

The upstream influence of swirling flow requires that the guidelines for assuming no coupling between fluid components or for the selection of the type of boundary conditions needed in numerical models are different compared to non-swirling flows (Greitzer et al., 2004).

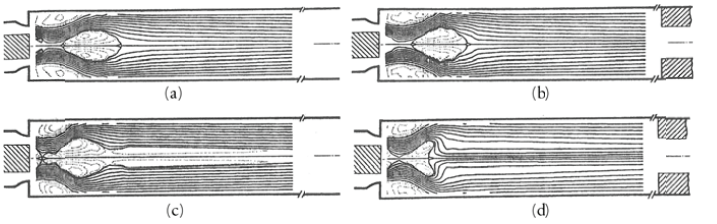

Figure 2.8:

Sketch of Streamlines for Swirl Combustor test model (Escudier et al., 1987).

2.3.5 *Instabilities and Vortex Breakdown in swirling Flows*

In swirl flows, instabilities (unsteady phenomena) have many aspects to be studied. Generally, in case of mostly laminar swirl flows, a steady flow is subjected to small unsteadiness/ disturbance and the response of the flow is observed in the form of whether there is growth or decay. With the presence of swirl in the flow, the instability associated means that some tangential velocity distributions consistent with the simple redial equilibrium are unstable and not achievable in practice (Greitzer et al., 2004). This method is called the 'linear stability analysis' and in case of turbulent flows such introduced 'small' fluctuations are smaller than the turbulent fluctuations and any conclusion of growth or decay of the disturbance always has the growth and decay of turbulent fluctuations as the major contributor (Moene, 2003). Other significant stability studies involve studying vortex break down, precession of vortex cores (PVC), growth and decay of Reynolds normal stress components and the anisotropy of the Reynolds stress tensor etc.

The vortex breakdown is an important aspect of swirling flows. In general the vortex breakdown has two distinct types: (i) Bubble or axis symmetric type where there is rapid expansion of vortex core in to a near axis symmetric bubble shape (Figure 2.9a) and (ii) Spiral type where the vortex core deforms into a spiral (Figure 2.9b). Sarpkaya (1972) also observed a double helix type.

Benjamin (1962) described vortex breakdown as abrupt and drastic change of flow structure and Ludwieg (1961) suggested that it might be a finite-amplitude manifestation of the instability of the core flow. Velte et al., (2010) define vortex breakdown as explosion or abrupt growth of the slender vortex core with different changes in the flow topology. So far a lot of experimental measurements, observations and numerical studies have been conducted to understand this phenomenon but still the physical mechanism of vortex breakdown is not well understood. The phenomenon remains largely in the qualitative, descriptive realm of knowledge (Novak et al., 2000). In case of confined swirling flows, the experiments conducted by Escudier et al. (1982), show that the consequence of a vortex breakdown is a profile shape change for the axial velocity i.e. from jet-like to wake-like with an intermediate stagnation region. Escudier et al. (1982) discusses that the spatial growth rate of instability waves is very different in the two axial velocity profile types. The upstream jet-like profile becomes unstable and instability waves amplify slowly. Then the core flow undergoes a shock-like transition at some downstream position and the waves grow rapidly on a low velocity wake-like profile. Escudier et al. (1982) suggests that the swirl intensity (flow criticality) is the main parameter that determines the basic characteristic of the downstream flow and the effect of instability waves are superimposed over it.

Alekseenko at el. (2007) has given pictures of many different vortex breakdown structures both in confined and unconfined swirling flow experiments.

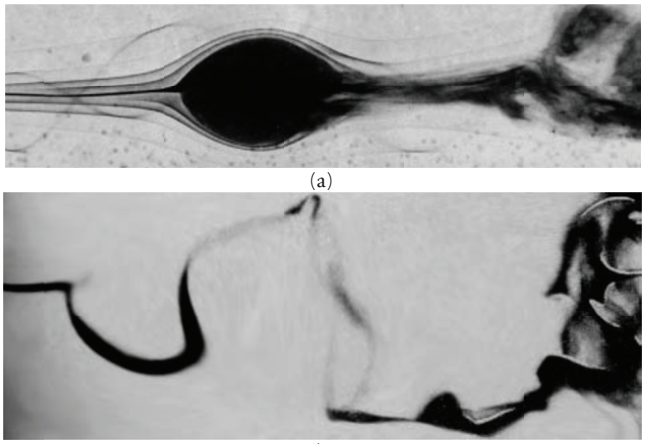

(a)

(b)

Figure 2.9:

Vortex Breakdown Types: (a) Bubble (b) Spiral. (Alekseenko et al., 2007).

The vortex breakdown is often not only asymmetric but also highly time dependent in nature (Lucca-Negro et al., 2000). Novak et al. (2000) using high speed camera, conducted visualization of vortex breakdown at high Reynolds number in the range of 10^5. The observations revealed the existence of single and double spiral breakdowns which previously was observed by Sarpkaya et al. (1995) to be a conical shape using a comparatively lower speed camera. This conical shape is observed due to rotations of spirals at high rotational speeds of 1000 rev/s. The measurements by Novak et al. (2000) show that at high Reynolds number of 3×10^5 the mean axial velocity at the center line never becomes negative/ reversed. Additionally, the results show that for high Reynolds numbers the spiral breakdown bypasses the two celled bubble form and bursts into turbulence.

At high Reynolds numbers, a large three dimensional time dependent instability is developed called as 'Precessing vortex core (PVC)' (Yazdabadi et al., 1994). This is the result of the forced vortex region of the flow becoming unstable and displaced from the axis of symmetry and start to precess about the axis (Lucca-Negro et al., 2000). The PVC has a regular frequency and amplitude and in some cases can cause many problems by locking onto other system instabilities and resonating with them (Yazdabadi et al., 1994). At high Reynolds numbers, the vortex breakdown is also observed to dart back and forth along the axis (Novak et al., 2000).

2.3.6 *Helical Vortex Structures*

In swirl flows with filament type vortices, the vortex filament almost never has a straight/ rectilinear axis due to different instabilities and waves

propagating along it (Alekseenko et al., 2007). Instead the vortex filament is radially displaced from the axis of the container (pipe/ cylinder in this case) and takes the shape of a helix wrapped around the cylinder axis along the flow. Swirl/ vortex flows exhibiting this characteristic are called 'helical swirl/ vortex flows' (Figure 2.10) (Alekseenko et al., 2007).

Helical swirl flows, like axis-symmetric and non-helical asymmetric swirl flows, involves the characteristics e.g. wave propagation on vortex core, vortex breakdown and PVC etc., that have been discussed in previous sections. However, the helical structure of the vortex core brings more complexity to the overall flow structure and its consequent behavior. For example in case of a helical swirl flow confined in a device like pipe/ cylinder etc., Figure 2.11 shows the streamlines (projections) when the vortex core is radially displaced (for further possible structures see Alekseenko et al., 1999 & 2007). The consequent effect of cylinder wall is like a 'mirror vortex' i.e. the actual vortex feels that there is another vortex of identical properties at the same radial distance from the wall but rotating in opposite direction (Figure 2.12).

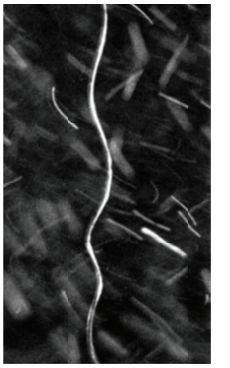

Figure 2.10:

Vortex Filament in a chamber with rotating bottom (Alekseenko et al., 2007).

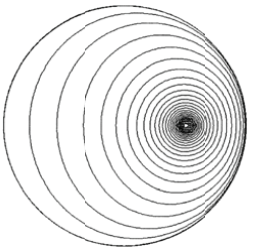

Figure 2.11:

Streamlines (Projections) in a cross-sectional plane for a helical vortex Filament in a tube (Alekseenko et al., 1999).

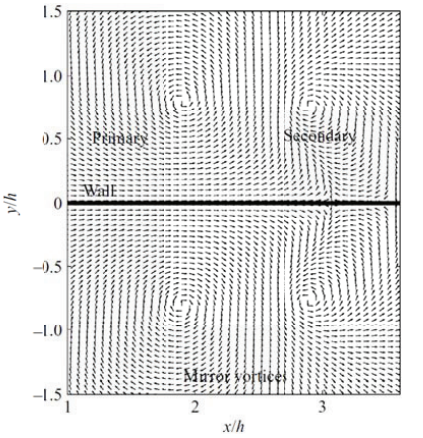

Figure 2.12:

Sketch of mirror vortex effect of wall. The wall is illustrated by a thick line at y/h=0 (Velte et al., 2009).

Figure (2.13) shows the sketches of different models of axisymmetric helical vortex filaments where l is pitch of the helix, V_z axial velocity and ω_z and ω_θ are the axial and tangential vorticity components respectively. For the same Reynolds and swirl numbers different axial velocity profiles can be observed i.e. uniform axial velocity with rectilinear vortex lines and infinite helix pitch (Figure 2.13a), jet-like axial velocity profile generated by right-handed helical vortex (Figure 2.13b) and wake-like profile generated by a left-handed helical vortex (Figure 2.13c). In some cases, the left handed helical vortex can result in generating a counter flow regime. Practically the existence of different vortex symmetries indicates that the Reynolds and swirl numbers are not sufficient to characterize the different aspects e.g. heat and mass transfers for the swirling flows (Martemianov et al., 2004). In real, the vortices have finite size cores and even in some cases the helix is not axis symmetrical. The radius of helix and the pitch can also vary at different cross-sectional positions along the flow and one of the many possible reasons may be the geometrical shape of the inlet and outlet of the vortex chamber which affects the flow properties (a contraction section at the outlet introduces axial strain etc.). Alekseenko et al. (2007) have also discussed the experimental where double helical vortex filaments are observed. In non-stationary helical vortices the helix also is a function of time in a periodic manner.

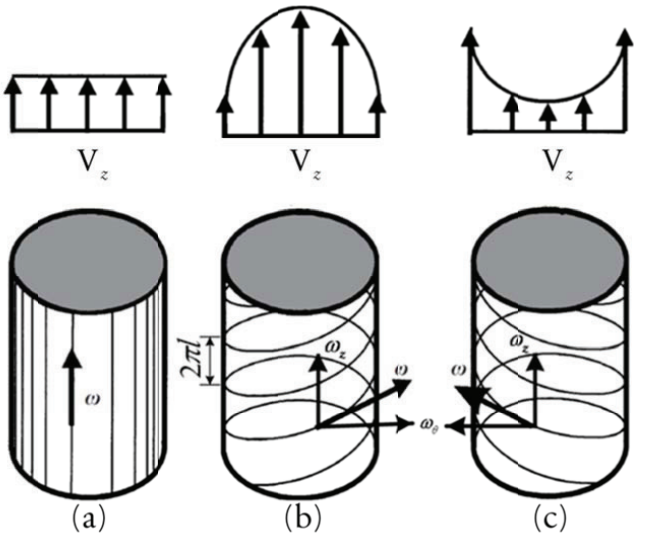

Figure 2.13:

Schemes of axisymmetrical helical vortex. Modification of original figure from (Alekseenko et al., 1999).

Okulov et al., (2002) have described the vortex breakdown as a spontaneous transition from right to left handed helical vortices and vice versa under the same integral flow parameters. This continuous transition between the two helical vortex types happens in two different ways as shown in figure 2.13:

(1) The pitch is positive for the right handed helical vortex and during the transition the pitch becomes infinite and then attains a negative value for left handed helical vortex. This type of transition is names L (linear)-transition (Figure 2.14a).

(2) In the other case the positive pitch for right handed vortex becomes zero during the transition before changing to negative value for left handed vortex. This type is called R (ring)-transition (Figure 2.14a).

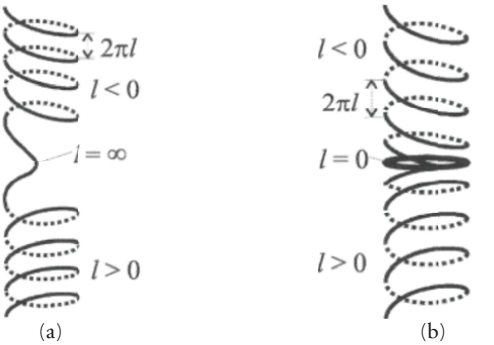

Figure 2.14:

Transition of helical vortices (a) L-Transition (b) R-Transition (Okulov et al., 2002).

In real confined swirling flows, there can exist many examples where in a single vortex chamber a helical swirling flow exists where the vortex core filament not only precess around the vortex chamber axis but also has a periodic behavior and undergoes vortex breakdown at some cross-sectional position. The presence of wall will make the overall behavior of this confined swirling flow even more complex as the 'mirror vortex' effect will make the flow behave as if two parallel helical vortex systems are existed inside the vortex chamber. In case of highly turbulent swirling flows, the empirical models developed (see Alekseenko et al., 2007) are compared with the averaged values obtained from the experimental results. For the computational models, the swirling flows are also one of the challenging areas.

2.4 CFD Modeling Challenges

There is a large amount of scientific literature available on the Computational Fluid Dynamics (CFD) modeling of swirling flow. However, the purpose of this section is to discuss some of the aspects of swirling flows that make it very difficult or in other words, require special treatment to model them using standard turbulence models i.e. Two-equation turbulence models and Reynolds Stress Models.

Swirl flows has some challenging features that are absent in simple flows e.g. streamline curvature which is viewed as an extra strain rate (relative to simple shear) if the velocities would be expressed in Cartesian rather than cylindrical coordinates (Moene A.F., 2003), strong departure from local energy equilibrium and effects of turbulence anisotropy (Jakirlic´ et al., 2002).

The standard two equation models such as $k-\varepsilon$, based on Boussinesq's eddy viscosity hypothesis have failed to reproduce important swirling flow features like velocity component decay, jet spreading or diffusion rate, degree of entrainment, characteristics of recirculation zones and Reynolds stress

levels etc. (Sloan et al., 1986). The adoption of a relation that local stresses being directly proportional to local strain rates rules out any special sensitivity to the streamline curvature (Craft et al., 2008). The assumption of turbulent/ eddy viscosity as isotropic cannot be valid in flows influenced by body forces acting in a preferred direction, such as buoyancy, rotation and streamline curvature (Sloan et al., 1986). Algifri et al. (1988) proposed, using experimental data on confined swirling flow, that the eddy viscosity is function of Reynolds and swirl numbers. Further, the $k-\varepsilon$ model is a simplistic function of a single time scale (proportional to a turbulence energy turnover time k/ε) which implies that the spectral energy transfer rates for production of turbulent kinetic energy by mean shear, the intermediate transferal regime and the viscous dissipation regime are equal without any characteristic lag (Sloan et al., 1986).

The second order closure schemes having transport equations for individual components of Reynolds Stress tensor account for the curvature of streamlines however the effect is at least an order of magnitude large than expected (Moene A.F., 2003) i.e. a 1% curvature strain produces for a boundary layer a 10% or greater effect on the turbulent stresses (Bradshaw, 1973). The source terms in dissipation ε equation, to a significant degree control the magnitude of turbulent kinetic energy, mean velocity decay and the spreading rates (Sloan et al., 1986). However, the transport equations for k and ε have no specific terms (source) to account for sensitiveness to rotation and swirl (Jakirlic´ et al., 2002). Since both of these transport equations are common in two-equation and second order closure schemes, the performance of second order closure schemes are also affected to some degree for modeling the swirling flows. Numerical issues also have significant impact on predicting the behavior of swirling flows (Craft et al., 2008).

Different modeling approaches so far have been adopted to improve the performance of the aforementioned turbulence models and some of them are discussed here in brief. In order to include a rapid response to streamline curvature, the coefficient C_μ in the turbulent viscosity equation (2.12) has been altered to a functional form (see Leshcziner et al., 1981). Sloan et al., (1986) reports that more complex versions of C_μ have been developed that include non-equilibrium turbulence and wall damping.

$$\mu_t = C_\mu . \rho . \frac{k^2}{\varepsilon} \tag{2.12}$$

Where μ_t is turbulent viscosity, C_μ is a constant and has empirically determined value of 0.09 and ρ is the fluid density.

Yakhot et al., (1992) developed the RNG $k-\varepsilon$ model which, unlike the standard $k-\varepsilon$ model, is derived using a statistical technique called

'Renormalization Group Theory'. The model has an additional term in the ε equation that improves the accuracy in terms of rapidly strained flows (Najafi et al., 2005). The model also accounts for the effect of swirl or rotation by modifying the turbulent viscosity, given in function form in equation (2.13) (ANSYS FLUENT, 2009).

$$\mu_t = \mu_{t_0} f\left(\alpha_s, S_c, \frac{k}{\varepsilon}\right) \tag{2.13}$$

Where μ_{t_0} is the value of turbulent viscosity calculated without swirl using equation (2.12), S_c is the characteristic swirl number and α_s is swirl constant having different values based on whether the flow is strongly or mildly swirl dominated.

In other attempts to account for streamline curvature involves modifications in the source term for ε equation by including the 'gradient Richardson number' which is the ratio of centrifugal force to a typical inertial force and in context of swirling flows, the extra mean rates of strain associated with a curved shear layer may be regarded as producing the effects of a centrifugal force on a displaced element (Sloan et al., 1986).

In case of second order closure schemes, the predictions in general are better compared to two equation models in some cases but still their performance is not universal to different swirling flow regimes in experimental and industrial devices. One of the weaknesses is that neither the modeling of terms nor the numerical values of the model constants are fully established (Sloan et al., 1986). Further, the stress transport equations are numerically very sensitive and using higher order discretization schemes may sometimes destabilize the computations. Jawarneh et al. (2006) also used first-order upwind discretization schemes for the Reynolds stresses. However, confined swirling flow calculations performed by Strugess et al. (1985) demonstrate that the errors due to numerical diffusion can make a suitable turbulence model to produce bad results. Further, Craft et al. (2008) demonstrated different performance of same Reynolds stress model for a given case but using 3D elliptic and parabolic solvers.

Experimental Setup

In this chapter a description of the experimental test model of scavenging flow is given and different aspects of the design are discussed in detail. Overall experimental setup is explained and results from smoke visualization test are presented. Setup arrangements for the Stereoscopic Particle Image Velocimetry and Laser Doppler Anemometry measurements are defined. A comparison between the real engine scavenging process and the test model is discussed.

3.1 Scavenging Flow Test Model

In order to simplify the problem an experimental down-scale and simplified model of the engine cylinder is developed which is analogous to a straight cylinder/ pipe connected to a swirl generator but having features like movable piston, cylinder head and guide vanes to divert the flow entering the cylinder at a desired angle etc. (Figure 3.1). The setup is developed as a part of a Bachelors thesis project by Andersen et al. (2008) co-supervised by the author. The focus in this study is on the characterization of in-cylinder confined swirling flow and at different Reynolds number. The experimental results thus are not only significant for understanding the in-cylinder swirling flow during scavenging process but also very useful for the fundamental studies in turbulent confined swirling flows.

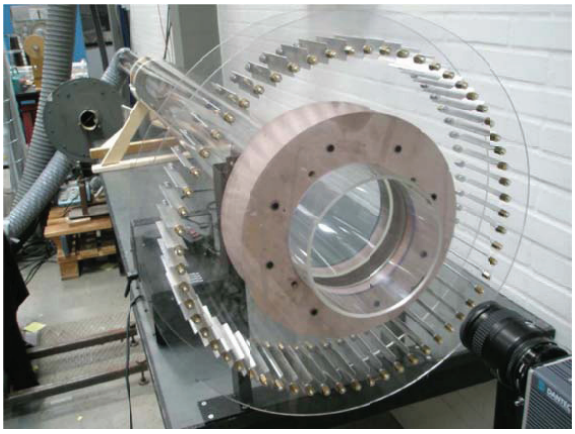

Figure 3.1:

Scavenging Flow Test model (Andersen et al., 2008).

3.1.1 *Cylinder*

A transparent acrylic cylinder (produced using casting process to give good optical properties) is used. The total length of the cylinder is (L=1945 mm) with internal diameter (D= 190 mm) and external diameter (Do=200 mm). One end of the cylinder is fitted inside the inlet section and at the other end an outlet section is fitted.

3.1.2 *Inlet Section (Swirl Generator)*

The inlet section consists of two transparent ring-shaped acrylic plates (Do=600 mm) (Figure 3.2). The plates are fitted in parallel by mounting 60 guide vanes in between them thus serving as walls bounding the flow. The distance between the internal walls of the plates/ height of individual blade is 100 mm. A screen with 51% open area ratio is glued around the outer periphery of the inlet section as shown in figure 1. A contraction section with larger end at 100mm and smaller end 40 mm is mounted internally at the inner periphery of the inlet section (profile given in Appendix D) (Figure 3.2).

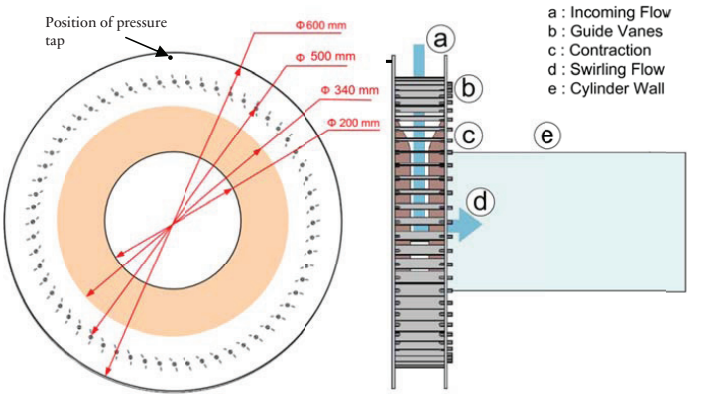

Figure 3.2:

Inlet Section design (modification of original figure by Andersen et al., 2008).

An overview of individual guide vane construction is shown in figure 3.3. Each guide vane has a thickness of 1 mm and a width of 26.16 mm. The guide vanes are then adjusted in a way that one end is aligned in radial direction with the inlet. The flow enters the guide vane in radial direction and diverts at an angle of 35°. The guide vanes are mounted at a large radial distance from the geometric center of the cylinder and close to the inlet (Figure 3.2). This will give some time to the flow after the vanes to settle thereby minimizing the wake effects. Further, before entering in to the

cylinder, the flow enters a bell-mouth shape contraction section which will accelerate the flow and reduce the velocity fluctuations. The acrylic cylinder is entered in to the inlet section from one side and from other side, a transparent piston is mounted. The piston can slide inside the cylinder thus partially/ fully closing the cylinder inlet section, similar in a way that in real engine the reciprocating piston uncovers and covers the scavenging ports during the scavenging process. However, current work is focused on studying the in-cylinder swirling flow when the piston is at the BDC (the inlet to the cylinder is fully open) and piston positions where it covers the intake port by 25%, 50% and 75%., depending on the two experiments described in Chapter 4 and 5.

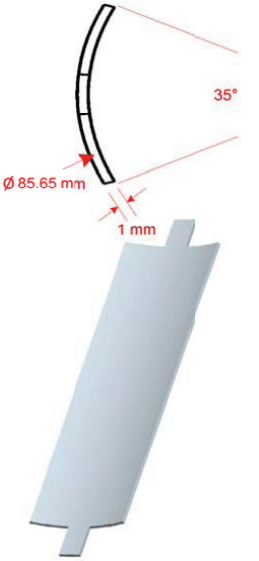

Figure 3.3:

Guide Vane design.

3.1.3 *Outlet Section*

The outlet section consists of a smaller internal diameter pipe (D_e=110 mm) and length (L_e=1415mm). Large length of the pipe will minimize any possible effect on the nature of the swirling flow inside the cylinder due to bending in connecting pipes to orifice plate and fan. The shape of the outlet provides a flat-bottom head to the cylinder. The outlet section can slide inside the cylinder and facilitates to conduct experiments at a desired effective length of the cylinder which in this study is kept at 4D, 6D and 8D.

3.2 Experimental Setup

An overview of the overall experimental setup is shown in figure 3.4.

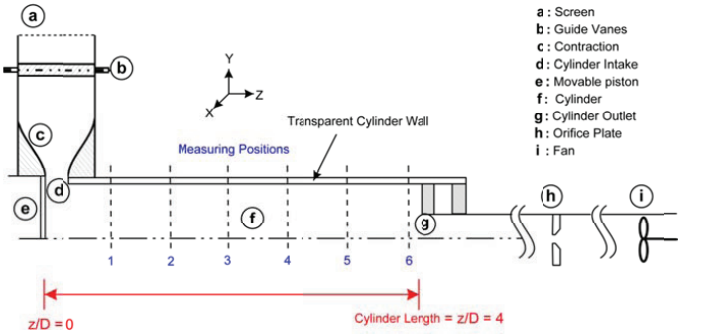

Figure 3.4:

Illustration of Scavenging Flow Experimental Setup.

The scavenging flow test rig is mounted horizontally on a table. The downstream end of the outlet pipe, using a flexible plastic pipe, is connected with another long and straight pipe fitted with the orifice plate. The pressure drop at the orifice plate is measured using a U-tube manometer and the volumetric flow rate is calculated. A blower with speed controller is connected to other end of the straight pipe.

A suction pressure is generated by the blower which in turn drives the ambient air to enter the inlet section Since the guide vanes are at a radial distance of 50 mm from the flow enters the inlet section in radial direction by passing through the screen. The screen 'a' in figure 3.4 will improve the uniformity of the flow at the inlet. The guide vanes 'b' in figure 3.4 divert the flow at a desired angle and the flow after passing through the guide vanes has both radial and tangential components. Any wake effects behind the blades are assumed to decrease significantly before the flow enters the contraction section which increases velocity magnitude, reduces the velocity fluctuations and suppresses the boundary layer ('c' in Figure 3.4). The outlet of the contraction section serves as an entrance/ intake port to the test cylinder and has a maximum width of 40mm when the piston is at BDC thus keeping the port fully open ('d' in Figure 3.4). The width of cylinder intake decreases when the piston is translated inward to positions partially covering the cylinder intake port (See Chapter 5).

The flow enters the cylinder at an angle to the radius and a swirling flow, downstream the test cylinder, is formed. Due to a 90º sharp edge, flow separation occurs at the cylinder wall region close to the intake port and a recirculation zone is expected to form ('d' in Figure 3.4). The swirling flow from the test cylinder enters the outlet pipe having smaller diameter. In order to conserve continuity, the flow accelerates and this acceleration,

introducing an axial strain to the swirling flow, is expected to begin at test cylinder regions very close to the outlet pipe. The flat-bottom-head of the test cylinder, fitted with the outlet pipe, provides 90º sharp edge and another near-wall recirculation/ separation zone is expected to form at the entrance to outlet pipe ('e' in Figure 3.4). The flow from outlet pipe enters a soft and bendable plastic pipe connected to the orifice meter assembly ('f' in Figure 3.4). The internal wall of the bending pipe is not very smooth and some head loss is expected to occur. The flow, after passing the orifice plate, enters the blower ('g' in Figure 3.4). The blower exhaust is connected to the laboratory building exhaust system which exhausts out the air/ glycerin mixture for ensuring safe and healthy working conditions inside. The experiments in this study are conducted mostly in non-gusty outside weather conditions in order to prevent any possible effect of pressure waves, traveling through building exhaust, to the test cylinder thus creating some unsteadiness to the in-cylinder swirling flow.

3.3 Differences between Test Model and Real Engine Scavenging process

The in-cylinder flow during scavenging process is very complex in nature and involves different aspects and phenomena occurring simultaneously. The test model developed in this study is an attempt to simplify that flow. In this way, it makes possible for each phenomenon to be studied and characterized separately/ individually. The major differences between the actual and this simplification of the scavenging process are given below:

- Flow: The in-cylinder flow is steady, incompressible and isothermal.
- Cylinder Geometry: The cylinder head is a flat bottom head without any exhaust valve and diesel spray nozzles. There are no scavenging ports on the lower part of the cylinder wall. The piston top surface is flat and no piston rings are mounted. Thus the clearance between the piston wall and cylinder wall is smaller than real engine.
- Swirl Generation: There is no scavenging box and the air enters the inlet section from surroundings in an axis-symmetric manner. Swirl is induced to the flow using the guide vanes. In real engine, air from the scavenging box enters the cylinder through intake ports which are grooved an angle to the cylinder radius. Thus the in-cylinder swirl can be thought of being generated by the air jets from each intake port. Moreover, the flow entering the engine cylinder is not axis symmetric.
- Fluid Compression and Moving Parts: The piston cannot be moved to complete a stroke thus there is no compression of the fluid inside

the cylinder and the flow is incompressible. The piston can slide to a position where it completely covers/ closes the cylinder intake port. Moreover, the piston is shifted manually from one position to another and it is not in continuous motion like in real engine. Thus the variation in in-cylinder flow characteristics is not a function of time.

- Chemical Species: A mixture of air and very small concentration (in ppm) of glycerol droplets as seeding is used as the working fluid. There is no fuel injection, chemical reaction and exhaust products/ gases.

- Combustion: The measurement is conducted with flowing fluid and experimental setup to be at room temperature. No combustion, heat sources and temperature gradients (in fluid and solid walls, piston and cylinder head) are involved.

- Stratified Flow: Contrary to real engine scavenging process, no fluid density variations occur inside the test cylinder. Therefore, there is no in-cylinder stratified flow regime where the incoming air interacts with exhaust gases which are lower in density than air. Also the test cylinder is mounted horizontally instead of being vertical in real engines. This factor can be significant if there exists a stratified flow.

3.4 Smoke Visualization

A qualitative analysis of the test model is performed by conducting visualization using glycerin smoke from a smoke generator. The smoke is blown in to the setup and pictures are taken using a digital camera. The smoke generator cannot produce a constant jet of smoke and instead injects intermittent puffs of smoke which gradually reduces in concentration at the end of each puff (smoke generator here is one used in Disco/ concerts etc that produces smoke by heating and evaporating glycerin). The smoke enters the experimental setup from one side and the distance is kept in a way that the smoke jet has minimum effect on the actual flow pattern at the inlet to the experimental setup. Figure 3.5 shows the smoke entering the inlet section and being diverted at an angle by the guide vanes thus helping in checking the general performance of the design. The flow then enters the cylinder with an angle to the radius and bends in the axial direction (Figures 3.6).

The pictures presented in figures 3.7-3.11 are taken using a 13W (blue color) energy saver light bulb as light source and pictures are taken using a webcam, Microsoft LifeCam Cinema®. The idea was to attempt to visualize flow patterns by making the blue light giving a fluorescence-like effect after being reflected from the smoke particles. The visualization was carried out by first keeping the experimental setup in darkness and then using blue light as the only light source. The light reflection from glycerin smoke particles

appeared to be the major source of light entering the camera compared to other objects. This made the flow patterns, to some extent, visible inside the test model. Here it must be mentioned that the camera is not perfectly aligned with the experimental setup. For all the pictures the position of the smoke generator was kept the same.

Figures 3.7-3.10 show the visualization of in-cylinder swirling flow observed from piston window i.e. the flow direction is into the picture plane (see Figure 3.4). Figure 3.11 shows observations taken from one side of the test setup. For a given piston position, the figures are not in a time sequence. It can be seen that in case of fully open cylinder intake port, the in-cylinder flow has a well-defined vortex core region (Figures 3.7 & 3.11a). The smoke after entering the cylinder remains confined mostly in the core region and does not mix to a large extent with the region surrounding the vortex. The core size increases in a conical shape downstream the flow. As the port is closed by 25%, the vortex core region becomes comparatively less defined and more mixing of the smoke is observed along the cylinder length (Figures 3.8&3.11b). However, at 50% closed port, the vortex core is no more visible. The smoke stream enters the cylinder and mixes with the surrounding air very quickly (Figures 3.9 & 3.11c). Similar pattern can be seen in case of 75% closed port (Figures 3.10&3.11d). During the smoke visualization experiment, the author observed that for fully open port the smoke stream, after entering the cylinder, entered in the center vortex core at regions adjacent to piston surface. Observing from the side of cylinder in Figure 3.11a, the smoke in the core region along the cylinder had a shape of expanding hollow cone with cone top side to be at the piston surface. However, with the gradual increase in blockage of intake port, the well-defined conical smoke pattern started to disappear. Instead the smoke pattern resembled to a jet (Figure 3.11 c & d). Viewing from the piston side in figures 3.7-3.10, the Smoke stream entered the cylinder center region after travelling some axial distance from the piston surface. This is probably due to piston wall favoring the flow to enter the cylinder with an axial component. The smoke stream was having a flapping behavior after entering the cylinder, just like a thread connected at one end with a fixed object in air stream. This indicates increased turbulence at the cylinder entrance and consequently an increases in the mixing of smoke with the surrounding air as can be seen in (Figure 3.11 c & d).

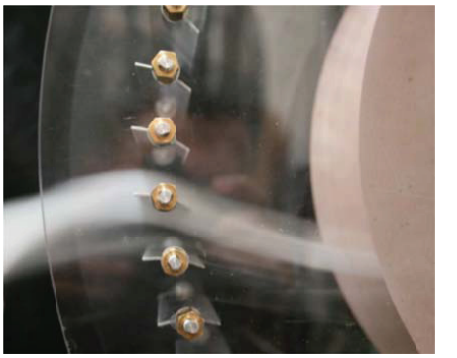

Figure 3.5:

Smoke Visualization of Guide Vanes (Andersen et al., 2008).

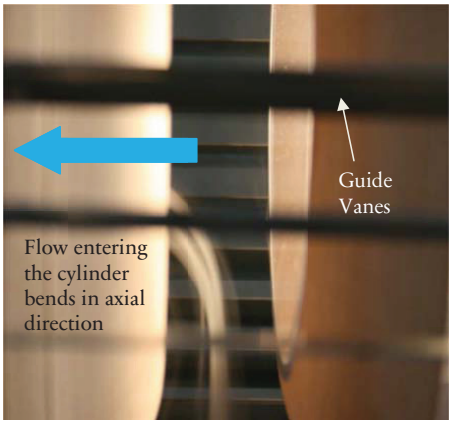

Figure 3.6:

Visualization of Flow Entering the Cylinder (as viewed from Inlet Section) (Andersen et al., 2008).

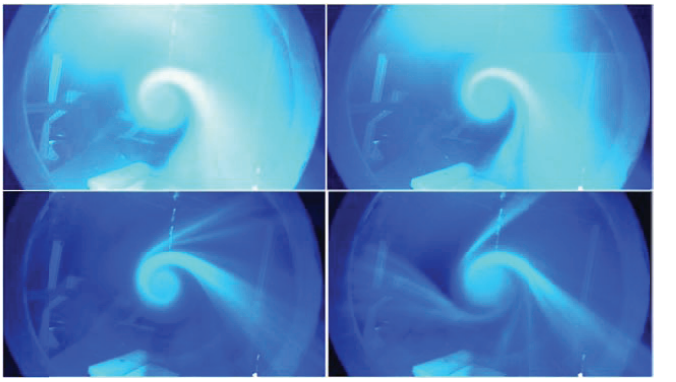

Figure 3.7:

Visualization of Flow Entering the Cylinder, Fully Open Port (as viewed from piston).

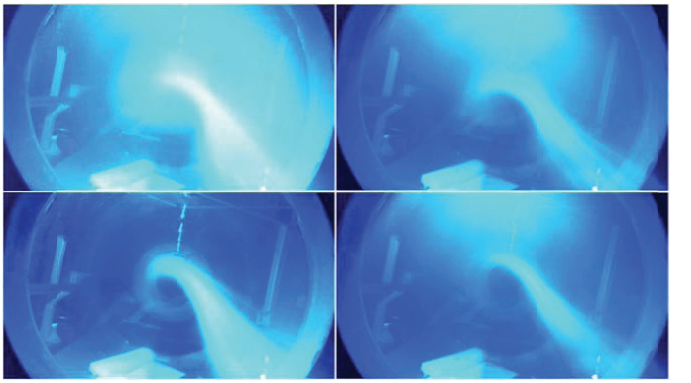

Figure 3.8:

Visualization of Flow Entering the Cylinder, 25% Closed Port (as viewed from piston).

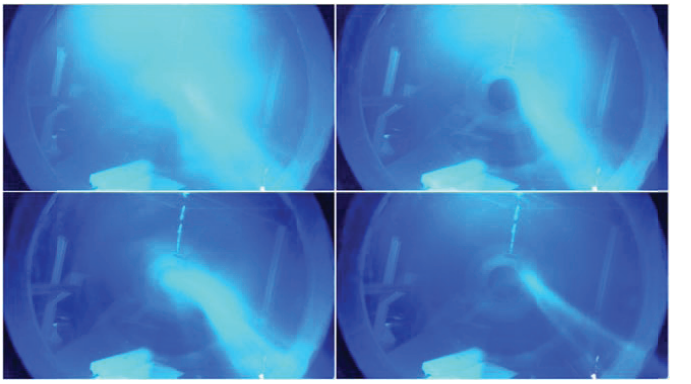

Figure 3.9:

Visualization of Flow Entering the Cylinder, 50% Closed Port (as viewed from piston).

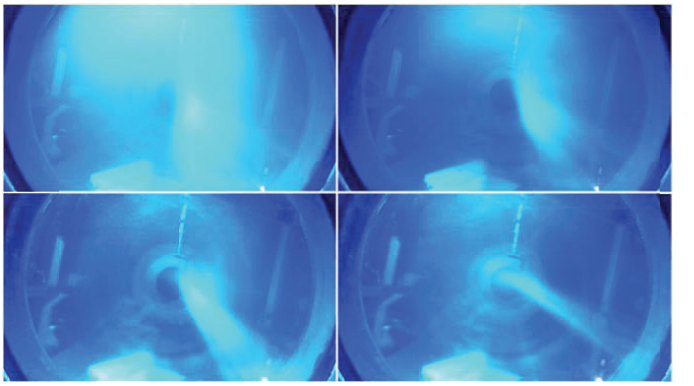

Figure 3.10:

Visualization of Flow Entering the Cylinder, 50% Closed Port (as viewed from piston).

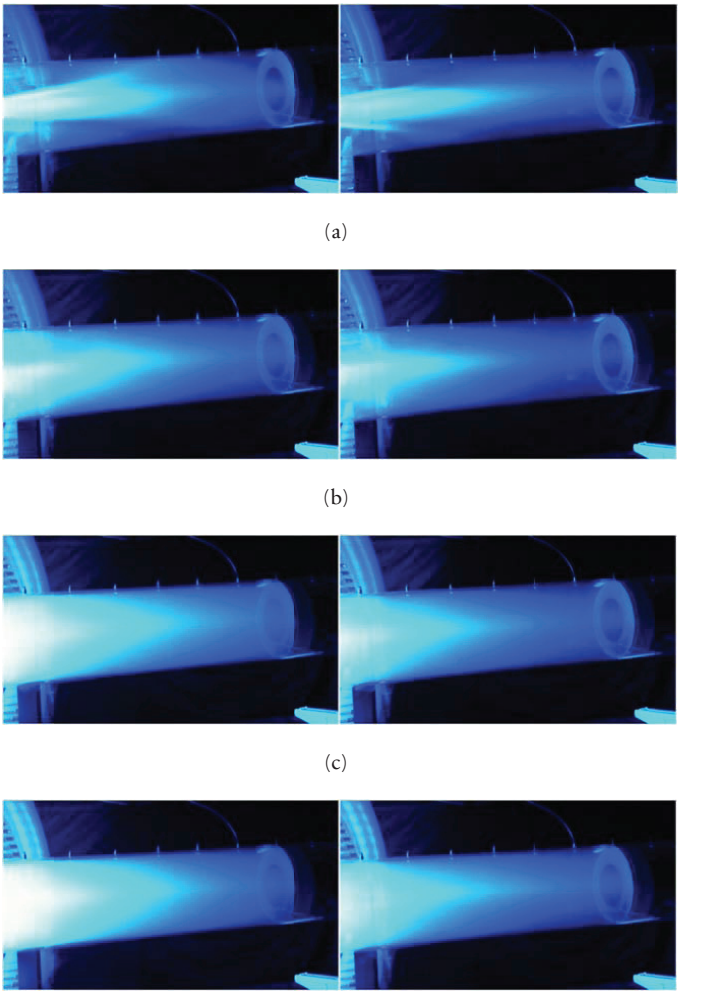

(a)

(b)

(c)

(d)

Figure 3.11:

Visualization of In-Cylinder Swirling Flow (as viewed from Cylinder Outside and flow direction is from left to right) (a) Fully Open Port (b) 25% Closed Port (c) 50% Closed Port (d) 75% Closed Port.

3.5 Stereoscopic PIV Setup

An overview of the Stereoscopic PIV setup is given in figure 3.12.

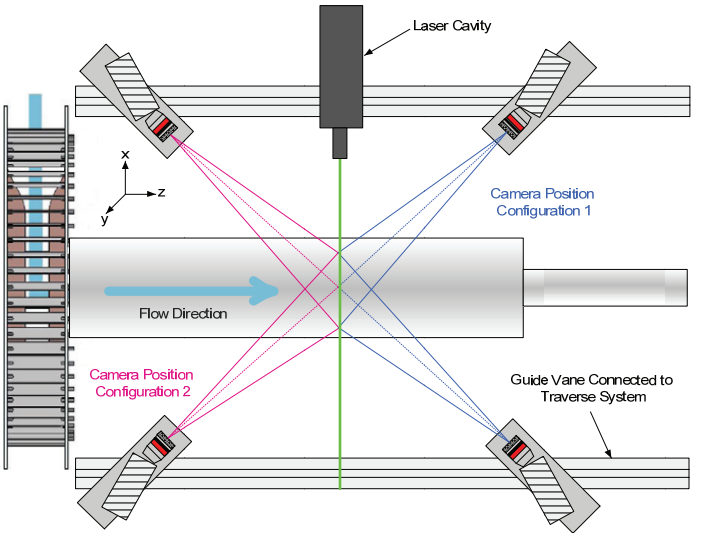

Figure 3.12:

Illustration of PIV Setup and Two Different Camera Configurations.

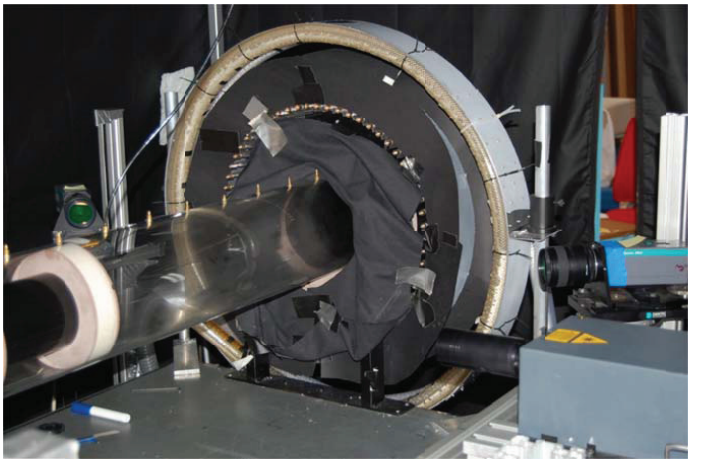

Figure 3.13:

PIV Setup and Different Camera Configurations.

The test rig is mounted on a table which is aligned in parallel with a traverse system. The laser cavity and two cameras are fitted on the traverse system. The traverse system is controlled using a software installed on PC and provides motion in axial direction only i.e. along the length of the test cylinder. The test cylinder is also aligned axially in parallel with the axial motion of the traverse because the table, on which the test cylinder is

mounted, is not fitted with the traverse. Laser cavity and cameras are mounted on the same traverse with their positions fixed relative to each other. Thus the traverse moves only laser and the cameras at the required measuring planes in axial direction (Z-axis).

3.5.1 *Alignment and Calibration*

The NewWave® Solo Nd:Yag pulse laser device (120 mJ pulses @ 15 Hz, Wavelength 532 nm) is mounted on the traverse in a way that the laser sheet is perpendicular to the cylinder. The laser sheet is aligned with the laser light reflected from the cylinder wall. This ensures that the laser sheet is perpendicular to the cylinder. Two Dantec HiSense cameras with 1344 x 1024 pixels and pixel size of 6.45µm are equipped with 60 mm focal length lenses and green light filters. Both cameras, mounted on the same traverse, are at one side of the laser sheet and the cylinder is placed between the two cameras (Figure 3.13). The calibration target is attached on a disc of same diameter as the internal diameter of the cylinder and is slided inside the test cylinder. The calibration target is kept aligned with the laser sheet at only one of the measuring cross-sectional position and considering the test cylinder being axially aligned; same calibration is used for all the other measuring cross-sections. The cameras were focused on a rectangular target plane within the pipe diameter, avoiding measurements close to the cylinder wall due to strong reflections of the laser light. In order to capture all the measuring positions, two position configurations for the cameras are used (Figure 3.10). Due to angle of view, for the measuring positions near the outlet in camera configuration 1, camera view is blocked by the cylinder outlet wall and thus configuration 2 is used. For each configuration, calibration is performed at single measuring position. Dantec DynamicStudio® software is used for PIV measurements and data processing. Calibration was performed using 3rd Order XYZ-Polynomial Imaging model which is capable of handling distortion caused by the lens or curved windows (DynamicStudio® user manual). In order to account for the possible misalignment of the calibration target with the laser sheet, disparity error correction is performed. For configuration 2, calibration and calibration refinement processes are repeated and is used only for the positions near the outlet.

One half of the test cylinder wall behaves like a concave reflecting surface and laser light reflections from the internal walls make a very bright spot near the concave wall facing the laser light (Figure 3.14). This will increase uncertainty in the measurement in that region. The F-number is set to 8 for the camera receiving the forward scatter and for the camera receiving the backward scatter, F-number is set to 4.

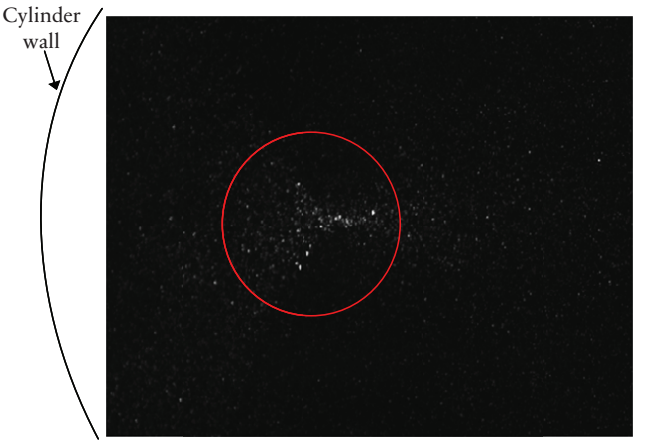

Figure 3.14:

Wall Reflection Effect on PIV images (View from Backward Scatter Camera. Cylinder wall location is an illustration and not in true scale.)

3.5.2 *Seeding Setup*

The seed generator contains 75/25 % by volume glycerol-Water solution and size distribution of seeding droplets is in range of 2-3 μm. For a uniform and adequate seeding, the particles should mix properly with the incoming air entering the inlet section. For this purpose a metal frame, diameter 860 mm and width 150 mm, is mounted around the inlet section (Figure 3.15).

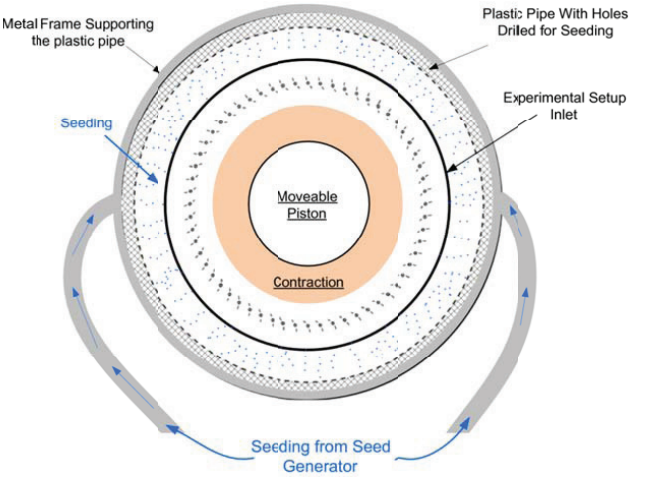

Figure 3.15:

Seeding Setup Illustration.

A plastic pipe (diameter 40mm) is tied with the internal periphery of the metal frame in a helical shape so as to cover the whole breadth of the metal frame and consequently the inlet surface. A lot of small holes are drilled in the pipe wall facing the inlet of the experimental setup and the two ends of the pipe are connected to the seed generator. The radial distance of the pipe wall from the inlet surface is sufficient enough not to affect the incoming flow and provides a uniform seeding across the inlet surface.

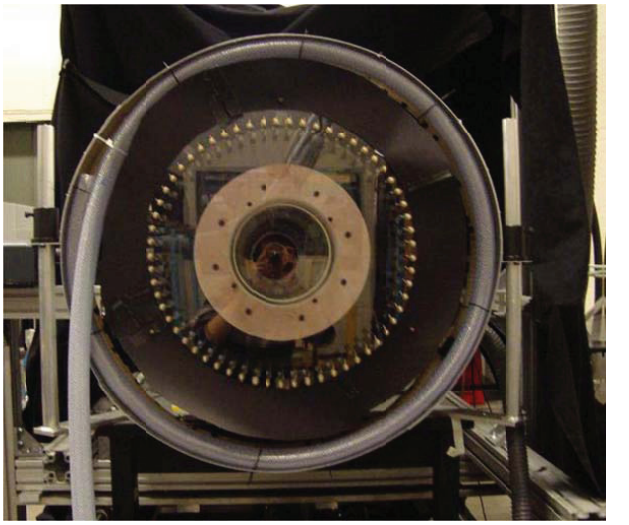

Figure 3.16:

Seeding Setup (Pergolesi F., 2009).

3.5.3 *Data Acquisition and Processing*

For each Re, measurements are conducted at different cross sectional planes along the length of the cylinder, with their distances measured from the piston surface as reference (Figure 3.4). At every position and a given Re, 994 PIV snapshots are taken. Data processing and analysis of the PIV images are performed using multi-pass 'Adaptive Correlation' algorithm in Dantec DynamicStudio® software. The initial interrogation window size is 128 x 128 pixels with two refinement steps to a final interrogation area of size 32 x 32 pixels and 50% overlap of the side of the interrogation area.

3.6 LDA Setup

LDA measurement has been conducted using two component laser Doppler anemometer system (Figure 3.17). Laser beam from 4W (maximum output) coherent Innova Ar-ion laser is splitted in to green (λ = 514.5 nm) and blue (

λ = 488 nm) lines using a beam splitter and then transmitted through optical fiber. The data is analyzed using Dantec Burst Spectrum Analyzer (BSA) Flow v 2.12. The flow was seeded using the seeding setup described in section 3.5.2. For measurements the laser power used is 3.5-4W and data acquisition are conducted by running the system in burst mode. The traverse system controlled using the BSA Flow software, is used for positioning the laser. The geometric center of the test cylinder is used as origin for X and Y axes. In axial direction (along Z-axis) the measurements are conducted at a distance of 20 mm from the surface of the piston. Thus the measurements conducted along X and Y axes give the velocity values in the middle of the two walls of the swirl generator i.e. 50 mm from each wall (Figure 3.18).

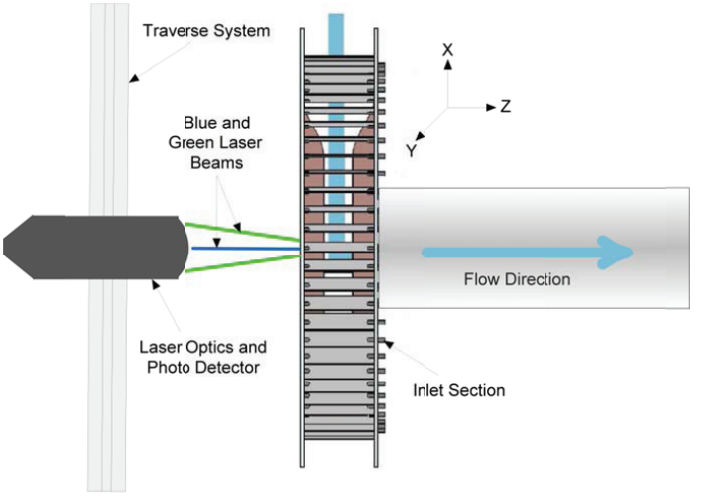

Figure 3.17:

LDA Setup.

Two sets of measurements are conducted. In first one conducted by the author, the measurements are conducted along a line following the X-axis at a distance of 20 mm from the piston surface and at a distance of z/D = 0.368. In the second set conducted by Schnipper (2010), the measurements are conducted along the circumference at a radial distance of 200 mm and 75 mm from the origin (label 'b' indicating red dots in Figure 3.18). In order to measure the flow profile behind the guide vanes and decay of corresponding wake effect at different radial positions, additional measurements are conducted along an arc and at radial positions of 230 mm and 200 mm (label 'a' indicating blue arcs in Figure 3.18).

Table 3.1:

Optical Details of LDA System .

Property	Beam 1	Beam 2
Wavelength	514.5 nm	488 nm
Focal Length	310 mm	310 mm
Beam Diameter	1.35 mm	1.35 mm

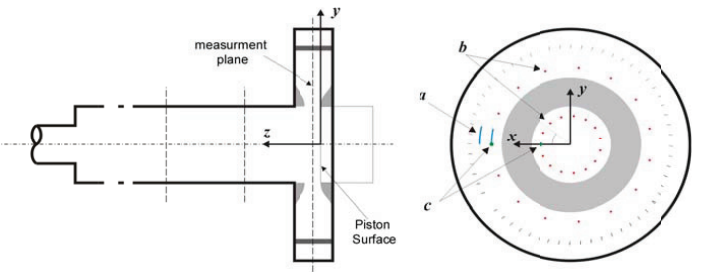

Figure 3.18:

Overview of LDA measurement positions (Schnipper, 2010).

Swirling Flow in a Pipe

Stereoscopic PIV measurements of in-cylinder confined swirling flow have been carried out. The measurements are conducted for three different cylinder lengths in order to characterize the effect of cylinder length on the swirling flow. LDA measurements have also been carried out at the inlet section to study the flow profile and distribution.

The swirling pipe flow experiments, conducted prior to current work, to the knowledge of author, generally focus on studying the effects of variation of parameters like Reynolds number, swirl intensity, swirl decay, relative roughness (Senoo et al., 1972) and vortex breakdown on heat and mass transfer application. Since the focus in this study is on the swirling flow for scavenging process in large and low speed two stroke diesel engines, the characterization of the effect of change in cylinder length on the in-cylinder confined swirling flow has been studied. The experiment is conducted on the test model described in Chapter 3 using stereo PIV technique. Since the outlet section assembly, containing outlet pipe fitted to cylinder head, can slide inside the cylinder, measurements are conducted for 3 different cylinder aspect ratios i.e. cylinder length equal to 8D, 6D and 4D. In this way it becomes possible to measure at same measuring position even after the cylinder length is changed. This helps in studying the variation in flow characteristics at a specific position while the cylinder length changes. For this experiment the internal diameter of the cylinder, degree of swirl (alignment of guide vanes in the swirl generator) is kept constant. Air at room temperature is used as the fluid and measurements are conducted at two different flow rates with average values of Q_A=0.149 m^3/s and Q_B= 0.0745 m^3/s (accuracy ± 2%) measured using an orifice plate with a U-tube differential manometer. The corresponding Reynolds numbers (Re_A = 6.5 x 10^4 ± 1870 and Re_B =3.25 x 10^4 ± 935) based on the average velocity calculated from the volumetric flow rate measured using an orifice plate with a U-tube differential manometer. It is, however, worth mentioning that the experimental results can also be useful for interested readers within different areas of fundamental studies in turbulent confined swirling flows.

Table 4.1 provides the detail for the axial position of different cross-sectional planes where measurements are conducted for each cylinder length. The axial distance 'z' is measured from cylinder bottom-dead-center (BDC) i.e. piston surface when the port is fully open (Figure 3.4). It can be seen that position 1-6 are common in all the three cylinder lengths (8D, 6D and 4D) and for cylinder lengths 6D and 8D position 1-9 are common. For this reason, in order to describe the effect on variation in cylinder length in a simple and clear way, the profile plots are divided in two parts for a given

Reynolds number. In the first part (marked by blue box), only first 6 positions for the aforementioned cylinder lengths are plotted. This provides a comparison of flow characteristics for measuring positions that are common in all the three cylinder lengths. The second part (marked by green box) describes the remaining positions i.e. position 7 and beyond which are common only for 6D and 8D cylinder lengths and also the positions which are only in 8D.

Table 4.1:

Axial Position of Measuring planes for different cylinder lengths.

Position No.	Axial Positions (z/D)	Cylinder Length (L/D)		
		L_1 =8	L_2 =6	L_3 =4
z_1	0.963	×	×	×
z_2	1.489	×	×	×
z_3	2.016	×	×	×
z_4	2.542	×	×	×
z_5	3.068	×	×	×
z_6	3.595	×	×	×
z_7	4.116	×	×	
z_8	4.642	×	×	
z_9	5.168	×	×	
z_{10}	5.695	×		
z_{11}	6.226	×		
z_{12}	6.747	×		
z_{13}	7.268	×		

Before discussing the results from stereoscopic PIV experiments on different cross-sectional planes along the cylinder length, it is necessary to study and understand the flow inside the swirl generator because the flow conditions and characteristics such as swirl angle (angle between radial and tangential velocity components), symmetric or asymmetric flow and turbulence level etc. in the swirl generator govern the resulting downstream in-cylinder swirling flow and knowing the flow inside swirl generator will help in better understanding of the PIV results at the downstream positions. Moreover, it will give an assessment of the design performance of swirl generator and also help in finding any possible manufacturing and human errors during construction, assembling and alignment of the inlet section. Proper and accurate alignment of all the guide vanes ensures a symmetric flow distribution/ swirl generation in the inlet section and any misalignment will introduce asymmetric swirl.

4.1 LDA Measurements (Inlet Section)

Two components LDA measurements were conducted at different locations in the swirl generator as described in Section (3.6). The main reason for using LDA technique has been the possibility of conducting measurements at locations where PIV measurement becomes very difficult to be conducted due to guide vanes blocking the laser light (see section 3.1). The measurements are conducted at volume flow rate of 0.154 m^3/s.

Different radial positions from origin see figure 3.18, between inlet to swirl generator and contraction section, are selected and then measurements are conducted at same radial positions along each of the axes lines (Table 4.2).

Table 4.2:

Radial Position of Measuring points along X-axis for LDA measurements.

Axis	Radial Positions from origin (mm)				
	275	230	215	200	185
X	×	×	×	×	×
-X	×	×	×	×	×

This must be mentioned here that in the real swirl generator the assumed axes lines, while crossing the blade row, do not lie on similar location between the two adjacent guide vanes e.g. the measurement at the radial position of 235 mm for negative Y axis is not possible due to the laser beam being blocked by a guide vane whereas for other axes measurements can be conducted at the same radial position.

The measured radial velocity profiles for each half axis are shown in figure 4.1a (flow direction is from radial position at 275 mm to 180 mm). The half-length of each error bar is one standard deviation. It can be seen that the radial velocity distribution is not symmetric. Flow accelerates while passing through the row of guide vanes and further downstream due to the contraction section. Due to wake behind the guide vanes a decrease in the magnitude is also observed for radial positions of 200 mm along positive X.

The tangential velocity profiles are shown in figure 4.1b. For both half axes, at radial position of 275 mm, a non-zero tangential velocity is observed which demonstrates either the flow feeling the presence of the guide vane being at downstream position or the blade edge facing the inlet section outlet is not perfectly aligned with the radius. Moreover, different values of tangential velocity and angle between radial and tangential velocity components along the axis lines indicate that there exists a small relative difference in alignment of guide vanes (Figure 4.1c).

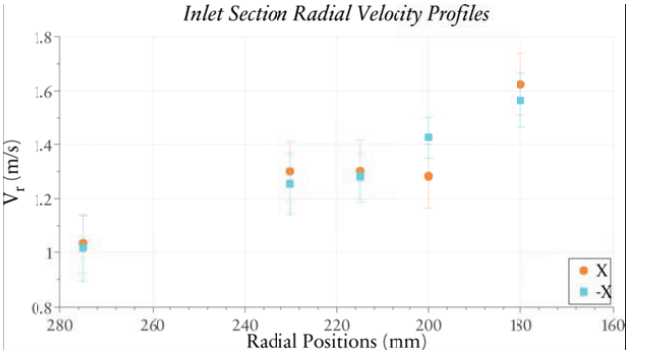

(a)

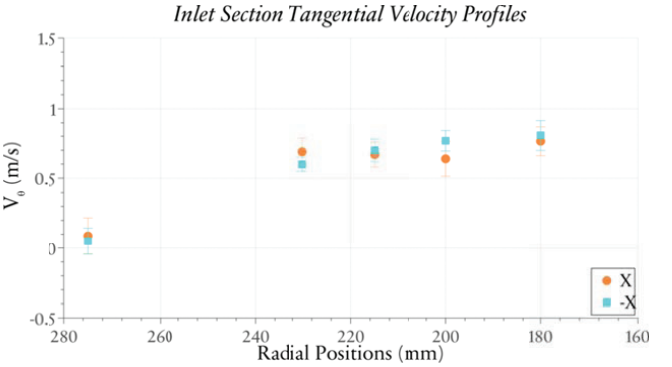

(b)

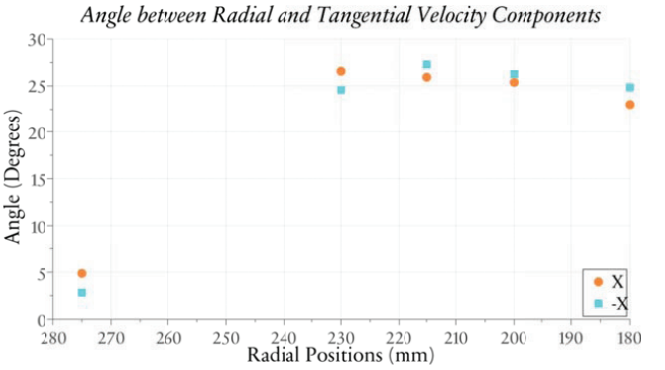

(c)

Figure 4.1:

LDA Measurements along X-axis (a) mean radial velocity profile (b) mean tangential velocity profile (c) angle between mean radial and tangential velocity.

At downstream radial position of 180 mm, the relative variation in magnitudes of individual velocity components reduces significantly. A possible reason is that the flow at a radial position of 170 mm enters the contraction region which will have a damping effect to any variations/ fluctuations in velocity and the flow at nearby upstream positions also feels the presence of the contraction section.

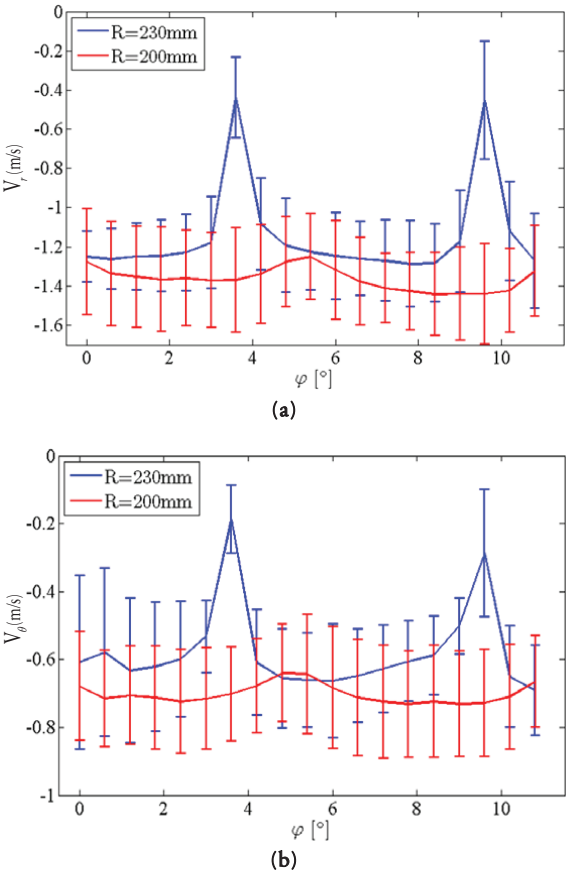

Figure 4.2:

LDA Measurements along an arc behind the blades (a) mean radial velocity profile (b) mean tangential velocity profile (Schnipper, 2010).

The measurements conducted along the two arcs behind the blades as mentioned in figure 3.18 are shown in figure 4.2. Where φ is the angular location of the measurement point on a given arc. The negative values of the velocity components are due to the orientation of LDA laser beams. Each half length of the error bar is one standard deviation. The results show that at a radial distance of 230 mm (the trailing end of the blade is approximately at

a radial distance of 238 mm), there exists a large wake behind each blade. However, at a radial distance of 200 mm the wake has considerably reduced. The flow enters the contraction section at a radial distance of 170 mm from the cylinder axis and it can thus be assumed that there will be no wake effect in the flow entering the contraction region.

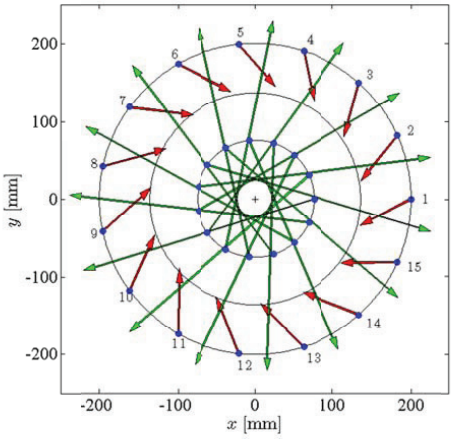

Figure 4.3:

Visual presentation of in-plane velocity distribution on the circumference line at radial distance of 200 mm and 75 mm (Schnipper, 2010).

Figure 4.3 is a visual representation of the distribution of in plane velocity at different circumferential positions at radial distance of 200 mm (outer circle with blue dots) and 75 mm (inner circle with blue dots). The length of the arrows indicate the magnitude of inplane velocity ($\sqrt{V_\theta^2 + V_r^2}$) and direction is based on the angle between the radial and tangential velocity components. The detailed results are given in figure 4.4 where the vertical axis on the left hand side represents the angle and on the right hand side it represents the inplane velocity magnitude. It can be observed that a radial distance of 200 mm, the magnitude and direction of the flow is not symmetric and vary at different circumferential positions (Figure 4.4a). The maximum variation in angle is measured to be approximately 6°. This indicates that the guide vanes in the inlet section are not perfectly aligned thus causing an asymmetric flow distribution. However, after the flow passes through the contraction section, the results at a radial position of 75 mm show that this variation in angle is reduced approximately to 1.5° and the flow is comparatively more symmetric.

Figure 4.5 shows tangential velocity profile across the cylinder cross section at z/D = 0.368 measured using LDA. It can be seen that despite small relative flow asymmetry in the swirl generator, an axis symmetric flow exists in the cylinder before the cross-sectional positions where PIV measurements are conducted. The measurement very close to the cylinder geometric center

(X/R=0) was not conducted due to bad signal and thus figure 4.5 may not give exact size of the vortex core at the given cross-sectional plane.

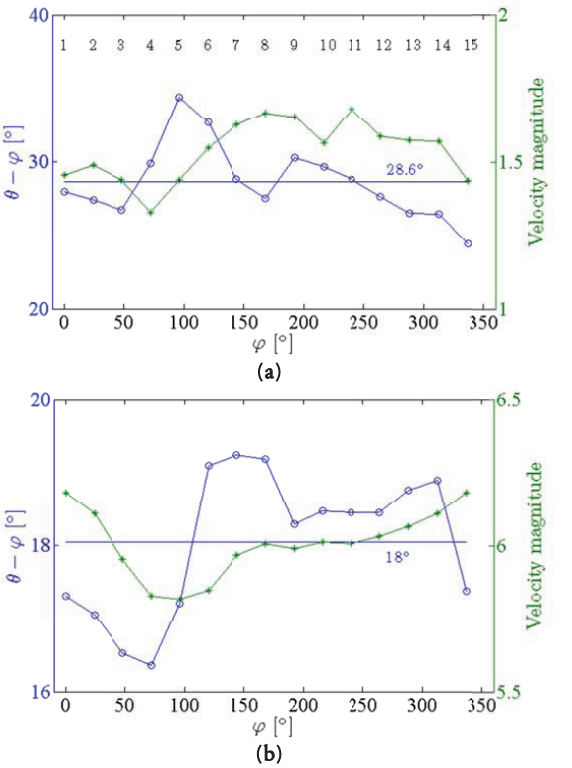

Figure 4.4:

Circumferential distribution of inplane velocity magnitude and angle between radial and tangential velocity components (a) radius = 200 mm (b) radius = 75 mm (Schnipper, 2010).

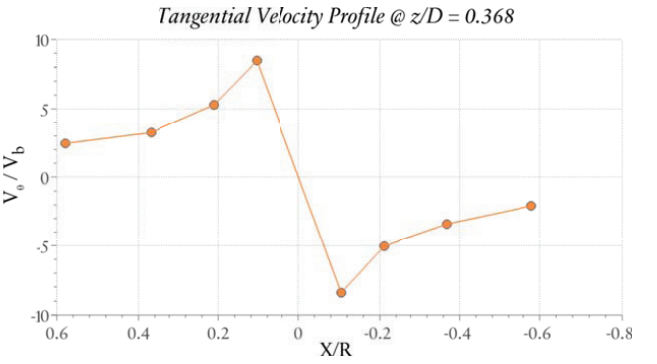

Figure 4.5:

Cross-Sectional Tangential Velocity Profle.

Based on the average angle of 28.6° at the radial position of 200 mm, using the conservation of angular momentum, the design swirl parameter for current experimental setup is 0.34 (Equation 2.8).

4.2 PIV Experimental Results (L_3)

The PIV experimental results are discussed here by describing the mean data for each flow characteristic. In order to present the results in a comprehensive and more understandable manner, at first, the results for the base case of cylinder length L_3 are discussed and then the effect of change in cylinder length is discussed by comparing the results for L_1, L_2 and L_3 at selected positions. The results for the remaining positions are presented in appendix A.

4.2.1 *Mean Velocity Field*

The mean velocity field at z_1 is presented for both the Reynolds numbers in figure 4.6. Each velocity component is non-dimensionalized with bulk flow velocity V_b.

It can be seen that the resulting in-cylinder swirling flow is comprised of a concentrated vortex with a small core surrounded by a high velocity region. The velocity magnitude in the vortex core is very low compared to its surroundings and mean position of the vortex core is slightly eccentric to the geometric center of the cylinder. A low velocity region exists at larger radial positions close to the cylinder wall. Moreover, it can be observed that the core size, in case of Re_B is relatively smaller than the velocity field at Re_A.

The flow decays downstream and the size of vortex core region increases indicating smaller localized velocity gradients compared to upstream positions (Figure 4.7). Moreover, the high velocity region exists at larger radial distances from the vortex core and the thickness of the high velocity region is also not uniform at all circumferential positions at the given radial distance from the core. This demonstrates the flow having three dimensional features. The size of the vortex core has further increased and the relative difference in the core size at two Reynolds numbers still exists.

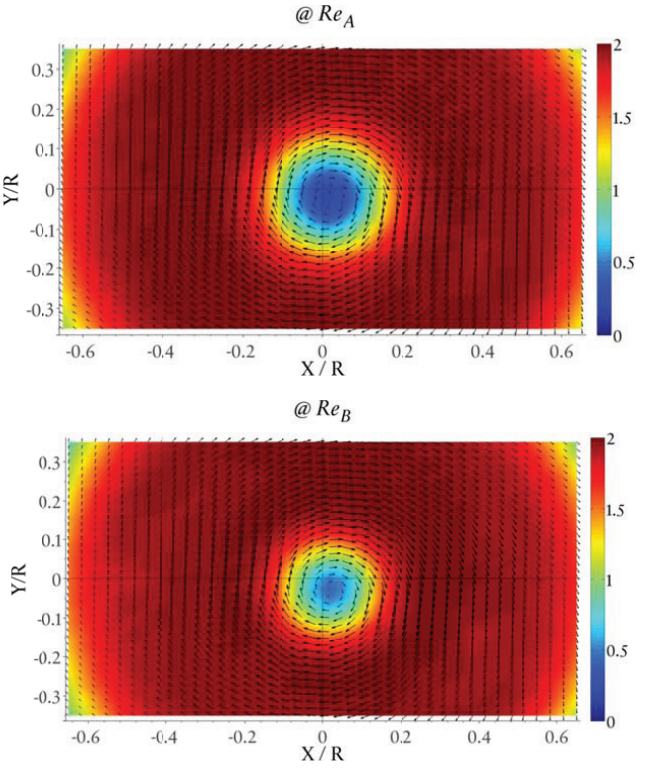

Figure 4.6:

Averaged 3D Velocity Field at z_1 for L=4D (Color Contour represent the Normalized out of the plane velocity component V_z / V_b.

If the size of vortex core is to be defined as the radial distance from vortex core to the high velocity region then at z_5 the size of the vortex has increased to almost half of the cylinder radius. Moreover it can also be observed that from axial location z_1 to z_5 the flow decays downstream and also position of vortex core moves in clockwise direction following the in-plane swirl velocity. For both Reynolds numbers the size of vortex is now nearly the same and the asymmetry/ three-dimensionality of the velocity field seems to have increased.

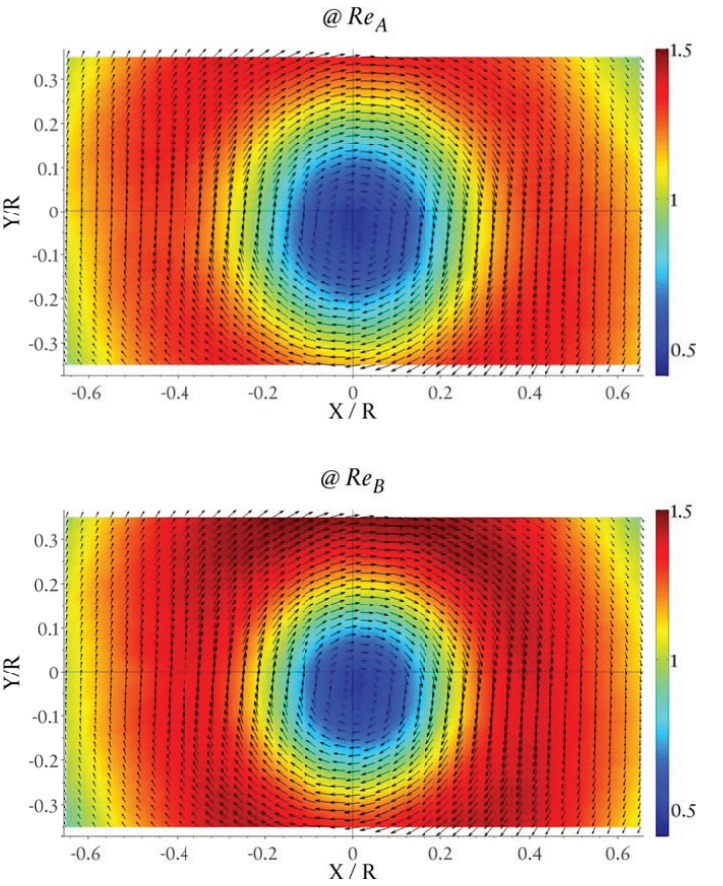

Figure 4.7:

Averaged 3D Velocity Field at z_3 L=4D (Color Contour represent the out of the plane velocity component V_z / V_b.

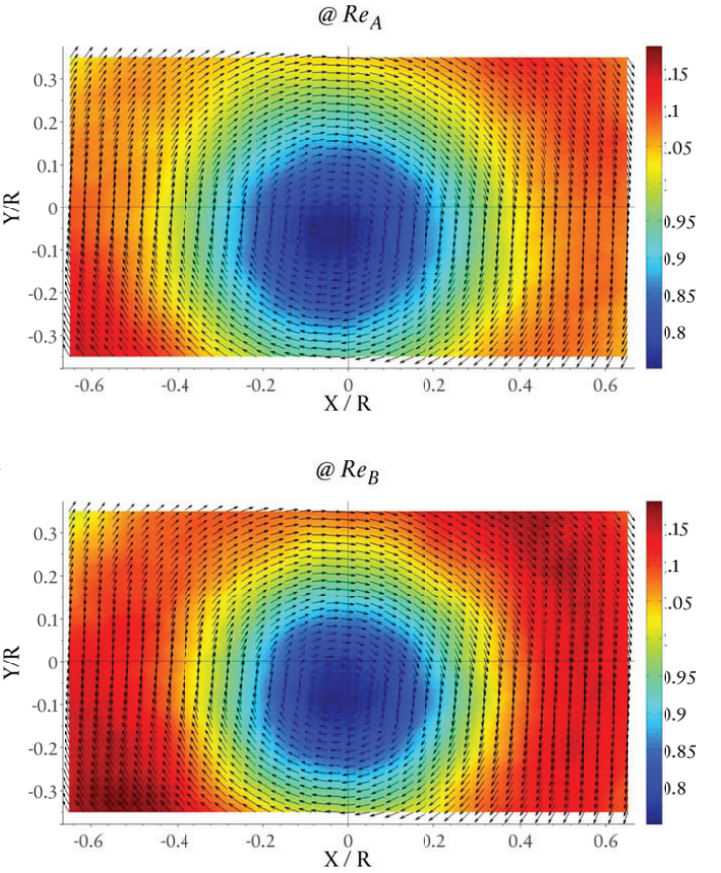

Figure 4.8:

Averaged 3D Velocity Field at z_5 L=4D (Color Contour represent the out of the plane velocity component V_z).

4.2.2 *Tangential Velocity Profile*

The tangential velocity V_θ profiles in figure 4.9 give an overview of tangential velocity distribution at all measuring planes and also provide a comparison at Re_A and Re_B. The profiles (V_θ and V_z) are presented along X-axis and at Y=0 but by first shifting the origin of the coordinate system from cylinder geometric center to the mean center of the vortex core i.e. along a horizontal line through the vortex center. A simple algorithm is used to find the approximate average position of the vortex center. The algorithm makes a cubic interpolation between different points in the PIV measurement grid

and scans for the local minimum of the in-plane velocity magnitude $\sqrt{u^2+v^2}$ (Cartesian coordinates) in the region close to the cylinder axis.

The profile shape resembles closely to the model of Burger vortex i.e. a rotational flow core region with rigid body rotation (forced vortex) followed by an irrotational/ potential flow region also referred to as 'free vortex' or 'annular' region. Since, in this experiment, no measurements were conducted close to cylinder wall, the velocity profile in the high velocity gradient 'wall layer' region cannot be seen.

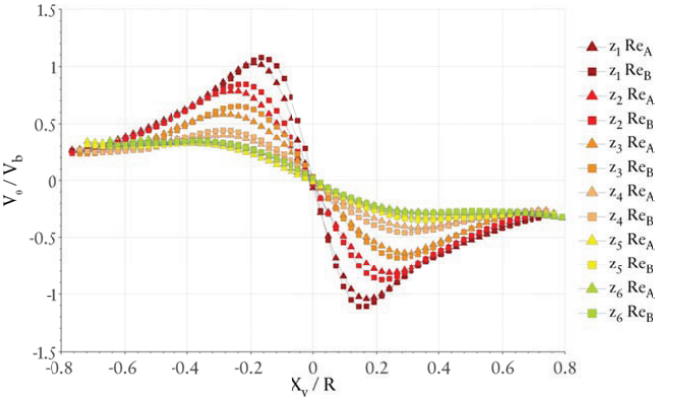

Figure 4.9:

Tangential Velocity for L_3=4D.

At positions very close to the cylinder inlet, the size of the vortex core is small compared to outer potential flow/ free vortex region and the peak value of non-dimensional tangential velocity in the rotational region is higher at low Reynolds number Re_B compared to Re_A. This difference diminishes with the swirl decay and growth in the forced vortex region downstream the flow direction at z_5. At z_6 a small peak in the magnitude of tangential velocity is observed as a result of the flow being accelerated due to small diameter outlet pipe (z_6 at L_3 is comparatively closer to cylinder outlet than z_9 and z_{13} at L_2 and L_1 respectively). In general, the effect of variation in Reynolds number is only observed in the vortex core region and the potential flow region seems to be insensitive to such variation at all the measuring positions.

4.2.3 *Axial Velocity Profile*

The axial velocity V_z exhibits a 'wake-like' profile (Figure 4.10). The effect of Reynolds number seems to be more pronounced compared to V_θ not only in terms of size of inner forced vortex but also in the magnitude of V_z at the

vortex core. At Re_A, compared to Re_B, the value of V_z in the vortex core is less and very close to zero but no reverse flow is observed at the vortex core. At z_1, in the potential flow region, V_z seems to be nearly the same at both Reynolds number and steep gradient in the values of V_z is observed at larger radial distances.

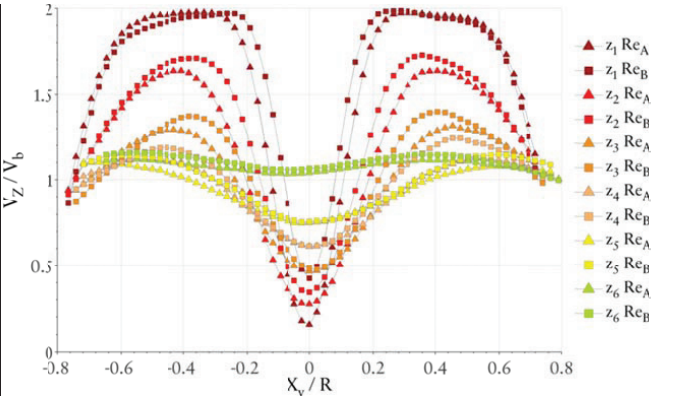

Figure 4.10:

Axial Velocity for L_3=4D.

Downstream the flow, at z_6, the wake like profile of axial velocity decays and becomes more flat and the sensitiveness to Reynolds number can only be seen in the region with peak values of V_z. This is very interesting because contrary to V_θ, the axial velocity seems to be more responsive to variations in Reynolds number and less to the downstream swirl decay. The V_z velocity gradient in the region at large radial distances has decreased and the cylinder outlet seems to have no effect in pronouncing a regeneration of wake-like profile at z_6.

4.2.4 *Mean Axial Vorticity*

The flow at z_1 has a core with a large value of normalized mean axial vorticity ω_z (calculated by first normalizing x, y with cylinder radius R and u, v with bulk flow velocity V_b) (Figure 4.11). The vorticity distribution seems to have a Gaussian like profile. The vortex core region has high vorticity with steep gradients at lower Re. Very low vorticity is observed only at large radial distances from the vortex core. The irregularity in the profile is due to the uncertainties in data acquisition and processing.

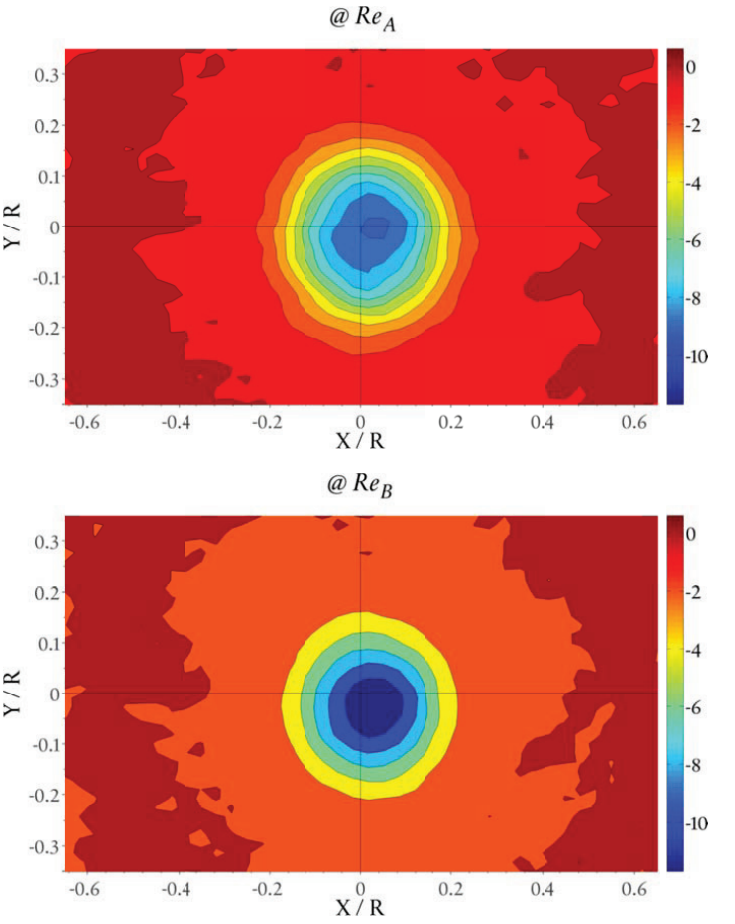

Figure 4.11:

Mean Normalized Axial Vorticity ω_z @ z_1 L_3=4D.

With the swirl decay the vortex core has lost its vorticity and seems to transfer Vorticity in outward radial directions. The size of the core has increased and the region with low vorticity is observed at smaller radial distance.

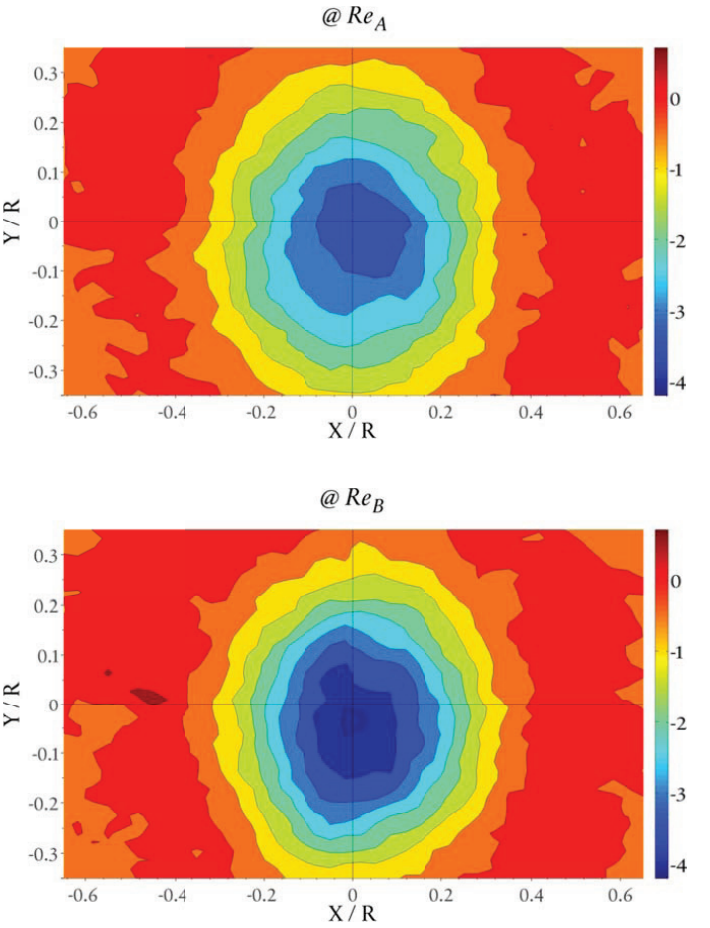

Figure 4.12:

Mean Normalized Axial Vorticity ω_z @ z_3 L_3=4D.

It should be noted that as in case of vortex models (Burgers Vortex), the vortical forced vortex core is surrounded by an irrotational/potential flow region. However, the experimental results seem to be different in a confined swirling flow having profiles similar to the Burgers vortex model. The possible reason is that outside the vortex core region, the vortex decays radially outward (Figure 4.11). The vortical fluid patches at the outer boundary of forced vortex region interact and exchanges vorticity with the neighbouring non-vortical fluid patches. As a result, a region with a very low vorticity is formed in the region where the vortex core and the annular region meet.

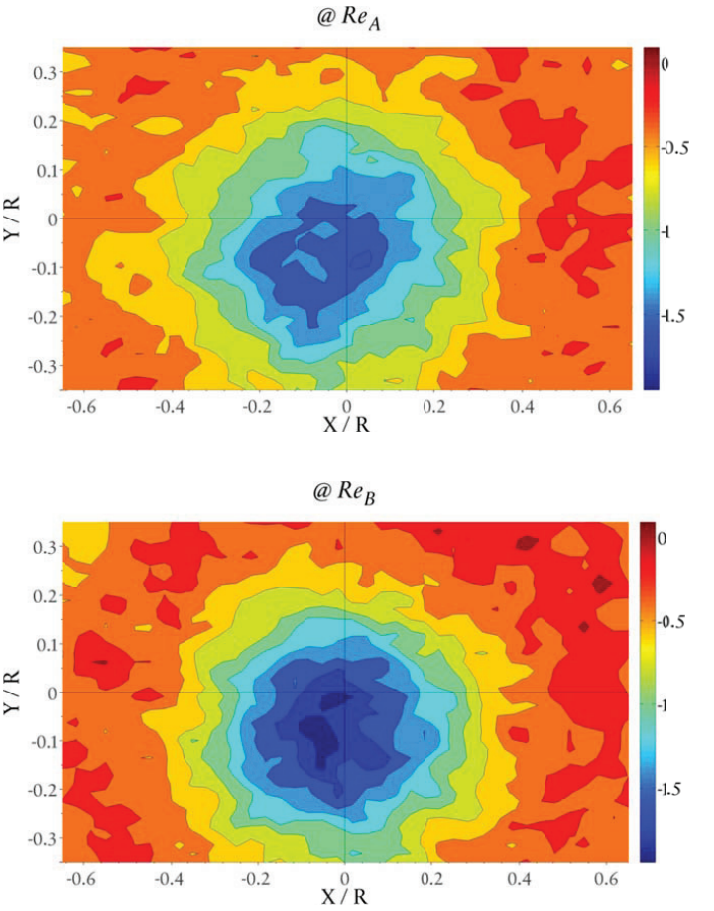

Figure 4.13:

Mean Normalized Axial Vorticity ω_z @ z_5 L_3=4D

The irrotational region diminishes downstream with the gradual decay of the swirl and the consequent decrease in the vorticity of the vortex core and transfer of vorticity to larger radial distances. However, this decay in potential flow region, as a function of downstream axial distance, seems to be faster at high Re with existence of a comparatively less vortical vortex core and large core size (Figure 4.13).

4.2.5 *Reynolds Normal Stresses*

The Reynolds stresses are expressed in Cartesian coordinates rather than cylindrical coordinates. The major reasons are (i) the particle image Velocimetry (PIV) measurement equipment gives data in Cartesian coordinate system and (ii) transforming the velocity components to the corresponding components in cylindrical coordinate is very difficult in instantaneous velocity filed due to the lack of a clear and single defined vortex core. In the current experiment only at z_1, there exist some instantaneous snapshots of the flow, among all snap shots for that particular measurement, where a single vortex core can reasonably be observed. (iii) to the knowledge of author, most of the major CFD codes are written for Cartesian coordinates and the model validation requires the experimental data to be in the same coordinate system.

The contour plots of velocity components in Cartesian coordinates can still provide some good information about the corresponding components in polar (cylindrical) coordinates. The only difference is to understand the relation of u and v components to V_θ and V_r because the w and V_z are the same in both the coordinate system. In case of swirling flow, the interpretation of Cartesian components in to polar components is easily understood. Along X-axis, the u component represents V_r and v component represents V_θ. In case of Y-axis, it is vice versa. Figure 4.14 show contour plots of u and v components and can thus be used as an example of understanding the distribution of tangential and radial velocities from contour plots of u and v components (signs denote the direction of a given vector component).

The contours of u along Y-axis indicate that the tangential velocity increases from cylinder axis to its peak value at a region r/R=0.17 (approximately) and then decreases again towards large radial positions. Whereas along X-axis, the value of u shows that radial velocity has a very low magnitude. The contour of v gives similar information about the distribution of tangential and radial velocity components but along opposite axis lines i.e. X-axis, as discussed before. The distribution of fluctuating/ turbulent part of the individual velocity components, for polar coordinates, can also be understood in the same manner.

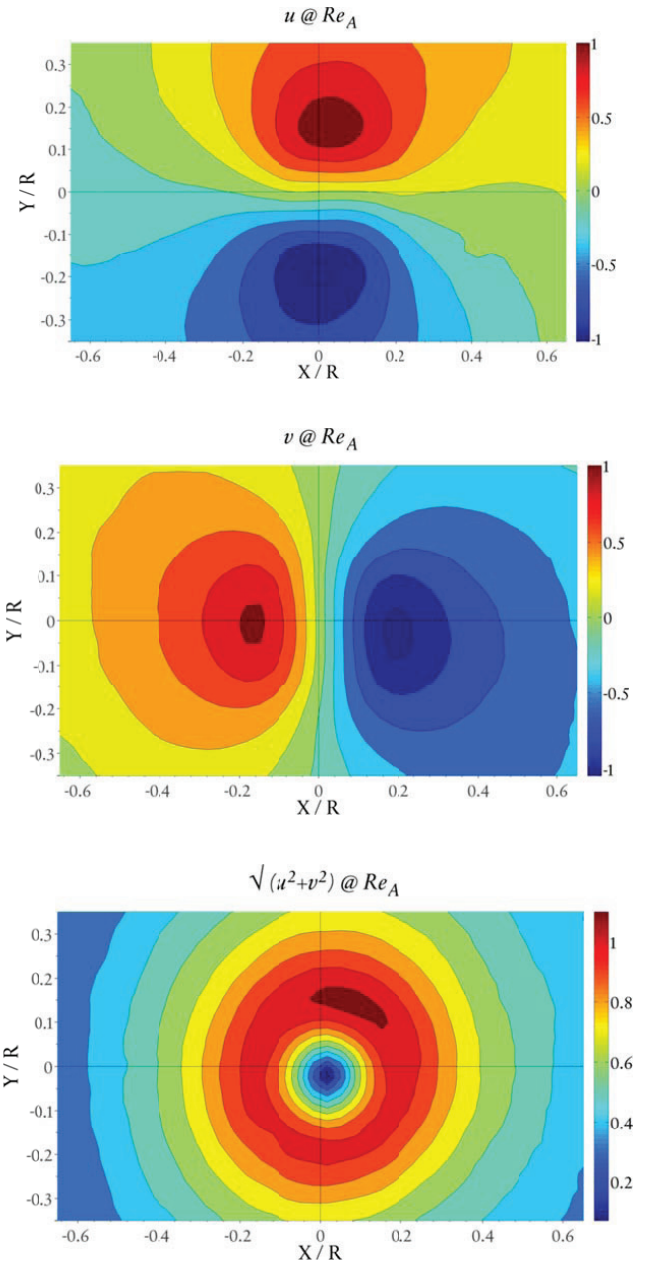

Figure 4.14:

Normalized Velocity Components in Cartesian Coordinates at z1.

From the contour plots of u and v, it can also be observed that the peak tangential velocity regions are not perfectly aligned with the axis lines and in fact are at an angle to the axis lines in clockwise direction. This is possibly due to the eccentric location of the vortex core from the cylinder axis. Another effect of asymmetric swirling flow can also be understood by plotting the contour plot for in-plane velocity ($\sqrt{u^2+v^2}$) (Figure 4.14). In case of axis symmetric swirling flow, the velocity contours will have a circular ring shape. However, in this case a high velocity quarter-moon shaped region (indicated by a white arrow) is observed. This is probably due to the effect of wall because the vortex core is radially closer to the wall in the direction of eccentricity from the cylinder axis compared to other direction. (Alekseenko et al., 2006) has discussed in detail about the changes in the structure of flow in helical vortices with and without the presence of wall.

The normal Reynolds stress components $\overline{u'u'}, \overline{v'v'}, \overline{w'w'}$, statistically, represent variance of u, v and w components of velocity respectively. In case of experimental measurements for swirling flow with precessing vortex core (PVC), the measured values of Reynolds stresses are actually a combination of true velocity variance and vortex core oscillation. The contribution of oscillating vortex core depends on its amplitude and frequency and in some cases can be the major contributor.

The $\overline{u'u'}$ component, at z_1, has high values concentrated around the vortex core and in an oval shape region elongated along x-axis (Figure 4.15). This may possibly be due to a precessing vortex core (PVC). The size of this region with peak velocity variations in the core is smaller at Re_A compared to Re_B. The region surrounding the vortex core has very low velocity variations but these variations gradually increase in radial direction towards the near wall region.

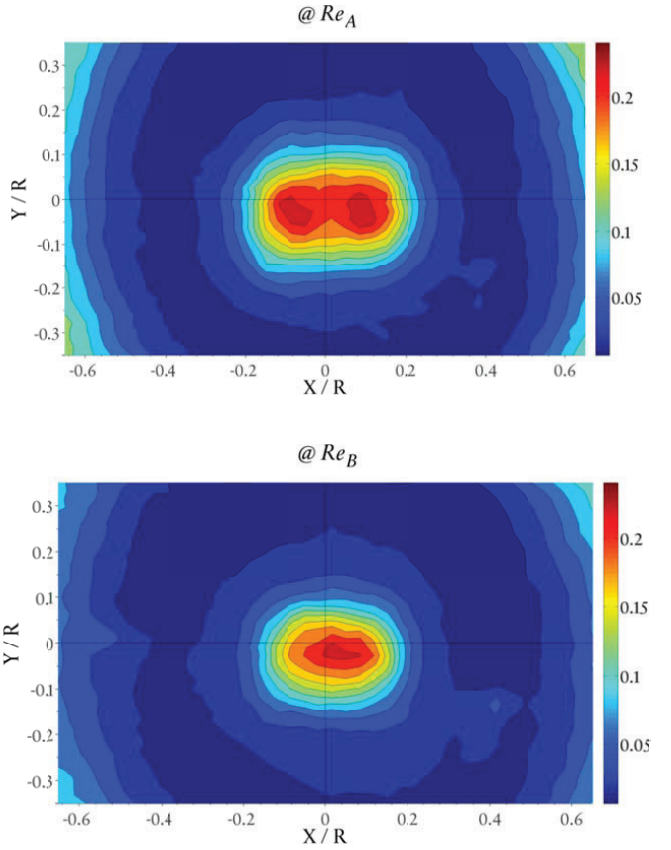

Figure 4.15:

Normalized Reynolds Stress Component $\overline{u'u'}$ *@ z1 L_3=4D*

At z_3 (Figure 4.16) the peak variations in $\overline{u'u'}$ seems to have decayed. However, the variations are comparatively not much concentrated around the cylinder axis and the oval shaped region has an angular shift along a line tilted at nearly 20° in anti-clockwise direction to the x-axis.

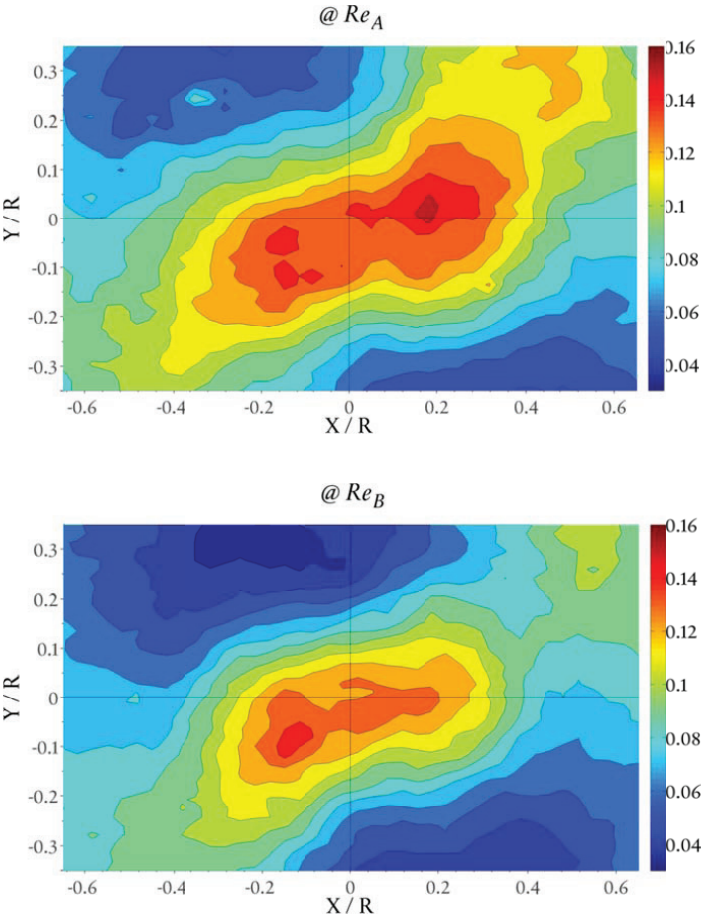

Figure 4.16:

Normalized Reynolds Stress Component $\overline{u'u'}$ *@ z3* L_3*=4D*

For Re_A and Re_B at z_5 in figure 4.16 the $\overline{u'u'}$ variance still has peak values, lower than at z_3, concentrated in the vortex core region (Figure 4.17). However for Re_A, variance is spacially more dispersed and the largest values, observed in the core region, are comparatively smaller than flow at Re_B. In addition, no further shift in angular direction of oval shaped region has been observed.

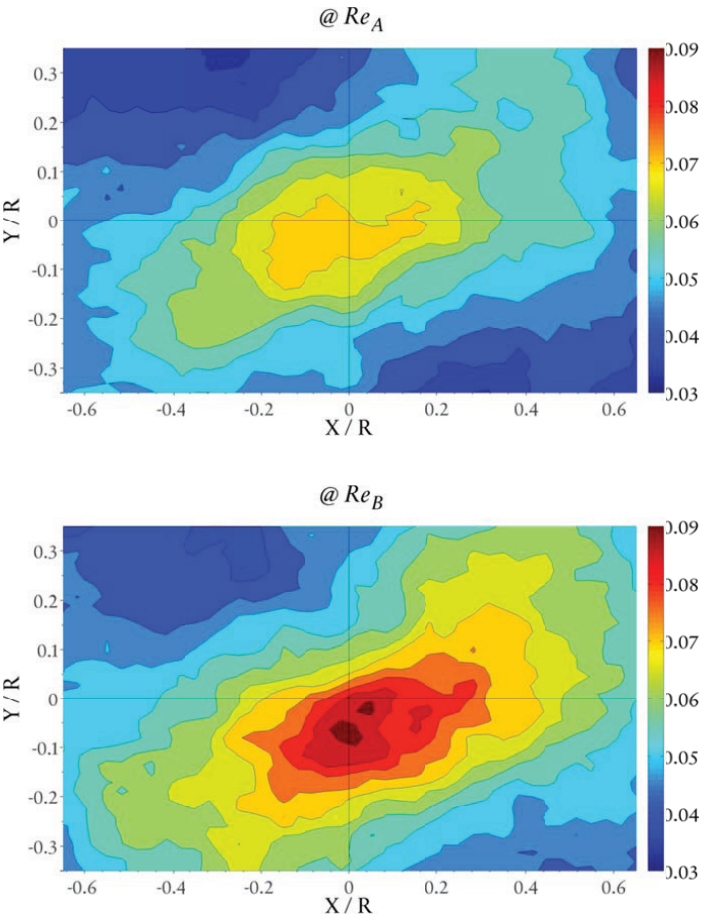

Figure 4.17:

Normalized Reynolds Stress Component $\overline{u'u'}$ *@ z5 L_3=4D*

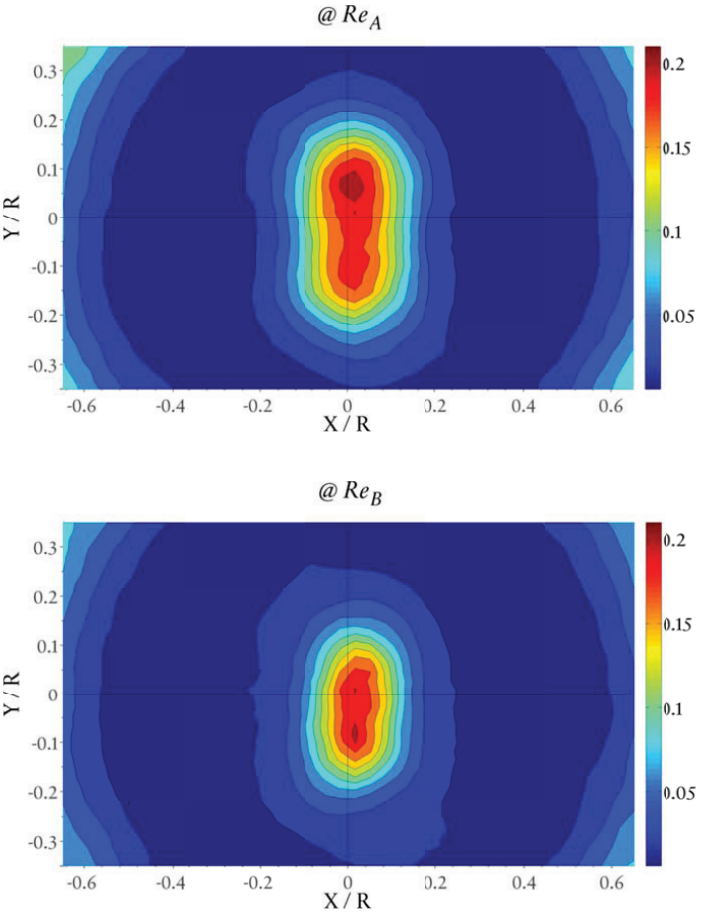

Figure 4.18:

Normalized Reynolds Stress Component $\overline{v'v'}$ *@ z1* L_3*=4D*

The $\overline{v'v'}$ component, behaving in the same manner as $\overline{u'u'}$ at z_1, is confined and concentrated in the vortex core as an oval shaped region aligned along the y-axis (Figure 4.18). Further, the deviation from the mean v values are minimum in the region outside the forced vortex core and in the near wall region at X/R =0.7 the value is almost half the maximum deviation.

At z_3 in figure 4.19, the alignment of oval shaped region is tilted to a small degree in anticlockwise direction and the deviation in v spreads to larger radial positions along its axis. The maximum deviations, along the oval shaped region, still are observed in the region closed to vortex core.

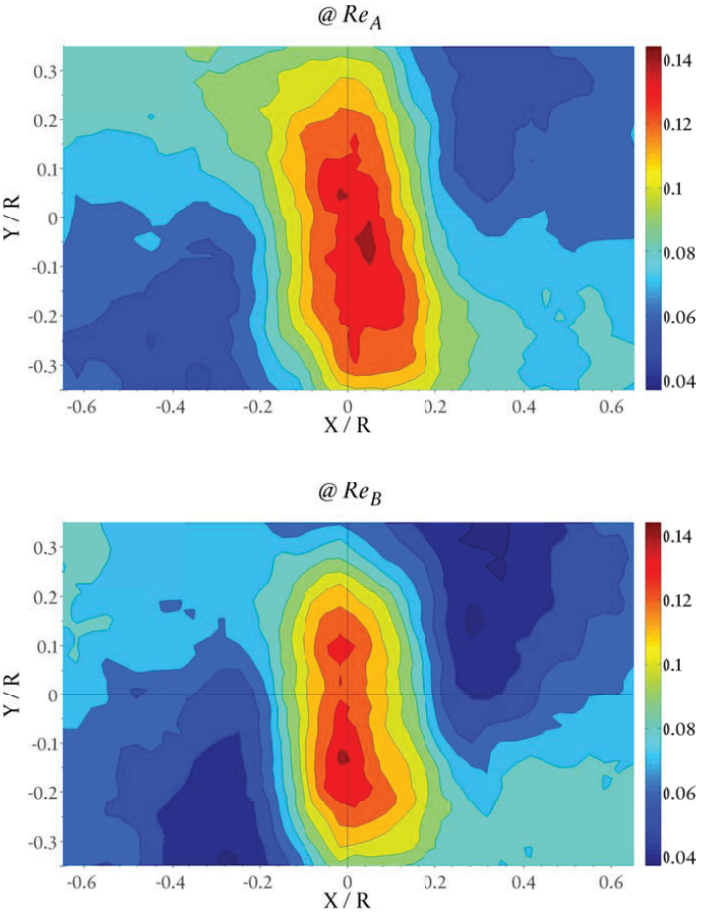

Figure 4.19:

Normalized Reynolds Stress Component $\overline{v'v'}$ *@* z_3 L_3*=4D*

At z_5 in figure 4.20, the oval shape region, with large deviations in v, elongates and tilts further in anticlockwise direction. Similar to u, the deviation in v component in the vortex core region, reduces quickly at higher Reynolds number Re_A compared to lower at Re_B (Figure 4.20). Further, the largest value in $\overline{v'v'}$ for Re_B is now almost half the peak value observed at z_1.

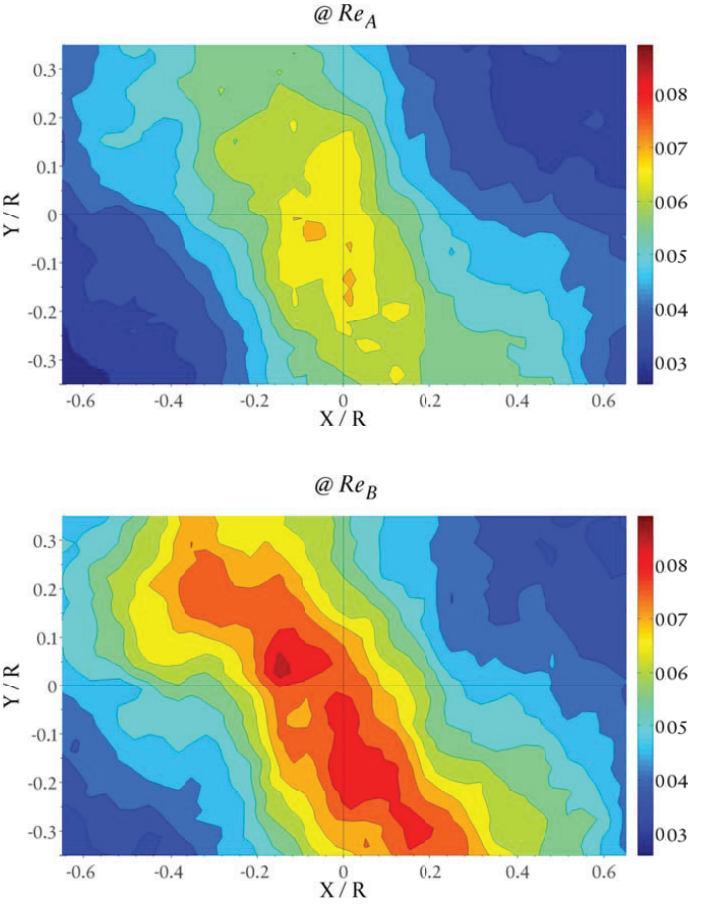

Figure 4.20:

Normalized Reynolds Stress Component $\overline{v'v'}$ *@ z5 L_3=4D*

The analysis of Reynolds stress components $\overline{u'u'}$ and $\overline{v'v'}$ (Cartesian coordinates) indicates that $\overline{v'_\theta v'_\theta}$ and $\overline{v'_r v'_r}$ are larger near the wall and in the vortex core regions at z_1. The radial distance, from the vortex center, where $\overline{v'_r v'_r}$ increases towards the vortex center, is larger than the $\overline{v'_\theta v'_\theta}$ and follows the same for both Reynolds numbers (Figures 4.15 and 4.18). As the swirl decays downstream, the magnitude of radial and tangential fluctuations decrease but their spatial distribution increase to larger radial distances of the cylinder cross-section. However, at all position $\overline{v'_r v'_r}$ is more spatially

distributed compared to $\overline{v'_\theta v'_\theta}$. The anti-clockwise tilt observed in the shape of oval region may possibly be because of the helical structure of vortex along the cylinder length.

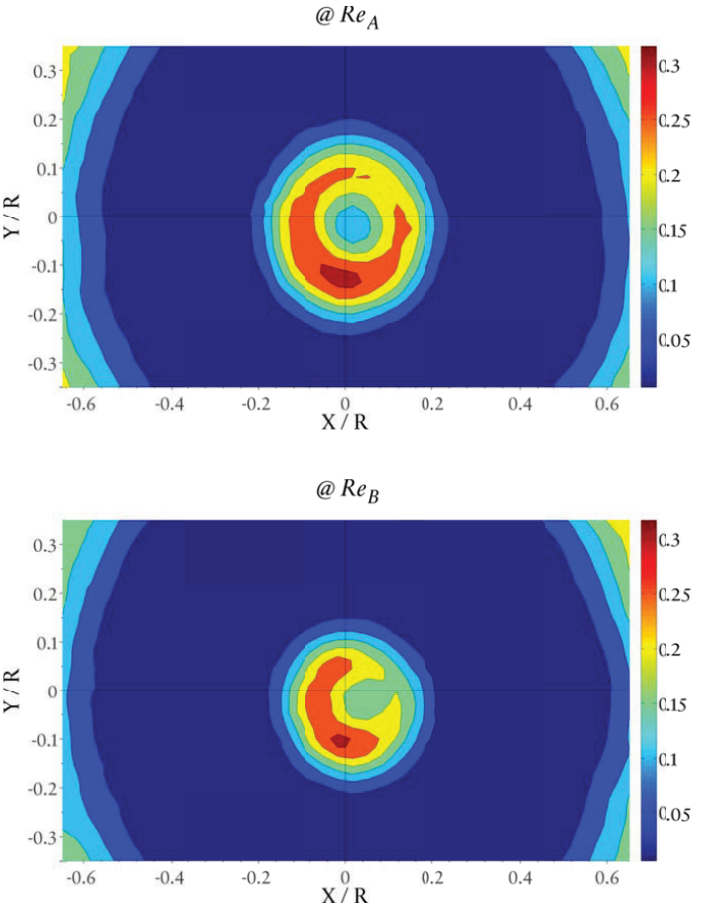

Figure 4.21:

Normalized Reynolds Stress Component $\overline{w'w'}$ *@* z_1 L_3=4D

The $\overline{w'w'}$ component at z_1 is shown in figure 4.21. The vortex core exhibits a non-axis symmetric distribution of $\overline{w'w'}$ that indicates the three dimensionality of the flow and its consequent effect on w variance. The effect of vortex core precession is significant but the half circle arc-like shape of the region with high variance seems to indicate the vortex precession superimposed on the three dimensional velocity variations. The region with

minimum variance or in other words comparatively steady axial velocity distribution is between the core and the wall region where high values of axial velocity are observed (Figure 4.10). $\overline{w'w'}$ is also large in the near wall region. The relatively smaller size of large w variance region at Re_B is due to smaller vortex core compared to one at Re_A.

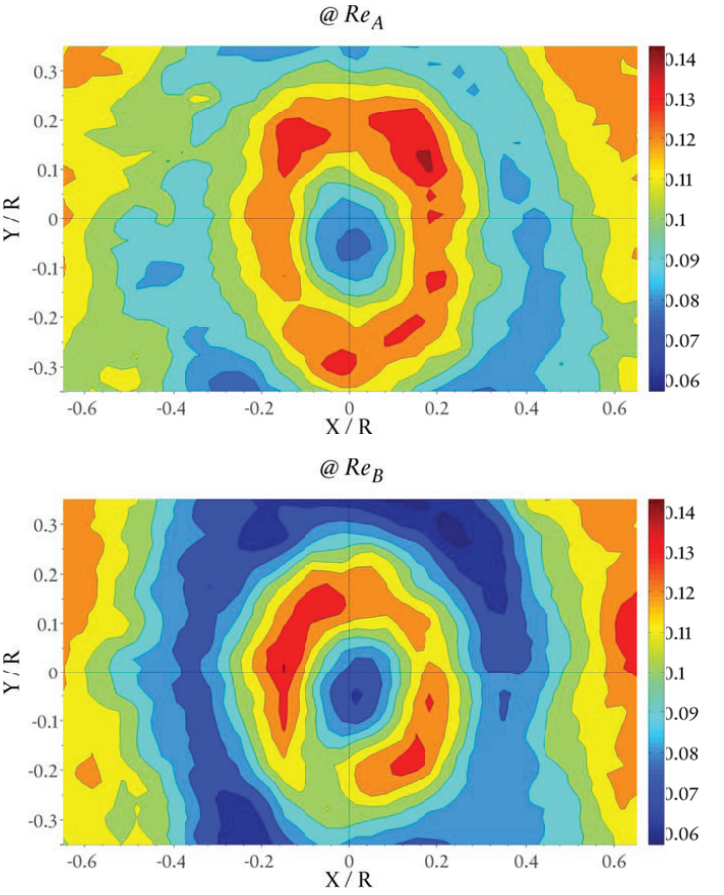

Figure 4.22:

Normalized Reynolds Stress Component $\overline{w'w'}$ *@ z3 L_3=4D*

The largest w variance at z_3 is nearly half the value at z_1 (Figure 4.22). The forced vortex region has large $\overline{w'w'}$ value except vortex center where it is low. Near wall region also demonstrate large axial w' disturbances with the swirl decaying downstream the flow.

At further downstream position z_5 in figure 4.23, the decay in the largest $\overline{w'w'}$ is half the largest value at z_3. The flow at high Reynolds number Re_A has stronger tendency towards axial disturbance w'. The high $\overline{w'w'}$ region in the vortex core and the near wall region grow in size in radial direction and few regions with patches of very low w variance are remained. In general, with the swirl decay, the spatial distribution of $\overline{w'w'}$, however low in magnitude, becomes more uniform.

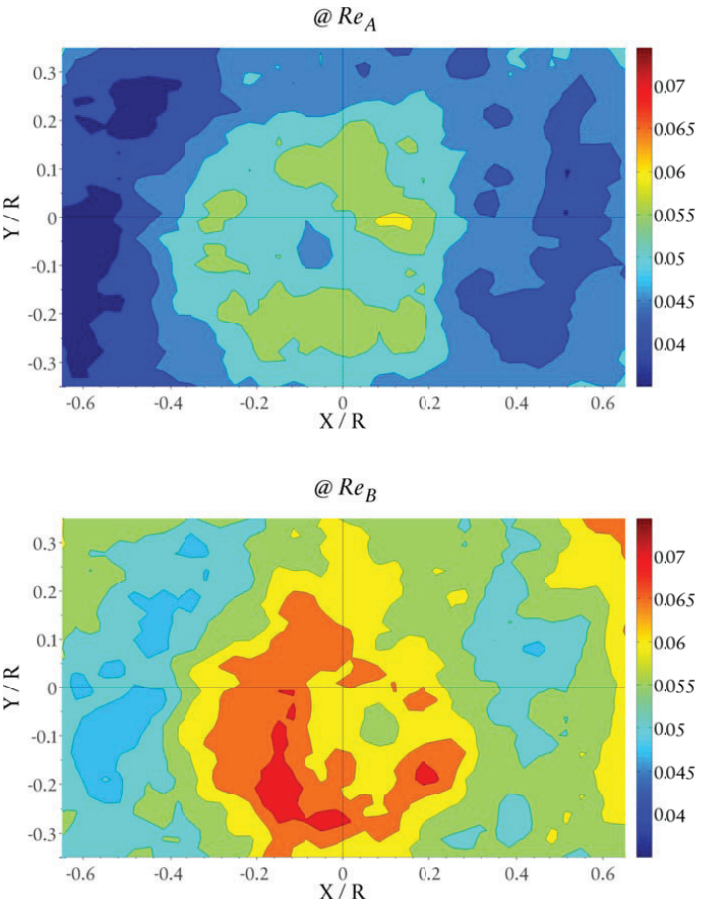

Figure 4.23:

Normalized Reynolds Stress Component $\overline{w'w'}$ *@ z5 L_3=4D*

4.2.6 *Reynolds Shear Stresses*

The shear stress components of Reynolds stresses, statistically, are a measure of the covariance between different velocity components. The distribution of Reynolds shear stress components are defined here in Cartesian coordinates as described in section 4.2.5 and a possible interpretation for their counter parts in polar coordinates is also discussed.

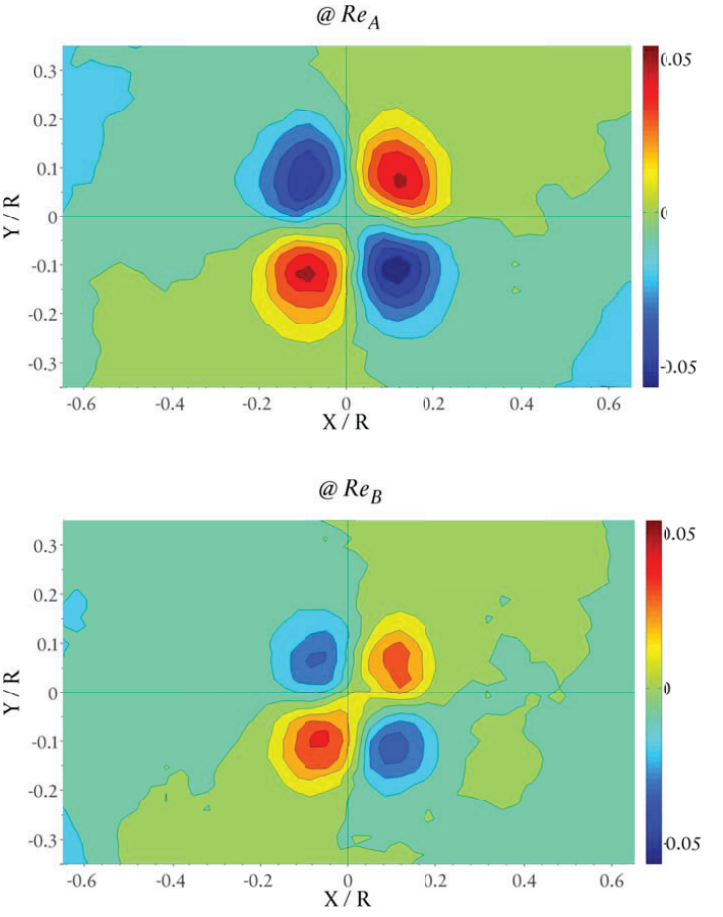

Figure 4.24:

Normalized Reynolds Stress Component $\overline{u'v'}$ *@ z1 L_3=4D*

The $\overline{u'v'}$ contour plots are shown in figure 4.24 for z_1 at both Reynolds numbers. The $\overline{u'v'}$ has large values near the cylinder axis and at large radial

distances the values are very small. The contours show four rather small circular shaped zones of high covariance between u and v velocity components with two having positive and two having negative covariance.

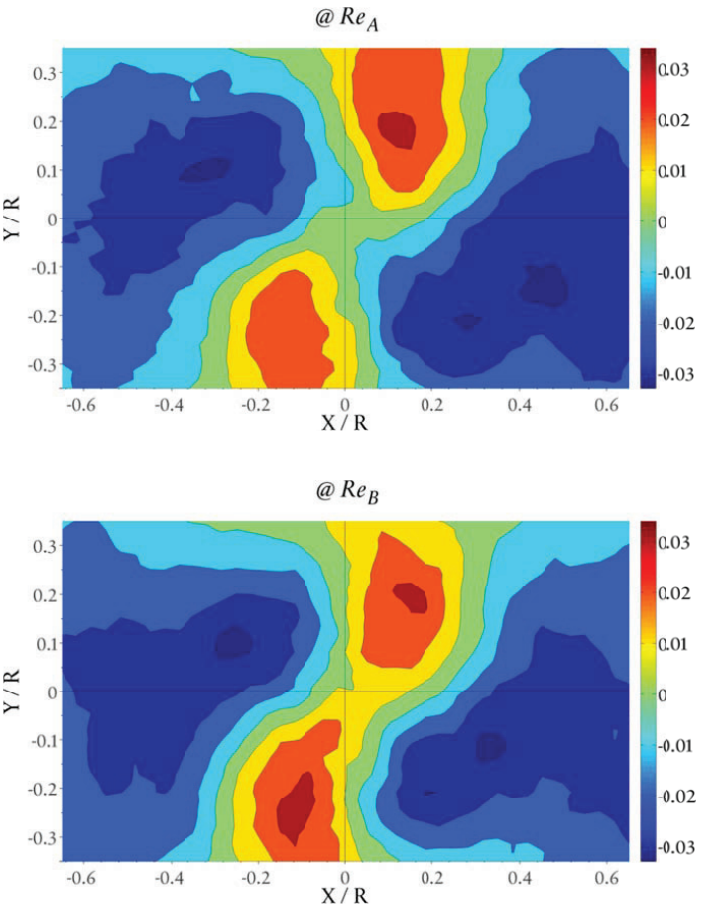

Figure 4.25:

Normalized Reynolds Stress Component $\overline{u'v'}$ *@ z3* L_3*=4D*

As the swirl decays downstream, the maximum absolute values of $\overline{u'v'}$ decreases and are no more confined near the cylinder axis (Figure 4.25). The Reynolds shear stress distribution is observed in outward radial direction with enlargement of the zones having highest values of $\overline{u'v'}$.

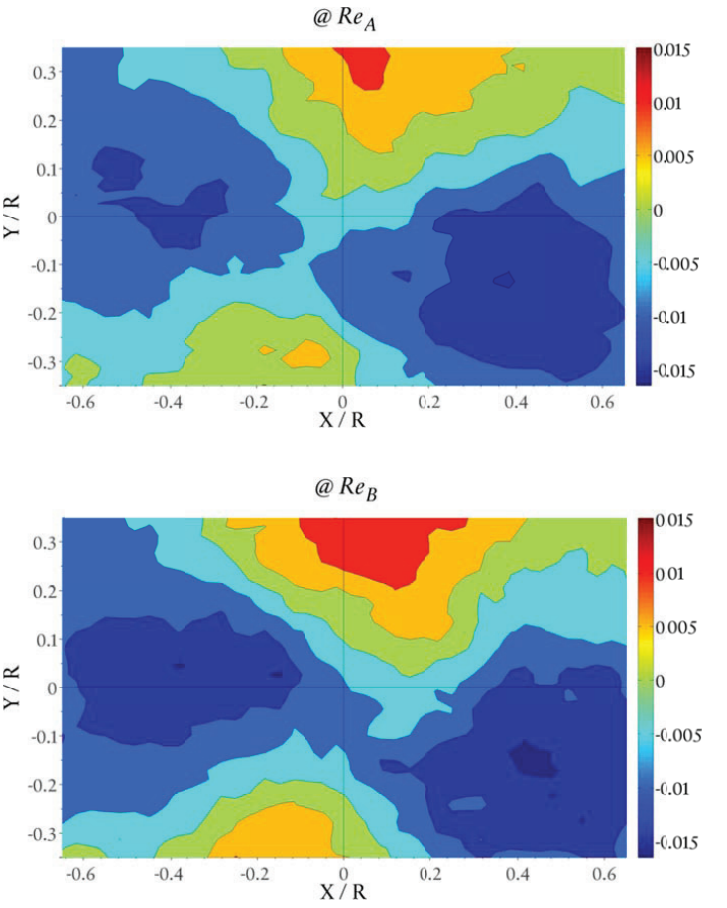

Figure 4.26:

Normalized Reynolds Stress Component $\overline{u'v'}$ *@ z5 L_3=4D*

The high $\overline{u'v'}$ zones weaken in intensity and move further radially outward resulting in region near to cylinder axis with low values (Figure 4.26). In general, the overall spatial distribution of $\overline{u'v'}$ is in the form of patches of fluid regions with high values in the middle of them and moving radially outward as the swirl decays downstream and vortex core size increases.

Figures 4.24-26, describes that initially at z_1 the Reynolds shear stress component $\overline{v'_\theta v'_r}$ is higher in the vortex core region. The peak values are observed at the radial position at the interface of forced vortex core and the outer annular region. In the annular region, the core has very small values of

$\overline{v'_\theta v'_r}$. Downstream the flow this covariance between v_θ and v_r expands to larger radial distances with comparatively smaller magnitude. It seems that the peak values, for all given cross sectional plane, are observed at the radial distance where the forced vortex has its boundaries.

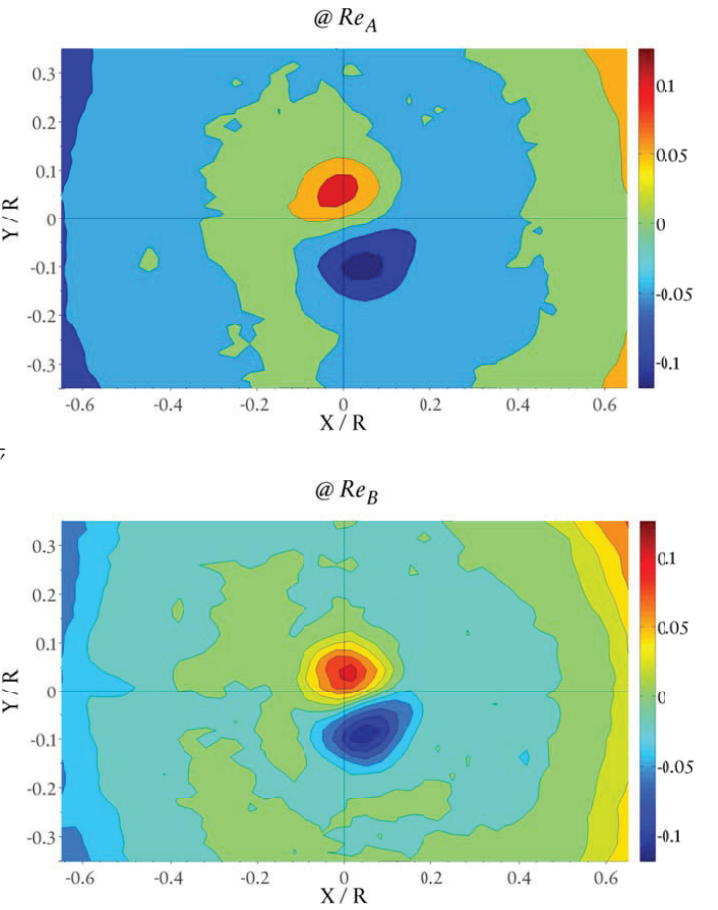

Figure 4.27:

Normalized Reynolds Stress Component $\overline{u'w'}$ *@ z1 L_3=4D*

Figure 4.27 show high values of $\overline{u'w'}$ near cylinder axis and cylinder wall regions at z_1 and the region in between has very low values. Near the cylinder axis, where the vortex core exists, high values are concentrated in two regions with opposite but same magnitude of covariance between u and w components.

At z_3 in figure 4.28, the maximum absolute values of $\overline{u'w'}$ decreases, however, in the near wall region it grows radially inward towards the vortex core and the concentrated $\overline{u'w'}$ region in the vortex core, spreads radially outward.

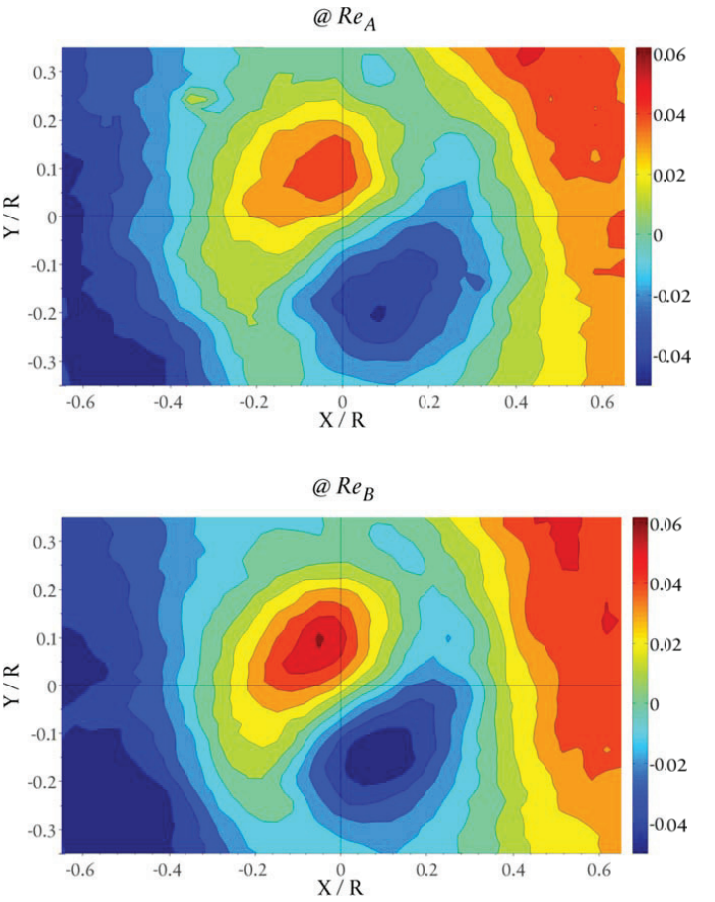

Figure 4.28:

Normalized Reynolds Stress Component $\overline{u'w'}$ *@ z3* L_3*=4D*

Further downstream at z_5 in figure 4.29, the overall magnitude of $\overline{u'w'}$ decreases and is an order of 10 smaller than at z_1. Comparing contour plots for Re_A and Re_B in figure 4.28, $\overline{u'w'}$ distribution at Re_A has small gradients in the flow domain. In other words, the flow at Re_B is more resistant towards a uniform spatial distribution of $\overline{u'w'}$ in the flow domain. Another feature

that can be observed for plots at z_1, z_3 and z_5 is that near wall regions, at the two ends of X-axis, has opposite signs of $\overline{u'w'}$. This shows that similar to the two regions near the cylinder axis, an opposite covariance also exists between u and w components in the near wall regions at two sides of cylinder axis.

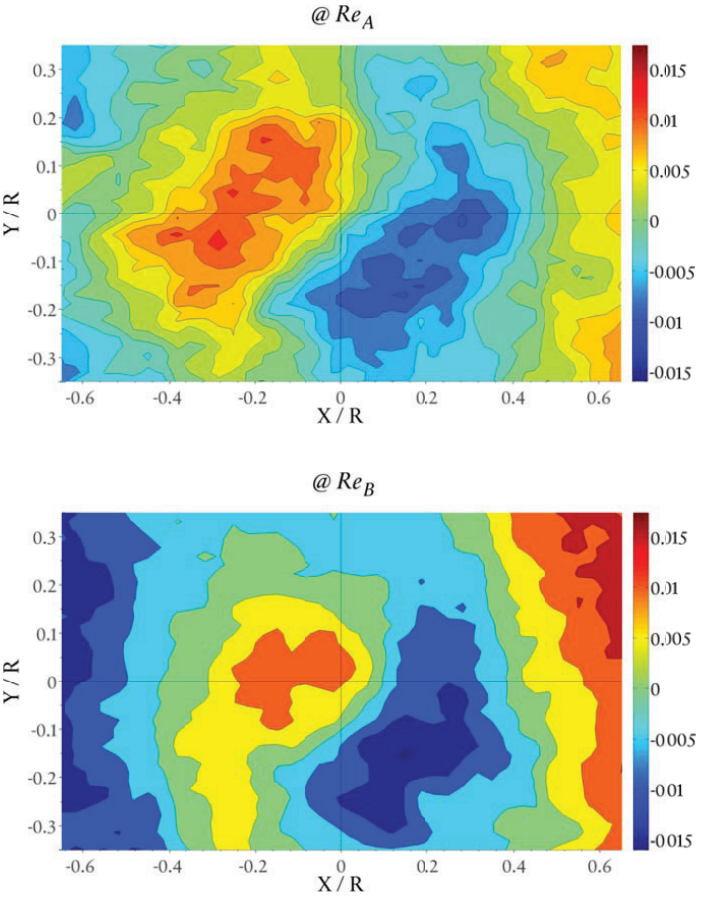

Figure 4.29:

Normalized Reynolds Stress Component $\overline{u'w'}$ *@ z5 L_3=4D*

The contour plots for $\overline{v'w'}$ at z_1 in figure 4.30, show similar distribution as for $\overline{u'w'}$ i.e. large values of $\overline{v'w'}$ exit in the near wall region and two small regions near the cylinder axis although with opposite signs. The significant difference is that the orientation of the two regions is approximately

orthogonal (in anticlockwise direction) to those in case of $\overline{u'w'}$ (Figure 4.27). The peak values of $\overline{v'w'}$ are also nearly the same as $\overline{u'w'}$.

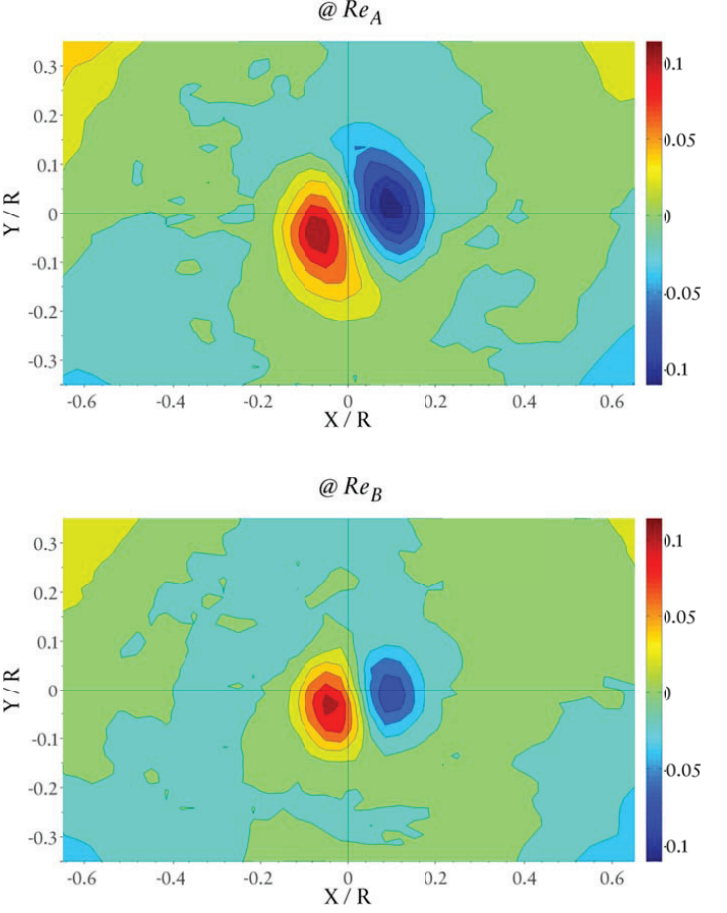

Figure 4.30:

Normalized Reynolds Stress Component $\overline{v'w'}$ *@ z1 L_3=4D*

The $\overline{v'w'}$ stress starts spreading in the other regions however the peak values at z_3 are almost half the values at z_1 (Figure 4.31). The spread of $\overline{v'w'}$ is not purely in radial direction. From the contour plots it can be seen that the two small regions with high values of $\overline{v'w'}$ near the cylinder axis enlarge in outward radial direction as well as in clockwise tangential direction whereas the near wall region enlarges radially inward and tangentially in

anticlockwise direction. This feature was comparatively less clear from the contour plots of $\overline{u'w'}$ stress.

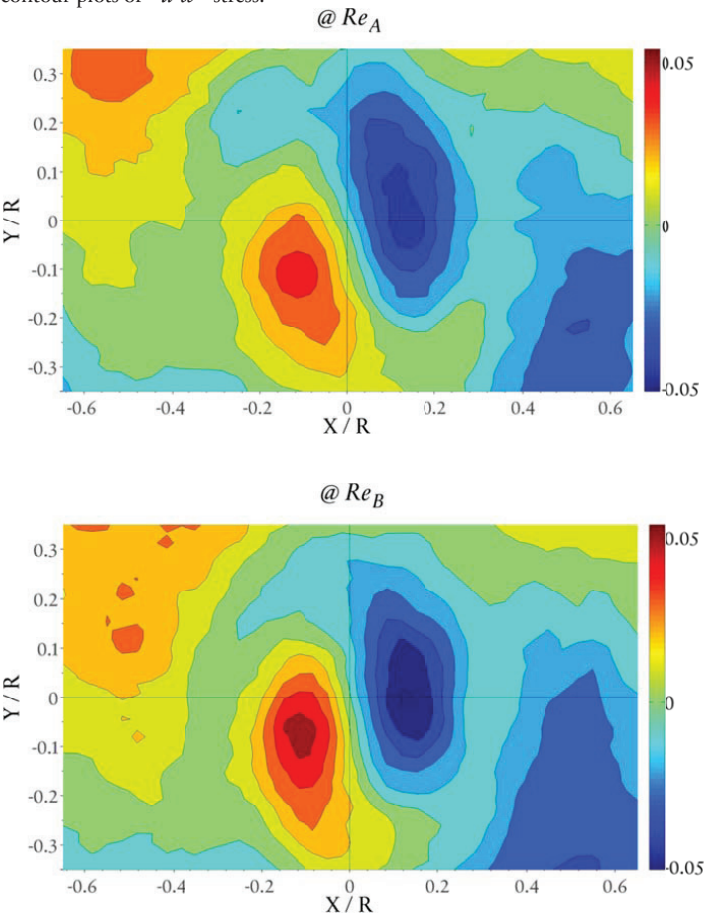

Figure 4.31:

Normalized Reynolds Stress Component $\overline{v'w'}$ *@ z3* L_3*=4D*

At z_5 in figure 4.32, similar to $\overline{u'w'}$, the maximum value of $\overline{v'w'}$ across the cylinder cross-sectional plane has decayed almost 10 times its maximum value at z_1. At Re_A the size of the region with smallest values of $\overline{v'w'}$ has increased again, however, for both Re_A and Re_B with decay in swirl downstream, the magnitude of $\overline{v'w'}$ decreases but the spatial distribution increases thus tending towards a more homogenized distribution in the flow.

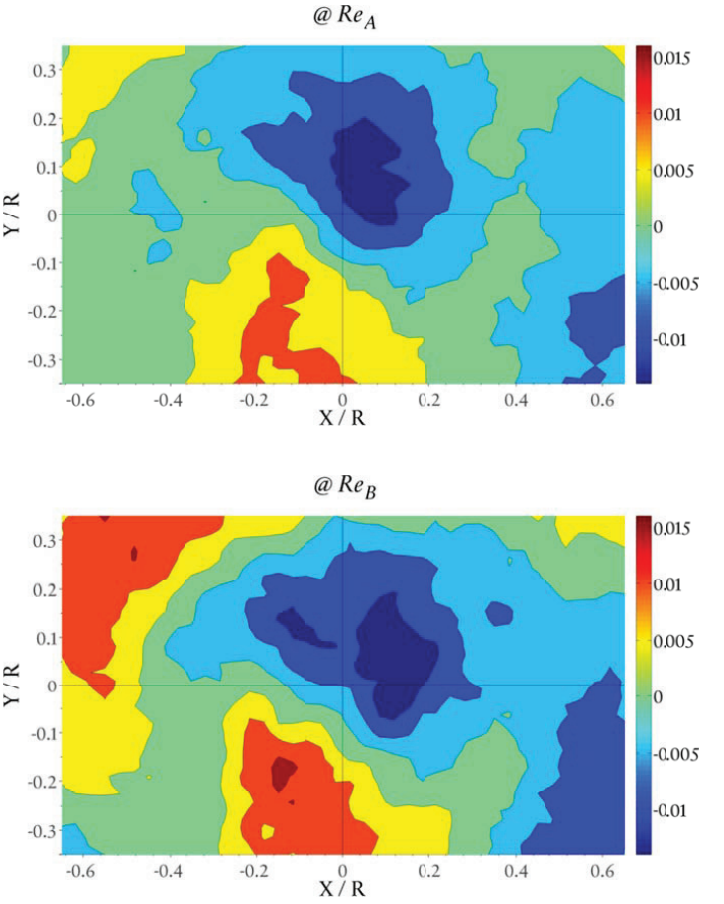

Figure 4.32:

Normalized Reynolds Stress Component $\overline{v'w'}$ *@ z5 L_3=4D*

The distribution of Reynolds shear stress components $\overline{v'_\theta v'_z}$ and $\overline{v'_r v'_z}$ can be understood by considering the plots for both $\overline{u'w'}$ and $\overline{v'w'}$. Since the axial velocity is same in both coordinate systems, the covariance of axial velocity component with tangential and radial velocities can be understood by considering (Figure 4.14). As discussed in section 4.2.5, in the contour plot of u the radial velocity is observed along X-axis tangential velocity along Y-axis. In figure 4.27 for $\overline{u'w'}$, the two small regions along Y-axis and in figure 4.30 for $\overline{v'w'}$, similar regions along X-axis represent regions with large covariance between tangential and axial velocity components i.e. $\overline{v'_\theta v'_z}$ .Similarly, the near wall regions in figures 4.27 and 4.30 represent the large

values of $\overline{v_r' v_z'}$. An overall picture of the distribution can be understood in this way that at z_1, the highest values of $\overline{v_\theta' v_z'}$ are observed in the vortex region whereas the $\overline{v_r' v_z'}$ are dominant in the near wall region. The region in between has the minimum values for both the shear stress components. With swirl decay along the flow, the spatial distribution of these shear stresses increase and magnitude decreases.

4.2.7 *Average Turbulent Kinetic Energy*

The average turbulent kinetic energy (TKE) k is given by

$$k = \frac{1}{2}\left(\overline{u'u'} + \overline{v'v'} + \overline{w'w'}\right) \tag{4.1}$$

From equation (4.1), the turbulent kinetic energy represents half the sum of normal components of Reynolds stresses. Thus a possible bias, as discussed in section 4.2.6, due to vortex core precession can also be expected in the values of k in the vortex core region.

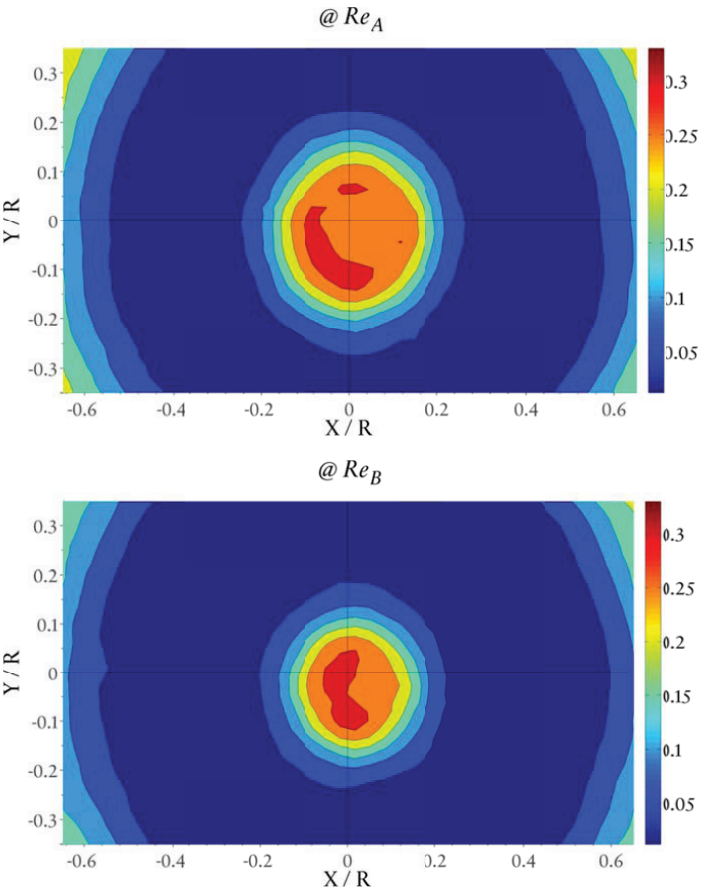

Figure 4.33:

Normalized Turbulent Kinetic Energy k @ z1 L_3=4D

At z_1 the largest value of k is observed in the vortex core region with the contour showing an asymmetric distribution (Figure 4.33). This asymmetry can also be observed in case of $\overline{w'w'}$ in figure 4.20 which may possibly be due to the effect of wall on the flow. k decreases outside the vortex core and attains minimum value outside the vortex. At larger radial distance of X/R = 0.5, k starts increasing again towards the cylinder wall region.

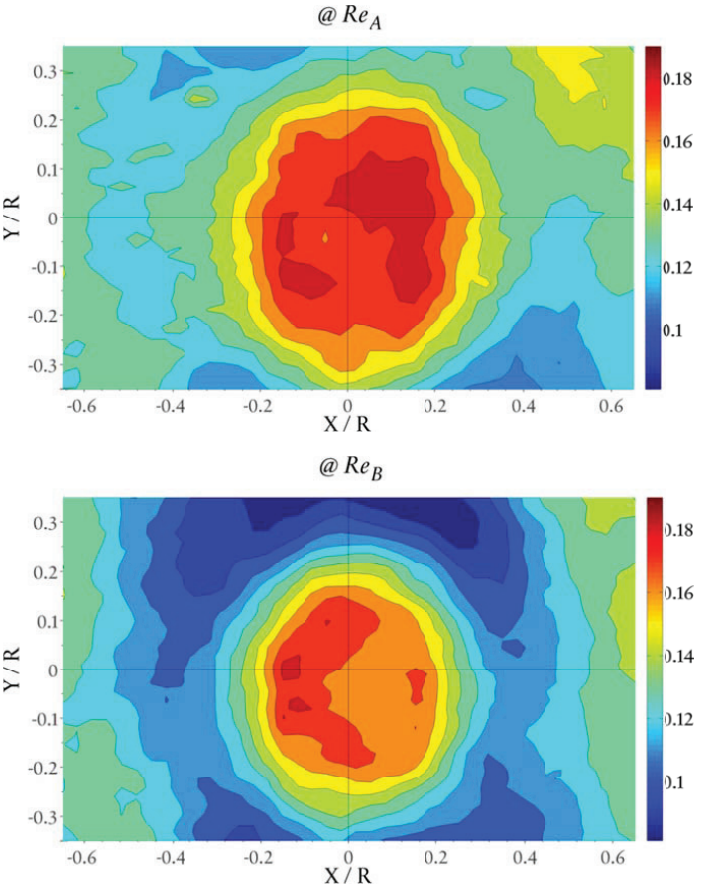

Figure 4.34:

Normalized Turbulent Kinetic Energy k @ z3 L_3=4D

With the enlargement of vortex core at z_3, the maximum value of turbulent kinetic energy decreases (Figure 4.34). The forced vortex region, however, still has largest value of k. For Re_B, the region surrounding the vortex core with minimum values of k, is observed only in a small region of the cross sectional plane at z_3. Turbulent kinetic energy is very low along Y-axis at radial position Y/R= ±0.35 from cylinder axis and along X-axis, turbulent kinetic energy has comparatively increased. For both axes, the values of k at large radial distance from cylinder axis indicate an increase in the turbulence level at larger distance from the cylinder wall. This demonstrates the existence of asymmetric distribution of k also outside the forced vortex.

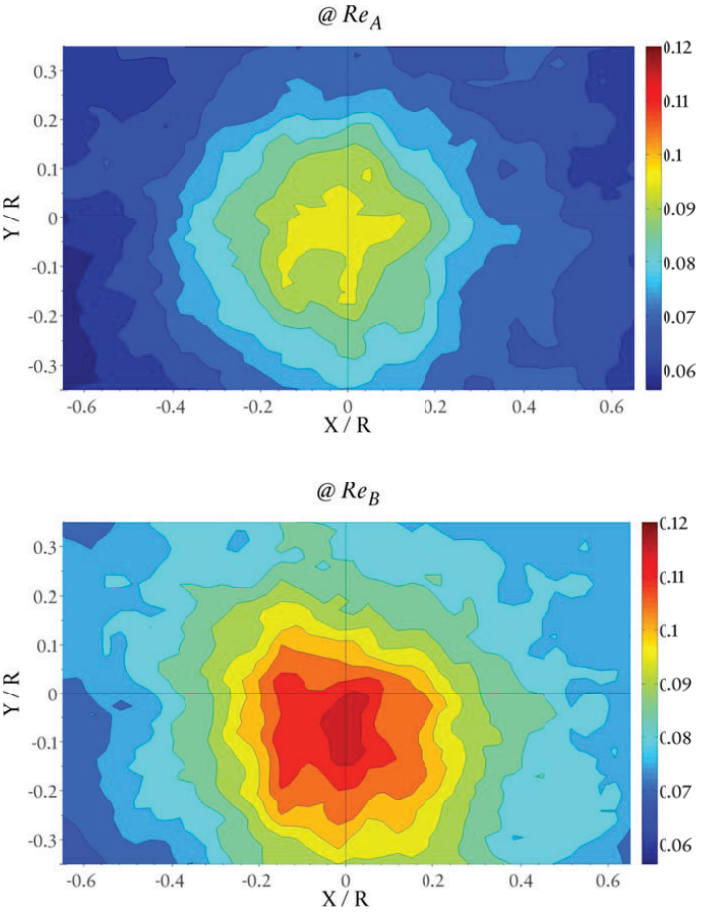

Figure 4.35:

Normalized Turbulent Kinetic Energy k @ z5 L_3=4D

At z_5, k has decreased in the near wall region and large values are observed only in the vortex core region (Figure 4.35). The vortex core at Re_B contains more turbulent kinetic energy than at Re_A.

4.3 *Effect of Cylinder Length*

In the previous section 4.2 the PIV results for L_3=4D are analyzed and the effect of Reynolds number at selected measuring positions are discussed. In this section the PIV experimental results are studied to understand the effect

of variation in cylinder length for each Reynolds number. The profile plots for different flow characteristics are presented separately for each Reynolds number and as described in table 4.1, first a comparison of results for cylinder lengths of 4D, 6D and 8D are discussed i.e. measuring planes (z_1-z_6) and then the results for z_7-z_{13} are given for the cylinder lengths of 6D and 8D. The contour plots for 3D velocity field, axial vorticity, Reynolds stresses and turbulent kinetic energy are discussed only for selected measuring positions and remaining results are given in Appendix C.

4.3.1 *Tangential Velocity Profile*

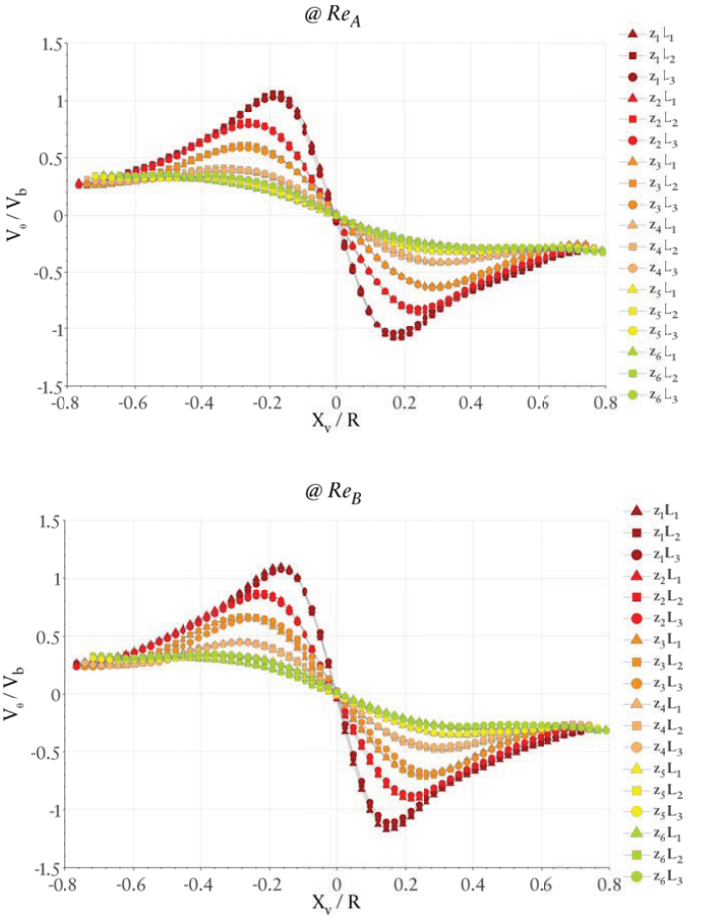

Figure 4.36:

Normalized Tangential Velocity Profiles for L=4D, 6D, 8D ($z_1 - z_6$).

The normalized tangential velocity profiles at measuring positions z_1-z_6 are shown in figure 4.35 for cylinder lengths of 4D, 6D and 8D. X_v indicates X-axis after the origin of the coordinate system is shifted to the approximated mean vortex center. It can be seen that despite the change in cylinder length, there is almost no variation in the V_θ profile at z_1-z_5. Only very small variations are observed near the peak V_θ values. At z_6, the V_θ profile for L_3 has slightly higher peak value at negative X_v /R positions compared to L_2 and L_3. The reason is that the position z_6 is located very close to the cylinder outlet and flow at that position feels the effect of being accelerated with increase in axial strain due to smaller diameter of cylinder outlet i.e $d_i / D_i = 0.58$.

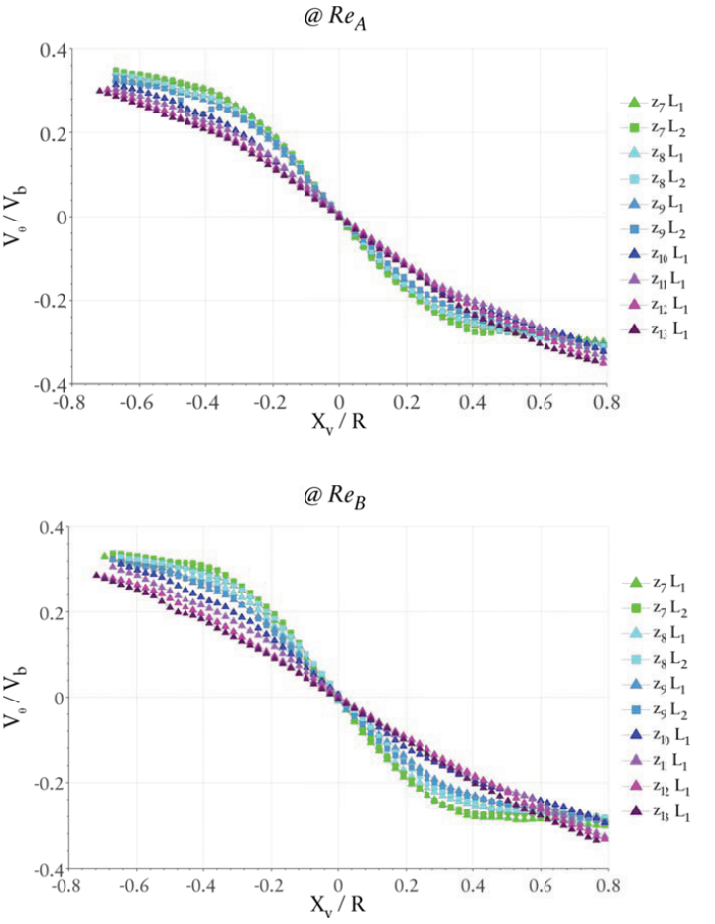

Figure 4.37:

Normalized Tangential Velocity Profiles for L=6D, 8D ($z_7 - z_{13}$).

For $L_2$and L_3 the tangential velocity decays in almost the same manner as L_3 except at z6. Figure 4.37 shows the V_θ profiles for the remaining positions i.e. z_7-z_9 for L_2 and z_7-z_{13} for L_1. The swirl decay results in the decrease in the V_θ values downstream to z_6 and increase in the size of the vortex. For both Reynolds number the peak V_θ value moves to larger radial distances downstream and at z_{11} for L_1, it seems that the profile shape has changed from Rankine/burger vortex to nearly solid body rotational forced vortex. In general, it can be concluded that V_θ gradually decays downstream and the vortex enlarges in size with a gradual transition from Rankine/ Burgers vortex to forced vortex profile.

4.3.2 *Axial Velocity Profile*

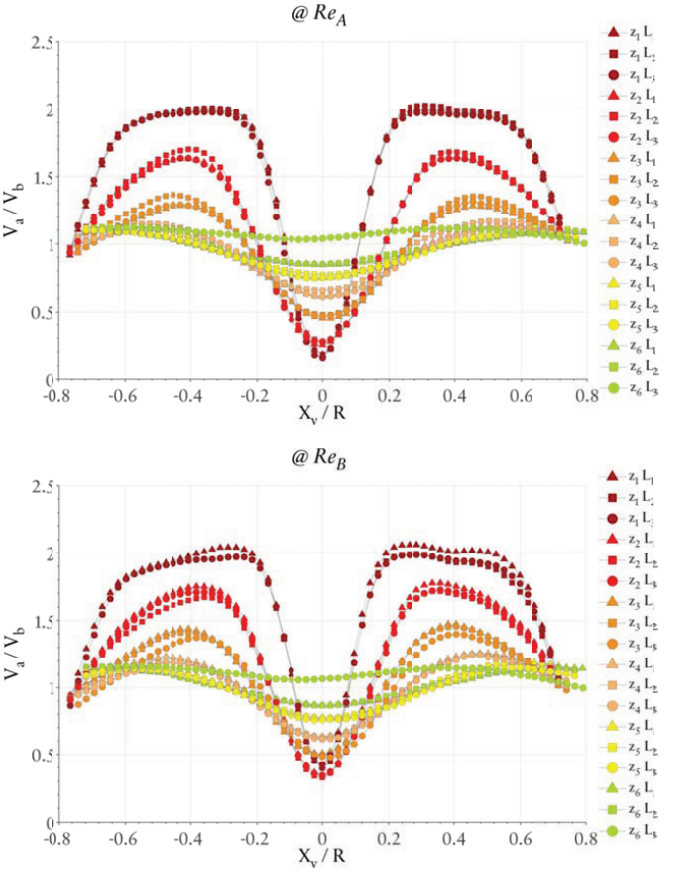

Figure 4.38:

Normalized Axial Velocity Profiles for L=4D, 6D, 8D ($z_1 - z_6$).

The normalized axial velocity profiles at positions z_1-z_6 for cylinder lengths of 4D, 6D and 8D are shown in figure 4.38. The profiles are nearly the same for a given position except at z_6 for cylinder length 4D where due to the presence of cylinder outlet an increase in the axial velocity is observed. Very small variations in magnitude of axial velocity are observed in the annular region.

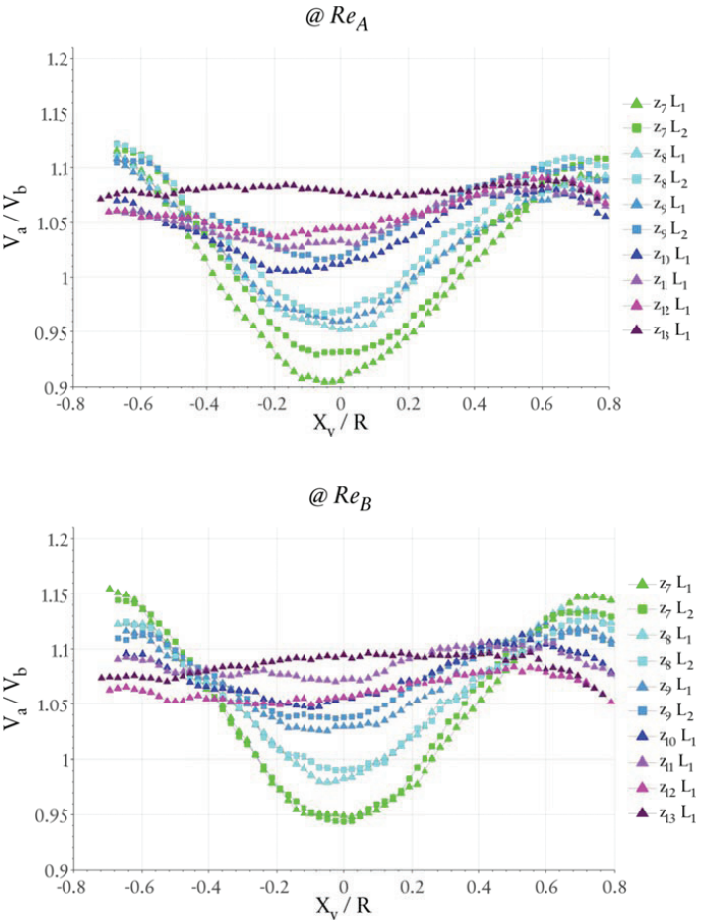

Figure 4.39:

Normalized Axial Velocity Profiles for L=6D, 8D ($z_7 - z_{13}$).

At Re_A and z_7-z_9, the V_z values in the vortex core are lower for L_3 compared to L_2. Considering the Y-axis scale this difference however is very small. For Re_B no such difference is observed. With the decay in the swirl the axial velocity distribution for L_2 and L_3 gradually changes from a 'wake-like'

profile towards a more uniform distribution by an increase in the V_z in the vortex core and decrease in its maximum value (Figure 4.39). At positions z_{11}-z_{13} for L_3, the axial velocity becomes nearly constant in most of the regions of cylinder cross-section except near wall regions.

4.3.3 *Radial Velocity Profile*

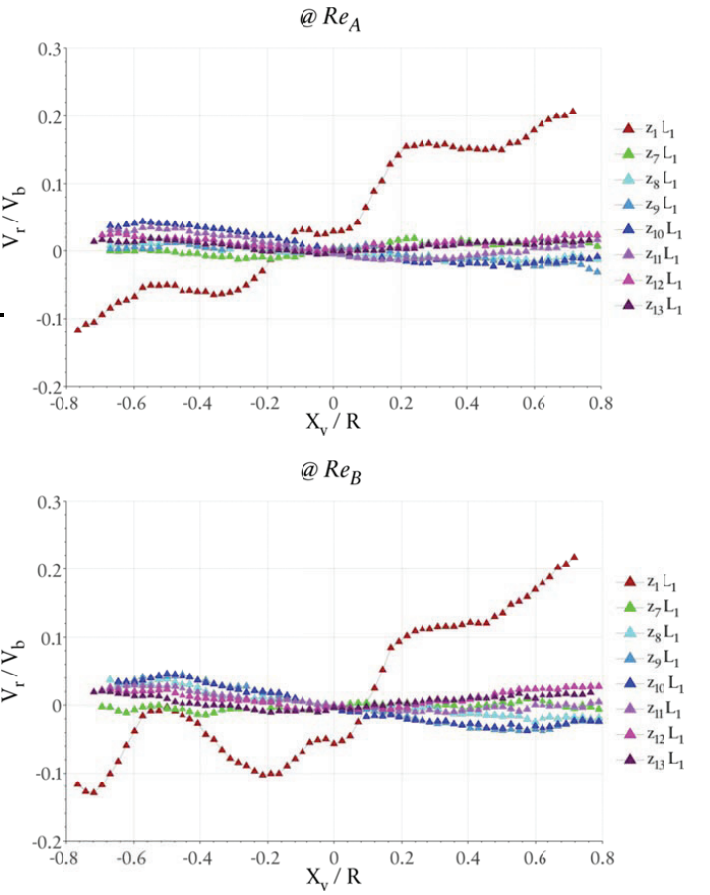

Figure 4.40:

Normalized Radial Velocity Profiles for L=8D.

The magnitude of radial velocity V_r is small compared to V_θ and V_z i.e. almost a factor of 10 lower (Figure 4.40). The figure shows V_r profile for z_1

and then from z_7-z_{13}. The decay in the radial velocity downstream the flow can be understood from V_r profiles at z_1 and z_7. At z_7 the radial velocity is very close to zero and then at further downstream position z_8 it starts increasing again but with its direction reversed along X_v i.e. from z_1-z_6 the positive values (vector direction notation) of V_r are along positive X_v and z_8-z_{11} along negative X_v. At z_{12} and z_{13} V_r is in the same direction on both sides of X_v. Flow exhibits same behavior for V_r at both Reynolds numbers Re_A and Re_B.

4.3.4 *Swirl Parameter*

The swirl parameter S as defined in Chapter 2 is the ratio of V_θ to V_z. Since the variation in cylinder length, in general, has no significant effect on the tangential and radial velocity profile at a given measuring position, only the results for L_1 are presented here (Figure 4.41). This will provide an overview of local swirl distribution as well as the decay in the swirl along the flow direction for Re_A and Re_B.

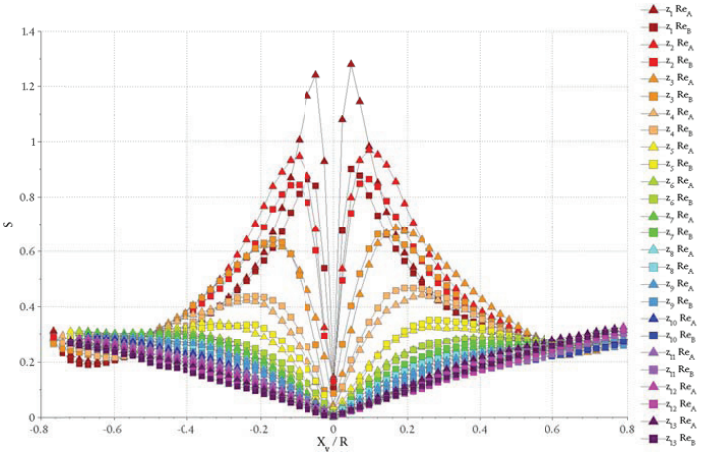

Figure 4.41:

Swirl Parameter S Profiles (absolute values) for L=8D.

To get a better overview of swirl parameter along the cylinder, figure 4.42 gives the profile of S_{max} which is the maximum value of local swirl parameter for a given measuring position. Profile generally demonstrates a sharp linear like decay in swirl from z_1-z_4 and then a very small. The linear fit has a slope of 1.7732 and a Y-axis intercept of -0.52964. For L_3 at z_6 a increase in S_{max} is observed which, as described before, is due to the effect of cylinder

outlet. Similarly for L_1 from z_{10}-z_{13} a small increase in S_{max} is also observed which may be an indication of cylinder outlet effect. The overall profile of S_{max} at different axial positions is fitted using a 7^{th} degree polynomial fit (Table 4.3). However, it must be remembered that in the current experiment, measurements are not conducted for the whole cylinder diameter and as discussed before at further downstream positions maximum V_θ is observed to be at larger radial distance from cylinder axis and V_z values are also not measured in the near wall region. Therefore, the actual S_{max} value may slightly be different for z_9-z_{13}. An integrated value of S for the whole cylinder diameter will give the average value of swirl at a given measuring position.

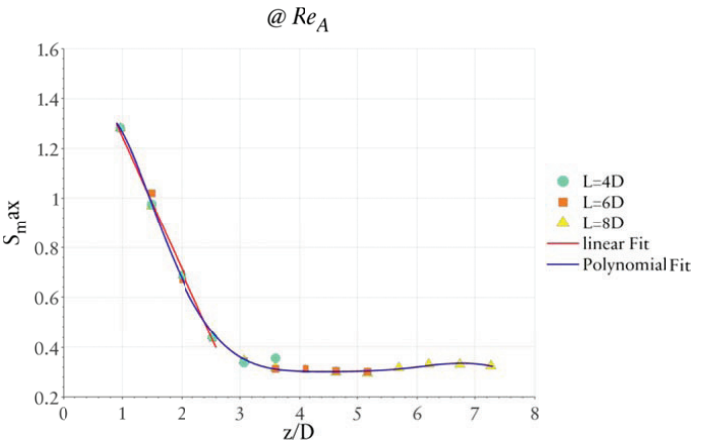

Figure 4.42:

Maximum Swirl Parameter (absolute values) for L=8D, 6D and 4D.

Polynomial Coefficients	Values
a_0	0.526703922
a_1	2.866913238
a_2	-3.379260164
a_3	1.590002361
a_4	-0.391679792
a_5	0.053433717
a_6	-0.003825368
a_7	0.000112153

Table 4.3:

Values of Polynomial Coefficient for data fitting the Maximum Swirl Parameter Value.

4.3.5 *Mean Axial Vorticity*

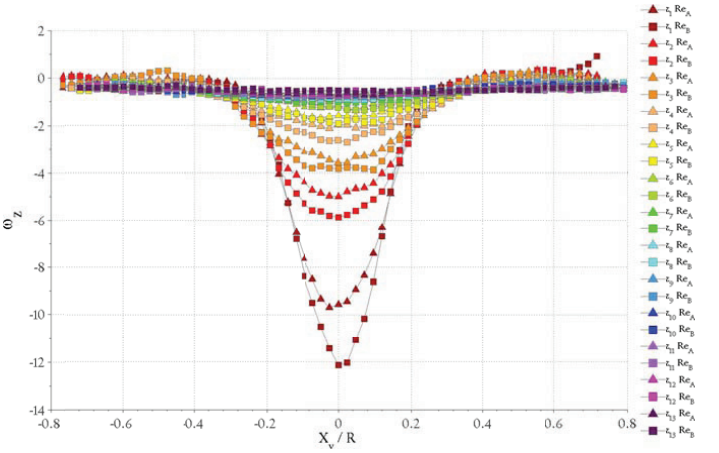

Figure 4.43:

Mean Normalized Axial Vorticity ω_z profiles for L_1=8D @ Re_A and Re_B.

The mean axial vorticity profiles for L_1 are shown in figure 4.43 for both Re_A and Re_B. Since there is no significant difference between ω_z profiles at z_1-z_9 for L_2 and L_1, only the results for L_1 are presented here.

The vorticity has a Gaussian like profile at z_1 with its peak higher at Re_B than Re_A. This higher vortical behavior of flow at low Reynolds number is observed until z_6 where the difference in ω_z in the vortex core region is very small for the two Reynolds numbers. As the swirl decays downstream the profile peak also decreases and tends to become gradually more uniform along the cylinder cross-section. For measuring positions z_{11}-z_{13} the ω_z profiles become like a straight line and can be considered as uniform.

4.3.6 *Mean Vortex Core Position*

The mean vortex core location at different measurement positions along the cylinder length are given in figures 4.44-4.46. Figures show the vortex core location for both Reynolds numbers at a given cylinder length Re_A and Re_B.

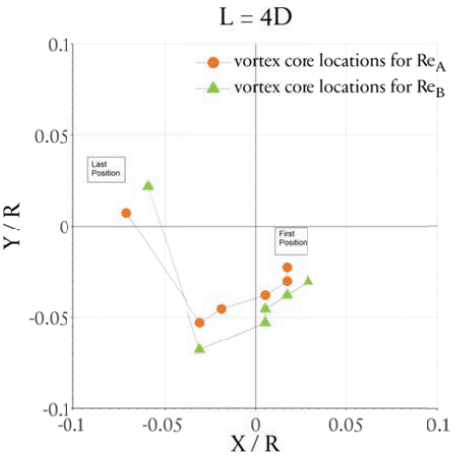

Figure 4.44:

Mean Vortex Core positions for L_3=4D.

For all cylinder lengths L_1, L_2 and L_3 the mean position of the vortex core moves in a clockwise direction from z_1 near the cylinder inlet to the last position. This demonstrates that the vortex core has a helical path that rotates in the same direction as the swirl direction (Figures 4.6-4.8). The radius of the helical path is small and lies with X/R= 0.1. For a given cylinder length, the radius of the helical path is not the same for all the measuring positions and the vortex core location does not coincide at all measuring positions for both the Reynolds numbers. At z_1, the helical path has a small radius which increases at downstream positions. Only for few consecutive measuring positions, the helix radius is same. For L_3 and L_2 in figures 4.44 and 4.45 respectively, the helical vortex core path does not complete one revolution.

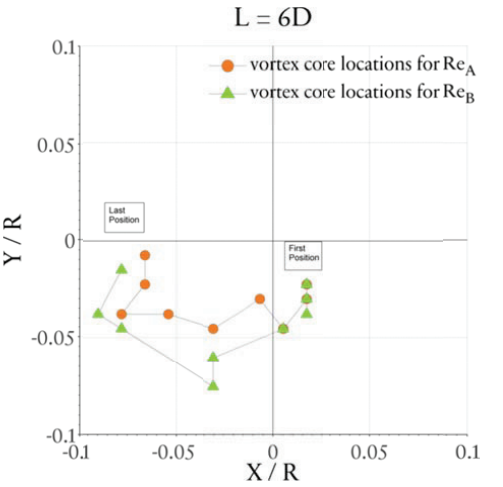

Figure 4.45:

Mean Vortex Core positions for L_2=6D.

For L_1, an interesting feature is observed where the helical vortex path does not complete one revolution and instead seems to re-twists at one side of the X-axis. This re-twist behavior in the helical path is observed from z_{10}-z_{13}. A complete re-twist in the helical vortex path may be possible to observe for cylinder lengths more than 8D.

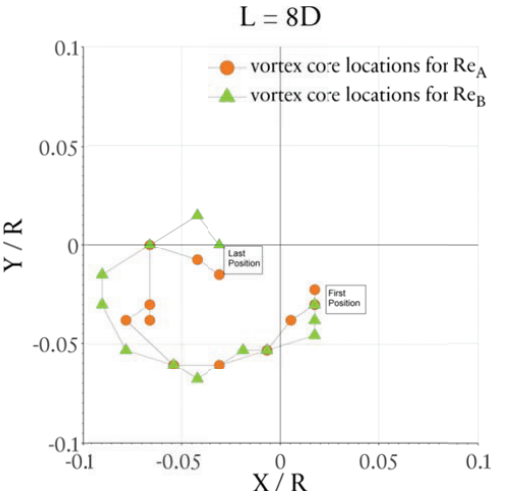

Figure 4.46:

Mean Vortex Core positions for L_1=8D.

4.4 Cylinder Wall Pressure Measurements

For each measuring position and at a given Reynolds number, static differential pressure is measured between a point close to the swirl generator inlet (radial distance of 1 cm from inlet) as the reference point and the cylinder wall at that given position (Figure 3.2).

$$\Delta P = P_{in} - P_z \tag{4.1}$$

Where P_{in} is the pressure at the inlet and P_z is the pressure at a given measuring position as mentioned in (Table 4.1).

The pressure taps are mounted at single point on the circumference of each measuring cross sectional plane (Figure 4.47). The measured pressure difference at different positions thus provides pressure drop downstream along the cylinder length with respect to test model inlet.

The measurements are conducted using a high resolution Furness® FC0510 digital differential micro manometer. For each position the pressure is measured for a time period of 3-5 min with data acquisition frequency of 1s. The measured differential pressure will represent an average value because in case of three dimensional swirling flows especially flow with asymmetric or helical behavior of the vortex, the pressure at the wall changes with time i.e. following the vortex behavior inside the cylinder and a measurement interval of 1s may not resolve the high frequency fluctuation of wall static pressure at high Re.

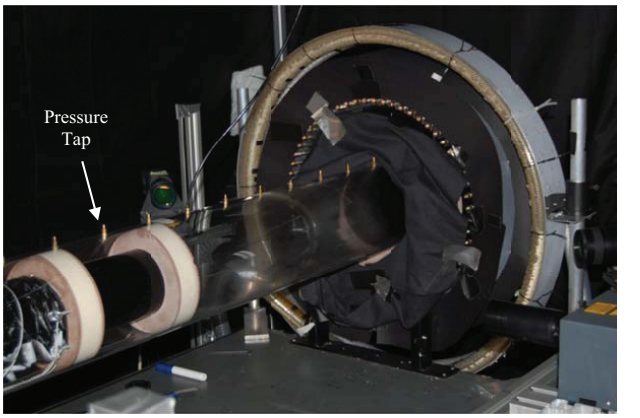

Figure 4.47:

Pressure Taps Location on Scavenging Flow Test model.

Figures 4.48 and 4.49 show the normalized pressure drop along the cylinder for different cylinder lengths at Re_A and Re_B respectively. It can be seen that for both Reynolds numbers the pressure drop along the cylinder decays rapidly for the first 4 positions.

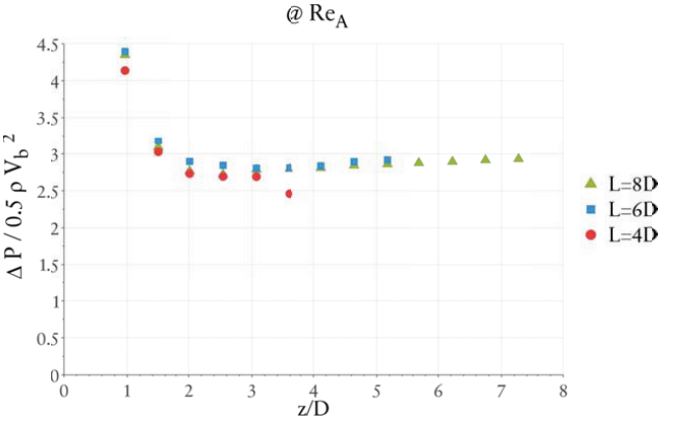

Figure 4.48:

Average Static Pressure Drop along the Cylinder @ Re = 1.2 x 10^5.

The pressure drop at position z_1 is relatively high compared to other positions and at the next position z_2 the pressure drop reduces significantly. A possible reason is the shape of inlet to the cylinder where the flow from the swirl generator (Inlet Section) gets a sharp bending and creates a near cylinder wall re-circulating zone (Figure 3.4).

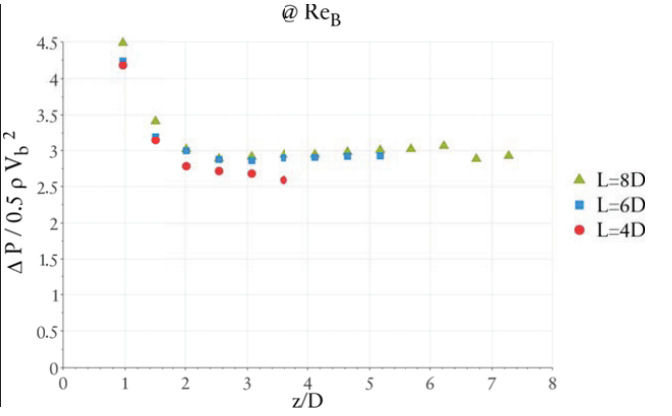

Figure 4.49:

Average Static Pressure Drop along the Cylinder @ Re = 0.6 x 10^5.

For cylinder length L_3 at position z_6, the pressure drop reduces further indicating the effects of cylinder outlet wall, as this position for L_3 is closer to

the cylinder outlet wall compared to z_9 and z_{13} for L_2 and L_1 respectively. There is a small relative difference observed in the overall magnitude of the data values among the three cylinder lengths due to human error involved in reading the lower meniscus position of water level in the U-tube manometer.

4.5 Discussion

The current experiment studies a confined swirling flow in a circular cylinder. The focus has been to understand not only the characteristics of the confined swirling flow but also to study the possible effect. In other words the behavior of the swirling flow, when the length/ aspect ratio of the cylinder in which the swirling flow is confined, is changed while keeping the same inlet and outlet conditions. Conducting the experiment at two different Reynolds numbers has also provided additional information on the flow characteristics.

The turning section in figure 4.50 facilitates in transition of radial and tangential momenta (from swirl generator) to radial and axial thus resulting in very small magnitude of radial velocity in the cylinder as can be observed in Kitoh (1991). For the setup developed in this study, in order to keep some engine cylinder features in the test model, there exists is no center body. The flow enters in the cylinder with a strong radial component (blade angle diverge the flow at an average angle of 26 degree from the radius) and then this radial momentum decreases significantly. This indicates that in the current setup the radial velocity magnitude is possibly larger at the cylinder cross section very close to the cylinder inlet compared to the radial velocity magnitude measured by aforementioned vane type swirl generator design by (Kitoh, 1991). A very confined and small size vortex core, at z_1 in this experiment, may be because of stronger radial velocity component at the cylinder inlet (Okulov, 2010). However, the details of the 3D velocity distribution at the cylinder cross-sections, prior to z_1, where the vortex is generated was not possible to measure using PIV due lack of optical access to laser and cameras.

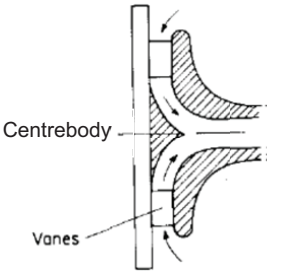

Figure 4.50:

Sketch of Centrebody and turning section (Faler et al., 1977).

The averaged data results from PIV experimentation have shown a helical vortex flow inside the cylinder. However, the LDA experimental results for mean tangential velocity at a measuring plane, prior to the first measuring plane z_1 in case of PIV measurements, have shown a symmetric profile. This demonstrates the transition of an axis symmetric swirl to asymmetric swirl at cylinder cross-sections very close to cylinder inlet. The asymmetric velocity distribution measured in the swirl generator seems to die out when the flow, after passing through the contraction section, enters the test cylinder.

The tangential velocity profile at z_1 shows a Burger vortex like profile i.e. a rotational forced vortex core surrounded by an irrotational annular region. Contrary to the theoretical profile of Burgers vortex and the experimental results discussed by Leibovich (1984), the forced vortex is not surrounded by an irrotational region. In fact, the forced vortex is surrounded by a weak vortical region followed by a small region where the vorticity values are very small (Figure 4.11). This is possibly due to Görtler vortices in the near cylinder wall region. As the swirl decays downstream and the vortex size increases, this weak vortical region almost disappears. The axial velocity has a wake-like profile with no reverse flow at the vortex core. With the decay in the swirl, for the axial velocity, the local maximum decreases and the local minimum, also defined as vortex advection velocity (Velte et al., 2008), increases. For the cylinder length of 8D this trend continues until at positions z_{11} where the axial velocity profile becomes nearly flat. Similar velocity profiles and behavior, along the cylinder/ pipe for tangential and axial components, have been observed by Steenbergen et al. (1998) for the experimental measurements of swirling flow with 'concentrated vortex'.

The distribution of velocity components is not symmetric for measured cross sectional planes given in table 4.1. For example figure 4.49 shows the axial velocity profiles along positive and negative X and Y axis using the approximate position of vortex core as the origin. A line plot has been used for the experimental data to give a clear presentation of the velocity asymmetry. Due to rectangular shape of camera view, the data for larger radial positions along Y-axis could not be measured.

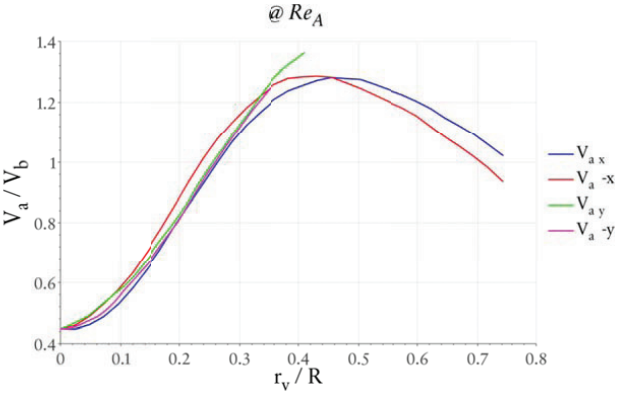

Figure 4.49:

Normalized mean Axial Velocity in different radial directions at z_3.

The presence of a precessing vortex core (PVC) is a very important characteristic to be identified because if present, the value of its frequency and amplitude will affect the experimental results in different ways. For example in case of profile plots for velocity components with precession of vortex core there will be a shift in the radial position of the profile lines for each time step/ instantaneous snapshot in case of PIV. This shift is proportional to the amplitude of the precession and a final temporal average of all the instantaneous measurements will result for example in a vortex core size larger than the actual one. On the other hand the frequency of precession will introduce a bias in RMS values of velocity components in the vortex precession region. This means that the measured values of Reynolds stress components and turbulent kinetic energy (TKE) include a bias in the vortex core region.

Figure 4.50 shows the instantaneous vortex core position for z_1 at Re_A using the algorithm defined in section 4.3.6. The algorithm is only applicable to instantaneous data for z_1 only because for the other downstream positions the instantaneous data can have more than one vortex in the vortex core region. From figure 4.51 it can be seen that for most of the instantaneous measurements the vortex core location is not fixed and moves in an area between r/R= ± 0.2. However, to conclude any further details like precession frequency and amplitude, high speed and time resolved PIV measurements are necessary compared to current PIV experimentation used in this experiment. The periodicity in the vortex core precession can be detected by well-defined peaks in the frequency spectra and in case there is no peak observed then the vortex precession is considered to be random (Escudier et al., 2006).

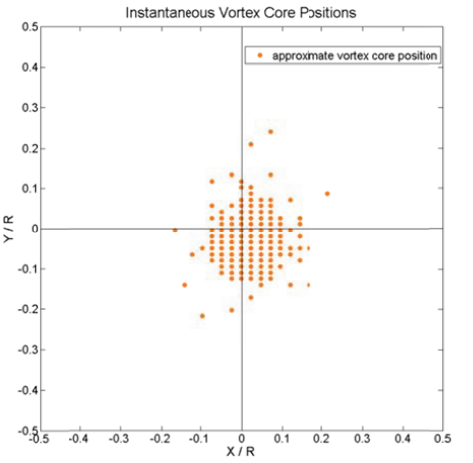

Figure 4.50:

Instantaneous position of vortex core at z_1.

In order to find out the existence of a precessing vortex core and its consequent frequency, LDA measurements are conducted at a radial distance

of 10 mm from the origin and an axial distance of 20 mm. The results show the existence of PVC and a linear dependency of precession frequency on the flow rate (Figure 4.51). Alekseenko et al. (1999) also found this linear dependency of precession frequency with flow rate at a given swirl number.

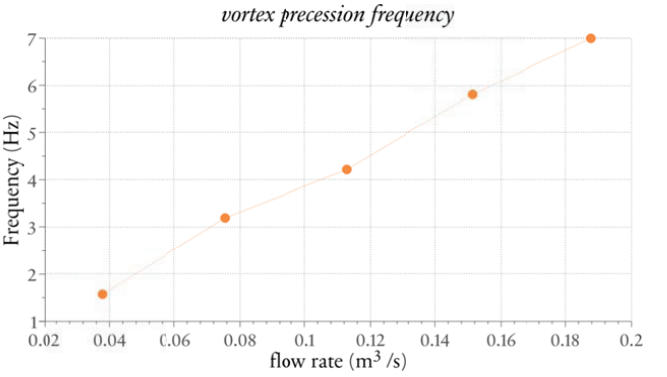

Figure 4.51:

Vortex Precession Frequency at different flow rates (Schnipper, 2010).

The effect of Reynolds number is very obvious on the flow characteristics. The high Reynolds number Re_A exhibits comparatively larger vortex size than lower Re_B. The flow at Re_B is less responsive or in other words more resistive to variations in vorticity and Reynolds stresses as the swirl decays along the pipe. In case of Reynolds stresses by comparing contour plots for Re_A and Re_B, it can be seen that with swirl decay downstream, the flow at high Reynolds number has higher tendency towards a more uniform spatial distribution of individual Reynolds stress components in the flow domain (see section 4.2.5 and 4.2.6).

The aforementioned effects of Reynolds number can also have a possibility due to vortex core precession by assuming vortex core precession to be a major contributor to the measured values of instantaneous velocity data in the region around the cylinder axis. This assumption will qualitatively give some new information about the effect of Reynolds number on the precession frequency and amplitude. For example if the vortex core precession has a large amplitude then the temporal average of velocity components will result in a large mean vortex core size. From the experimental results, it can probably be concluded that, in the current experiment, with increase in Reynolds number the amplitude of vortex precession increases and with swirl decay downstream its frequency decreases compared to low Reynolds number. However, the effect of swirl decay along the pipe on the vortex core precession frequency, to the knowledge of author, has not been reported and requires more experiments for a detailed and quantitative analysis.

The Reynolds stress normal components are high in the core and near wall regions. On average the magnitude of shear stress components, at different measuring positions are smaller than normal stress components. Considering the maximum values, for normal stresses at z_1 $\overline{w'w'} > \overline{u'u'} \simeq \overline{v'v'}$ and for shear stresses $\overline{u'w'} \simeq \overline{v'w'} > \overline{u'v'}$ indicating anisotropy of the flow. However, with swirl decay downstream at z_5, the maximum values become almost equal for individual components of both normal and shear stress components i.e. $\overline{w'w'} \simeq \overline{u'u'} \simeq \overline{v'v'}$ and $\overline{u'w'} \simeq \overline{v'w'} \simeq \overline{u'v'}$. The Reynolds stresses decay with the swirl and distribution of normal and shear components tends to become comparatively and gradually more uniform in the flow domain. For $\overline{u'u'}$ and $\overline{v'v'}$, the rotation of the oval shape region to an angle with the axes lines for downstream positions is not easy to explain. Probably it is the three dimensionality of the flow parameters like asymmetric velocity distribution, helical vortex and wall effect etc. that spreads the velocity variance unevenly and tilts the oval shaped region in anticlockwise direction. Another possible reason may also be the downstream increase in amplitude of precessing of vortex core which is statistically observed at positions between the axes lines in the instantaneous PIV snapshots.

The distribution of Reynolds stress components in polar coordinates along X-axis at z_1 and Re_A is given in figure 4.52. Yan et al. (2000) used LDA to measure turbulent kinetic energy distribution in a confined swirling flow using a vortex chamber that used similar geometry of vortex chamber i.e. there is a 90° bending when the flow enters the cylinder from swirl generator. For $\overline{v'_\theta v'_\theta}$ and $\overline{v'_r v'_r}$, the result obtained by Yan et al. (2000) show qualitatively similar behavior to results shown in in figure 4.52 i.e. large values are observed in the vortex core region and at large radial distance from the cylinder axis.

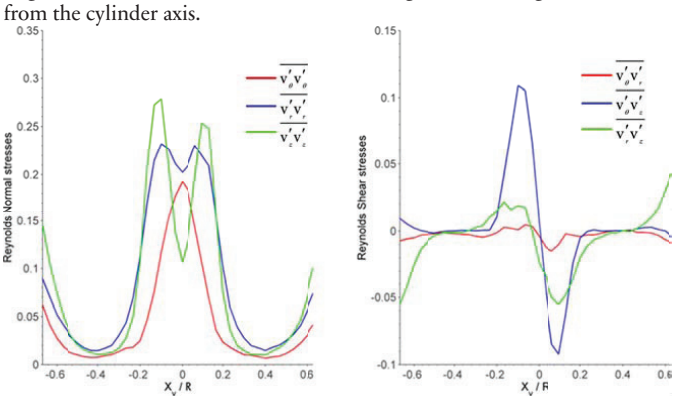

Figure 4.52:

Normalized Reynolds Stresses in Polar Coordinates at z_1 and Re_A.

The outlet section that provides a flat-bottom cylinder head has the outlet pipe with the ratio of outlet to cylinder diameter as 0.579. The current

experiment has been conducted using a single blade angle, therefore, all the measurements are conducted at a constant swirl number. Thus it is not possible to study the upstream effect of this exit contraction on the flow profile in the cylinder as a function of swirl number, similar to studies conducted by (Escudier et al. 1985, Escudier at el. 2006). The experimental results from different cylinder lengths, however, indicate that the flow does not feel the presence of outlet contraction until cylinder cross-sections very close to it as in case of z_6 with cylinder length 4D. The downstream change in cylinder length is not detected by the flow at upstream positions and thus the flow mainly depends on the upstream conditions at the cylinder inlet. The flow behavior remains the same for a given Reynolds number and whether or not the variation in the velocity profiles at different Reynolds number is due to outlet contraction needs further experimental investigation.

For all the cylinder lengths used in this experiment, the vortex core follows a helical path downstream the flow. The radius of the helix is not constant and actually increases along the flow direction. However, in all the cylinder lengths the helical path does not complete one rotation. Experiments conducted by (Escudier et al., 2006) observed a helical vortex path when the outlet contraction is made eccentric with respect to cylinder axis but in the current experiment the outlet is aligned with the cylinder axis. The helix rotation is clockwise representing a left-handed helical vortex. However, contrary to the results obtained by (Alekseenko et al., 1999), the helical path and fluid particles (swirl) have same direction i.e. clockwise.

At z_1 the flow has a tangential velocity like Burgers vortex and the wake-like profile of axial velocity does not show any reverse flow. As mentioned by (Alekseenko et al., 2007) this represents that the helical path, followed by the vortex core downstream the cylinder, has a negative pitch. For the cylinder length 8D, at z_{10} and positions downwards, the tangential velocity profile becomes like forced vortex and the axial velocity profile becomes almost uniform. Besides, the vorticity profiles having Gaussian profile at z_1 also becomes uniform. This demonstrates that for cylinder length 8D at far down stream positions the negative pitch changes to infinite value indicating a transition of left-handed helical vortex to right handed helical vortex called as 'L-Transition' and is one of the characteristics of vortex breakdown (Okulov et al., 2002) (see Section 2.3.6). However, since z_{13} is close to outlet for cylinder length of 8D, the complete transition of the left handed helical vortex to right handed type cannot be seen from experimental results. It probably requires conducting measurements by keeping the cylinder length more than 8D. Another interesting feature is observed from the helical vortex path for 8D cylinder length where instead of completing one revolution the vortex path tries to re-twist at far downstream cross-sections. Similar results are obtained from experiments by (Alekseenko et al., 2007) but the difference is that in their experiment the outlet contraction is made eccentric to cylinder axis. Further, this re-twisting of helical path, in their case, is observed in the bottom vicinity (near inlet) whereas in current experiment it is observed near cylinder outlet. This re-twisting indicates distortion of helix and change in its direction (Alekseenko et al., 2007). Thus it can be concluded that in case of cylinder length 8D, at far downstream positions,

the flow indicates a vortex breakdown. However, from the current experimental results, the location of the vortex breakdown being before or after the outlet contraction cannot be predicted.

Effect of Piston Position

In this chapter the effect of piston position on the in-cylinder swirling flow during the scavenging process is studied using the stereoscopic particle image velocimetry technique. The measurements are conducted at different cross-sectional planes along the cylinder length and at piston positions covering the air intake port by 0%, 25%, 50% and 75%.

In this experiment, stereoscopic PIV measurements are carried out using the same setup as described in Chapter 3. The cylinder length is kept at 4D and measuring positions are also kept the same as described for L_3 in Table 4.1 and also given here in Table 5.1.

Table 5.1:

Measuring Positions.

Position No.	Axial Positions (z/D)
z1	0.963
z2	1.489
z3	2.016
z4	2.542
z5	3.068
z6	3.595

The length and diameter of exhaust pipe is kept constant for all measurements. The opening of the cylinder inlet has a width of 4 cm. The measurements are conducted at 4 fixed piston positions. For fully open cylinder inlet/ intake port[1] the piston is kept aligned with the lower end of the cylinder inlet. The piston is then translated inside the cylinder by 1cm thus partially closing the inlet by 25%. For 50% closure the piston is translated further by 1cm. In the next step for 75% port closure, the piston is translated again by 1cm with a total translation of 3cm inside the cylinder compared to its position with fully open intake port. This means that at 75% the width of the cylinder inlet is reduced to 1cm and the cylinder length also has reduced by 3cm compared to 4D. However, from the experimental

[1] In this chapter and other parts of the thesis the cylinder inlet is also named as intake port analogous to scavenge ports in a Two-Stroke low speed marine diesel engine.

results in Chapter 4, the variation in cylinder length may not be having any significant effect on the in-cylinder. The axial positions mentioned in table 5.1 are all relative to the origin fixed at piston position at fully open port.

The PIV data acquisition is performed by keeping the piston at any aforementioned fixed position and then taking measurements at cross-sectional planes z_1 to z_6 along the length of the cylinder. The piston is then moved manually to one of the next aforementioned position and the same procedure is repeated. Thus measurements are not conducted in a varying in-cylinder flow Reynolds number and continuous piston translation. This makes the measurements in this experiment to be conducted in a quasi-steady state because in real engine scavenging process, in addition to stratified flow and large temperature gradients, the piston accelerates or decelerates continuously (covering and uncovering the intake ports) and the in-cylinder flow rate and Reynolds number change accordingly. The presence of exhaust valve has an aerodynamic effect on the in-cylinder flow e.g. it acts as a bluff body to the flow at the cylinder outlet and also changes the cross-section of the cylinder outlet. Studying the effect of exhaust valve on the in-cylinder flow is considered as the future work.

In order to study the effect of variation in flow rate and Reynolds number on the in-cylinder swirling flow, for each given piston position, the measurements are conducted at two different Reynolds numbers ($Re_A = 6.5 \times 10^4 \pm 1870$ and $Re_B = 3.25 \times 10^4 \pm 935$) as in the experiment discussed in Chapter 4. In a real engine, the flow rate changes as the piston movement closes ports. For simplicity, in this experiment, the flow rate has been kept constant for different port openings, but by using two different flow rates (High and comparatively low), the effect of change in flow rate on the in-cylinder flow can be studied. Thus the current experiment is focused on the effect of piston position on the in-cylinder confined swirling flow. The experimental results can also be useful for the computational modeling where, at first, the performance of a given model is validated against the experimental results at different quasi-steady state piston positions and a given Reynolds number and then a transient simulation of swirling flow during scavenging process is performed using computationally dynamic/ moving mesh techniques for piston and exhaust valve motions.

5.1 Results and Discussion

The results for the piston position with fully open cylinder inlet port has already been discussed in Chapter 4 for the cylinder length L=4D. However, only the tangential and axial velocity profiles for ports fully open are discussed briefly from the prospect of discussing the comparison of the effect of piston motion/ position on in-cylinder swirling flow. The rest of the chapter will present the results for piston positions at cylinder inlet closure of 25%, 50% and 75%.

The profiles plots are presented by first moving the origin of the coordinate system to the approximate position of vortex center and then interpolating along new X-axis defined as 'X_v' and at Y_v=0 for a flow characteristic of interest. The data for different flow characteristics are normalized in the same manner as in case for the experimental results in Chapter 4.

This chapter includes results selected from the experimental measurements in order to cover the topic in a comprehensive manner. The remaining and detailed results are given in Appendix B.

5.1.1 *Tangential and Axial Velocity Profiles*

Fully Open port

With the piston at bottom-dead-center (BDC) the cylinder inlet is fully open. The flow, after being accelerated in the contraction section enters the cylinder with tangential and stronger radial component. Since the cylinder inlet is fully open i.e. the piston surface is aligned with the bottom wall of the cylinder inlet, the flow on the piston surface resembles to flow on a flat surface. The other end of the cylinder inlet is aligned with the lower end of cylinder and makes a 90° bend. Due to this sharp bending, the flow entering the cylinder at the other side of cylinder inlet will form a large recirculation zone at the cylinder wall. The flow entering from in between the two ends of cylinder inlet loses majority of its radial momentum and after traveling to some radial distance towards the cylinder axis, bends to axial direction. This radial distance that flow travels at the cylinder cross-sections in front of the inlet is governed by the magnitude of radial component of incoming velocity and the size of the recirculation zone at the cylinder wall. Further, for the cylinder cross-sections close to cylinder inlet, the peaks in tangential and axial velocity profiles are approximately observed at this radial distance from the cylinder axis. The resulting tangential velocity V_θ profiles are shown in (Figure 5.1)[1].

When the intake port is fully open, the tangential velocity V_θ profile is similar to the Burgers vortex which is comprised of a solid body rotation forced vortex region and an outer region with very low rotationality or weak vorticity. Higher velocities are observed in the radial position where the inner forced and outer regions meet.

[1] The results for fully open port case are same as for cylinder length 4D in Chapter 4. The repetition is intended to provide a flow to the reader.

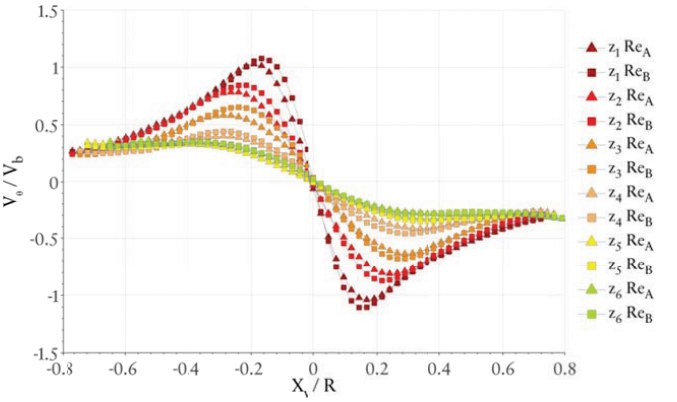

Figure 5.1:

Tangential Velocity for Intake port Fully Open.

The axial velocity V_z exhibits a 'wake-like' profile throughout the cylinder. However, no reverse flow is observed at the vortex core (Figure 5.2). At positions close to cylinder inlet, low velocities exist in the vortex core region and the near-wall region. The axial velocity profile in the region in between the core and near-wall has near flat profile and has peak V_z value for a given cross-sectional plane. With swirl decay along the flow, gradually smaller velocity gradients are observed at downstream cross-sections. The contraction due to smaller diameter of the cylinder exit accelerates the flow at cross-sections close to it.

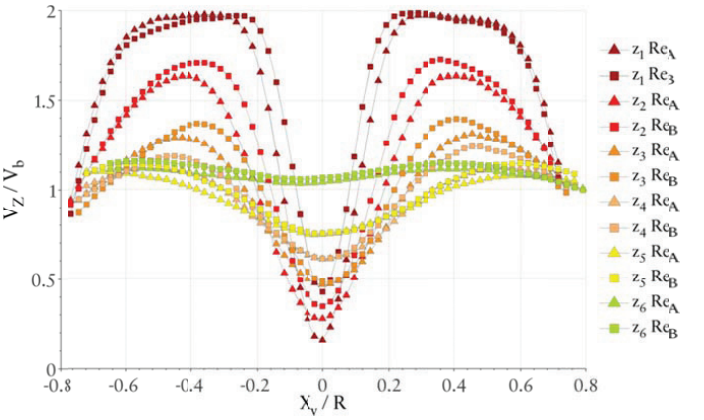

Figure 5.2:

Axial Velocity for Intake port Fully Open.

Thus for a fully open cylinder inlet, the in-cylinder swirling flow is similar to concentrated vortex type. The experiments conducted by Escudier et al. (1982) suggest that similar type of confined swirling flow at higher Reynolds number is actually a result of upstream effect of vortex break down in the exhaust pipe. However, in the current experiment, this reason cannot be verified since no measurements are conducted in the exhaust pipe.

25% Port Closure

When the piston is translated to partially close the intake port by 25%, the piston serves as a small forward-step facing the incoming flow in the cylinder. This step will affect the intensity of the radial component of incoming velocity and transform a part of it into axial direction at the cylinder inlet interface. The tangential velocity may also reduce due to friction with the piston outer wall surface exposed to the flow. The decrease in the radial and tangential components is compensated by the increase in axial velocity component due to continuity. The intake port area reduces and piston also behaves like a bluff-body in the flow path. Unsteady fluctuations/ disturbances are generated at the sharp-edge interface of the piston top and outer wall and recirculation regions are formed at the side of piston wall and piston surface (Figure 5.3). These fluctuations result in growth of instabilities and waves and are superimposed on already precessing helical vortical flow that exists when the port is fully open. Thus the resulting in-cylinder swirling flow becomes comparatively more transient and chaotic. In order to get a better average, for most of the measurements with piston partially covering the intake port, more number of instantaneous PIV snapshots has been taken compared to measurements for fully open port. From the point of view of Stereoscopic PIV experimentation, a significant aspect to be considered during the measurements is that the general method of setting the time between two laser pulses or PIV images by accepting in-plane particle displacements by 25-30% of the side of interrogation area is no more a good estimation. In stereoscopic PIV the third component of velocity is obtained mathematically after processing the snapshots of two cameras viewing in-plane displacement of particles. The increase in magnitude of the axial component and large variations in out-of-plane component (in this experiment is axial velocity) require the time between pulses to be chosen by considering the maximum displacement of particles in the axial direction by 25% of the laser sheet thickness. In the presence of a large axial velocity component, this axial displacement limit for the particles is achieved by setting the time between pulses in a way that allows the particles to have an in-plane displacement less than 25-30% of the side of interrogation area. Otherwise, the magnitude of particles with high axial velocity magnitude will not be measured correctly. Thus there will be a trade-off between the error/ uncertainty in the measurement of in-plane components (radial and tangential components in this case) and the out-of-plane component (axial velocity). For this reason, the measurements for some positions have been conducted with different times between pulses and only the selected ones are presented.

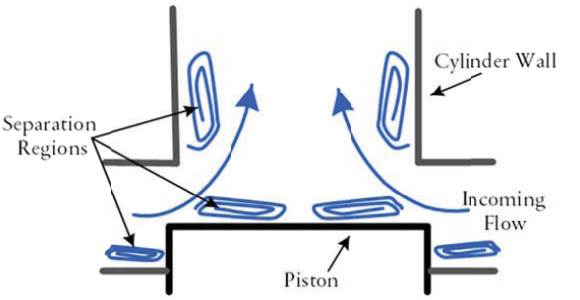

Figure 5.3:

Cartoon of flow at piston interface with partially closed cylinder inlet.

Since the flow rate is kept constant, the average velocity of the flow entering the cylinder will increase at the inlet port compared to when it is fully open. The decrease in the radial velocity will result in the increase in the size of the vortex core at position close to the cylinder inlet i.e. z_1. For the given Reynolds numbers, the magnitude of mean tangential velocity has decreased. The profile shows a less distinct peak at the interface of outer region and a comparatively bigger vortex core at z_1. The V_θ profile on both sides of the origin is different and indicates asymmetry in tangential velocity distribution. The size of the forced vortex increases along the flow downstream and at position z_5 the in-cylinder tangential velocity changes to solid body rotation.

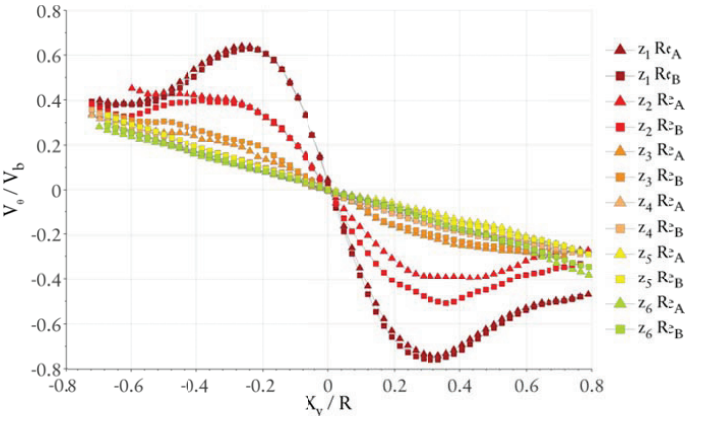

Figure 5.4:

Tangential Velocity for Intake port 25% Closed.

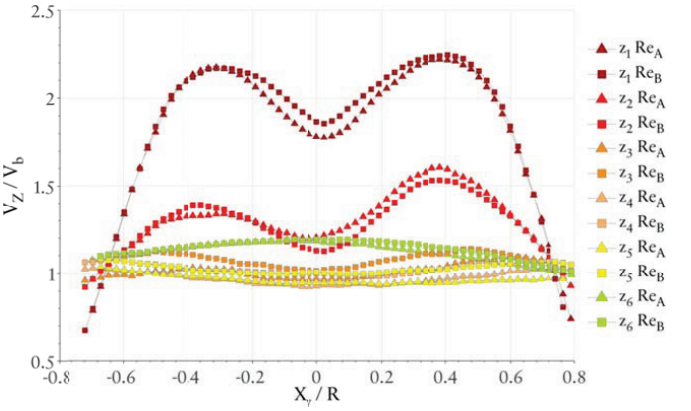

Figure 5.5:

Axial Velocity for Intake port 25% Closed.

The axial velocity at z_1 still has wake-like profile, however, the velocity deficit in the vortex core region has reduced indicating more mass entering into that region. The maximum value of V_z has also increased compared to fully open intake port. Between positions z_1 and z_2 there is a rapid decrease in the axial velocity peak. The difference between the V_z minimum in the vortex core and the peak V_z value outside the core has also decreased. This difference continues to reduce until at z_6 where the wake-like profile at z_5 has transformed into jet-like profile due to entrainment of more mass into the wake region. Further, Escudier et al. (1982) also observed a similar behavior in one of the experimental results, however, with a nearly axis-symmetric swirling flow.

50% Port Closure

With the piston covering 50% of the intake port, the shift in the asymmetry in the distribution of V_θ at z_1 increases further (Figure 5.6). Along positive X_v /R, the profile is still having a single peak. However, along negative X_v/R, the tangential velocity has two peaks. One comparatively smaller peak is at X_v/R=0.2 and the other larger peak in the near wall region. This is probably due to the effect of the cylinder wall. For confined swirling flows, the effect of presence of wall on the vortex is like the effect of a 'mirror vortex' as discussed in section 2.3.6. In case of helical swirling flows, when the vortex core position is at a larger distance from the cylinder axis or in other words closer to the cylinder wall, the effect of wall will enhance on the vortex side closer to wall. This picture gets more complicated when we consider a precessing and helical vortex.

At z_3 and further downstream the tangential velocity profile changes and attains a solid body like profile. In figure 2.1d, the profile also resembles to a

wall-jet profile in because the profile line has a small curvature from origin to larger radial positions. However, the profile type cannot be concluded here in the absence of measurement data near the cylinder wall. Comparing V_θ profiles in figures 5.1, 5.4 and 5.6 it can be seen very clearly that with the increase in intake port closure, a solid body rotation profile (if the tangential velocity profiles at z_3 and downstream is assumed to be a forced vortex) is attained by the flow at downstream positions. This profile moves in the upstream direction as the piston continues to increase the intake port closure.

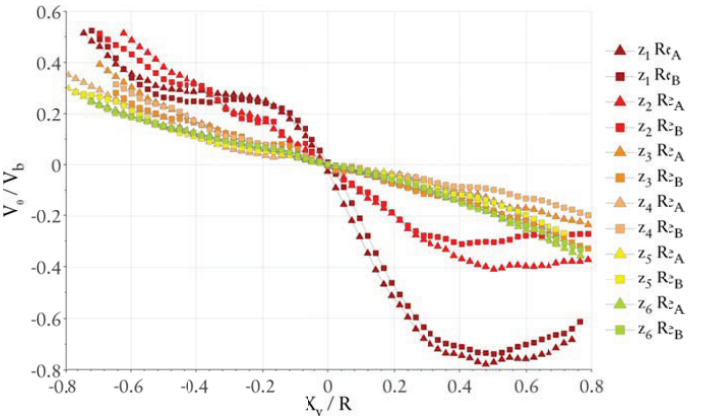

Figure 5.6:

Tangential Velocity for Intake port 50% Closed.

The axial velocity at z_1 is higher than at 25% port closure (Figure 5.7). The distribution of V_z attains a jet-like profile for all the measuring positions throughout the cylinder cross-sections. The profile has a broad central peak. With the decay in swirl, for positions z_4 and z_5, the V_z profile becomes nearly uniform. However, due to exit contraction the jet-like profile for V_z enhances again at z_6. Analogous to V_θ, with the intake port closure a jet-like profile of axial velocity is introduced at downstream position and this distribution profile moves to upstream positions with more port closure (Figures 5.2, 5.5 and 5.7).

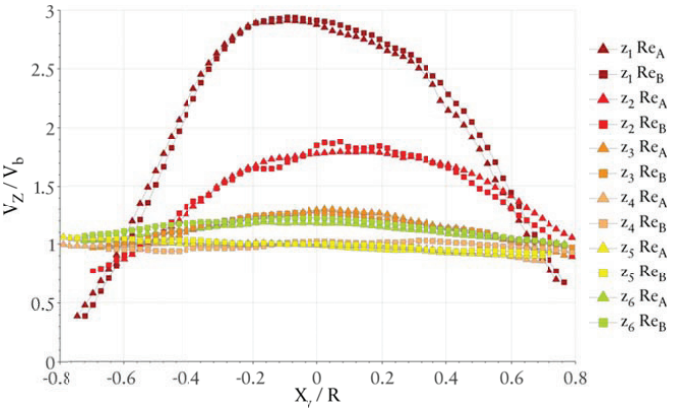

Figure 5.7:

Axial Velocity for Intake port 50% Closed.

75% Port Closure

At 75% intake port closure, the tangential velocity has a solid-body rotation throughout the cylinder which decays along the flow downstream (Figure 5.8). The peak V_θ in the entire cylinder is shifted to the near wall positions. This shows that closure of the intake port has a direct relation to the development of solid body rotation V_θ profile in the cylinder. As discussed in Chapter 1, in real Low speed engines (LSE), the scavenging starts when piston gradually uncovers the intake ports. A similar tangential velocity profile in real engine will introduce high velocities at the regions close cylinder liner walls when the piston uncovers the intake ports to start the scavenging process.

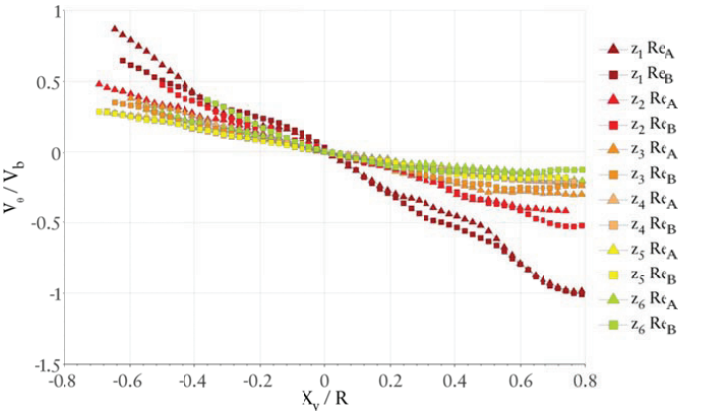

Figure 5.8:

Tangential Velocity for Intake port 75% Closed.

At z_1 in figure 5.9, the jet-like profile of axial velocity has a sharp peak compared to 50% intake port closure in figure 5.7. The magnitude of axial velocity has increased further. With port covered by 75%, there is very small opening at the inlet port. The piston outer wall diverts the flow to enter the cylinder through the small opening. The flow enters the cylinder with a strong axial component at the inlet and it is very likely to have a fluid jet in the near wall region.

At position z_2, the axial velocity profile changes to wake-like. This indicates a vortex breakdown like characteristic between the two measuring positions z_1 and z_2 where the vortex core with a jet-like upstream profile becomes unstable and the core flow undergoes a shock-like transition (Escudier et al., 1982). This characteristic is opposite to the one observed at z_6 for 25% closed ports where a wake-like axial velocity profile, along the flow downstream, changed to a jet like. At 75% intake port closure, unfortunately no measurements have been taken in the cylinder cross-sections in between the two measuring positions z_1 and z_2 where a change in the axial velocity profile occurs. Therefore, the type of the vortex breakdown (spiral, bubble shaped etc.) in this experiment cannot be found out. Physically, during the PIV experiment for 75% piston closure, the glycerin tracer particle started to be deposited on the cylinder internal walls close to the intake port (Figure 5.10). That required cleaning the internal walls after short intervals because the rate of deposition was fast and otherwise could not make it possible to take PIV measurements. For a real engine scavenging, such a phenomenon can result in condensation of certain exhaust gas species (high heat loads) on the cylinder liner wall close to scavenge ports. However, due to presence of dynamic effects of piston motion and stratification etc. it cannot be said that if such vortex breakdown is happening during real engine scavenging process.

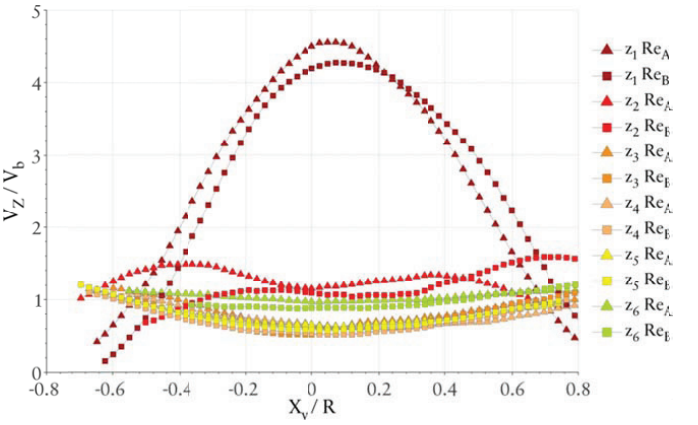

Figure 5.9:

Axial Velocity for Intake port 75% Closed.

For positions z_3 to z_6, the V_z continues to exhibit a wake-like profile, however, the peak values are observed at large radial positions indicating that the core radius has increased to be more than r/R= 0.8.

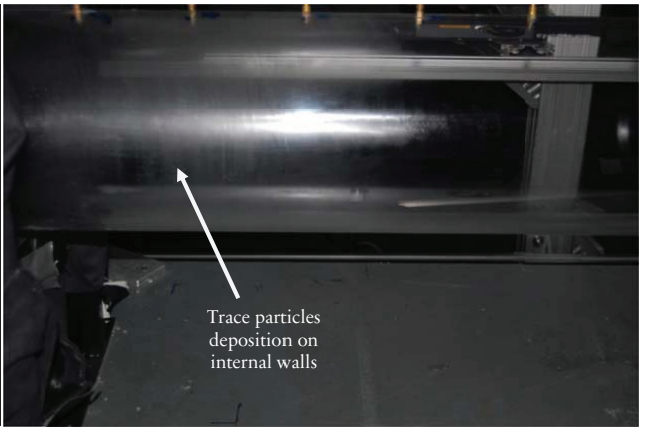

Figure 5.10:

Glycerin particles deposition on internal cylinder wall.

In general, for a given port closure and measuring position, the normalized tangential and axial velocity profiles are nearly the same for both Reynolds numbers Re_A and Re_B. Small variations in magnitude are observed at some radial positions for a given measuring position.

5.1.2 *Mean Velocity Field*

The mean three dimensional velocity field data is presented for fully open intake port are already discussed in Chapter 4 and therefore not discussed here. For the remaining piston positions, the results are discussed only for few specific positions. The results are presented for Re_A only. For Re_B and the remaining positions, the results are given in Appendix B.

25% Port Closure

At z_1 the vortex core has enlarged and still surrounded by a high velocity region (Figure 5.11). The core is still eccentric from the cylinder axis and has less steep gradients. The radial thickness of the high velocity region has reduced compared to fully open port. The velocity gradually decreases at larger radial distances from the high velocity region. The in-plane swirl is in clockwise direction.

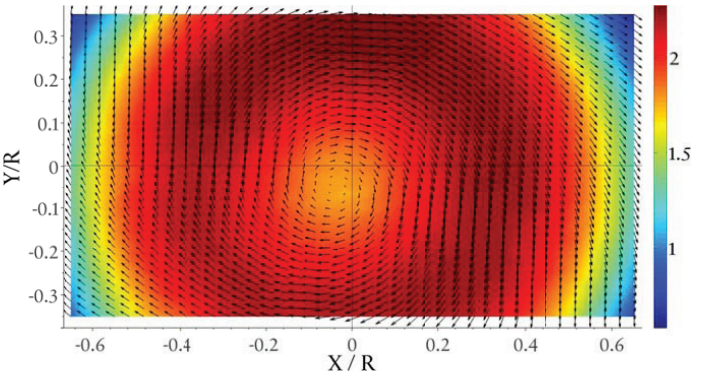

Figure 5.11:

Averaged 3D Velocity Field at z_1 25% port closure (Color Contour represent the Normalized out of the plane velocity component V_Z / V_b.

Flow at z_6 results in axial velocity to be large near and around the cylinder axis (Figure 5.12). The direction of in-plane swirl velocity is clockwise and the arrow vectors indicate that the core region behaves like a sink i.e. the fluid particles from large radial distances moves towards the vortex core while following a curved path. This is possibly due to the cylinder outlet contraction as z_6 is close to the cylinder outlet.

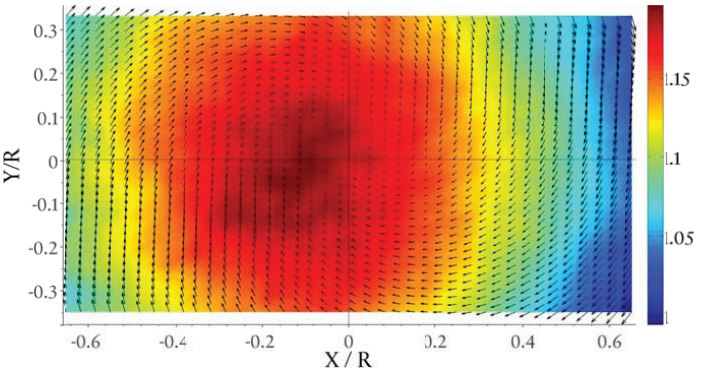

Figure 5.12:

Averaged 3D Velocity Field at z_6 25% port closure (Color Contour represent the Normalized out of the plane velocity component V_Z / V_b.

50% Port Closure

For 50% port closure, the three dimensional velocity distribution is discussed only for positions z_1 and z_5.

At z_1 the axial velocity has a jet-like profile. The peak of the profile is broader and the gradients are spatially more smooth and distinct (Figure 5.13). The in-plane velocity vectors indicate that the tangential velocity at one side of the vortex is higher than the other due to the effect of wall. It must be noted that in figure 5.13, the peak in axial velocity does not coincide with the vortex core. Repeated measurements and also variation in time between pulses for PIV measurement resulted in the similar behavior. The reason of this non-coincidence for being statistical or some fluid characteristic is could not be found out by the author.

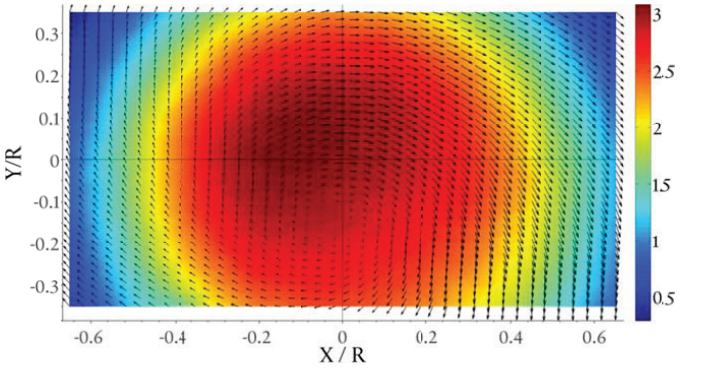

Figure 5.13:

Averaged 3D Velocity Field at z_1 50% port closure (Color Contour represent the Normalized out of the plane velocity component V_Z / V_b.

The axial velocity has almost a uniform distribution at cylinder cross-section at z_5 (Figure 5.14). The regions with maximum and minimum values are

observed at extreme radial positions of the diagonal line. However, the difference between the values of maximum and minimum V_z is very small. The in-plane velocity vectors indicate an increase with radial distance from the cylinder axis.

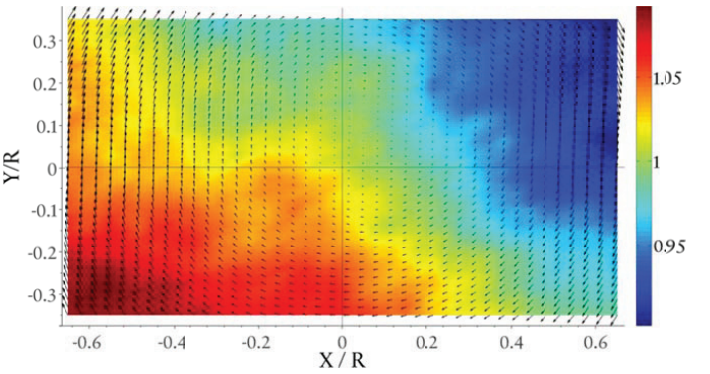

Figure 5.14:

Averaged 3D Velocity Field at z_5 50% port closure (Color Contour represent the Normalized out of the plane velocity component V_Z / V_b.

75% Port Closure

The velocity field at z_1 has also axial velocity distribution concentrated near the cylinder axis i.e. jet like profile (Figure 5.15). The profile has a sharp peak compared to V_z at z_1 and 50% closed port in figure 5.13. Besides the axial velocity peak does not coincide with the vortex core but it is less pronounced than V_z at z_1 and 50% closed port.

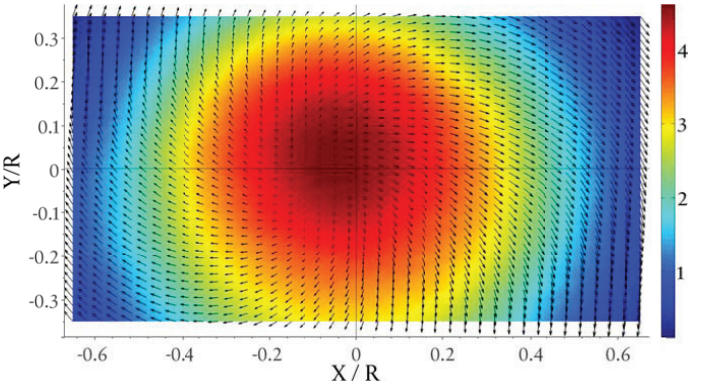

Figure 5.15:

Averaged 3D Velocity Field at z_1 75% port closure (Color Contour represent the Normalized out of the plane velocity component V_Z / V_b.

Here in this case, instead of z_5 the results are given for z_2 and z_3 in order to present and discuss an important feature of the flow.

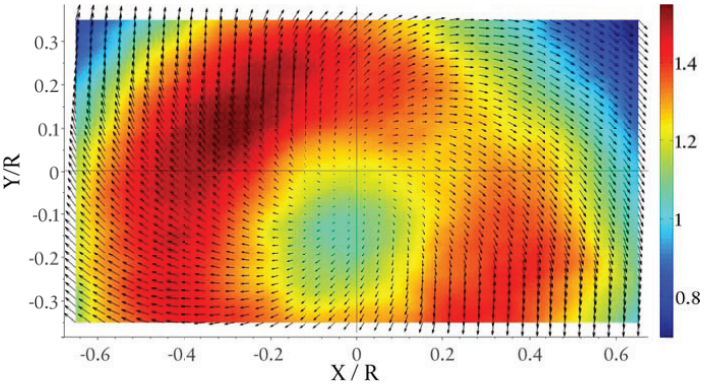

Figure 5.16:

Averaged 3D Velocity Field at z_2 75% port closure (Color Contour represent the Normalized out of the plane velocity component V_Z / V_b.

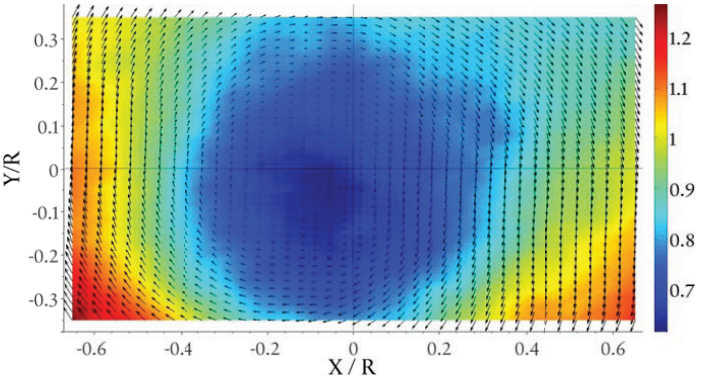

Figure 5.17:

Averaged 3D Velocity Field at z_3 75% port closure (Color Contour represent the Normalized out of the plane velocity component V_Z / V_b.

The in-plane velocity profile represents an increase in magnitude with the increase in radial distance from the vortex core indicating a forced vortex. However, a very distinct feature that is observed is that the vortex core is behaving like a source i.e. the fluid moves outward from the vortex core following a curved path. This indicates that fluid is undergoing an outward movement with vortex core being the source point. This pattern continues to z_2 where due to vortex breakdown between positions z_1 and z_2 the axial velocity has a wake like profile i.e. low velocity at the vortex core (Figure 5.16). However, when flow reaches position z_3, this pattern changes and the in-plane velocity distribution has now a regular swirling flow pattern (Figure 5.17). It must be noted that throughout the flow from position z_1 to z_3, the tangential velocity has same profile i.e. solid body rotation (Forced vortex). A possible reason for this behavior is that at high Reynolds number for 75% port closure, the cylinder inlet provides a very small area for fluid to enter into cylinder resulting in a high velocity jet of the fluid at the intake port. This jet, from every direction may meet at some axial distance and then move

outward. As discussed before, the presence of piston will make major portion of the flow to enter in to the cylinder at an angle to the piston top surface (Figure 5.3). This angle makes the fluid jet coming from intake port along the cylinder circumferential periphery to meet at some axial distance from the piston surface facing the cylinder axis. The fluid after meeting at that axial distance will then move outward to other regions of a given (near cylinder inlet) cross section. The solid body rotation and low pressure near the cylinder wall (near the cylinder intake port) provides favorable condition for transporting the fluid to other regions.

5.1.3 *Reynolds Normal Stresses*

The distribution of Reynolds normal stress components are expressed in Cartesian coordinates. For a given cross-sectional position all the three normal components are presented under a single figure and scaled to same color values so as to get a comparison of the relative magnitude of each component. Each Reynolds stress component is normalized by square of the bulk velocity and the symbols represent normalized stress components. The results are also discussed from the perspective of polar coordinates as discussed earlier in Chapter 4.

25% Port Closure

At z_1, figure 5.18 shows that all the Reynolds normal stress components are higher compared to fully open port (see Section 4.2.5). This indicates an increase in the variance/ fluctuations of corresponding velocity components. It can be seen that $\overline{w'w'}$ attains the highest and $\overline{v'v'}$ has the lowest values. For all the three components, the vortex core and the near wall region has higher fluctuations. The region in between the vortex core and the wall has fewer fluctuations. In the near wall region $\overline{w'w'}$ is the dominant component and has comparatively large values. The spatial distributions of all the components show increased anisotropy of the normal components. Thus vortex core and near wall regions have most of turbulent kinetic energy for the given cross-sectional plane. Considering polar coordinates, $\overline{v'_\theta v'_\theta}$ and $\overline{v'_r v'_r}$ at z_1 are higher in the vortex core and near wall regions and the annular region has smaller values.

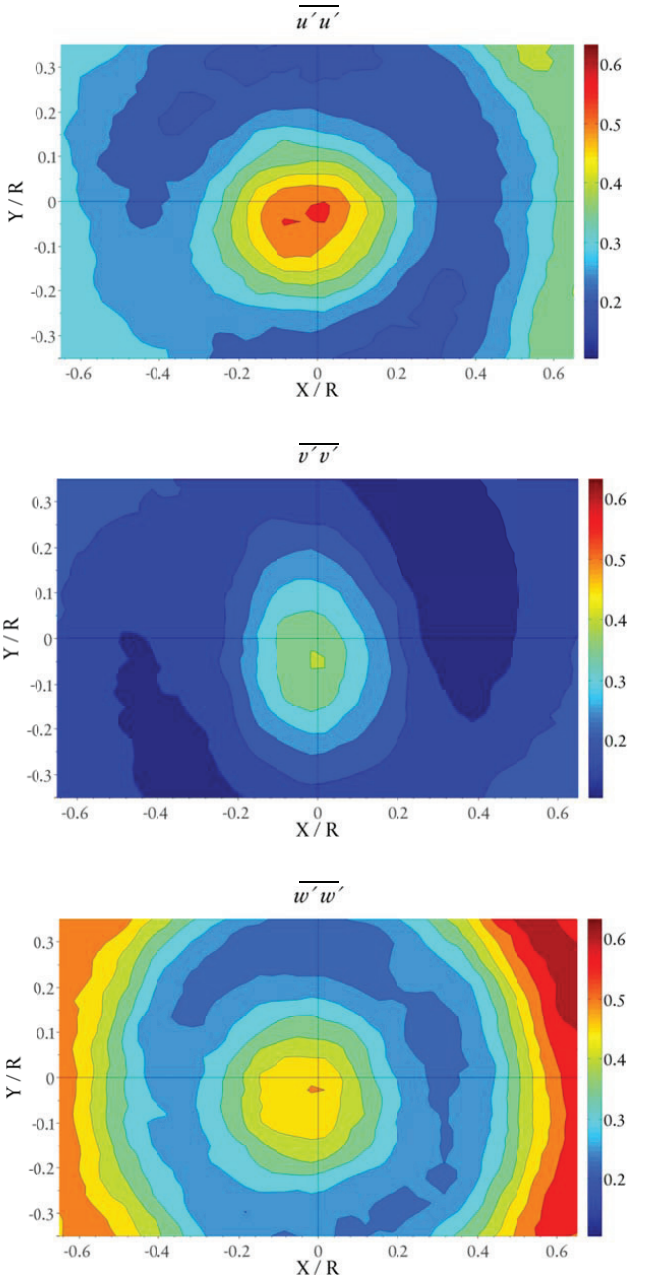

Figure 5.18:

Normalized Reynolds Normal Stress Components @ z_i and 25% port closure.

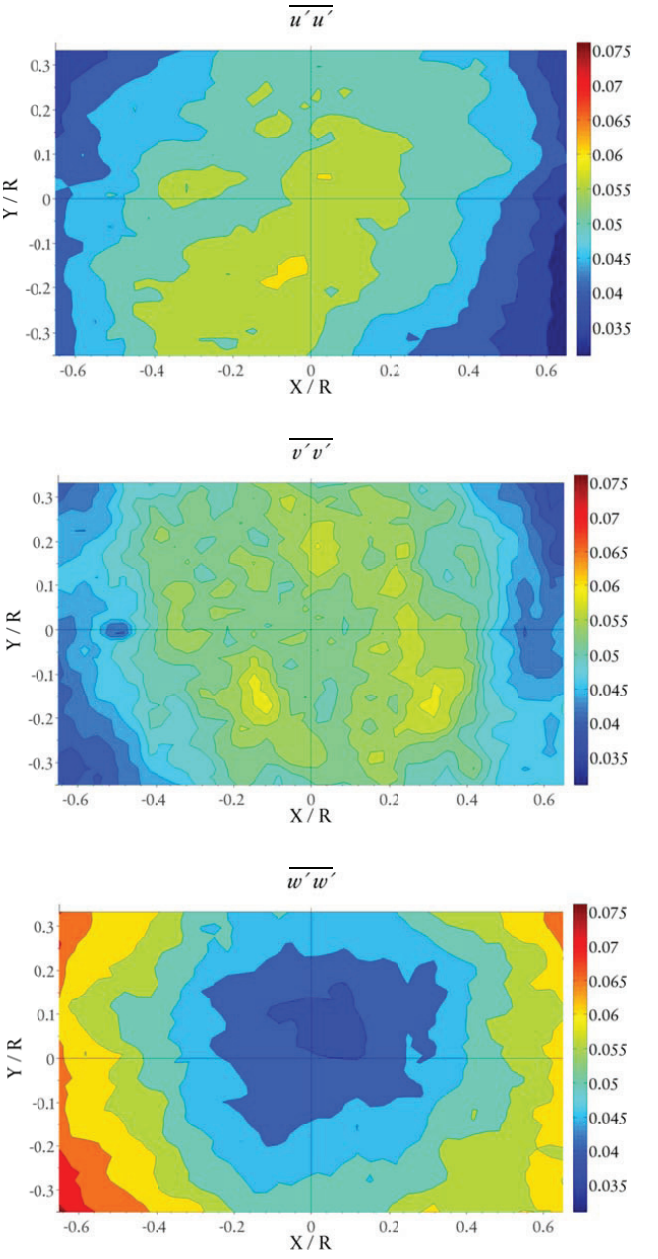

Figure 5.19:

Normalized Reynolds Normal Stress Components @ z_6 and 25% port closure.

At z_6 the overall magnitudes of the normal stress components have decayed approximately by an order of 10 with $\overline{w'w'}$ still having the highest values (Figure 5.19). $\overline{u'u'}$ and $\overline{v'v'}$ have nearly the same magnitude and since they represent the variance in tangential and radial velocity components, the values are higher in the vortex core region. However, $\overline{w'w'}$ is very low in the core region and gradually increases in the radial direction towards the cylinder wall. As discussed in section 5.1.1, at z_6 for 25% port closure, the mean axial velocity has a jet-like profile. This indicates that in the center of the jet the axial velocity is comparatively more stable and fluctuates more around the mean value as the radial distance from the vortex core increases.

However, for u and v components it is the vortex core region where higher fluctuations are observed. $\overline{v'_\theta v'_\theta}$ and $\overline{v'_r v'_r}$ at z_6 has higher values in a large region around the cylinder axis and gradually decreases in the radial direction towards the wall.

50% Port Closure

Figure 5.20 shows that at z_1 with 50% port closure, the magnitude of all the Reynolds normal stress components have further increased. Compared to 25% port closure, the peak value of $\overline{w'w'}$ at z_1 has increased almost twice. The difference in magnitude of in-plane normal components $\overline{u'u'}$ and $\overline{v'v'}$ at z_1, as observed in case of 25% port closure in figure 5.18, does not exist and have nearly the same range. The spatial distribution of $\overline{u'u'}$ and $\overline{v'v'}$ show two distinct regions lying side by side where one has the highest values and the other has the lowest values. This distribution can be understood by looking at the tangential velocity and the three dimensional velocity distribution in figures 5.6 and 5.13 respectively. The mean vortex core location is in the third quadrant at a radial distance of approximately r/R=0.15 and very close to negative Y-axis line. Due to the effect of wall an asymmetric tangential velocity distribution is observed which has higher peak at r/R=0.4 along positive X-axis compared to negative X-axis where small dip in the profile is observed. The contour plots for $\overline{u'u'}$ and $\overline{v'v'}$ show that if they are added together, a region with high values will be obtained almost very close to the position where the vortex core is located. The adjacent region with low values is possibly, due to wall effect here, a distorted shape of the region observed in (Figure 5.18) in between the wall and vortex core where the minimum values are observed for $\overline{u'u'}$ and $\overline{v'v'}$. The $\overline{w'w'}$ although having anisotropic spatial distribution still exhibit some features as in case of z_6 with 25% port closure i.e. the minimum values exist in the jet center and increases along the radius towards the wall. However, a different feature is observed that after a radial distance of approximately r/R=0.5 the fluctuations in axial velocity starts decreasing towards the wall. This feature, however, could not be observed for z_6 with 25% port closure possibly due to location of peak value region being outside the PIV measurement area.

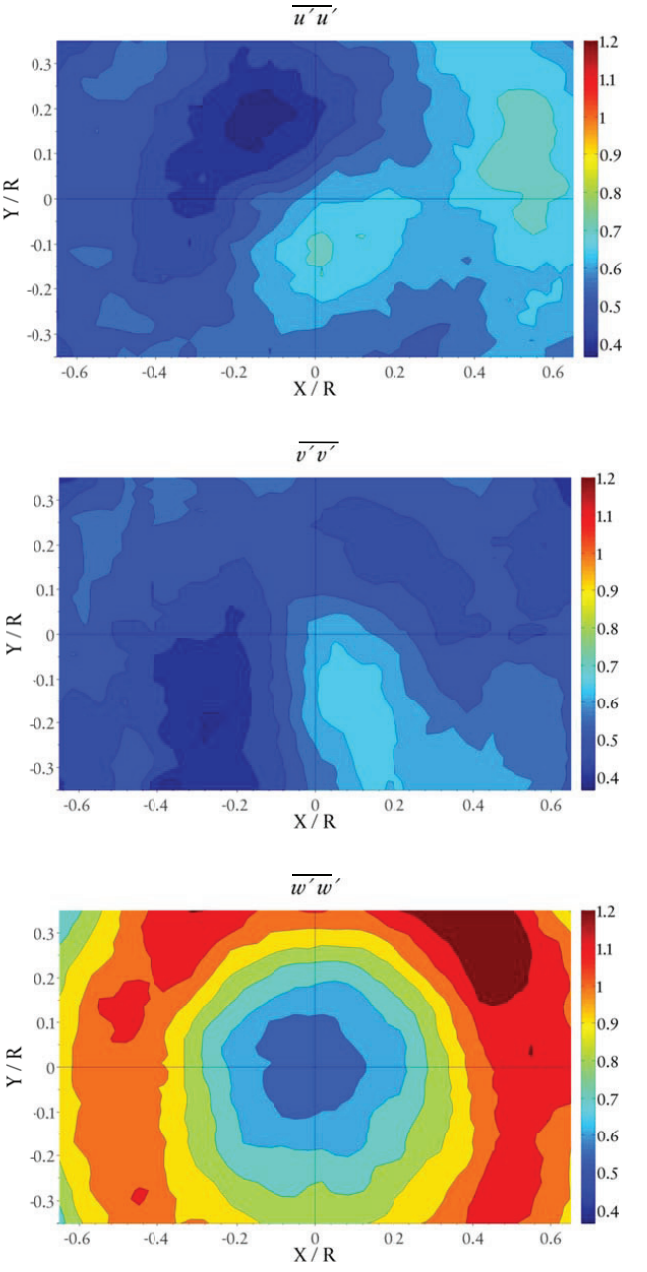

Figure 5.20:

Normalized Reynolds Normal Stress Components @ z1 and 50% port closure.

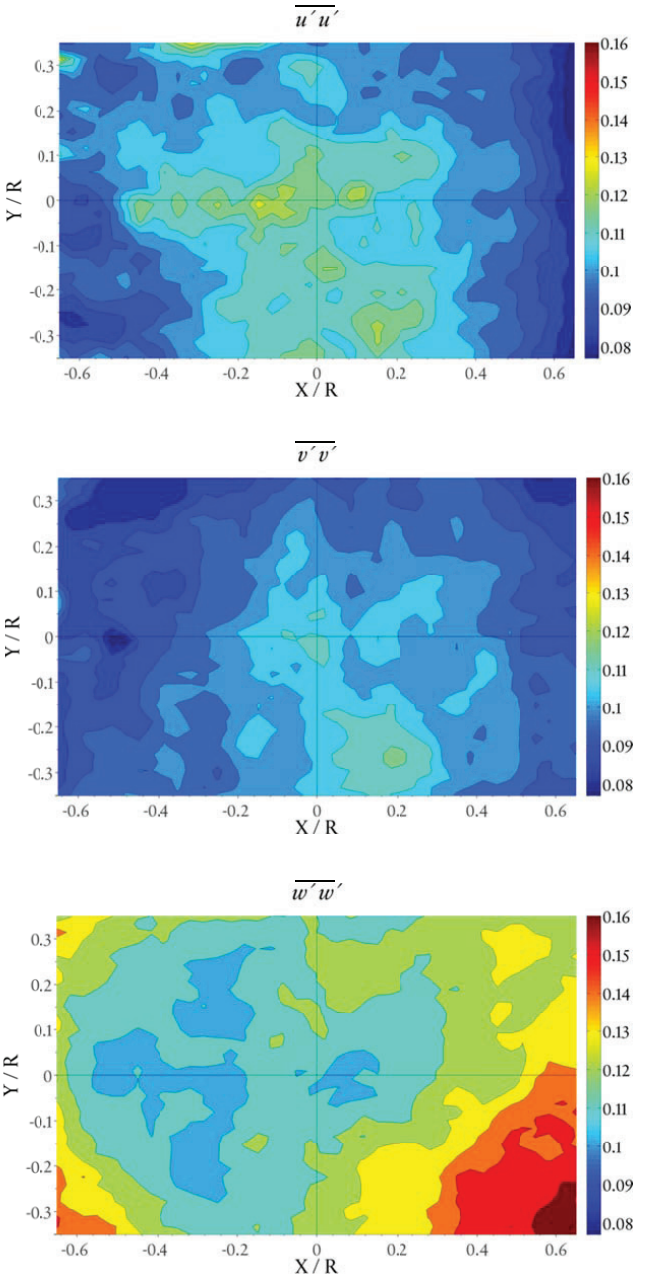

Figure 5.21:

Normalized Reynolds Normal Stress Components @ z5 and 50% port closure.

At z_5 in figure 5.21 the fluctuations in u and v velocity components are higher in the region around cylinder axis and lower at large radial positions near cylinder wall. Due to increase in the size of the vortex core this region with higher values is large. However, the relative difference between the minimum and maximum values is small. Fluctuations in the axial velocity component w is still dominant. The cylinder center region has minimum $\overline{w'w'}$ values and the near wall region has the highest values. For all the normal Reynolds stress components, the decrease in magnitude from z_1 to z_5 is by an order of 10. Compared to fully open port, the magnitude of all the normal Reynolds stress components are nearly twice the value at z_5.

The effect of wall at z_1 has changed the distribution of Reynolds stress components $\overline{v'_\theta v'_\theta}$ and $\overline{v'_r v'_r}$ in the cross-sectional plane. The region around the vortex core location still has higher values but the region with low magnitude of $\overline{v'_\theta v'_\theta}$ and $\overline{v'_r v'_r}$,as in case of 25% closure, is distorted. However, at z_5 a more clear picture can be seen where their values increase from large radial positions in the direction of cylinder axis region where the vortex core is resided.

75% Port Closure

When the intake port is 75% closed, the variance in the axial velocity is very large at z_1 compared to u and v velocity components (Figure 5.23). The spatial distribution is also very anisotropic for $\overline{w'w'}$. For all aforementioned cases where the axial velocity has a jet-like profile, the fluctuations in axial velocity are comparatively low at the center of the jet. The gradual increase in the outward radial direction decreases again towards the wall, after attaining a high value. The radial location of this peak $\overline{w'w'}$ region seems to exist at the outer periphery of the jet where a mixing occurs with the fluid near the wall region. In the current case, this peak region is at a smaller distance from the jet center than previous cases possibly because the wall recirculation zone has comparatively grown in case of 75% port closure at z_1. $\overline{u'u'}$ and $\overline{v'v'}$ components have lowest values at large radial positions from the vortex core. There is radially large region around the cylinder axis where patches of high and low values are observed. The peak values of $\overline{u'u'}$ and $\overline{v'v'}$ are nearly half the value of $\overline{w'w'}$.

A resultant of the $\overline{u'u'}$ and $\overline{v'v'}$ components given in figure 5.23 with the same color scale as figure 5.22 shows that the in-plane Reynolds normal stresses are higher in the central region around cylinder axis and decreases towards the wall region.

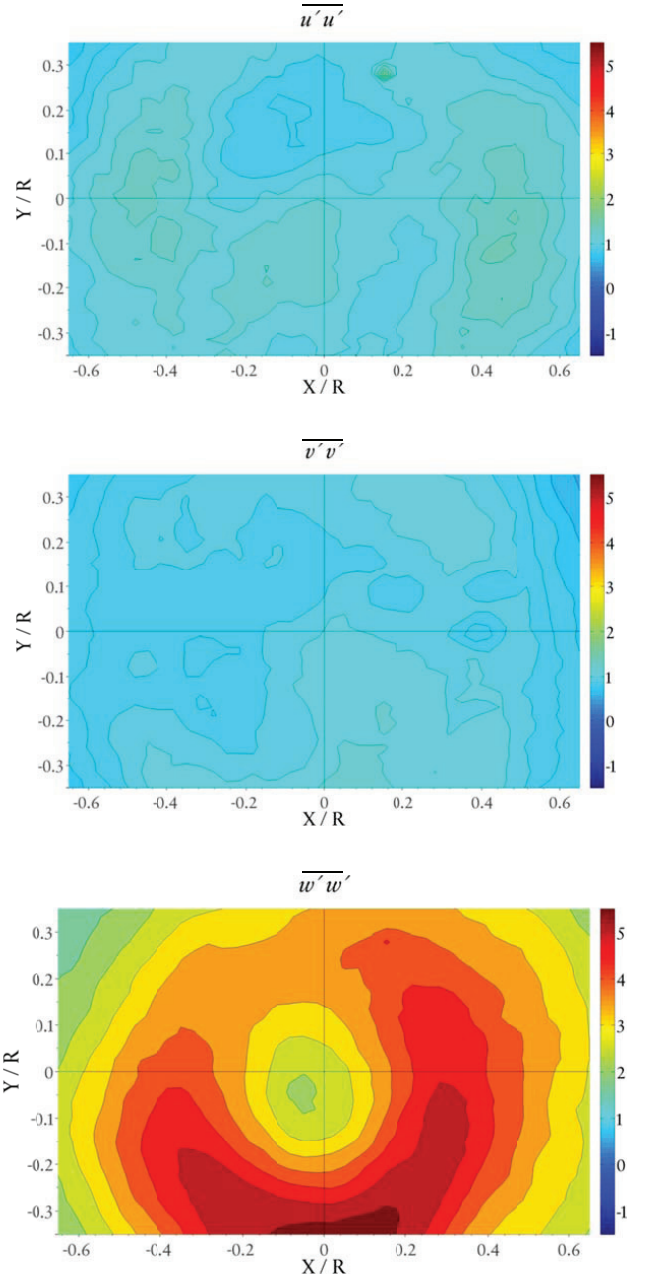

Figure 5.22:

Normalized Reynolds Normal Stress Components @ z1 and 75% port closure.

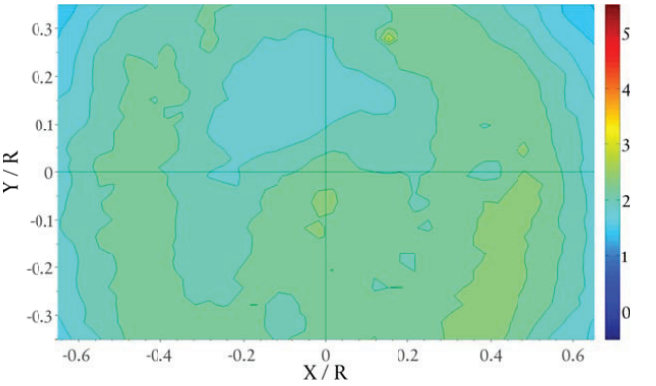

Figure 5.23:

Resultant of Normalized in-plane Reynolds Normal Stress Components ($\sqrt{\overline{u'u'}^2 + \overline{v'v'}^2}$) *@ z1 and 75% port closure.*

$\overline{v'_r v'_r}$ at z_1 is low in the near wall region and increases to its peak value at a radial position r/R=0.5 and the again decreases towards the cylinder axis. For $\overline{v'_\theta v'_\theta}$ the value is also low at the near wall region and increase towards the cylinder axis.

At z_2 the $\overline{u'u'}$ and $\overline{v'v'}$ have two pairs of orthogonal zones with each pair having the high and low values respectively (Figure 5.24). The zones pairs are at large radial distance from cylinder axis. For $\overline{u'u'}$ the pair with high values are along X-axis and for $\overline{v'v'}$ along Y-axis. This will add-up to give higher values in cylinder center region and low values in the near wall regions. The $\overline{w'w'}$ is still the dominant component. The peak value is reduced to a small extent compared to z_1. Spatial distribution is anisotropic and has low values in the vortex core and near wall region and peak values in the intermediate region.

At z_2 the spatial distribution of $\overline{v'_\theta v'_\theta}$ and $\overline{v'_r v'_r}$ is opposite to each other. i.e. the fluctuations in the radial direction $\overline{v'_r v'_r}$ are large at larger radial distances and decreases towards the cylinder axis. Whereas in case of $\overline{v'_\theta v'_\theta}$ the tangential velocity fluctuations are low at larger radial distances and increases towards the cylinder axis.

Despite a large increase in the magnitude of normal stress components at z_1, the values at z_e do not increase in the same order compared to fully open port (see Appendix B). This indicates that the downstream decay in the velocity fluctuations also increases with the increase in partial closure of the intake port. This may be the upstream influence or in other words the damping effect of the outlet contraction on the in-cylinder flow.

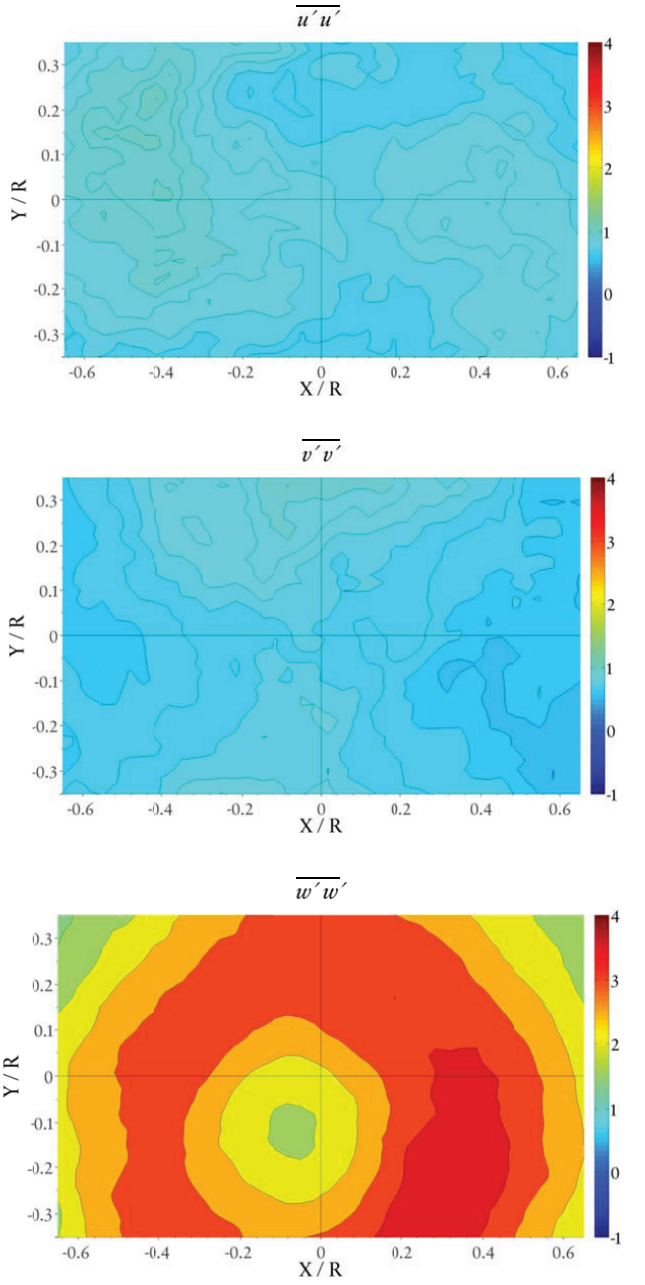

Figure 5.24:

Normalized Reynolds Normal Stress Components @ z2 and 75% port closure.

5.1.4 *Reynolds Shear Stresses*

25% Port Closure

The shear stress components of Reynolds stresses are given in figure 5.25 for z_1. It can be seen that the covariance of in-plane velocity components u and v is small compared to $\overline{u'w'}$ and $\overline{v'w'}$ components. Shear stress component $\overline{u'v'}$ is weak in the region around cylinder axis and large values are observed in two pairs of distinct regions/ zones. These regions lie adjacent to each other and have opposite signs, however, with almost same absolute value of their magnitude. Shear stresses $\overline{u'w'}$ and $\overline{v'w'}$ are high in the cylinder axis and near wall region. In the cylinder axis region, $\overline{u'w'}$ and $\overline{v'w'}$ have high values in two small adjacent zones with opposite signs. The zones in the near wall region also exhibit opposite signs for two ends of X-axis and Y-axis for $\overline{u'w'}$ and $\overline{v'w'}$ respectively.

At z_6, the Reynolds shear stresses are reduced by a factor of 10 (Figure 5.26). The spatial distribution of $\overline{u'v'}$ component still has the zone pairs as discussed for z_1. However, their shape is more distorted showing small gradients of $\overline{u'v'}$ in the cross-sectional plane. For $\overline{u'w'}$ and $\overline{v'w'}$ the two adjacent zones around the cylinder axis have grown in size and cover large portion of the cross-sectional plane. The zones in the near wall region have high values but seem to have radially shrunk toward cylinder wall. In general it can be said that with the decay in the swirl along the cylinder, the magnitude of Reynolds shear stresses decreases and their spatial distribution increase. For z_6, the region in between the cylinder axis and the near wall exhibits large covariance values among the velocity components.

For 25% port closure, the covariance between v_θ and v_r is large at larger radial distances. The Reynolds stress component $\overline{v'_\theta v'_r}$ at z_1 decreases slowly towards the cylinder axis and increase again to a small extent in the vortex core region. $\overline{v'_\theta v'_z}$ is low in the near wall region and increases to its peak value at a radial distance of r/R=0.15 and then decreases again in the vortex center. $\overline{v'_r v'_z}$ has largest values in the near wall region and decreases towards the vortex core region. At z_6, the distribution of $\overline{v'_\theta v'_z}$ and $\overline{v'_r v'_z}$ spread to distances around the cylinder axis. Both the components attain high values at a comparatively larger radial distance from the cylinder axis and decreases in the vortex center.

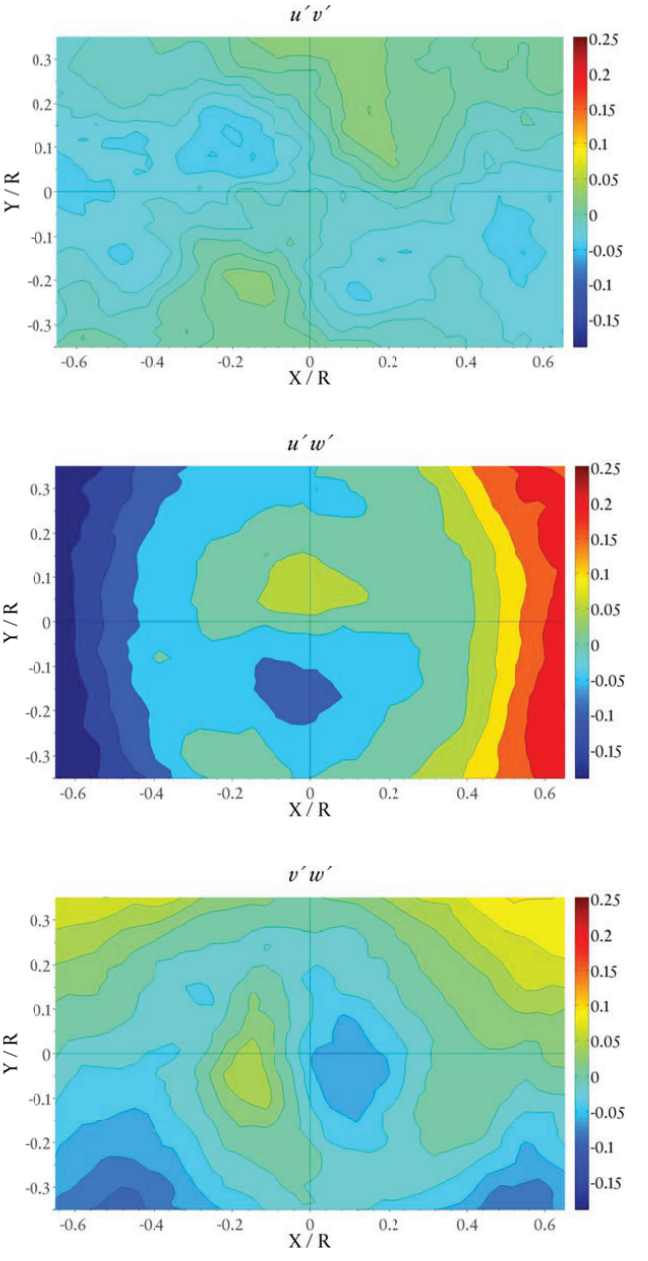

Figure 5.25:

Normalized Reynolds Shear Stress Components @ z1 and 25% port closure.

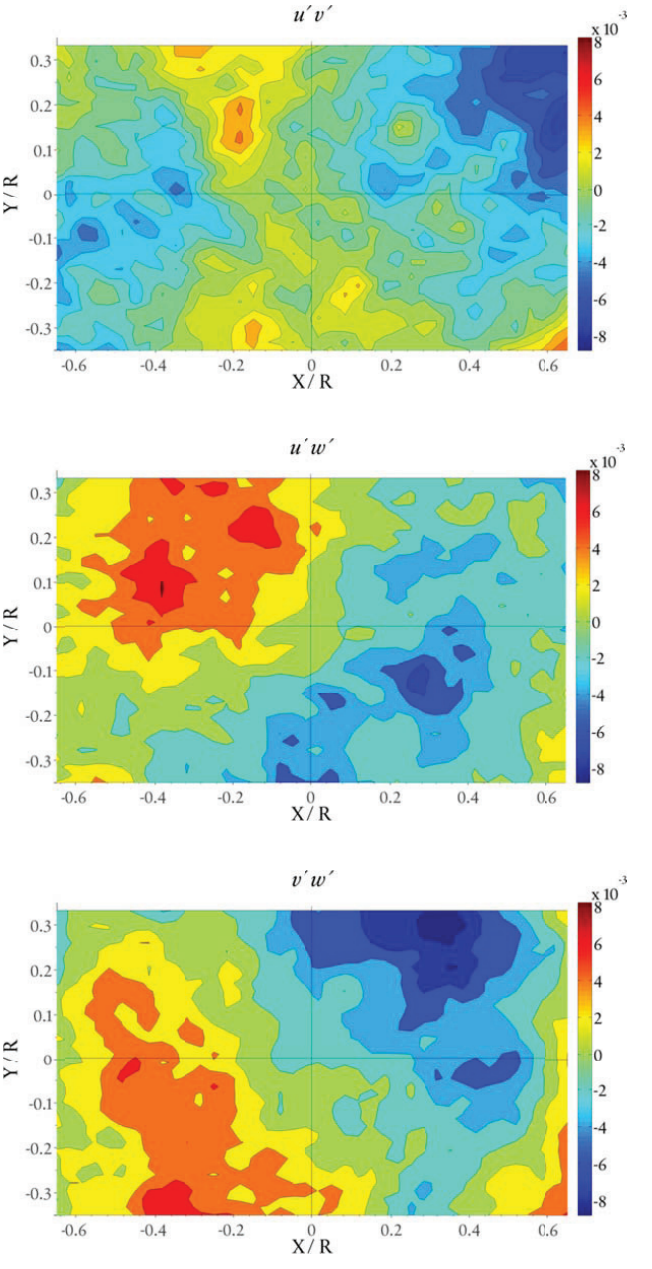

Figure 5.26:

Normalized Reynolds Shear Stress Components @ z6 and 25% port closure.

50% Port Closure

At position z_1, the contour plots for shear stresses are given in figure 5.27. For component $\overline{u'v'}$ the distribution profile is following nearly the same pattern as in case of 25% port closure i.e. large values are observed at larger radial distances and decrease towards the vortex core region. This shows that the covariance between u and v components of velocity is high at larger radial distance and low near the vortex center. For $\overline{u'w'}$ along X-axis, the peak value is observed in a region at a radial distance of r/R=0.6 from the cylinder axis. Decrease gradually on both sides of this peak region i.e. both towards cylinder axis and near wall region. Similar pattern is observed for $\overline{v'w'}$ but along Y-axis. This distribution gets very clear by looking at this from the perspective of cylindrical coordinates. Considering contour plots for both $\overline{u'w'}$ and $\overline{v'w'}$ components, it becomes clear that $\overline{v'_r v'_z}$ is the dominant component and $\overline{v'_\theta v'_z}$ is very small at this cross-section plane.

At z_3, the magnitude of shear stress components has reduced by an order of 10 (Figure 5.28). For all the $\overline{u'v'}$, $\overline{u'w'}$ and $\overline{v'w'}$ components, the distribution in the center part of the cylinder exhibit very low values. $\overline{u'w'}$ and $\overline{v'w'}$ have large values observed in the near wall region. The main reason is that the axial velocity is nearly constant in most of the central portion of the cylinder and fluctuates mostly at the near wall region.

75% Port Closure

At position z_1, the $\overline{u'v'}$ is very weak compared to $\overline{u'w'}$ and $\overline{v'w'}$ (Figure 5.29). The distribution pattern of the regions with high $\overline{u'v'}$ is still the same. For $\overline{u'w'}$ and $\overline{v'w'}$ the orientations of the regions with peak values are at an angle to X and Y axes respectively. The radial location of these regions has moved to comparatively lower radial distance from the cylinder axis. Regarding the shear stress components $\overline{v'_r v'_z}$ and $\overline{v'_\theta v'_z}$, it still seems that the $\overline{v'_r v'_z}$ is stronger than the $\overline{v'_\theta v'_z}$.

The possible vortex breakdown between positions z_1 and z_2 has, in general, no significant effect on the distribution pattern of Reynolds shear stress components. For $\overline{u'v'}$ the magnitude has reduced to a small extent compared to $\overline{u'w'}$ and $\overline{v'w'}$. The covariance between the radial and axial velocity component is still large compared to the covariance between the tangential and axial components. This means that for any disturbance in axial velocity the radial velocity is more sensitive than the tangential velocity. Such axial disturbances are low in the jet center and high in the outer region.

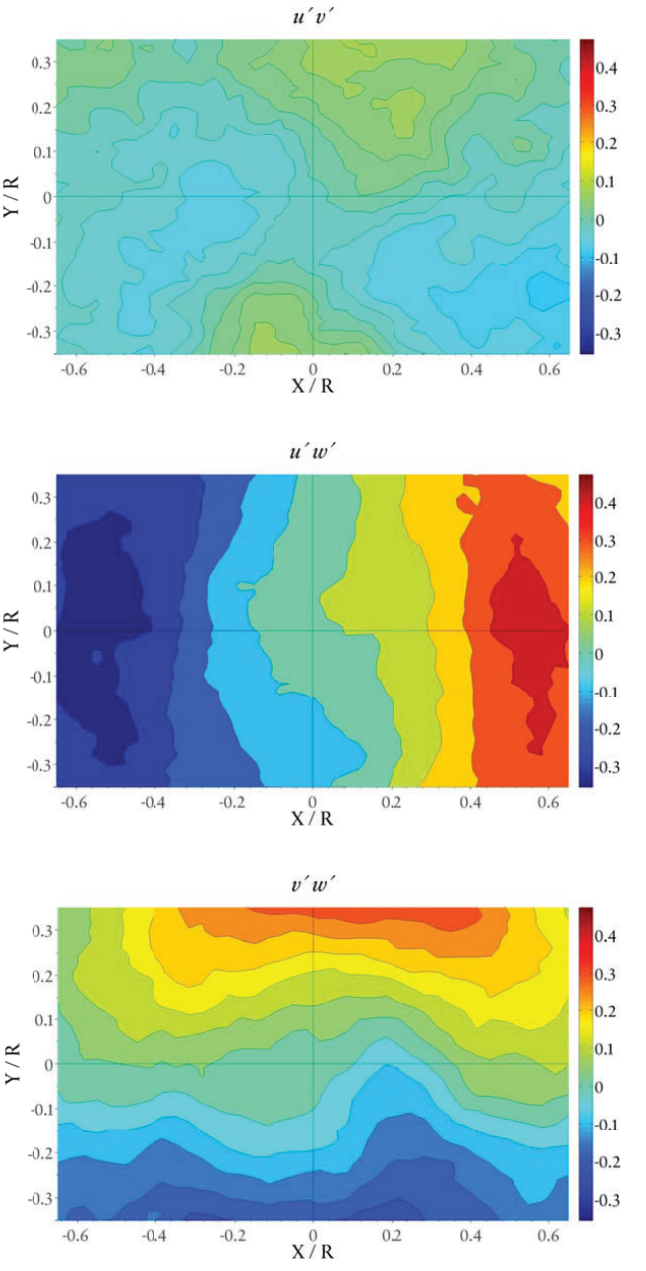

Figure 5.27:

Normalized Reynolds Shear Stress Components @ z1 and 50% port closure.

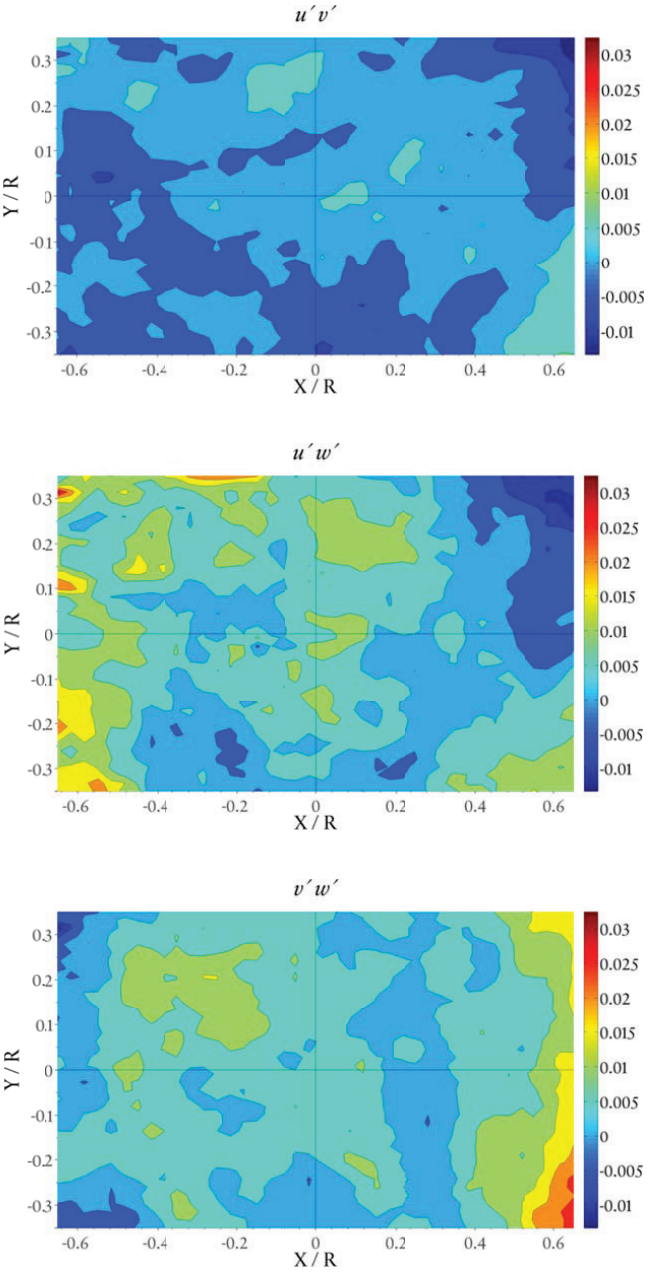

Figure 5.28:

Normalized Reynolds Shear Stress Components @ z5 and 50% port closure.

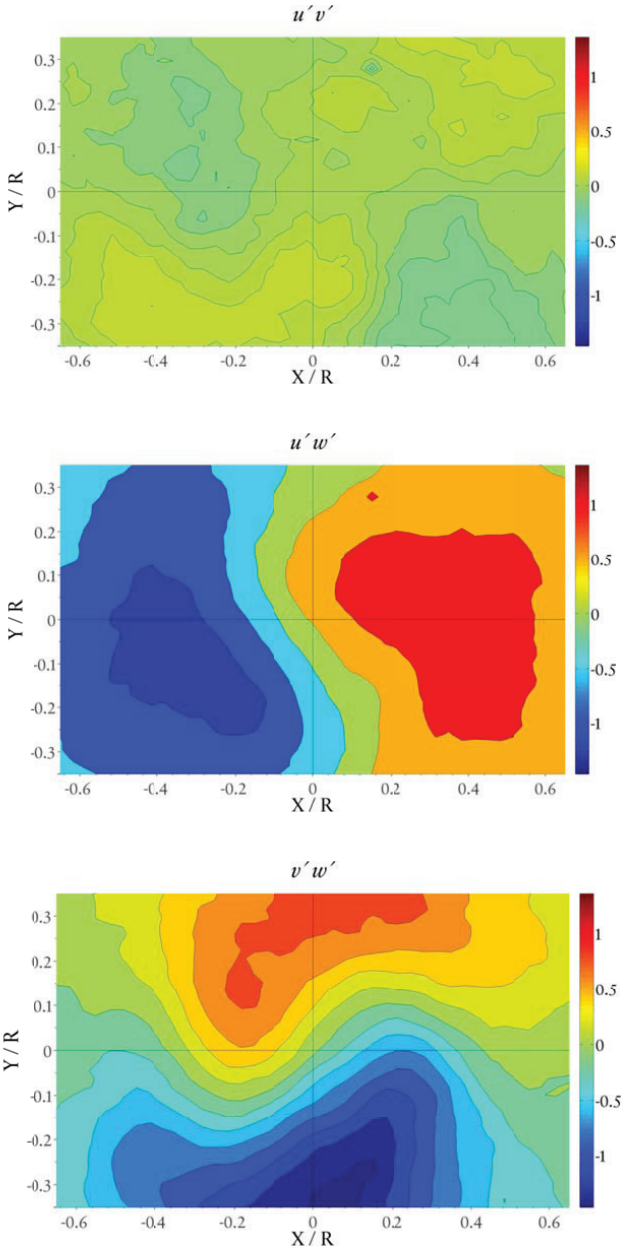

Figure 5.29:

Normalized Reynolds Shear Stress Components @ z1 and 75% port closure.

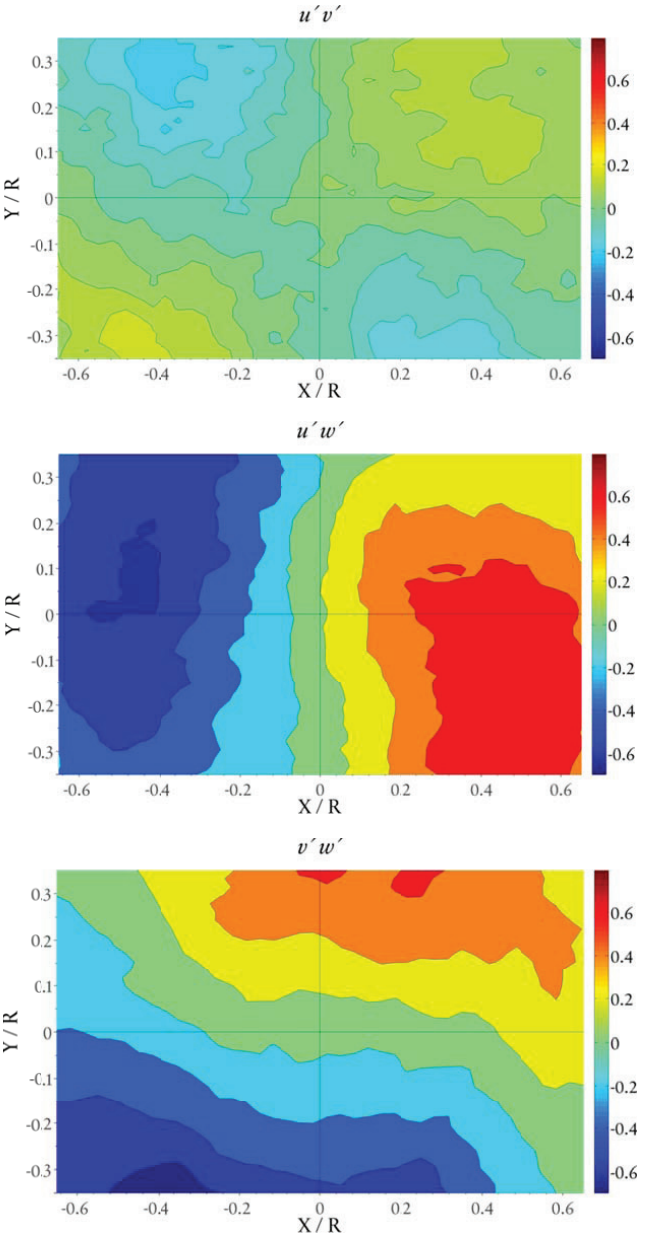

Figure 5.30:

Normalized Reynolds Shear Stress Components @ z2 and 75% port closure.

5.1.5 *Mean Axial Vorticity*

Figure 5.31 shows the mean axial vorticity ω_z for positions z_1 and z_6 at Re_A with cylinder intake port closed by 25%. At z_1, similar to z_1 for fully open port in figure 4.11, the vortex core region has the strongest vorticity. However, the vorticity magnitude is comparatively less and the very weak-vortical region is now limited to few small/ localized regions. The vorticity is distributed to more regions outside the vortex core. At extreme edges (X/R=0.65) in the contour plot, the vorticity value seems to have increased. This indicates diminishing of the burgers vortex profile in a way that the vorticity of the weak-vortical (Annular) region increases.

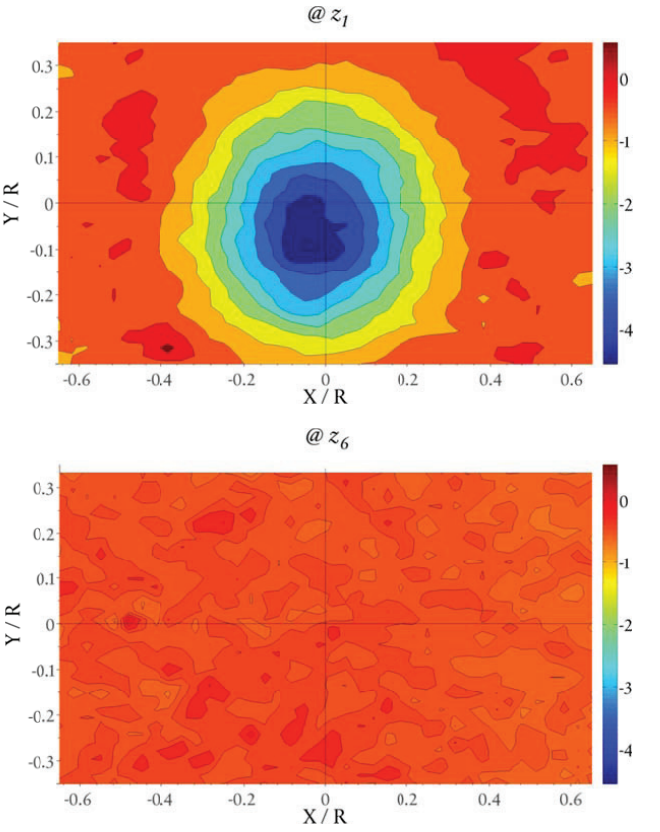

Figure 5.31:

Mean Normalized Axial Vorticity ω_z @ Re_A and 25% port closure.

At z_6 in figure 5.31 unlike z_1, a distinguished and relatively strong vortical vortex core region no more exists (the contour plot shows a lot of noise because due to relatively uniform vorticity distribution the gradients are very

small and PIV measurement induces some noise in this case). From z_1 to z_6, the vorticity seems to have been distributed from strong to weak vortical regions thus resulting in a comparatively more uniform vorticity distribution.

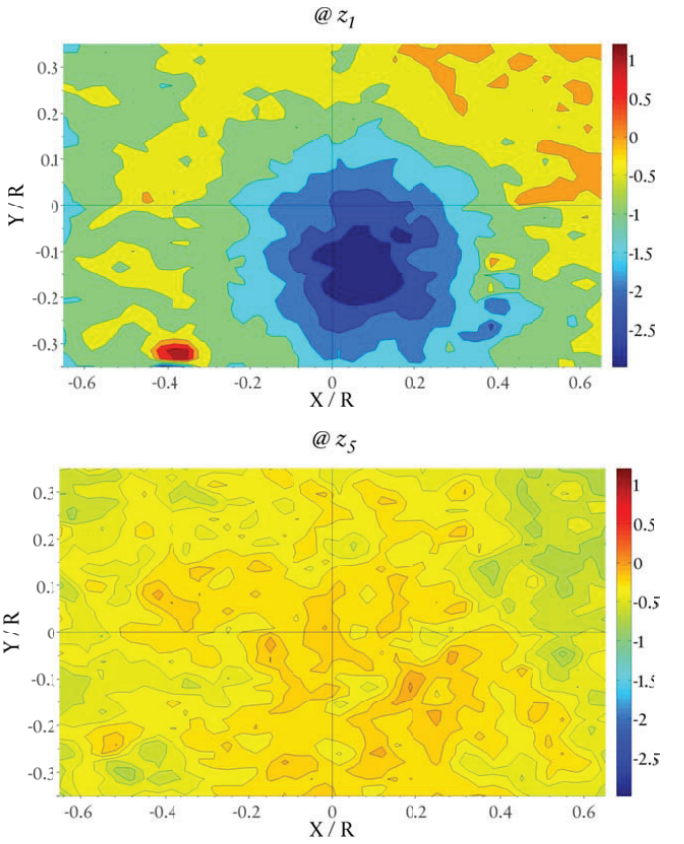

Figure 5.32:

Mean Normalized Axial Vorticity ω_z @ Re_A and 50% port closure.

For 50% intake port closure, the mean axial vorticity at z_1 and z_5 are shown in figure 5.32. The vorticity of vortex core region at z_1 is still stronger than other radial positions at that cross-sectional plane but less distinguished compared to z_1 at 25% port closure. The maximum value of axial vorticity has reduced nearly half the maximum value at z_1 for 25% intake port closure. At the left side of the mean vortex core position i.e. along X/R<0, the very weak vortical regions almost disappear. One of the possible reasons may be the effect of the wall on flow because from figure 5.13 it can be seen that vortex core is closer to the wall along negative Y-axis. This, in addition to the asymmetric velocity

distribution, will also increase the vorticity distribution in the region between vortex core and the near wall region. Thus eliminating the very-weak vortical region to the side where vortex core is closer to the wall. The mean axial vorticity distribution at z_s in figure 5.32 is low and more uniformly distributed.

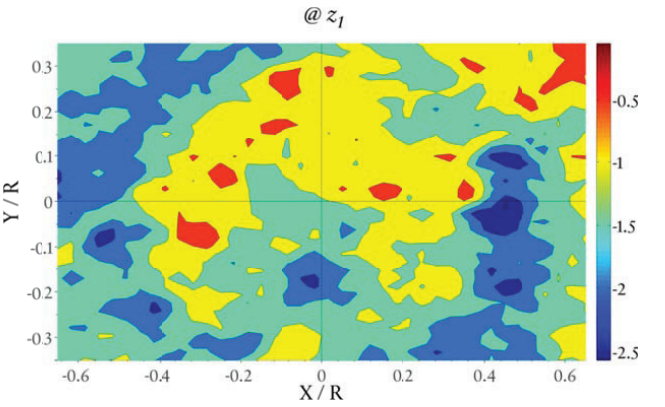

Figure 5.33:

Mean Normalized Axial Vorticity ω_z @ Re_A and 75% port closure.

When the intake port is closed by 75% as shown in figure 5.33, compared to other positions of piston, at z_1 the strong vorticity of the vortex core region no longer exist. Instead the vorticity distribution is uniform with a comparatively lower value. The vorticity distribution is also uniform and the plots are not shown due to noise inclusion as mentioned earlier. In general it can be concluded that with the increase in intake port closure the mean axial velocity distribution in the cylinder becomes more uniform starting from downstream and moving to upstream cross-sectional positions.

5.2 Cylinder Wall Pressure Measurements

For each piston position the static differential pressure has been measured in the same manner as discussed in section 4.4. Extech® HD755 differential pressure manometer (resolution of 1 Pa) is used for the cases where the Furness® digital differential micro manometer could not be used due to limited range. For a given position and Reynolds number, using Extech® HD755, the measurements were conducted for 5 minutes (using data logging software with a acquisition frequency of 1 reading per second) and then an average value is obtained. Figures 5.34 & 5.35 give the normalized pressure

drop along the measuring cylinder for different piston positions/ intake port opening and Reynolds numbers Re_A and Re_B.

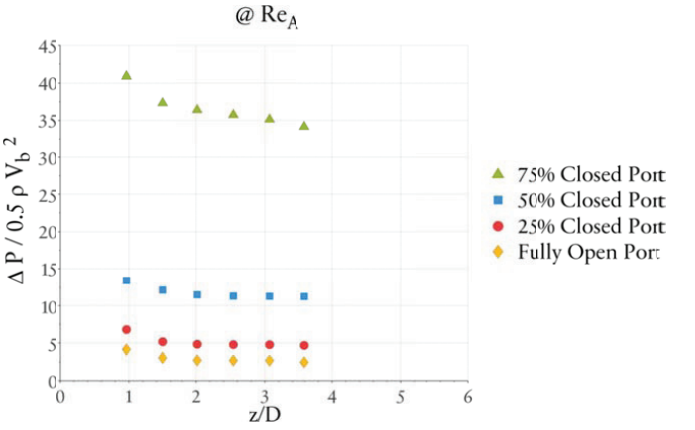

Figure 5.34:

Average Static Pressure Drop along the Cylinder @ Re = 6.5 x 10^4.

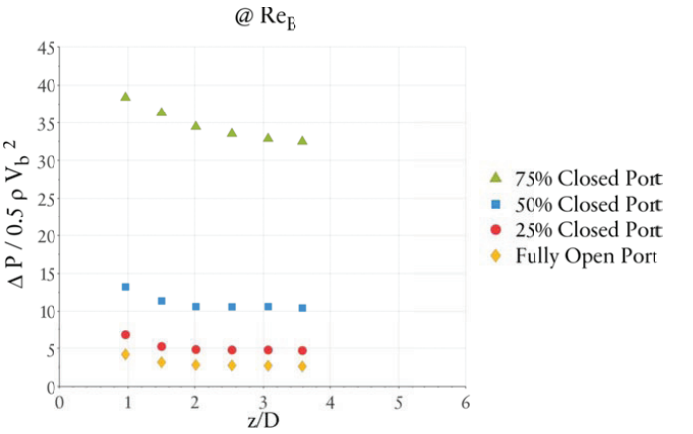

Figure 5.35:

Average Static Pressure Drop along the Cylinder @ Re = 3.25 x 10^4.

It can be observed that pressure drop profiles along the measuring cylinder exhibit nearly same shape for different piston positions providing fully open and partially closed intake ports. However, the significant aspect is the variation in magnitude of the normalized pressure drop at a given measuring position. Although the closure of intake port is increased in a linear behavior i.e. 0%, 25%, 505 and 75%, the consequent cylinder static wall pressure drop at a given measuring position increases in a non-linear behavior. Figure 5.36 shows the normalized wall static pressure drop at z_2 and Re_A. The measurement data has been fitted using a power law function. This indicates

that with the partial closure of cylinder intake port, the cylinder static wall pressure drop increase follows a behavior that can be approximated by a power law.

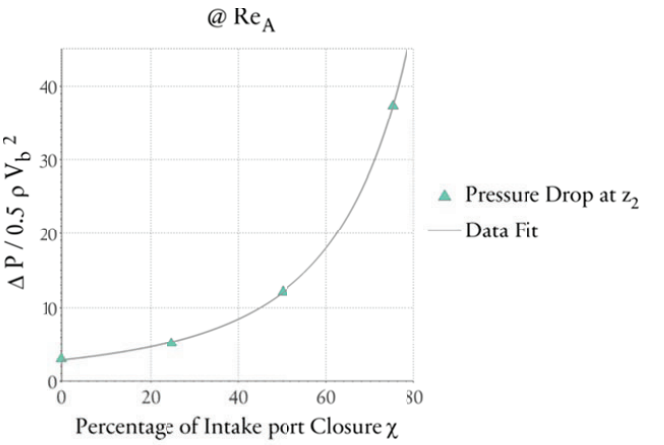

Figure 5.36:

Average Static Pressure Drop at z_2 with intake port closure % @ Re = 6.5 x 10^4.

5.3 Discussion

This experiment studied the effect of piston position on the incylinder confined swirling flow. The experiment, however, did not include the dynamic effect of the piston and instead the measurements are conducted at fixed piston positions. The design swirl parameter remains the same for all piston positions.

The magnitudes of tangential and axial velocities decay downstream the flow due to friction with cylinder internal wall. The tangential velocity profile, at fully open port, is similar to a "Burger Vortex" i.e. an inner forced vortex core and free vortex outer region. The higher velocities are observed at some intermediate radial position between cylinder wall and the geometric center where force and free vortex regions meet. With the decay in swirl downstream the flow, the size of the forced vortex region increases. As the piston is positioned to close the intake port by 25%, both the tangential and axial velocity profiles changes at z_1. The tangential velocity becomes more asymmetric and for the axial velocity the wake effect of the vortex core decreases. The downstream decay of the swirl additionally affects the tangential and axial velocity profiles. The tangential velocity profile at far downstream positions starts changing to a forced vortex i.e. higher velocities are observed near the cylinder walls and the wake like profile of axial velocity diminishes until it develops a jet like profile at z_6. This shows that the downstream decay in the swirl is decreasing the wake effect by transferring

more mass into the wake region. This change in velocity profile begins from cross-sectional positions near the cylinder outlet and moves to upstream positions as the piston gradually closes the port. However, in case of piston position with 50% port closure, at cross-sectional positions close to cylinder inlet, the tangential velocity profiles resembled more towards a wall-jet like profile rather than the forced vortex. The axial velocity in the whole cylinder exhibits a jet-like profile with a broad peak. For the cross-sectional positions close to the intake port, the partial closure of the intake port introduces asymmetry and variation in the mean tangential velocity profile. At 75% port closure the tangential velocity in the cylinder has a forced vortex like profile indicating high velocities in the near wall region. At z_1, the axial velocity still has a jet like profile but with a sharp peak. This jet-like mean axial velocity profile changes back to wake-like at the adjacent downstream cross-sectional position z_2. This indicates a vortex breakdown like characteristic. The mean axial velocity profile then continues to have the wake-like profile at the remaining downstream positions. The wake effect however is small compared to when the port was fully open.

The mean axial vorticity of the mean velocity field has a Gaussian like profile when the intake port is fully open. However with the decay in the swirl downstream as well as the partial closure of the intake port, the vorticity confined in the vortex core region is transmitted to the outer regions. This results in a comparatively uniform mean axial vorticity distribution throughout the cylinder for 75% port closure.

The increase in port closure increases the magnitude of Reynolds stress components as well as the anisotropy. The distribution of normal Reynolds stress components can be understood and summarized from the profiles of axial and tangential velocity components. In case of tangential velocity having the burgers vortex like profile, the u and v velocity components have high fluctuations in the vortex core region and the near wall region. For a forced vortex like profile, $\overline{u'u'}$ and $\overline{v'v'}$ attain higher values in the region close to vortex center than to region with higher tangential velocities. In case of axial velocity with wake like profile, the fluctuations w is high in the vortex core region and near wall region. As the axial velocity profile attains a jet like profile, the $\overline{w'w'}$ in the jet center seems to be very low and increase as the radial distance from the jet center increases. In general, the turbulent kinetic energy increases with the partial closure of the intake port.

For the incylinder flow at all piston positions, the Reynolds shear stresses have lower magnitude compared to normal components. Figure 5.37 give profile of Reynolds shear stress components (in polar coordinates) at z_1 and Re_A for each piston position. An important thing to be noted is the rise in the magnitude of $\overline{v'_r v'_z}$ with percentage of piston closure especially from the region at X/R=± 0.6. At 75% port closure, increase in values of $\overline{v'_r v'_z}$ and $\overline{v'_r v'_z}$ show that the covariance of axial velocity with both tangential and radial velocity components is large.

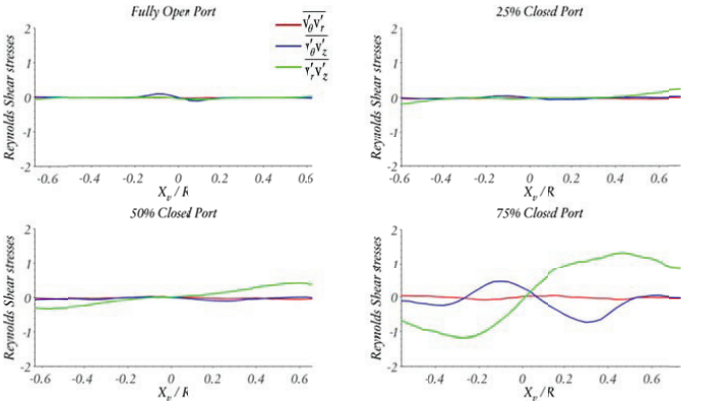

Figure 5.37:

Normalized Reynolds Shear Stress at z_1 and Re_A.

The experimental results show the complexity of the incylinder confined swirling flow even without the dynamic effect of a moving piston. The variation of both axial and especially the tangential velocity with different piston positions indicate that in addition to engine rpm and scavenging port angle, as studied by Nishimoto et al. (1984), the incylinder flow also changes during a single scavenging cycle. Improving the performance of scavenging process thus cannot be possible by considering the velocity profile averaged over a scavenging cycle. Additional challenge will be for the modeling task to develop a model that performs better for different regimes of confined swirling flow. The results of this experiment can be a test bench for performance of different turbulence models in simulating different swirling flow.

Numerical Modeling

This chapter presents the results from the numerical modeling of the swirling flow test case. Unsteady simulations are conducted using two RANS based approaches and the results are compared with the experimental data. The simulations results only represent the case with fully open cylinder intake port and at Reynolds number of 65,000. A discussion has also been made on the possible approaches for improving the simulation results.

The results of the numerical models included in this chapter are those obtained until the time of writing this thesis. For mesh generation, Ansys® GAMBIT v2.4 is used and for CFD processing Ansys® FLUENT v12.1 is used. The post processing of the numerical data is done in Fieldview® v 12.

The computational domain does not include the guide vanes and the inlet to the domain is defined at a radial distance of 200 mm from the axis of rotation (Figure 6.1). In the experimental setup the inlet to the setup is at a radial distance of 300 mm with guide vanes mounted at 250mm radial distance from the cylinder axis/ axis of rotation (Figure 4.1). This is adopted to avoid the inlet to be in the region with large wake effects behind the guide vanes and also not close to the contraction section. The LDA measurements in section 4.1 show a very small wake effect at this radial distance. Another purpose is to see if it is possible to achieve good results by neglecting the guide vanes region in the computational mesh and defining the magnitude of radial and tangential velocity components at some radial position after the guide vanes region. The computational mesh has Y-axis as its rotational axis, therefore, the velocity component along Y-axis represents the axial component and for velocity component along Z-axis it is vice versa.

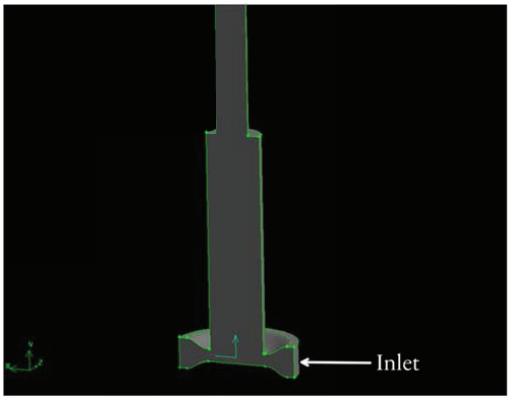

Figure 6.1:

Outline of the section-cut of mesh geometry for Fully Open Intake Port.

The numerical simulations presented here are conducted for cylinder length L=4D and piston positions with fully open intake port only.

6.1 Computational Details

The mesh used for fully open port case is unstructured hex mesh and has approx. 2 million cells.

6.1.1 Turbulence Models

The turbulence models used are already available in the Ansys® FLUENT v12.1 and the values of model constants used are the ones available by default. The computations are conducted first by running a steady state case with standard $k-\varepsilon$ model. The Reynolds Stress model used is the SSG model by (Speziale et al., 1991) with quadratic formulation for the rapid part of the pressure strain term. This RSM model does not require a correction to account for the wall-reflection effect in order to obtain a satisfactory solution in the logarithmic region of a turbulent boundary layer and has improved accuracy particularly for flows with streamline curvature (Ansys, 2009). Figure 6.2 shows a flow chart showing the steps followed to perform different simulations using different turbulence models.

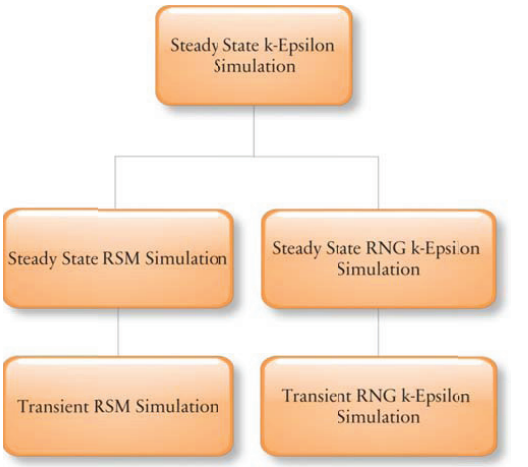

Figure 6.2:

Flow Chart Showing steps followed to perform different Simulations (Fully Open Port Case).

The converged solution for the steady state $k-\varepsilon$ model is then used as a starting point for the steady state RNG $k-\varepsilon$ and Reynolds stress models (RSM). This step is adopted to see if the steady state solution converges i.e. if the numerical simulation does not converge then it indicates the unsteadiness of the flow. In case of steady state simulations for both RNG $k-\varepsilon$ and Reynolds stress (RSM) models, the residuals dropped to 1e-02 and then remained constant (periodic behavior with small amplitude). The steady state results for individual models are then used as the starting point for the unsteady RANS (URANS) simulations.

6.1.2 *Boundary Conditions*

At the inlet of the computational domain 'velocity inlet' boundary condition is defined. For the coordinate system at the inlet, cylindrical coordinates system is defined for the velocity components. This facilitates defining the velocity in terms of radial, tangential and axial components which for this given case is very reasonable. The total inlet velocity is calculated from the volume flow rate and the magnitude of radial v_r and tangential v_θ velocities are calculated from the mean velocity by defining the angle between them (Equation 6.1-6.3). The value of angle θ for all the simulations has been kept at 26° which is close to the data based on LDA results (Figure 4.4). Since the inlet section geometry allows the flow only to be in radial and tangential direction, the value of axial velocity component at the inlet is defined v_z =1.46 e-04 instead of zero value to avoid any numerical issue.

$$v_r = \frac{Q_{in}}{A_{in}} \tag{6.1}$$

$$v_\theta = v_r \tan\theta \tag{6.2}$$

Where Q_{in} is the inlet volume flow rate and A_{in} is the inlet area.

The values of k and ε at the inlet boundary is defined based on the empirical relations given in ANSYS FLUENT manual (Equation 6.3 & 6.4).

$$k = \frac{3}{2}\left(\mathrm{V}_{av}.I\right)^2 \tag{6.3}$$

$$\varepsilon = C_\mu^{3/4}\frac{k^{2/3}}{\mathrm{l}} \tag{6.4}$$

Where V_{av} is average velocity in (m/s), I is the turbulent intensity (T.I) and 'l' is the turbulent length scale. The length scale is assumed to be 0.05 m based on assumption that the size of largest eddy at the inlet is half the width of inlet which is 0.1 m. For the fully open port cases the two turbulent intensity levels 1% and 10% are defined.

For the Reynolds stress turbulence model (RSM), the values of shear stress components at the inlet are considered negligible and the normal stress components are derived from k (Equation 6.5).

$$k = \frac{1}{2}\overline{v_i' v_i'} \tag{6.5}$$

$$\overline{v_i' v_j'} = 0 \tag{6.6}$$

The velocity components profiles at the inlet are assumed to be uniform and a constant value is assigned. Similarly no profiles at the inlet are defined for k, ε and Reynolds stress components.

At the outlet the pressure outlet boundary condition is defined with radial equilibrium pressure distribution which assumes radial velocity to be negligible as discussed in chapter 2. The solid boundaries are defined as walls with no-slip condition i.e. all the velocity components are assumed to be zero at the wall.

6.1.3 *Near Wall Treatment*

The near wall region is defined by adopting the wall function approach. For all the simulations the two-layer-zone model 'Non-equilibrium wall function' is used. In this model, the flow is divided into viscosity affected and turbulent regions. The turbulent kinetic energy budget is computed in the wall neighboring cells (ANSYS, 2009). This model needs less grid points compared to low-Reynolds number models (Najafi et al., 2005). It also accounts for the effect of pressure gradients on the distortion of the velocity profiles i.e. in cases where the assumption of local equilibrium, when the production of the turbulent kinetic energy is equal to the rate of its destruction, is no longer valid (ANSYS, 2009).

6.1.4 *Solution Methods*

For all the simulation cases same solution methods are used. For pressure-velocity coupling SIMPLE algorithm is used. PRESTO scheme is used for spatial discretization of pressure equation. For momentum, turbulent kinetic energy, turbulent dissipation rate and Reynolds stresses second order upwind scheme is used. For temporal discretization, first order implicit integration method is used. The time step Δt for fully open case is defined as 1e-04 seconds.

6.2 *Results*

The results presented in this section are from transient or URANS simulations only. For the case of fully open port case, the maximum y+ value for all the simulation cases are between 126.5 to 130. The cell courant number range from 0.018 to 1.67.

6.2.1 *Tangential Velocity*

The comparison of normalized tangential velocity profiles are given in figures 6.3-6.8 for positions z_1- z_6. It can be observed that, in general, for all the positions the results of both RNG $k-\varepsilon$ model and RSM are not predicting the (free vortex type) tangential velocity profile in the annular region. The RNG $k-\varepsilon$ model, for both inlet turbulent intensities (T.I = 1% and 10%), show a tendency towards predicting a forced vortex profile for the tangential velocity. At z_1, all the models predict a larger size of the vortex core (Figure 6.3). However, RNG $k-\varepsilon$ model with T.I 1% and RSM with T.I 10%, give a good prediction of the magnitude of the peak tangential velocity whereas the RNG $k-\varepsilon$ model with T.I 10% under predicts the value. At further downstream positions, all the models show a smaller decay in the swirl intensity and thus over predict the peak tangential velocity value

compared to experimental data. The effect of different T.I levels defined at the inlet can be seen very clearly for the RNG $k-\varepsilon$ model. At T.I 10%, the predicted tangential velocity profiles show a rapid increase in the size of the vortex core from z_3 to z_4 compared to T.I 1% until z_6 where they both predict the same vortex core size. However, it can be seen that for the two T.I values, the difference in the predicted tangential velocity gradient in the core region remains at all positions i.e. steeper gradients in the core region is predicted at lower T.I.

For the RSM, the tendency to predict the annular region of the tangential velocity profile seems better than the RNG $k-\varepsilon$ model but still the profiles do not follow the experimental data in that region. For positions z_2 and z_3, the tangential velocity gradient in the core region shows good agreement with the experimental data, however, at other positions it shows a poor agreement.

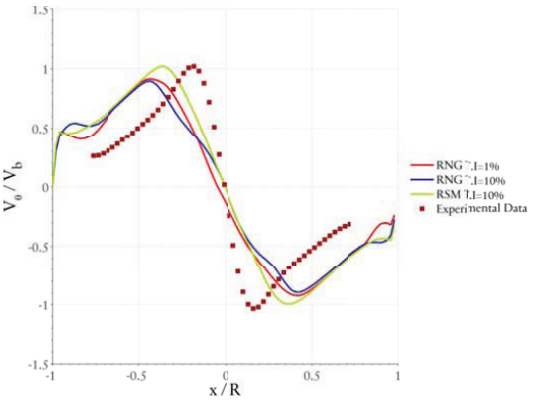

Figure 6.3:

Comparison of Normalized Tangential Velocity Profile at z_1.

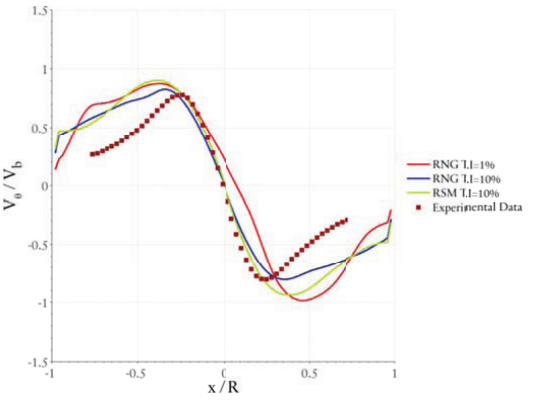

Figure 6.4:

Comparison of Normalized Tangential Velocity Profile at z_2.

Figure 6.5:

Comparison of Normalized Tangential Velocity Profile at z_3.

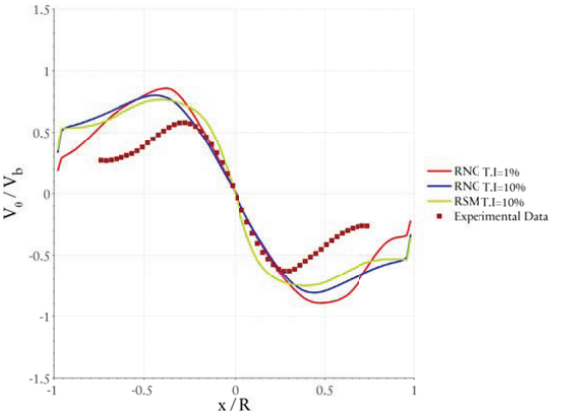

Figure 6.6:

Comparison of Normalized Tangential Velocity Profile at z_4.

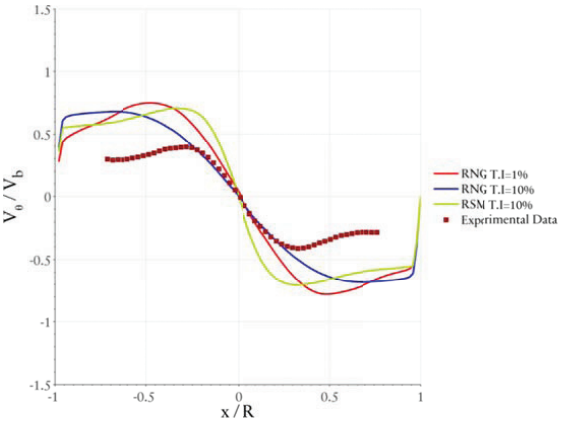

Figure 6.7:

Comparison of Normalized Tangential Velocity Profile at z_5.

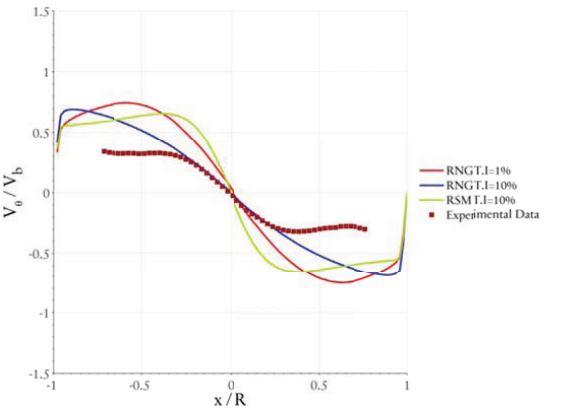

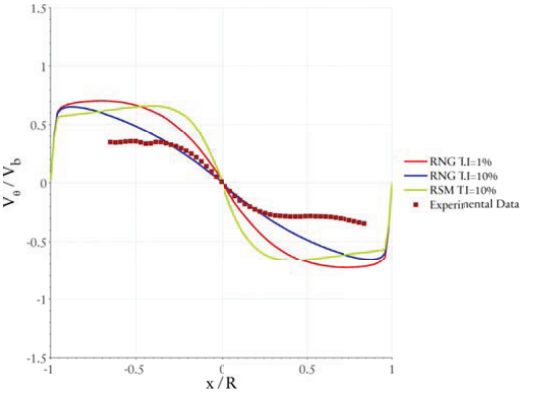

Figure 6.8:

Comparison of Normalized Tangential Velocity Profile at z_6.

6.2.2 *Axial Velocity*

For normalized axial velocity profiles, at z_1, all the simulation cases result a wake-like profile but with a recirculation zone in the vortex core region (Figure 6.9). This seems to be a major difference between the experimental and numerical results because the experimental data, at z_1 does not show any recirculation. Since no measurements have been carried out at cross sectional positions before z_1, it is however unknown whether or not in the experiment setup there exists any recirculation prior to z_1. The vortex core size is also predicted to be larger than the experimental data. This shows a poor agreement with the experimental data. RNG $k-\varepsilon$ model with T.I 10% predicts a comparatively lower peak axial velocity magnitude than the other simulation cases. All the models show reasonable agreement with the experimental axial velocity profile in the region close to the wall i.e X/R =0.6 to 0.8.

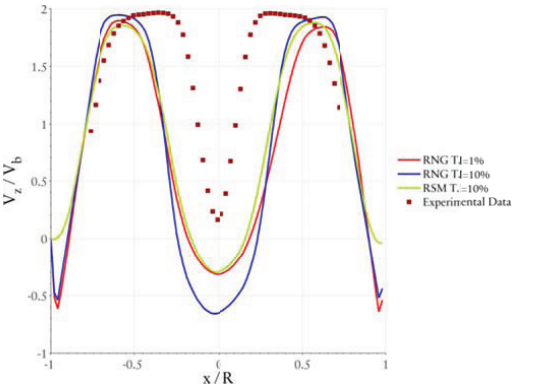

Figure 6.9:

Comparison of Normalized Axial Velocity Profile at z_1.

Figure 6.10:

Comparison of Normalized Axial Velocity Profile at z_2.

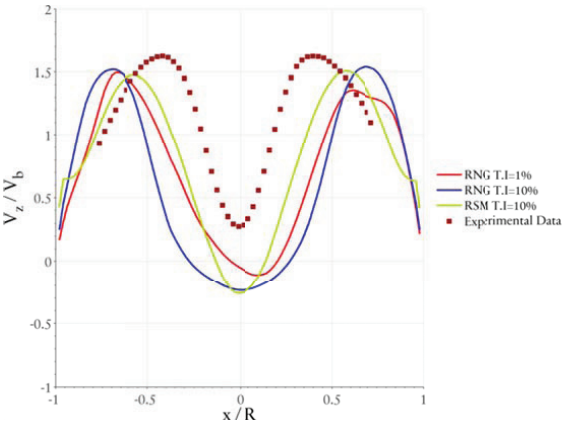

Figure 6.11:

Comparison of Normalized Axial Velocity Profile at z_3.

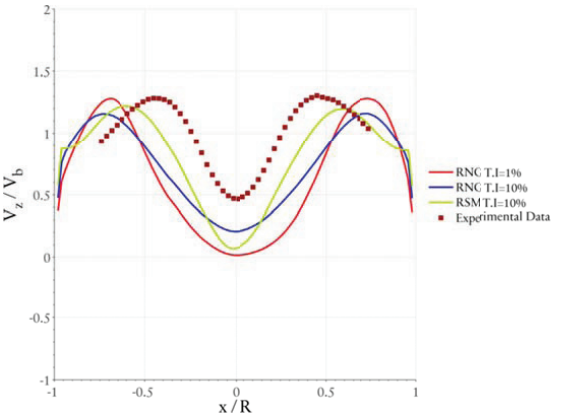

Figure 6.12:

Comparison of Normalized Axial Velocity Profile at z_4.

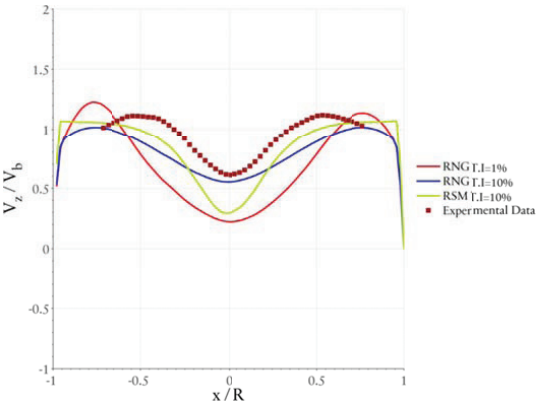

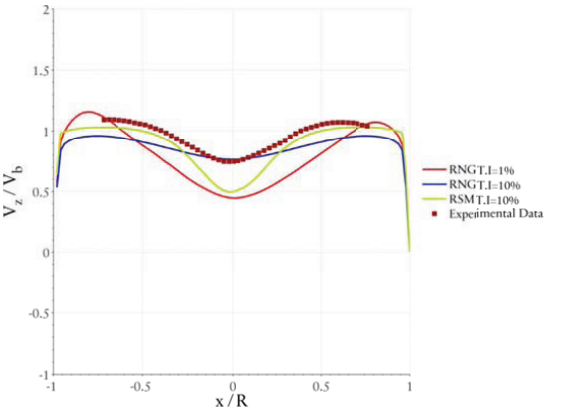

Figure 6.13:

Comparison of Normalized Axial Velocity Profile at z_5.

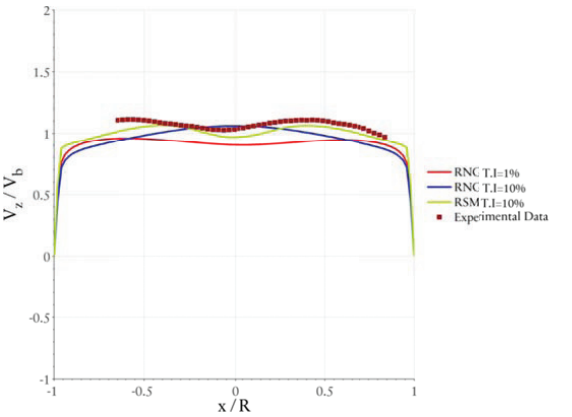

Figure 6.14:

Comparison of Normalized Axial Velocity Profile at z_6.

At z_2 in figure 6.10, RNG $k-\varepsilon$ with T.I 1% and RSM still show a reverse flow in the vortex core region and RNG $k-\varepsilon$ with T.I 10% does not show any reverse flow. However, the vortex core size is still over predicted and also the peak axial velocity magnitude is comparatively less than the measured value at that cross-sectional position.

At z_3, all the simulation cases show a positive axial velocity in the vortex core region (Figure 6.11). However, the vortex core size is still over predicted with RSM predicting the smallest and RNG $k-\varepsilon$ with T.I 1% the largest size. The maximum axial velocity is still under predicted.

At further downstream positions from z_4 and z_5 in figures 6.12-6.14) the axial velocity predicted by RSM has similar profile shape but with a smaller overall magnitude. RNG $k-\varepsilon$ model show faster mass entrainment in the

velocity deficit region near the cylinder axis compared to RSM. At z_6, the RNG $k-\varepsilon$ model with T.I 10% case predicts a jet-like velocity profile whereas the T.1 1% case gives a fully developed axial velocity profile.

6.2.3 *Velocity Magnitude*

The contour plots for the velocity magnitude is shown in figure 6.15. The plots does not show the data averaged over all the time steps but is instead just an instantaneous numerical snapshot of the flow prediction by all the aforementioned simulation cases after 0.05s flow time.

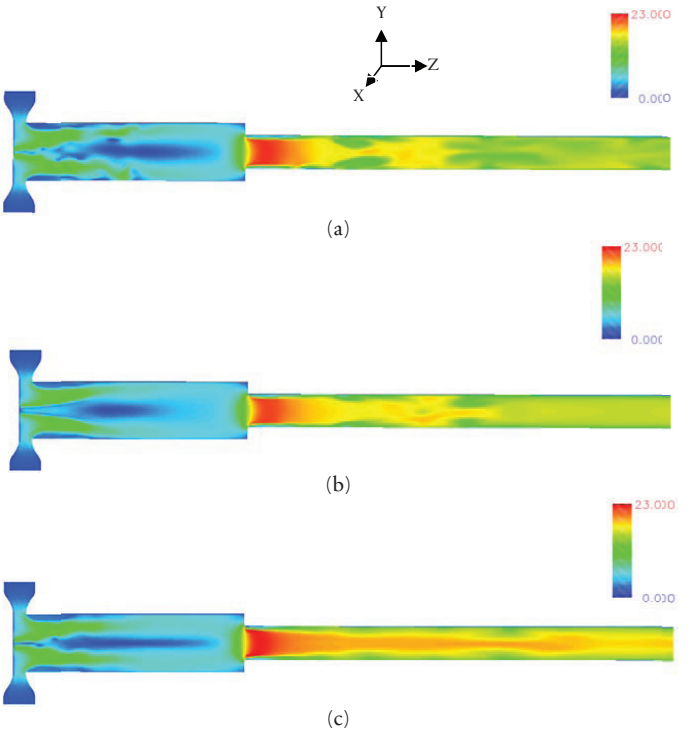

Figure 6.15:

Snapshot of Velocity Magnitude (a) RNG $k-\varepsilon$ Model T.I 1% (b) RNG $k-\varepsilon$ Model T.I 10% (c) RSM T.I 10%.

From figure 6.15 for all the simulation cases, it can be seen that there exists a large flow separation at the wall when the flow enters the cylinder. This is obviously due to the 90° bend that exists between the outlet of the convergent section and the flow cylinder. This wall flow separation region exists approximately between one to two diameter lengths along the cylinder.

However, the RNG $k-\varepsilon$ model with T.I 10% predicts the existence of the separation to a comparatively shorter distance downstream.

The vortex core seem to get instantaneously instable in case of RNG $k-\varepsilon$ model with T.I 1% and with RSM the vortex core seems to be stable in the cross-sections very close to the piston surface and then gets unstable further downstream. One of the possible reasons may be the effect of the aforementioned flow separation at the wall. For RNG $k-\varepsilon$ model with T.I 10%, the vortex core is comparatively stable and also predicts a smooth growth in the vortex core size along the flow.

The flow in the outlet pipe has been predicted different by RNG $k-\varepsilon$ model and RSM. For all cases the flow in the outlet pipe initially has a jet like velocity profile but cases with RNG $k-\varepsilon$ model show that after nearly half of the outlet pipe length, this jet-like velocity profile becomes unstable and then develops a nearly uniform velocity profile. RSM predicts a jet-like velocity profile throughout the outlet pipe.

6.2.4 *Normalized Reynolds Normal Stresses*

The Reynolds normal stress components at z_1 and z_3 are shown in figures 6.16 and 6.17) respectively. As mentioned earlier, these contour plots show a temporal snapshot of normal components of Reynolds stresses from RSM simulation case and do not include the contribution from unsteady flow simulation. Therefore, an exact comparison may not be possible here with the experimental data. Compared to the experimental results shown in Chapter 4, the results to some extent give reasonable qualitative agreement.

At z_1, higher values of the normal stress components are observed in the region near the axis of the cylinder and the wall region and the region in between has low values. In case of $\overline{w'w'}$, the model also give a half circle arc-like shape region with peak $\overline{w'w'}$ values. The magnitude of peak values for all the normal stress components are close to the experimental values (Figures 4.15, 18 and 21).

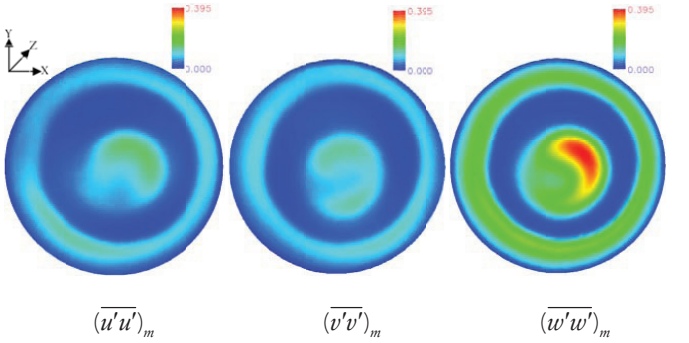

Figure 6.14:

Normalized Reynolds Normal Stress Components at z_1.

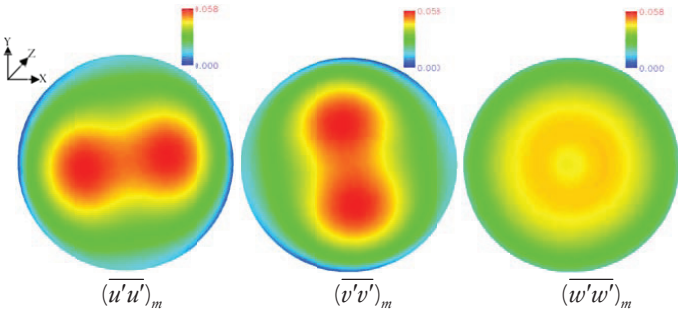

Figure 6.15:

Normalized Reynolds Normal Stress Components at z_3.

At z_3, for $\overline{u'u'}$ and $\overline{v'v'}$ the model also predicts an elongated oval-shaped region. Remarkably, it also shows that this oval shaped region is tilted at some angle with X and Y axes lines respectively. However, the magnitude of peak values for $\overline{u'u'}$, $\overline{v'v'}$ and $\overline{w'w'}$ are a bit lower than the experimental results in Figures 4.17, 4.20 & 4.23) respectively. For $\overline{w'w'}$ also the model gives similar features as the experimental data.

6.2.5 *Normalized Reynolds Shear Stresses*

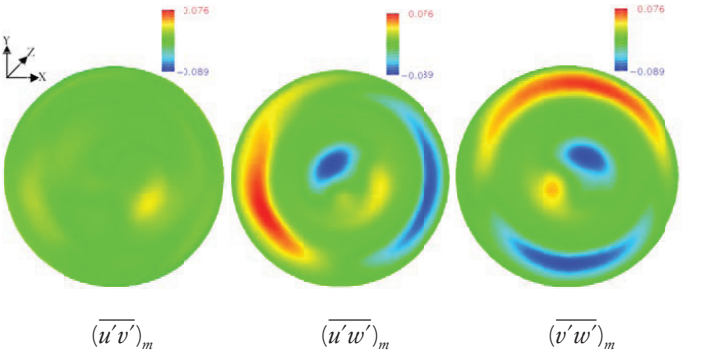

Figure 6.16:

Normalized Reynolds Shear Stress Components at z_1.

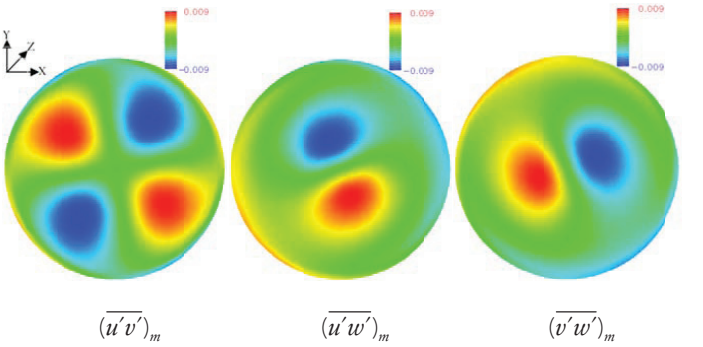

Figure 6.17:

Normalized Reynolds Shear Stress Components at z_5.

At z_1, for all the shear stress components the RSM model predicts comparatively lower peak values compared to experimental data (Figures 4.24, 4.27 & 4.30) respectively. $\overline{u'w'}$ and $\overline{v'w'}$ are maximum in the vortex core and near wall region (Figure 6.16). Similar to experimental results discussed in section 4.2.6, $\overline{v'_\theta v'_z}$ is large in the vortex region whereas the $\overline{v'_r v'_z}$ is dominant in the near wall region. $\overline{u'v'}$ have lower values than $\overline{u'w'}$ and $\overline{v'w'}$ but the spatial distribution to some extent shows similar features as the experimental data. However, at z_5 in figure 6.17, $\overline{u'v'}$ has decayed and has similar distribution as experimental data. In case of $\overline{u'w'}$ and $\overline{v'w'}$ also, the model predicts decay in the magnitude and enlargement of the zones having peak values. The magnitude of peak values for all the

shear stress components are under predicted compared to experimental data in figures 4.29 & 4.32 respectively.

6.3 Discussion

The results of CFD simulations presented in this chapter do not show a satisfactory agreement with the experimental data. However, there are some qualitative features like profiles of velocity and modeled Reynolds stress components that, to some extent, have reasonable agreements. The factors affecting the performance of the CFD models possibly lie both in the treatment of turbulence and the numerical aspects.

The performance of RANS based models for swirling flows have already been discussed in Section 2.4. Numerically, defining the boundary conditions at the inlet of the computational domain has very significant impact. In the current simulations, a constant value of the parameters like velocity components and turbulence parameters like k and ε have been given at the inlet. Considering the real experimental setup, this approach may not be good because the inlet in the computational domain is placed after the guide vanes and close to the contraction section. The profile of velocity components may not be uniform at that radial position. The possible reasons are the wake that is generated behind the guide vanes and the upstream effect of in-cylinder swirling flow (PVC and instability waves). Both of these factors can make the velocity profiles and magnitude, at the selected inlet position (a radial distance of 200 mm from cylinder axis in this case), non-uniform and unsteady respectively. Similar effect can be on the turbulence parameters like k, ε and Reynolds stress components. This requires experimental measurements to be conducted in order to define the realistic boundary conditions. (Dong et al, 1993) also studied the effect of different inlet profiles for the velocity components in a swirling flow and suggested experimentally measured profiles for better simulation results. In case of outlet, since the outlet pipe length is very long, therefore, the effect of outlet boundary condition on the in-cylinder swirling flow may not be very significant. (Xia et al., 1997) have found significant effect of outlet boundary conditions but at regions close to outlet i.e. only to a small upstream distance from the outlet.

The other aspect is the RANS modeling approach itself. In the RANS based models, the turbulent scales are not fully or partly resolved. Instead the whole range of turbulent scales is modeled and the simulation results represent the influence of all the turbulent scales. Thus RANS have a strong damping influence on any resolved turbulence or unsteady structures, which is desirable for steady state flows (Gyllenram et al., 2008). In case of unsteady flows, the time dependent features that unsteady RANS (URANS) may resolve is restricted only to the coherent periodic motions and not the wide range of frequencies of broadband turbulence (Spencer et al., 2009). The unsteady behavior requires the turbulence model to be able to distinguish between resolvable and unresolvable scales and the RANS based equations

do not distinguish between turbulence and unsteadiness (Gyllenram et al., 2008). The main reason is RANS assumption of all turbulence being stochastic and averaging thus removes all unsteady motion (Leschziner M. A., 2010). This (ensemble averaging) leads the solution to be determined by initial and boundary conditions and one can get same solution repeatedly by keeping the same computer and initial and boundary conditions (Gyllenram et al., 2008).The URANS simulation conducted by (Spencer et al., 2009) could only resolve the ensemble or phase averaged coherence unsteadiness with small fluctuating amplitude.

Compared to eddy viscosity based URANS, the RSM based simulations in several cases e.g. (Hirai et al., 1988) (Benim et al., 2005) and (Lübcke et al., 2001) etc. gives better results. The main reason is a better treatment of Reynolds stresses by solving a transport equation for each component. However, for a better understanding and prediction of the flow, turbulence modeling approaches are required where, considering the computational costs, a part of the turbulence spectrum is resolved and the rest are modeled (Hanjalic K., 2005). Such modeling approaches include LES and hybrid LES-RANS etc.

In the current simulation cases, a steady state converged solution could not be achieved with RNG $k-\varepsilon$ and RSM. This indicated that the problem to be inherently unsteady in nature and led to run URANS simulations. Figure 6.18 shows a comparison of normalized root mean square (RMS) values of axial velocity for experimental data and the simulation cases at position z_1.

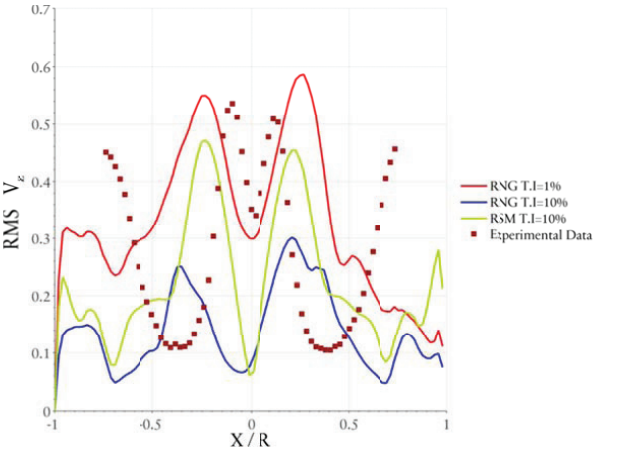

Figure 6.18:

Comparison of Experimental and Numerical Results of Normalized RMS Values of Axial Velocity at z_1.

It can be seen that the URANS simulations of all the current cases show an unsteady behavior. The RMS values are almost of the same order as experimental data but profiles are not in good agreement with the

experimental data. Addressing the aforementioned issues of properly defining the inlet boundary conditions may also improve the RANS/URANS results to some extent, however, the major reason may simply lie in the inadequateness of the RANS/URANS based methodology in this particular case. This indicates that using Hybrid RANS-LES or purely LES approach will probably give better simulation results by resolving a portion of the turbulence scales. Thus performing a grid independence study by increasing the computational mesh size in the current simulation cases may not significantly improve the simulation results compared to what already have been obtained using URANS. Due to very limited number of Ansys® FLUENT licenses available at MEK-DTU, Hybrid RANS-LES or LES models could not be applied. The URANS simulations with a computational gird containing the guide vanes and for cases with partially closed cylinder intake port are currently under progress.

Summary & Conclusions

The aim of this thesis was to study and understand various aspects of the confined swirling flow during the uniflow scavenging processes for large two-stroke marine diesel engines. A description of the working of large two stroke marine diesel engines were given in order to understand the role of scavenging process and its significance on the overall engine performance and efficiency. Different features of uniflow scavenging process in currently operational marine diesel engines were discussed and it was identified that the real engine scavenging process is very complex, scientifically less understood in detail and one of the potential processes for making improvements in order to develop future fuel and environmentally efficient marine diesel engines.

Out of the many aspects of complex physics of scavenging process, the focus in this thesis was to study and characterize the confined swirling flow during the scavenging process. The study was conducted by developing a simplified experimental model with air at room temperature and pressure without considering mixing and stratification. The model comprised of a transparent acrylic cylinder fitted to a swirl generator having guide vanes. Features like a movable piston and changing cylinder length were also included. The design is more close to features of engine cylinder and makes it different from the confined swirling pipe flow experimental setups earlier reported in scientific literature. Different experimental techniques were used and CFD simulations were performed and the results were compared with the experimental data.

1.1 Experimental Measurements

Two different experiments are conducted using Stereoscopic PIV measurements at different cross-sectional planes. For both the experiments the measurements are conducted at fixed guide vane angle of the swirl generator and two Reynolds numbers in the cylinder i.e. 65,000 and 32,500. For each measurement, nearly 1000 instantaneous PIV snapshots were taken. For the fully open intake port, LDA measurements are also conducted in the inlet section and also at the entrance of the cylinder. The design swirl parameter for the experimental setup is found to be 0.34 and is kept constant for all the measurements.

1.1.1 *Swirling Flow in a Pipe with different Lengths*

In this experiment the inlet to the measuring cylinder was kept fully opened and the measurements are conducted by changing the length of the cylinder to 8D, 6D and 4D.

The results from LDA measurement show that in the inlet section, the wake effect behind the guide vanes reduces significantly before entering the contraction region. The velocity distribution in the inlet section at different circumferential position is not symmetric at a radial distance of 200 mm. However, after the flow passes through the contraction region the variation of the angle between radial and tangential component (along the circumferential positions) is reduced to 1.5°. At an axial position z/D of 0.368, the LDA measurements show a near symmetric distribution of tangential velocity.

The PIV results show that the resulting confined swirling flow has a tangential velocity profile similar to Burgers vortex and the axial velocity has a wake-like profile. The tangential velocity profile shows that unlike the theoretical Burgers vortex profile, the region surrounding the inner forced vortex core region is not irrotational. Instead, the region has a very weak vorticity that may possibly be as a result of a radially decaying vortex causing a vorticity transfer from vortex core to the surrounding regions. This result is in accordance with some other experimental results reported earlier in the scientific literature. The swirl decays downstream the flow and the vortex core size increases. This changes the tangential velocity profile towards more forced vortex and the axial velocity to be more uniform by transferring more mass in to the central velocity deficit region. The effect of variation in Reynolds number is mostly observed in the vortex core region where for initial measuring positions the peak value of normalized tangential and axial velocity is found to be higher for low Reynolds number. Further, for axial velocity, the minimum velocity in the velocity deficit region is found to be lower in case of high Reynolds number. However, the axial velocity profile at all measuring positions does not show any reverse flow. The average size of the vortex core at low Reynolds number is observed to be relatively smaller than at high Reynolds number. For first five measuring positions close to cylinder inlet, which are common in cylinder lengths 8D, 6D and 4D, the variation in cylinder length seems to have no significant effect on the normalized tangential and axial velocity profiles for a given Reynolds number. Similar behavior is observed for the positions which are common in cylinder lengths 8D and 6D. For position z_6 (z/D=3.595) being very close to cylinder outlet for cylinder length 4D, a small increase in the tangential and axial velocity is observed due to small diameter outlet pipe. This indicates that the downstream change in cylinder length is not detected by the flow at upstream positions and thus the flow mainly depends on the upstream conditions at the cylinder inlet.

The magnitude of radial velocity at position z_1 (z/D=0.963), is almost a factor of 10 lower than tangential and axial velocity and decreases further

downstream the flow. At position z_7 (z/D=4.116) and cylinder lengths (8D and 6D), the magnitude of radial velocity becomes very close to zero and then slowly starts increasing again.

The mean axial vorticity has a Gaussian like profile at z_1 (z/D=0.963) i.e. for the regions at larger radial distance from the cylinder axis, except the near wall region, the vorticity is very weak and then in the vortex core region it gets very strong. With swirl decay downstream the flow, the vortex core loses its vortical strength by transferring it in outward radial directions. The rate of this vorticity transfer is higher in case of high Reynolds number thus leading to quicker decay of the weak vortical 'annular region' in the tangential velocity profile.

The detection of vortex core position in the instantaneous PIV measurements at z_1 (z/D=0.963) show that the vortex core position is not stationary and moves in an area of r/R= ±0.2. This indicates a precessing vortex core (PVC) and LDA measurements show that the precession frequencies at Reynolds number of 65000 and 32500 are 5.8 Hz and 3.15 Hz. The precession frequency is found to increase linearly as a function of flow rate. The mean vortex core position is not aligned with the cylinder axis at all measuring positions indicating an asymmetric swirling flow with core following a helical path. The radius of the helical path is not same for all measuring positions and initially the radius of the helical path is smaller but then gradually increases. The helix rotation is in a clockwise direction similar to the swirl which is also in clockwise direction. This together with a Burgers vortex like tangential velocity profile and wake-like axial velocity profile indicate a left-handed helical vortex and having a negative pitch. For all the cylinder lengths the helical vortex core does not complete one revolution. In case of cylinder length 8D, the helical vortex path at the downstream positions, instead of rotating around the cylinder axis, re-twists at one side of the X-axis. In addition, at those far downstream positions the tangential velocity has forced vortex profile, the axial velocity and mean axial vorticity profiles become uniform showing an infinite pitch of the helical path. This indicates a transition of left handed to right handed helical vortex called as 'L-transition' and is one of characteristics of vortex breakdown.

In the presence of a precessing vortex core (PVC), the measured values of Reynolds stresses are actually a combination of turbulence and vortex core oscillation. The Reynolds stress normal components are high in the vortex core and near wall regions. Considering the maximum values, for normal stresses (Cartesian coordinates) at z_1 (z/D=0.963) $\overline{w'w'} > \overline{u'u'} \simeq \overline{v'v'}$. Regarding the components in polar coordinates, $\overline{v'_\theta v'_\theta}$ and $\overline{v'_r v'_r}$ are larger near the wall and in the vortex core regions at z_1 (z/D=0.963). The radial distance, from the vortex center, where $\overline{v'_r v'_r}$ increases towards the vortex center, is larger than the $\overline{v'_\theta v'_\theta}$ and follows the same for both high and low Reynolds numbers. As the swirl decays downstream, the magnitude of radial and tangential fluctuations decrease but their spatial distribution increase to larger radial distances of the cylinder cross-section.

In general the magnitudes of shear stress components, at different measuring positions are observed to be smaller than normal stress components. Considering the maximum values, for shear stresses (Cartesian coordinates) $\overline{u'w'} \simeq \overline{v'w'} > \overline{u'v'}$ indicating anisotropy of the flow. However, with swirl decay downstream at z_5 (z/D=3.068), the maximum values become almost equal for individual components of both normal and shear stress components i.e. $\overline{w'w'} \simeq \overline{u'u'} \simeq \overline{v'v'}$ and $\overline{u'w'} \simeq \overline{v'w'} \simeq \overline{u'v'}$. The Reynolds stresses decay with the swirl and distribution of normal and shear components tends to become comparatively and gradually more uniform in the flow domain. With swirl decay downstream, the flow at high Reynolds number has higher tendency towards a more uniform spatial distribution of individual Reynolds stress components in the flow domain.

At z_1 (z/D=0.963) the turbulent kinetic energy is strong in the vortex core and near wall region. The maximum value is observed in the vortex core region and the contours show an asymmetric distribution. The turbulent kinetic energy decreases downstream.

The flow at low Reynolds number is less responsive or in other words more resistive to the variations in vorticity, Reynolds stresses and turbulent kinetic energy as the swirl decays along the pipe.

1.1.2 *Effect of Piston Position on the Confined Swirling Flow*

In this experiment the length of cylinder was kept 4D but the piston is translated and adjusted to fixed positions where it closes the intake to the cylinder by 0% (Fully Open intake port), 25%, 50% and 75%. For each piston position, stereoscopic PIV measurements were conducted at the aforementioned Reynolds numbers.

When the piston is partially closing the cylinder intake port, the piston serves as a forward-step facing the incoming flow into the cylinder and affects the magnitude of radial velocity in particular and also tangential velocity to some extent. This consequently increases the axial velocity magnitude. Since the flow rate is kept constant but the inlet area is reduced, therefore, the average velocity at the inlet increases. The piston also behaves as a bluff-body in the flow path generating unsteady fluctuations/ disturbances at the sharp-edge interface of the piston top and outer wall. These fluctuations result in growth of instabilities and waves and are superimposed on already precessing helical vortical flow that is observed when the port is fully open. This indicates that the resulting in-cylinder swirling flow becomes more transient. This also puts some challenge for making non-time resolved PIV measurements.

At 25% intake port closure and a given Reynolds number, the peak values of tangential velocity decreases and axial velocity increases. At z_1 (z/D=0.963),

the tangential velocity profile shows a less distinct peak at the interface of outer region and a comparatively bigger vortex core. Also the tangential velocity profile on both sides of the origin is different and indicates asymmetry in tangential velocity distribution. The axial velocity still has wake-like profile, however, the velocity deficit in the vortex core region reduces indicating more mass entering into that region. With the swirl decay downstream the flow, the tangential velocity at far down stream positions develops a forced vortex profile. Whereas for axial velocity the mass continue to enter the velocity deficit region until at position z_6 (z/D=3.595) where its profile changes to jet-like.

At 50% port closure, the asymmetry in the distribution of tangential velocity increases further z_1 (z/D=0.963) and the profile develops two peaks at one side of the diameter. This is possibly due to the effect of wall or 'mirror vortex'. For position z_3 (z/D=2.016) and downwards, the vortex core size increases significantly. The tangential velocity profile becomes difficult to be identified because of its shape to be more close to a 'wall-jet' rather than 'forced vortex' profile. At z_1, the axial velocity profile becomes jet-like with a broad peak and the magnitude of axial velocity profile is higher than at 25% port closure. With the decay in swirl, the velocity magnitude in the center of the jet gradually decreases becoming nearly uniform at downstream positions but increases again at z_6 due to effect of cylinder exit contraction.

At 75% port closure, the tangential velocity has a solid-body rotation throughout the cylinder which decays along the flow downstream. This shows that closure of the intake port has a direct relation to the development of solid body rotation profile of tangential velocity in the cylinder. At z_1, the axial velocity has jet like profile and its magnitude increases further. However, at next measuring position z_2 (z/D=1.489), the axial velocity profile changes to wake-like profile indicating a vortex breakdown like characteristic. For the downstream positions, the axial velocity profile continues to be wake like but with a small wake effect and a radially broad wake region. Since the cylinder inlet provides a very small area for fluid to enter into cylinder resulting in a local compression of the fluid at the intake port, a very distinct feature is observed at z_1 and z_2. The vortex core at these positions behaves like a source i.e. the fluid particles move outward from the vortex core following a curved path. However, at z_3, this pattern changes and the in-plane velocity distribution has now a regular swirling flow pattern i.e. vortex core behaving like a sink.

With the partial closure of the intake port as well as the decay in the swirl downstream, the mean axial vorticity distribution confined in the vortex core region is transmitted to the outer regions. This results in a comparatively uniform mean axial vorticity distribution throughout the cylinder for 75% port closure.

For the Reynolds normal stresses, the magnitude and anisotropy of all the components increases with the increase in the partial closure of the cylinder intake. However, for a given port closure, the variance in axial velocity is

dominant i.e. $\overline{w'w'} > \overline{u'u'} \simeq \overline{v'v'}$. At 25% port closure, initially the $\overline{v'_\theta v'_\theta}$ and $\overline{v'_r v'_r}$ are higher in the vortex core and near wall regions and the annular region has smaller values. However, at z_6, the overall magnitudes of the normal stress components have decayed approximately by an order of 10. At this cross-sectional position, the spatial distribution of variance in tangential and radial velocity components has a spread to larger radial positions around the cylinder axis gradually decreases in the radial direction towards the wall. The variance in axial velocity is very low in the core region and gradually increases in the radial direction towards the cylinder wall. This indicates that in the center of the jet the axial velocity is comparatively more stable and fluctuates more as the radial distance from the vortex core increases. At 50% port closure, the peak value of $\overline{w'w'}$ at z_1 increases almost twice the value at 25% port closure. For all measuring positions, $\overline{w'w'}$ has minimum values in the center of the jet and the near wall region has the highest values. The spatial distribution of $\overline{v'_\theta v'_\theta}$ and $\overline{v'_r v'_r}$ show high values in the vortex core region. With swirl decay downstream, this spatial distribution grows to larger radial positions. At 75% intake port closure, the value of maximum variance in the axial velocity increases almost 4 times the value at 50% port closure and spatial distribution is also very anisotropic. At z_1, the $\overline{w'w'}$ is low in the jet center, then increases to its peak value at (X/R=0.3) and then starts decreasing again towards the wall. $\overline{v'_\theta v'_\theta}$ and $\overline{v'_r v'_r}$ have higher value in a large central region around the cylinder axis and decreases towards the wall. In general, despite a large increase in the magnitude of normal stress components at z_1, the values at z_6 do not increase in the same order indicating that the downstream decay in the velocity fluctuations also increases with the increase in partial closure of the intake port. This may possibly be the upstream influence of outlet contraction having a damping effect. In general, the turbulent kinetic energy increases with the partial closure of the intake port. For a given cross-sectional plane, the distribution of turbulent kinetic energy seems to be understood from the mean axial velocity distribution. For a wake-like axial velocity profile, the maximum value of turbulent kinetic energy is observed in the vortex core region and minimum value is observed in the high axial velocity region. Similarly, for a jet-like V_z profile, the minimum value is observed in the center of the jet and maximum value is observed in the jet skirt region.

The magnitude of Reynolds shear stress components also increase with the increase in partial closure of the cylinder intake. At 25% port closure, $\overline{v'_\theta v'_r}$ decreases slowly towards the cylinder axis and increase again to a small extent in the vortex core region. $\overline{v'_\theta v'_z}$ is low in the near wall region and increases to its peak value at a radial distance of r/R=0.15 and then decreases again in the vortex center. $\overline{v'_r v'_z}$ has largest values in the near wall region and decreases towards the vortex core region. At z_6, the peak values of Reynolds shear stresses are reduced by a factor of 100. This distribution of all

the components in general remains the same but spreads to surrounding regions. At 50% port closure, the magnitude of Reynolds shear stresses increases approximately twice the value at 25% port closure. At z_1, $\overline{v'_\theta v'_r}$ and $\overline{v'_r v'_z}$ have almost similar distribution as in case of 25% port closure but for $\overline{v'_\theta v'_z}$ the region near the cylinder axis with peak value disappears indicating a very small value at large radial distance and almost zero value in the remaining central portion of the cylinder. As the swirl decays downstream, for all the shear stress components the magnitude decays and high values are observed in the larger radial distances from the cylinder axis and central region of the cylinder has very low values. At 75% port closure, the peak values of shear stresses is almost twice the value at 50% port closure. For individual components the distribution pattern at z_1 is nearly the same as previous piston position. An important aspect is observed that the vortex breakdown between positions z_1 and z_2 has no significant effect on the distribution pattern of Reynolds shear stress components.

The closure of cylinder intake port closure has a significant effect on the mean axial vorticity distribution for a given cross-sectional position and also along the flow downstream. With the increase in the closure of the intake port, at initial position z_1, the Gaussian like profile of mean axial vorticity starts to deteriorate until 75% port closure where it no longer exists. Also, the port closure enhances the vorticity transfer from strong localized vortical zones (vortex core) to other weak vortical region as the swirl decays downstream the flow direction. Thus, in general, the in-cylinder axial vorticity distribution is comparatively more uniform at higher cylinder intake port closures.

1.2 CFD Simulations

The numerical simulations are conducted using RANS based modeling Approach. The models used are high Reynolds number RNG $k-\varepsilon$ and Reynolds stress model (RSM) with quadratic formulation for the rapid part of the pressure strain term. The inlet to the computational domain is defined at a radial distance of 200 mm from the axis of rotation and does not include the guide vanes. This is carried out to study the possibility of achieving good results by neglecting the guide vanes region in the computational mesh and defining the magnitude of radial and tangential velocity components using the LDA data. The RNG $k-\varepsilon$ models are used with an inlet turbulence intensity of 1% and 10% whereas with the Reynolds stress model (RSM) turbulence intensity of 10% is defined.

The comparison of normalized tangential velocity profiles show that for all the positions the results of both RNG $k-\varepsilon$ model and RSM are not predicting the (free vortex type) tangential velocity profile in the annular

region. The RNG $k-\varepsilon$ model, for both inlet turbulent intensities (T.I = 1% and 10%), shows a tendency towards predicting a forced vortex profile for the tangential velocity. The models show a smaller decay in the swirl intensity downstream the flow and thus over predict the peak tangential velocity value compared to experimental data. For RNG $k-\varepsilon$ model with T.I = 10%, the predicted swirl flow shows a rapid transformation of tangential velocity from an initial burgers vortex like profile in to forced vortex type. Moreover, at all positions steeper gradients in the core region are predicted at lower T.I.

At z_1 all the simulation cases result a normalized axial velocity with a wake-like profile but with a recirculation zone in the vortex core region. This seems to be a major difference between the experimental and numerical results because the experimental data, at z_1 does not show any recirculation.

The overall performance of RANS based models used in this study are not satisfactory. From turbulence point of view, the main reasons lie in the modeling of turbulence scales and also a poor performance of RANS based models for flows involving streamline curvature. Numerically, an inlet boundary condition based on experimental results should perform better than assuming constant values for different turbulence parameters.

1.3 Future Work

The current project has been the initial work towards the ultimate and long term goal of an efficient scavenging process for a low speed two stroke marine diesel engine. The future challenges involve both experimental work and numerical computations. Some of the potential future works in author's view are given as follows:

- Conducting the experiments at different swirl numbers in order to study the effect of swirl number.
- Design and development of an experimental test setup having a moveable piston, scavenging ports similar to cylinder liner, exhaust valve at the outlet and a scavenging box.
- Designing intake ports with different radial thickness and conducting measurements to study the effect of cylinder liner wall thickness on the incylinder flow.
- Measurement of dynamic effect of the piston motion on the incylinder confined swirling flow.
- Studying the effect of exhaust valve on the incylinder swirling flow.
- Conducting experiments to study the effect of mixing and stratification during the scavenging process. This is probably the most challenging experiment both from point of view of design of setup and procedure to conduct useful measurements.
- CFD simulations based on LES or Hybrid LES RANS methods.

- Developing RANS based model to simulate the incylinder flow with good agreements compared to experimental data.
- Simulations using the moving boundary methods to predict the transient flow during the scavenging process.

References

Alekseenko S. V., Kuibin P. A., Okulov V. L. and Shtork S. I., "Helical vortices in swirl flow," JFM, **382**, pp. 195–243 (1999).

Alekseenko S. V., Kuibin P. A., Okulov V. L., "Theory of Concentrated Vortices: An Introduction, "Springer, (2007).

Algifri A. H., Bharadwaj R. K. and Rao Y. V. N., "Turbulence Measurements in Decaying Swirl Flow in a Pipe", App.lied Scientific Research, **45**, 233-250 (1988).

Algifri A. H., Bhardwaj R. K., and Rao Y. V. N., "Eddy Viscosity in Decaying Swirl Flow in a Pipe," App.l. Sci. Res., **45**, pp. 287–302 (1988).

Andersen L. and Plum M., "Modeling of the scavenging process in a two stroke Diesel engine," Bachelors Thesis, (2008).

ANSYS FLUENT v12.1 Manual, ANSYS INC.

Baker D.W. and Sayre C.K.J., "Decay of swirling turbulent flow of incompressible fluids in long pipes," Flow—Its Measurement and Control in Science and Industry, 1, Instrument Society of America, pp. 301–312 (1974).

Benjamin T.B., "Theory of vortex breakdown phenomenon," JFM, **14**, 4, pp. 593-629 (1962).

Benim A.C. and Nahavandi A., "URANS and LES Analysis of Turbulent Swirling Flows," Progress in Computational Fluid Dynamics, ***5***,8, (2005).

Blair G. P., "The Basic Design of Two-Stroke Engines," SAE, (1990).

Cazan R. and Aidun C. K., "Experimental Investigation of the Swirling Flow and the Helical Vortices induced by a Twisted tape inside a Circular Pipe," Physics of Fluids, **21**, 3, (2009).

Craft T., Iacovides H., Launder B. and Zacharos A., "Some Swirling-flow Challenges for Turbulent CFD," Flow Turbulence Combustion, 8, 4, pp. 419-434 (2008).

Dam B. S., "Experimental and Numerical Investigations of sprays in two-stroke diesel engines," PhD thesis, Technical University of Denmark, (2007).

Dantec DynamicStudio® user manual, Dantec Dynamics A/S.

Davidson L., Lecture slides for 'Turbulence Modeling' course. Chalmers University, Sweden., (2004).

Dedeoglu N., "Improvement of Mixture Formation in a Uniflow-Scavenged Two-Stroke Engine," SAE Technical paper, Document nr. 901536, (1988).

Dedeoglu N., "Improvement of Mixture Formation in a Uniflow-Scavenged Two-Stroke Engine," Future Transportation Technology Conference & Exposition, SAE, 1990.

Dong M. and Lilley D.G., "Effects of inlet velocity profiles on downstream flow development of turbulent swirling flows," Proceedings of the 28th Intersoc. Energy Conversion Engineering Conference, **1**, p. 707 (1993).

Ebrahimi M. and Nouri N. M., "Mechanism of vorticity generation for the near wall fluid flow problems", International Journal of Dynamics of Fluids, **3**, 1, pp. 95–105 (2007).

Escudier M. P., Bornstein J., Maxworthy T., "The dynamics of confined vortices," Proc. R Soc. London A, **382**, pp. 335–360 (1982).

Escudier M. P. and Keller J. J., "Recirculation in Swirling Flow: A manifestation of Vortex Breakdown", AIAA Journal, **23**,1, pp. 111-116 (1985).

Escudier M. P., "Confined Vortices in Flow Machinery," Ann. Rev. Fluid Mech., **19**, pp. 27-52 (1987).

Escudier M. P., Nickson A. K. and Poole R. J., "Influence of Outlet Geometry on Strongly Turbulent Flow through a Circular Tube," Physics of Fluids, **18**, 12, (2006).

Faler J. H. and Leibovich, S., "Disrupted States of Vortex Flow and Vortex Breakdown," Physics of Fluids, 20, pp. 1385-1400 (1977).

Flavio P., "Scavenging Process in two Stroke Marine Diesel Engine", Masters Thesis, (2009).

Greitzer E. M., Tan C. S., Graf M. B., "Internal Flows: Concepts and Applications," Cambridge University Press, (2004).

Gyllenram W. and Nilsson H., "Design and Validation of a Scale-Adaptive Filtering Technique for LRN Turbulence Modeling of Unsteady Flow," Journal of Fluid Engineering, **130**, 5, pp. 10 (2008).

Hanjalic K., "Will RANS survive LES: a view of perspectives," ASME J. Fluids Eng., **127**, pp. 831-839 (2005).

Heywood J. B., "Internal Combustion Engine Fundamentals," McGraw-Hill, (1988).

Hoffmann A.C. and Stien L.E., "Gas Cyclones and Swirl Tubes: Principles, Design, and Operation," 2nd Edition, Springer, (2002).

Islek A. A., "The Impact of Swirl in Turbulent Pipe Flow," Master's Thesis, Georgia Institute of Technology, (2004).

Hopkinson B., "The charging of two-cycle internal combustion engines," Trans. NE Coast Instn. Engrs. Shipbuilders, **30**, pp. 433, (1914).

Ito K. O. and Kuroda C., "Decay process of swirling flow in a pipe," Int. Chem. Eng. **19**, pp. 600–605 (1979).

Jakirlic S., Hanjalic K. and Tropea C., "Modeling Rotating and Swirling Turbulent Flows: A Perpetual Challenge," AIAA Journal,40, 10, pp. 1984 1996 (2002).

Jawarneh A. M. and Vatistas G. H., "Reynolds Stress Model in the Prediction of Confined Turbulent Swirling Flows," Transaction of the ASME, Journal of Fluids Engineering, **128**, 6, pp. 1377-1382 (2006).

Khanna V. K., "A Study of the Dynamics of Laminar and Turbulent Fully and Partially Premixed Flames," PhD thesis, Virginia polytechnic institute and state university, (2001).

Kitoh S., "Experimental Study of turbulent swirling flow in a straight pipe," JFM, **225**, pp. 445-479, (1991).

Lam H. C., "An Experimental Investigation and Dimensional Analysis of Confined Vortex Flows," PhD thesis, Concordia University, Quebec, Canada, (1993).

Leibovich S., "Vortex stability and breakdown - Survey and extension," AIAA Journal, 22, 9 (1984).

Leschziner M. A., and Rodi W., "Calculation of Annular and Twin Parallel Jets Using Various Discretization Schemes and Turbulence-Model Variations," ASME J. Fluids Eng., **103**, pp. 352–360 (1981).

Leschziner M. A., 'Hybrid RANS-LES Methods, Strategies, Variants, Strengths, Weaknesses," Lecture in ERCOFTAC-Best Practice Guidance Course Series, Munich Germany, (2010).

Litke B., "The influence of inlet angles in inlet ports on the scavenging process in two-stroke uniflow-scavenged engine," Trans. The built Environment, Marine Technology III, **45**, pp. 247-252 (1999).

Lucca-Negro O., O'Doherty T., "Vortex breakdown: a review," Prog. Energy Combust. Sci., 27, pp. 431–481 (2000).

Luweig H., Ergänzung zu der arbeit:"Stabilität der strömung in einem zylinderischen ringraum", Z. Flugwiss, **9**, 11, pp. 359-361 (1961).

Lübcke H., Schmidt S., Rung T. and Thiele F., "Comparison of LES and RANS for bluff-body flows," Journal of Wind Engineering and Industrial Aerodynamics, **89**, (2001).

MAN Diesel, Direct Communication with MAN DIESEL A/S personnel, 2010.

McGeorge H. D., "Marine Auxiliary Machinery," 7th edition, Butterworth-Heinemann, (1999).

Moene A. F., "Swirling Pipe Flow with Axial Strain: Experiment and Large Eddy Simulation," PhD thesis, Technical University of Eindhoven, (2003).

Najafi A. F., Saidi M. H., Sadeghipour M. S., Souhar M., "Numerical analysis of turbulent swirling decay pipe flow," International Communications in Heat and Mass Transfer, **32**, 5, pp. 627-638 (2005).

Nakagawa H., Kato S., Tateishi M., Adachi T., Tsujimura H., and Nakashima M., "Airflow in the Cylinder of a 2-Stroke Cycle Uniflow Scavenging Diesel Engine During Compression Stroke," JSME International Journal, 33-II, 3, pp. 591-598 (1990).

Nishimoto N. and Takeyuki K., "A Study on the Influence of Intel Angel and Reynolds Number on the Flow-Pattern of Uniflow Scavenging Air," SAE Transactions, **93**, (1984).

Novak F. and Sarpkaya T., " Turbulent Vortex Breakdown at High Reynolds Numbers," AIAA, **38**, 5, pp. 825-834 (2000).

Orszag S.A. and Yakhot V., "Renormalization-Group Analysis of Turbulence," Phys. Rev. Lett. 57, pp. 1722–1724 (1986).

Yakhot V. and Smith L.M., "The renormalization group, the ε-expansion and derivation of turbulence models," J. Sci. Comput., **7**, pp. 35–61 (1992).

Pani B.S. and Rajaratnam, N., "Swirling circular turbulent wall jets," IAHR Journal of Hydraulic Research, **14**, 2, pp. 145-154 (1976).

Parchen R. R. and Steenbergen W., "An Experimental and Numerical Study of Turbulent Swirling Pipe Flows," Journal of Fluids Engineering, **120**, pp. 54-61 (1998).

Pashtrapanska M., Jovanovic´ J., Lienhart H. and Durts F., "Turbulence Measurements in a Swirling Pipe Flow," Experiment in Fluids, **41**, pp. 813-827, (2006).

Pergolesi Flavio, "Scavenging flow in a model of two stroke Diesel engine," Masters Thesis, (2009).

Pevzner L. A., "Aspects of marine low-speed, cross-head diesel engine lubrication," Lubrication Engineering, ***54***, 6, pp. 16-21 (1998).

Pulkrabek, W. W., "Engineering fundamentals of the internal combustion engine," Pearson Prentice-Hall, (2003).

Rajaratnam N., "Turbulent Jets," Elsevier Publishing Co., Amsterdam and New York, (1976).

Raunek, "Uniflow & Loop Scavenging Procedure," article published online (www.brighthub.com), (2009).

Rocklage-Marliani G., Schmidts M. and Ram V.I.V., "Three-dimensional Laser-Dopp.ler Velocimeter Measurements in Swirling Turbulent Pipe Flow," Flow Turbulence and Combustion, **70**, pp. 43-67 (2003).

Schweitzer P. H., "Scavenging of two-stroke cycle diesel engines," The Macmillan Co., New York, N. Y., (1949).

Sturgess G. J. and Syed S. A., "Calculation of confined swirling flows," AIAA 23rd Aerospace Meeting, (1985).

Speziale C. G., Sarkar S. and Gatski T. B.,"Modelling the Pressure-Strain Correlation of Turbulence: An Invariant Dynamical Systems App.roach,"JFM, **227**, pp. 245-272 (1991).

Sarpkaya, T., "Effect of the Adverse Pressure Gradient on Vortex Breakdown," AIAA Journal, **12**, pp. 602-607 (1974).

Sarpkaya T., "Turbulent Vortex Breakdown," Physics of Fluids, **7**, 10, pp. 2301–2303 (1995).

Saric W.S., "Görtler Vortices," Annual Review of Fluid Mechanics, **26**: pp. 379-409 (1994).

Saffman P. G., "Vortex Dynamics," Cambridge University Press, (1995).

Senoo Y., Kawaguchi W. and Nagata T., "Swirl Flow in Conical Diffusers," Bulletin of the JSME, **21**, 112 (1978).

Sloan D., Smith P. and Smoot L., "Modeling of swirl in turbulent flow systems," Prog. Energ. Combust. Sci., **12,** pp. 163–250 (1986).

Steenbergen W. and Voskamp J., "The rate of decay of swirl in turbulent pipe flow," Flow measurement and instrumentation, **9**, pp. 67-78, (1998).

Schnipp.er T., Researcher at DTU MEK, direct correspondence, (2010).

Spencer A., Dunham D., McGuirk J.J., and Dianat M., "Comparison of Unsteady Reynolds Averaged Navier–Stokes and Large Eddy Simulation Computational Fluid Dynamics Methodologies for Air Swirl Fuel Injectors," J. Eng. Gas Turbines Power, **131**, 1, (2009).

The American Heritage® Dictionary of the English Language, Fourth Edition copyright© 2000 by Houghton Mifflin Company. Updated in 2009.

Vanyo J. P., "Rotating Fluids in Engineering and Science," Dover re-print Edition, (2001).

Velte C.M., Okulov V.L. and Hansen M.O.L., "Explosion of helical vortex core without a change of the flow topology," Article ready to be published (2010).

Velte C.M., Okulov V.L. and Hansen M.O.L., "Helical structure of longitudinal vortices embedded in turbulent wall-bounded flow," J. Fluid Mechanics, **616**, pp. 167-177 (2009).

Woodyard D., "Pounder's Marine Diesel Engines and Gas Turbines," 9th Edition, Butterworth-Heinemann, (2009).

Wu J., Ma H., Ming-De Z., "Vorticity and Vortex Dynamics," Springer, (2006).

Xia J.L., Smith B.L., Benim A.C., Schmidli J. and Yadigaroglu G., "Effect of inlet and outlet boundary conditions on swirling flows," Computers and Fluids, **26**, 8, pp. 811-823 (1997).

Yan L., Vatistas G. H. and Lin S., "Experimental studies on turbulence kinetic energy in confined vortex flows," Journal of Thermal Science, **9**, 1, pp.10-22 (2000).

Yazdabadi P.A., Griffiths A.J. and Syred N., "Investigations into the precessing vortex core phenomenon in cyclone dust separators," Proc. Instn. Mech. Engrs, 208, pp. 147-154 (1994).

Young A. D. and Rao K. N., "Some Low Speed Experimental Results on the Effects of Swirl and Velocity Distribution on an Axi-symmetric Jet", Aeronautical Quarterly, **29**,4, pp. 370-384 (1978).

Wikipedia article, "Vortex", Wikipedia Project page (http://en.wikipedia.org/wiki/Vortex), 10 June 2010.

Appendix A

A.1 PIV Experimental Results (L = 4D)

A.1.1 *Mean Velocity Field*

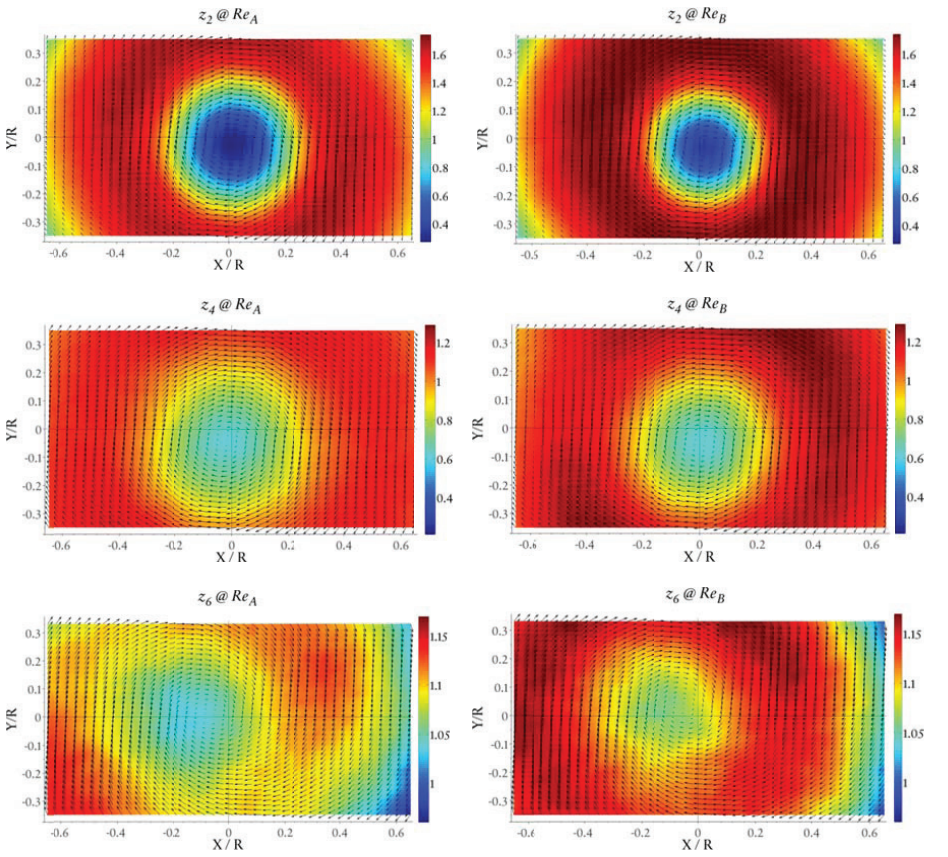

A.1.2 *Mean Axial Vorticity*

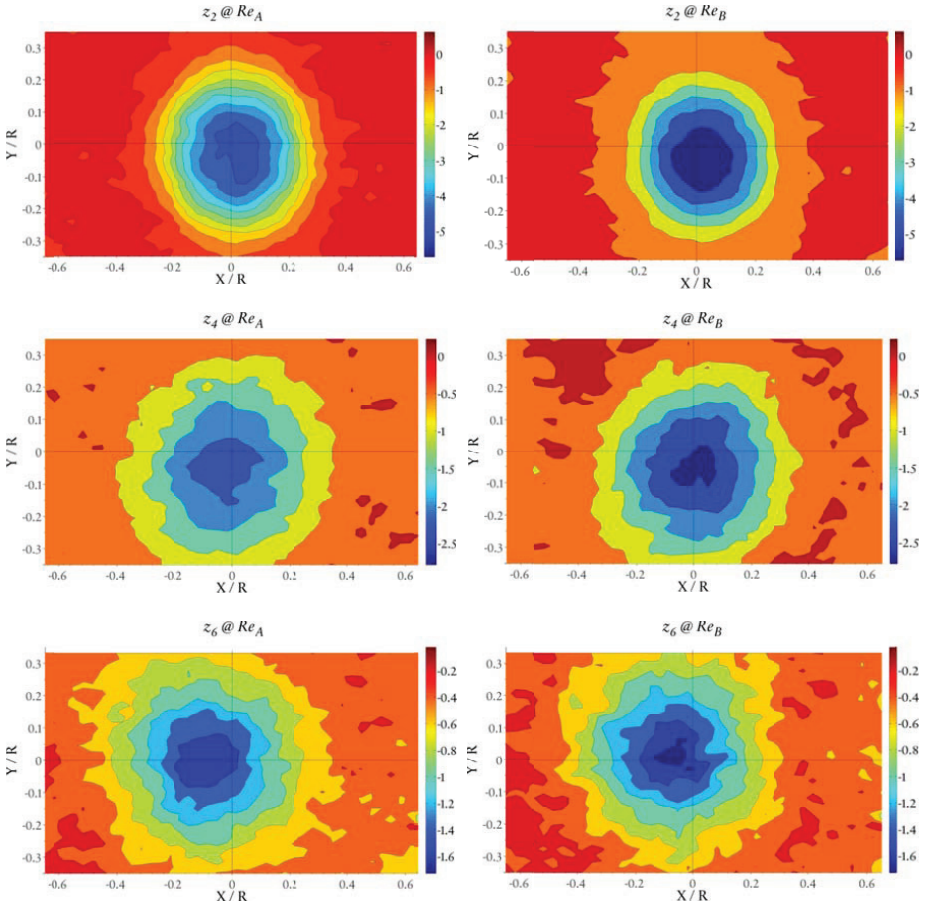

A.1.3 *Reynolds Normal Stress* $\overline{u'u'}$

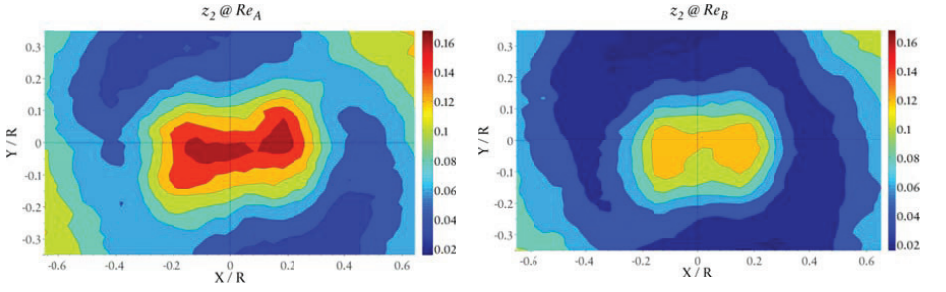

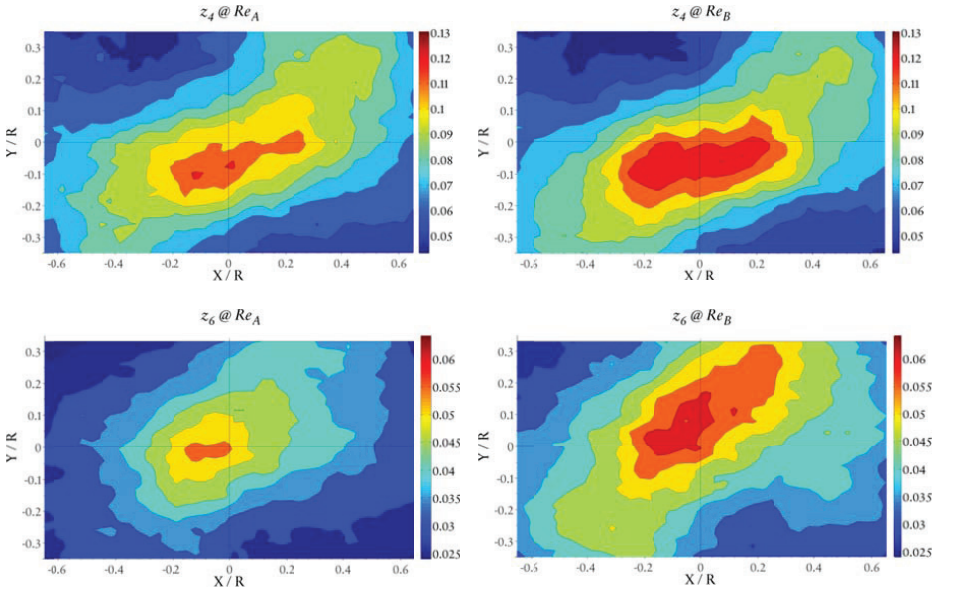

A.1.4 *Reynolds Normal Stress* $\overline{v'v'}$

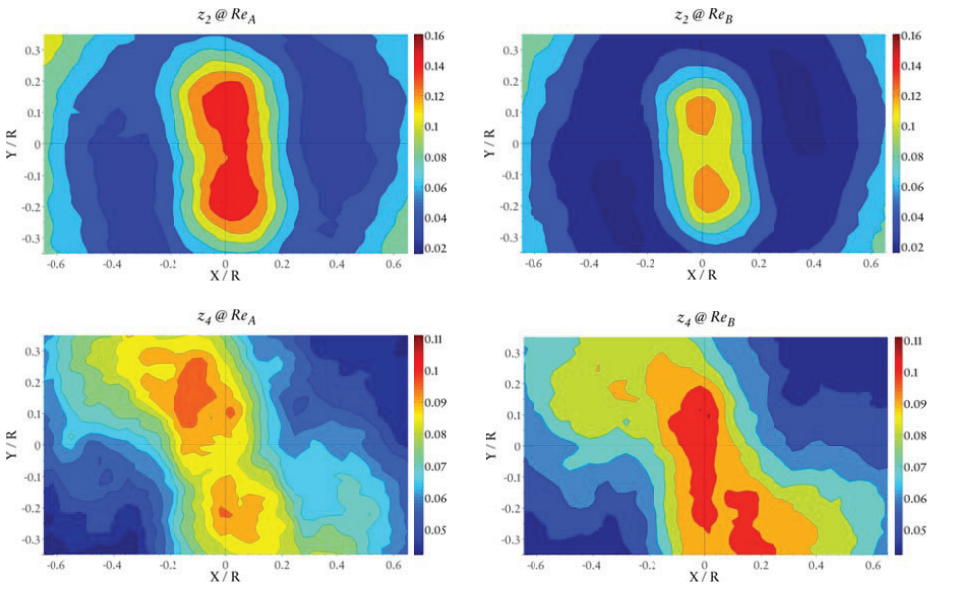

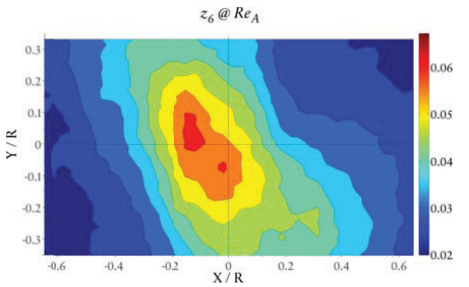

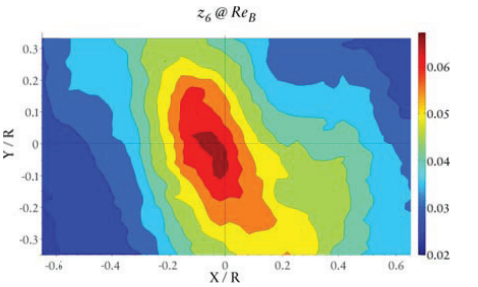

A.1.5 *Reynolds Normal Stress* $\overline{w'w'}$

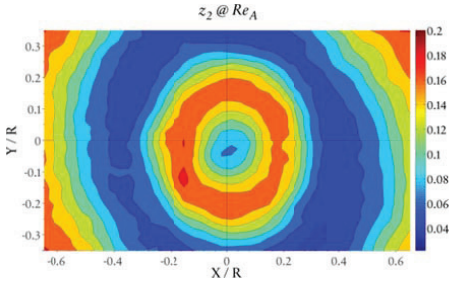

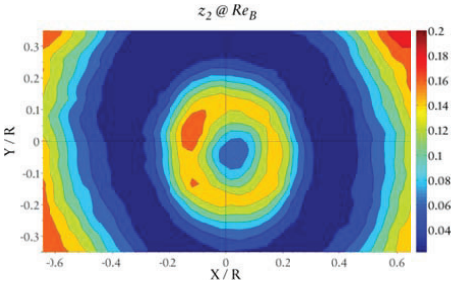

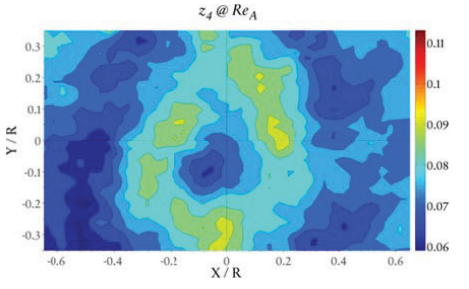

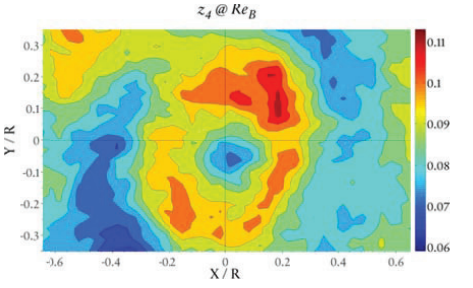

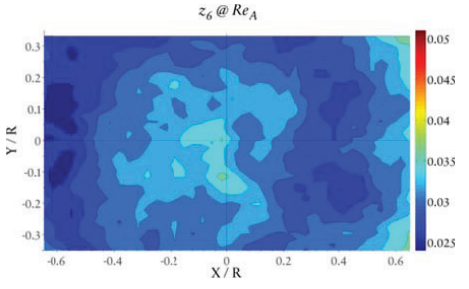

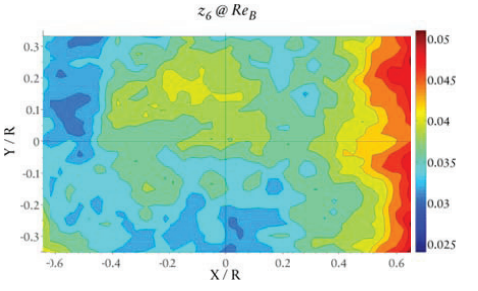

A.1.6 *Reynolds Shear Stress* $\overline{u'v'}$

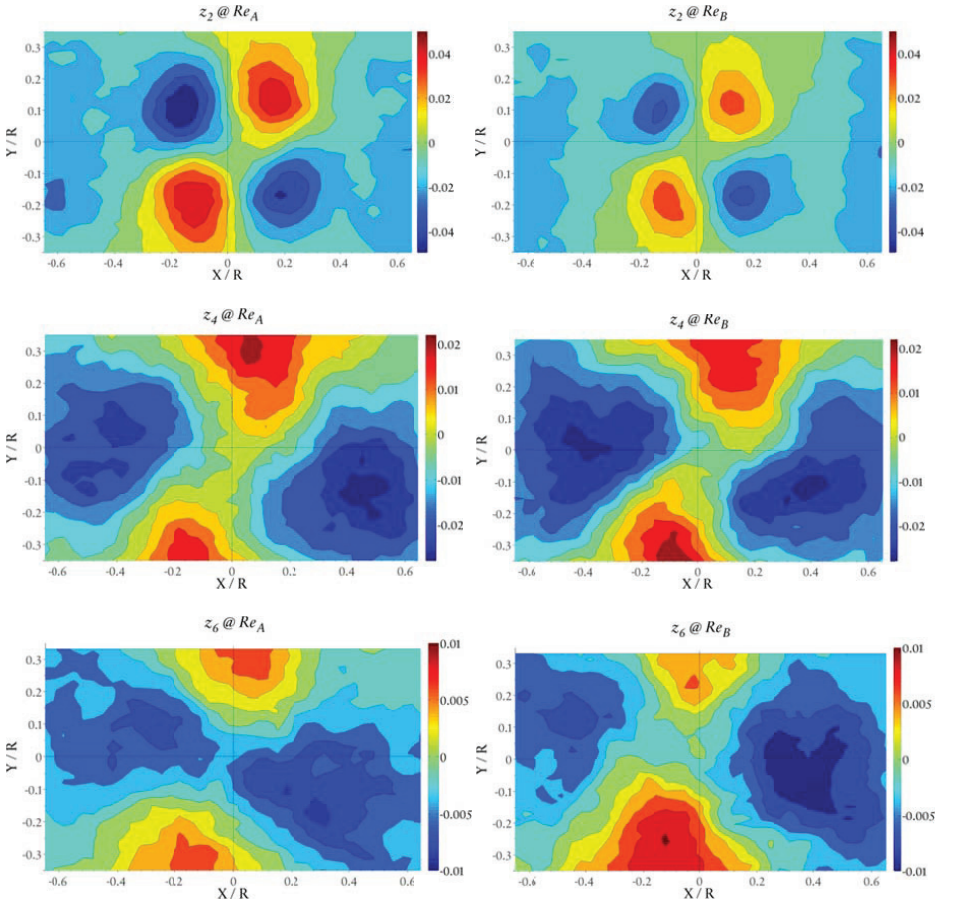

A.1.7 *Reynolds Shear Stress* $\overline{u'w'}$

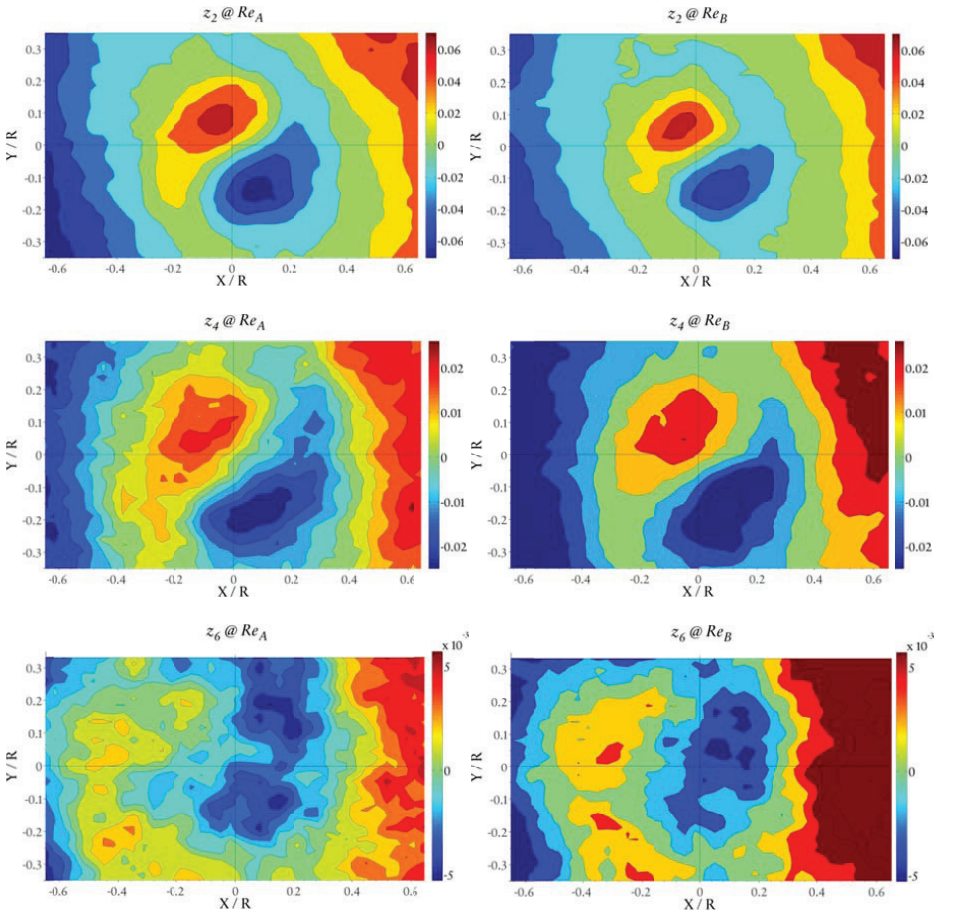

A.1.8 *Reynolds Shear Stress* $\overline{v'w'}$

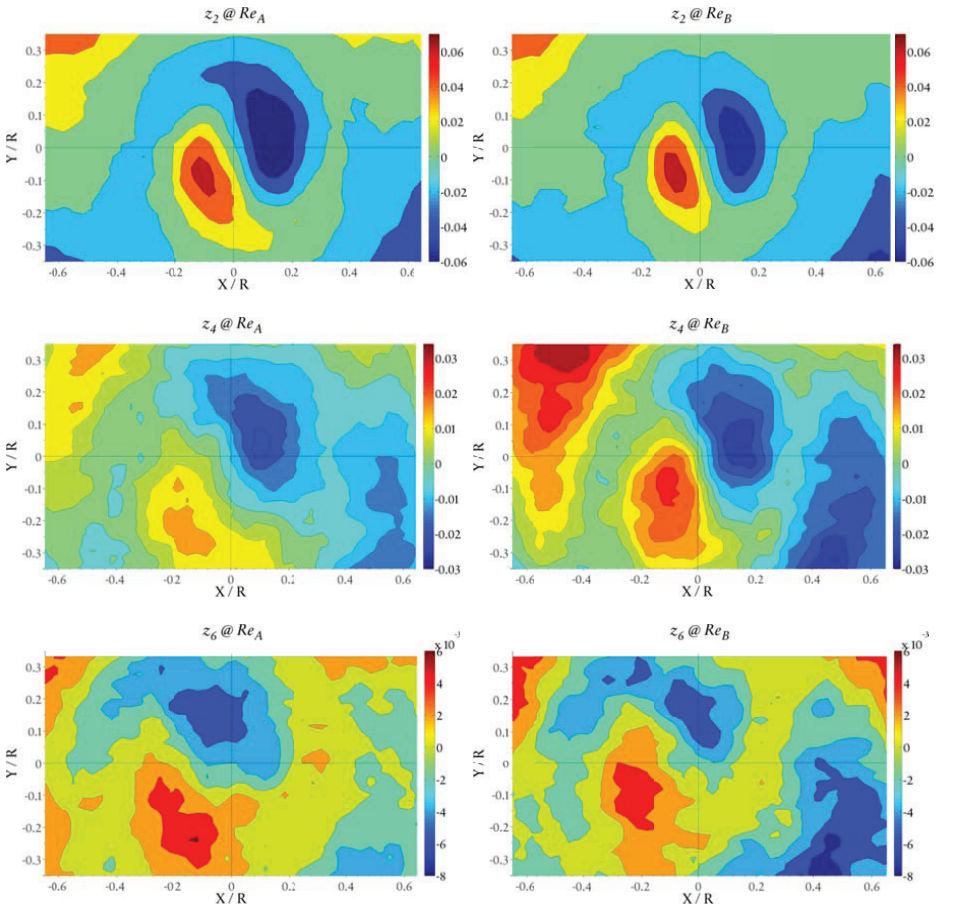

A.1.9 *Average Turbulent Kinetic Energy*

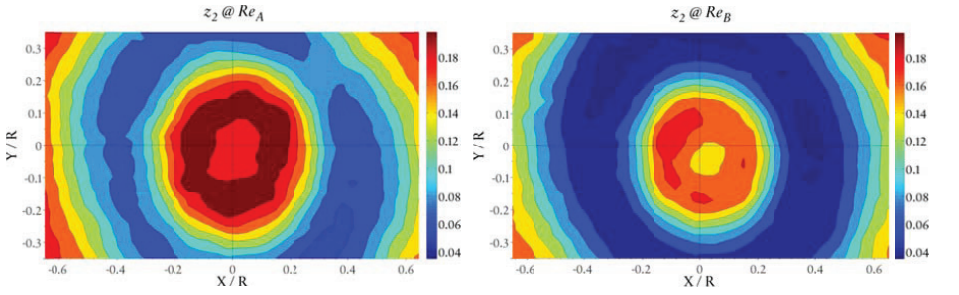

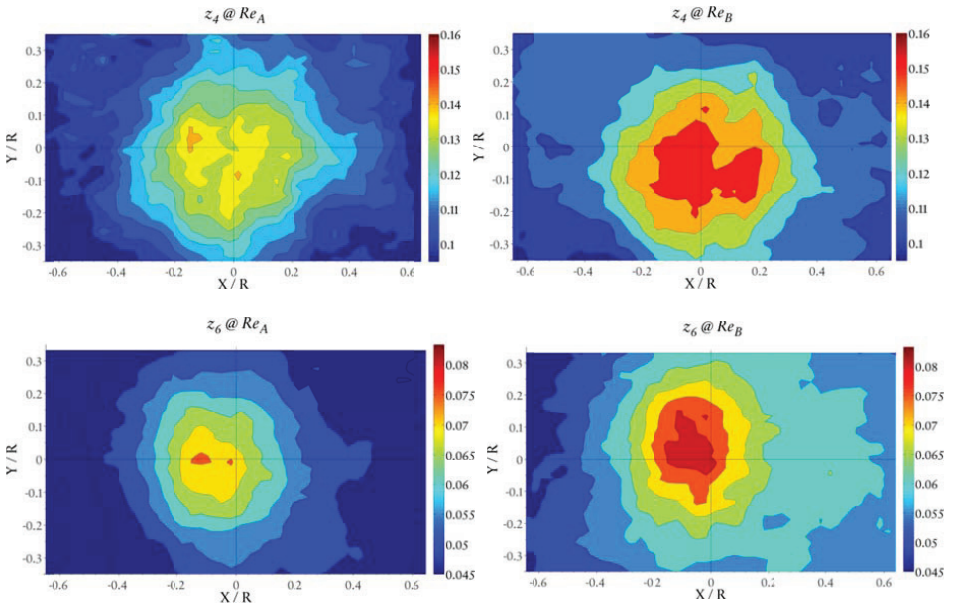

A.2 *PIV Experimental Results (L = 8D)*

A.2.1 *Mean Velocity Field*

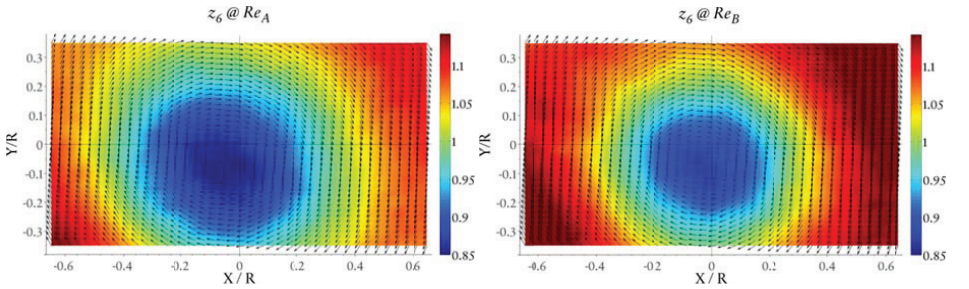

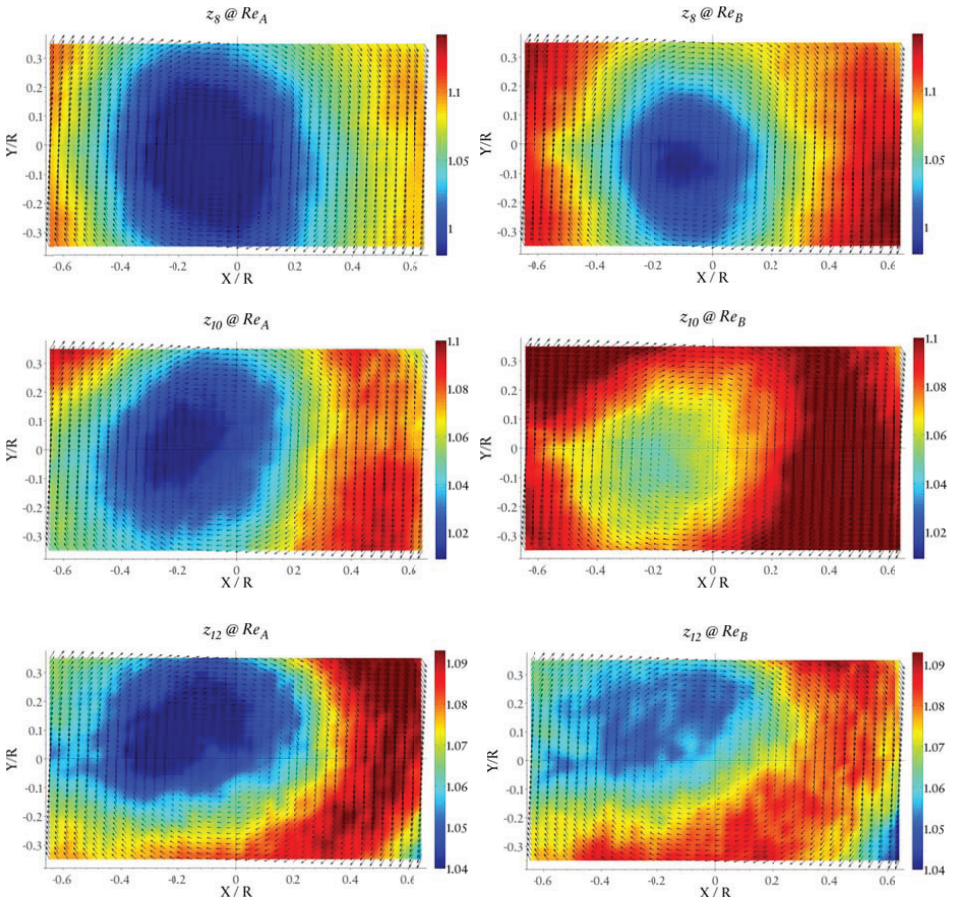

A.2.2 *Mean Axial Vorticity*

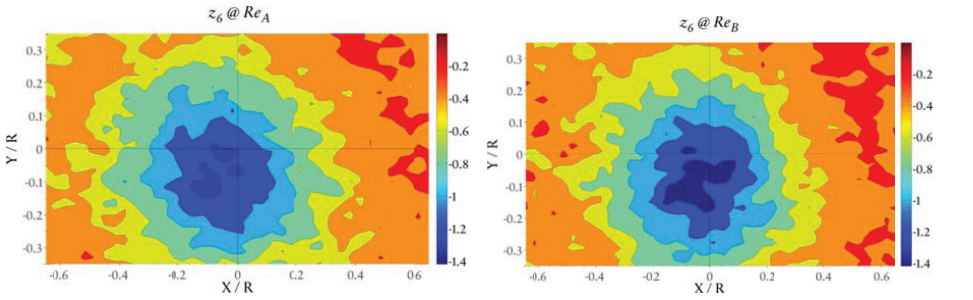

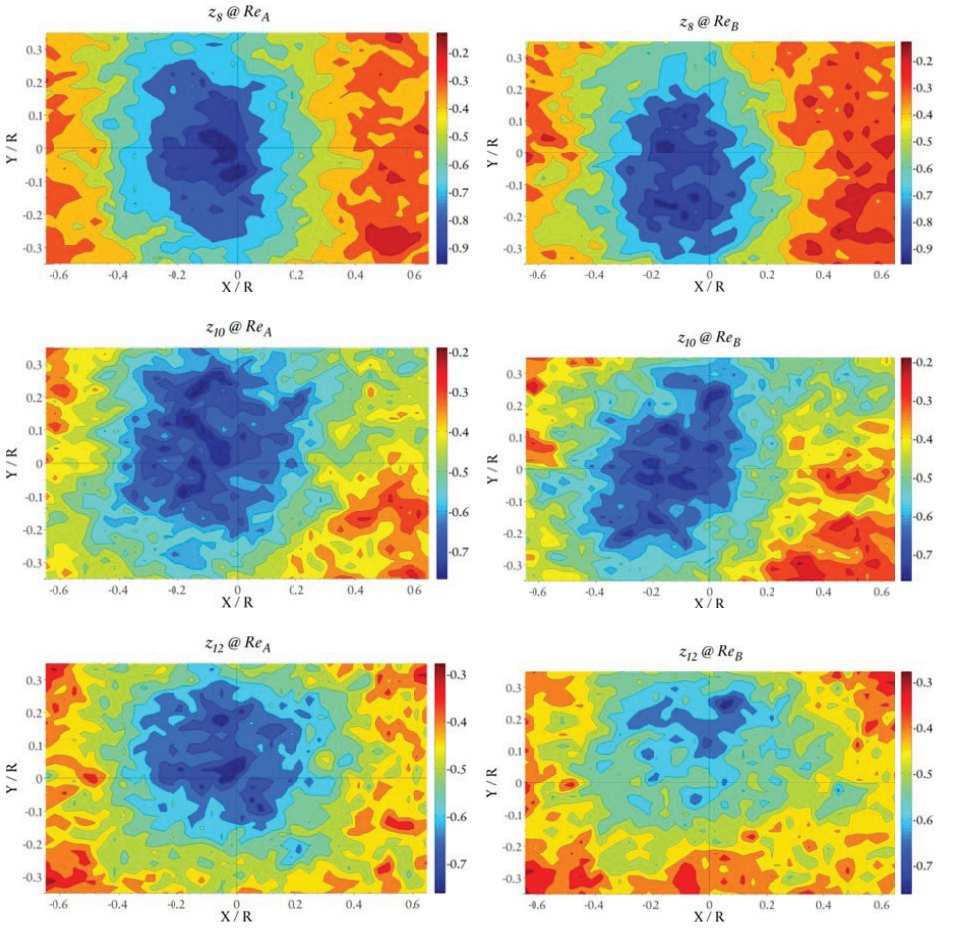
z_8 @ Re_A
z_8 @ Re_B
z_{10} @ Re_A
z_{10} @ Re_B
z_{12} @ Re_A
z_{12} @ Re_B
Y / R
X / R

A.2.3 *Reynolds Normal Stress* $\overline{u'u'}$

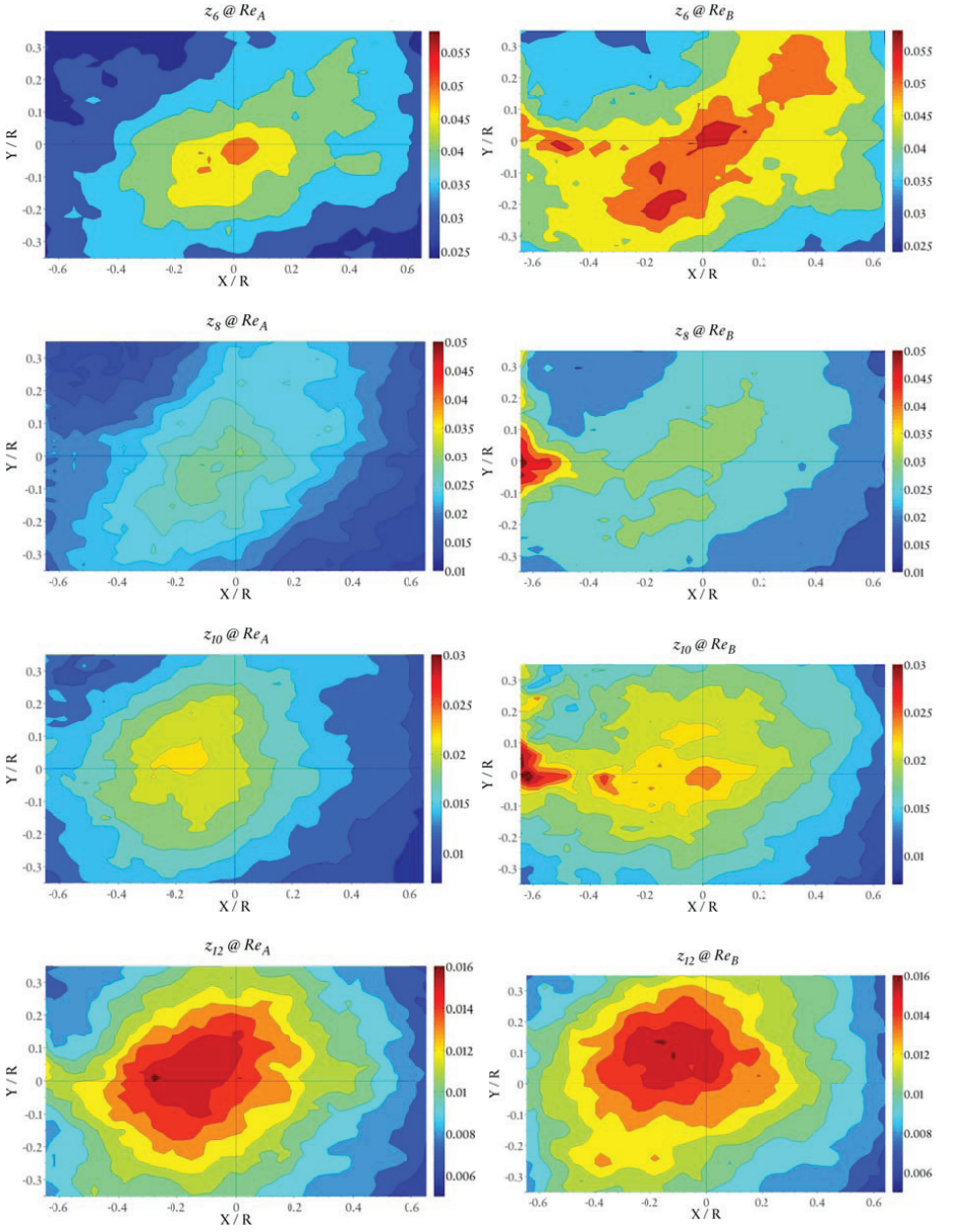

A.2.4 *Reynolds Normal Stress* $\overline{v'v'}$

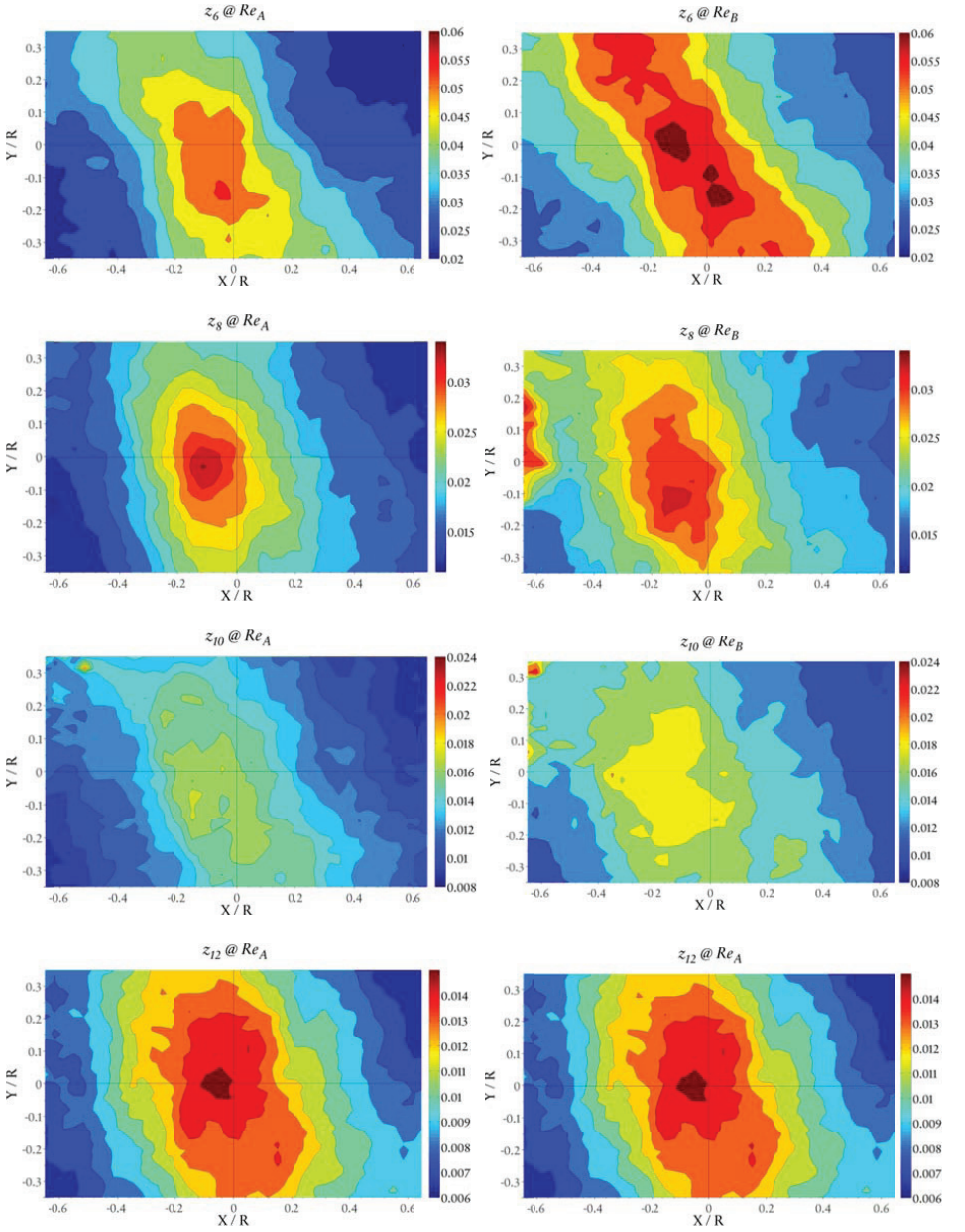

A.2.5 *Reynolds Normal Stress* $\overline{w'w'}$

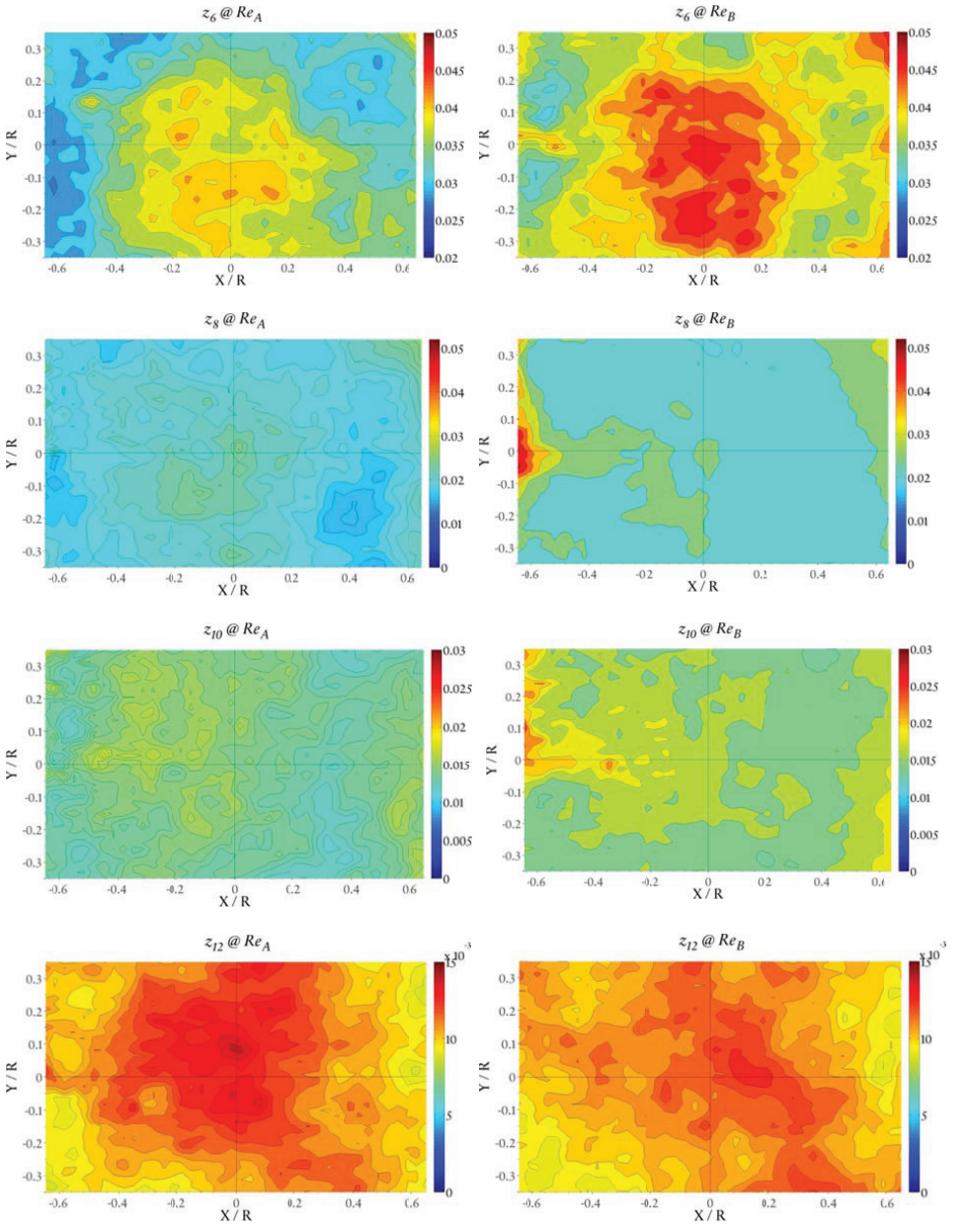

A.2.6 *Reynolds Shear Stress* $\overline{u'v'}$

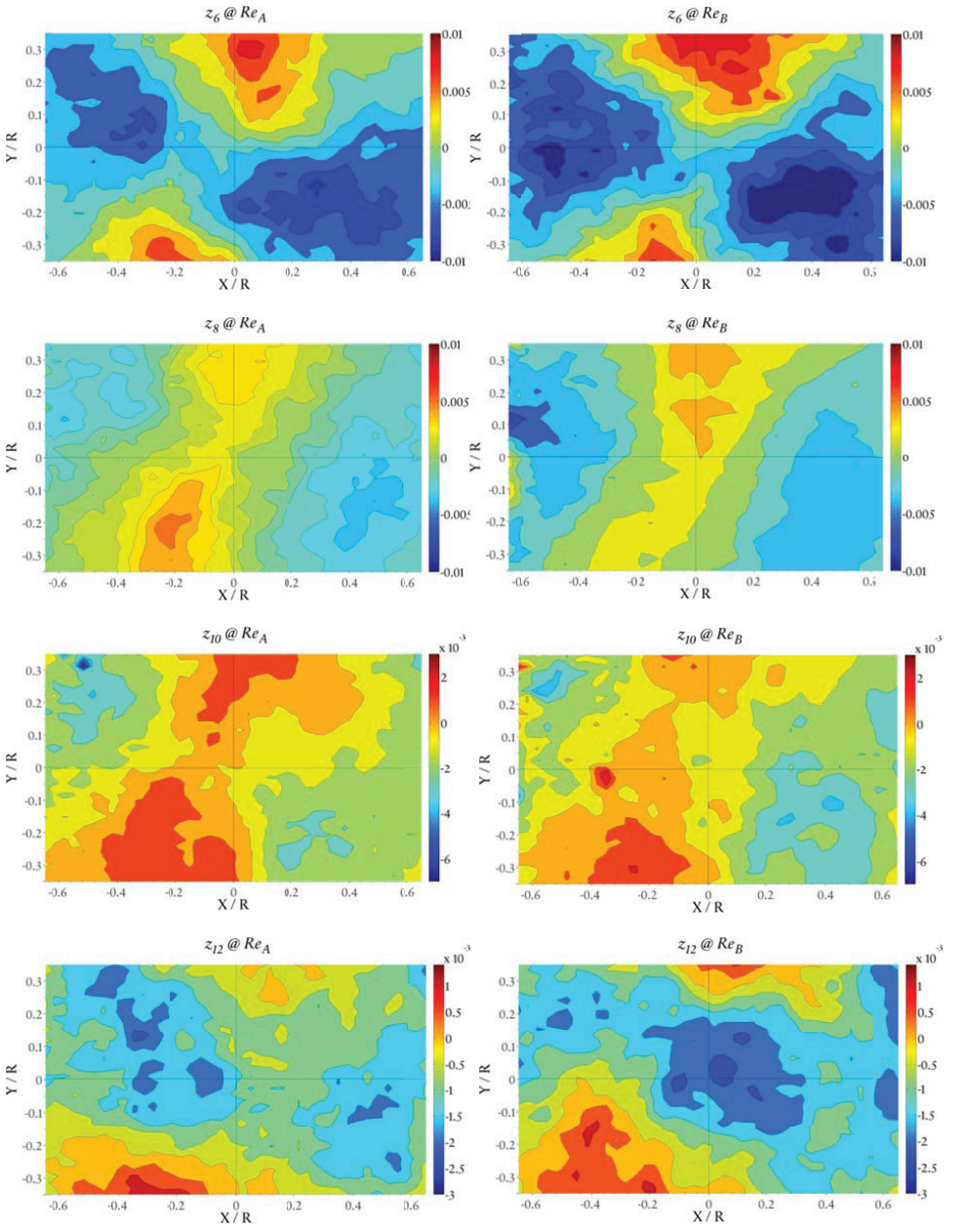

A.2.7 *Reynolds Shear Stress* $\overline{u'w'}$

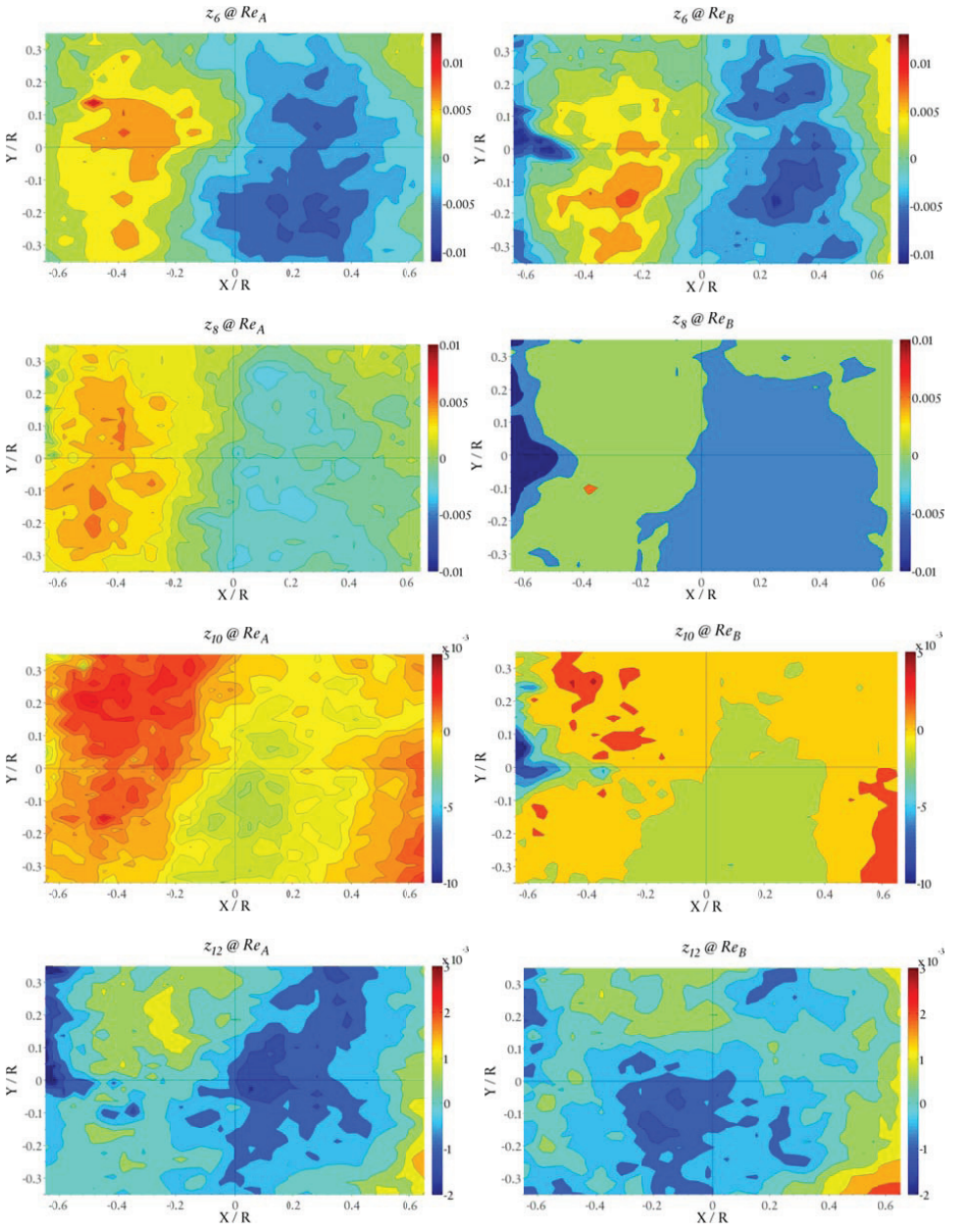

A.2.8 *Reynolds Shear Stress* $\overline{v'w'}$

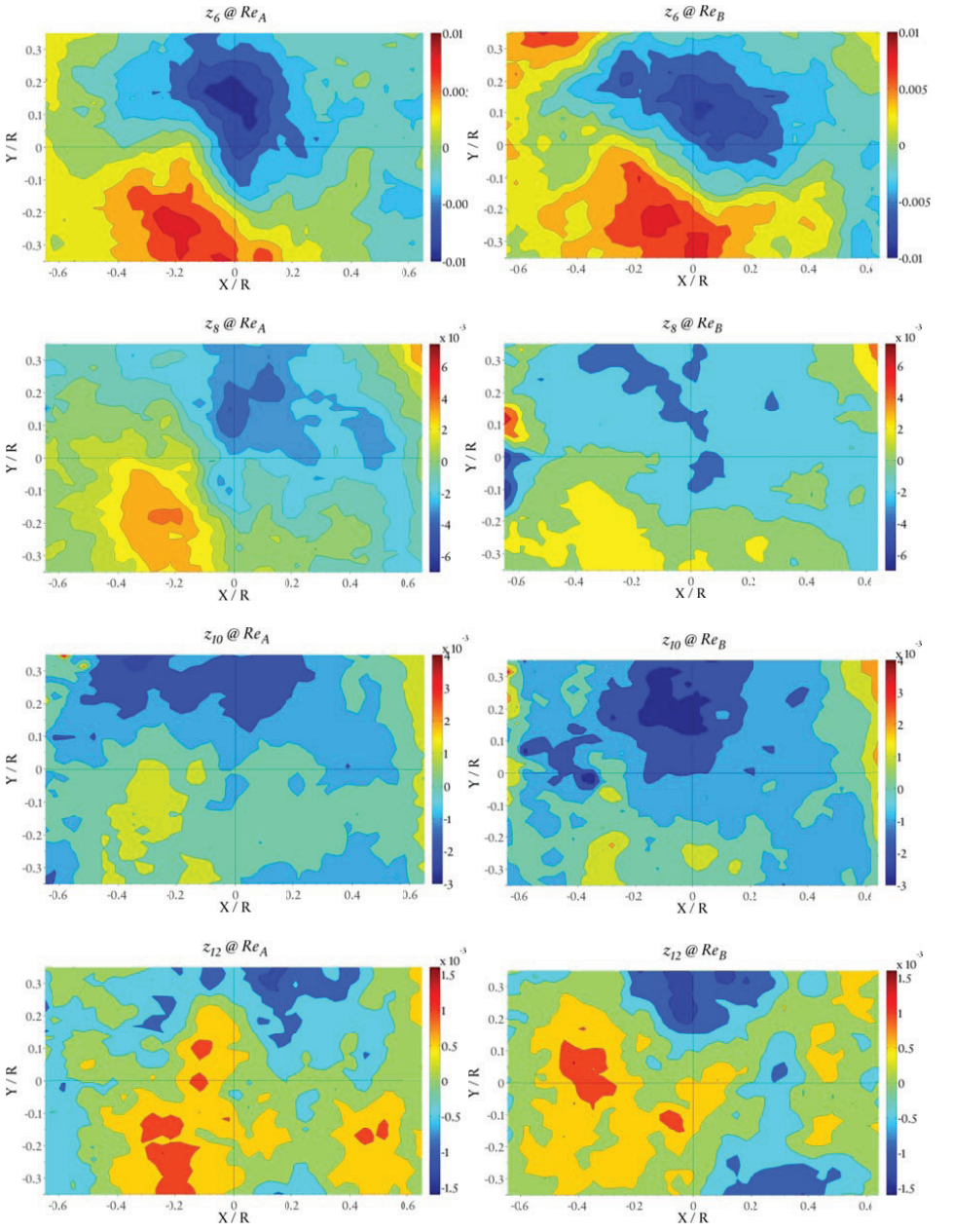

A.2.9 *Average Turbulent Kinetic Energy*

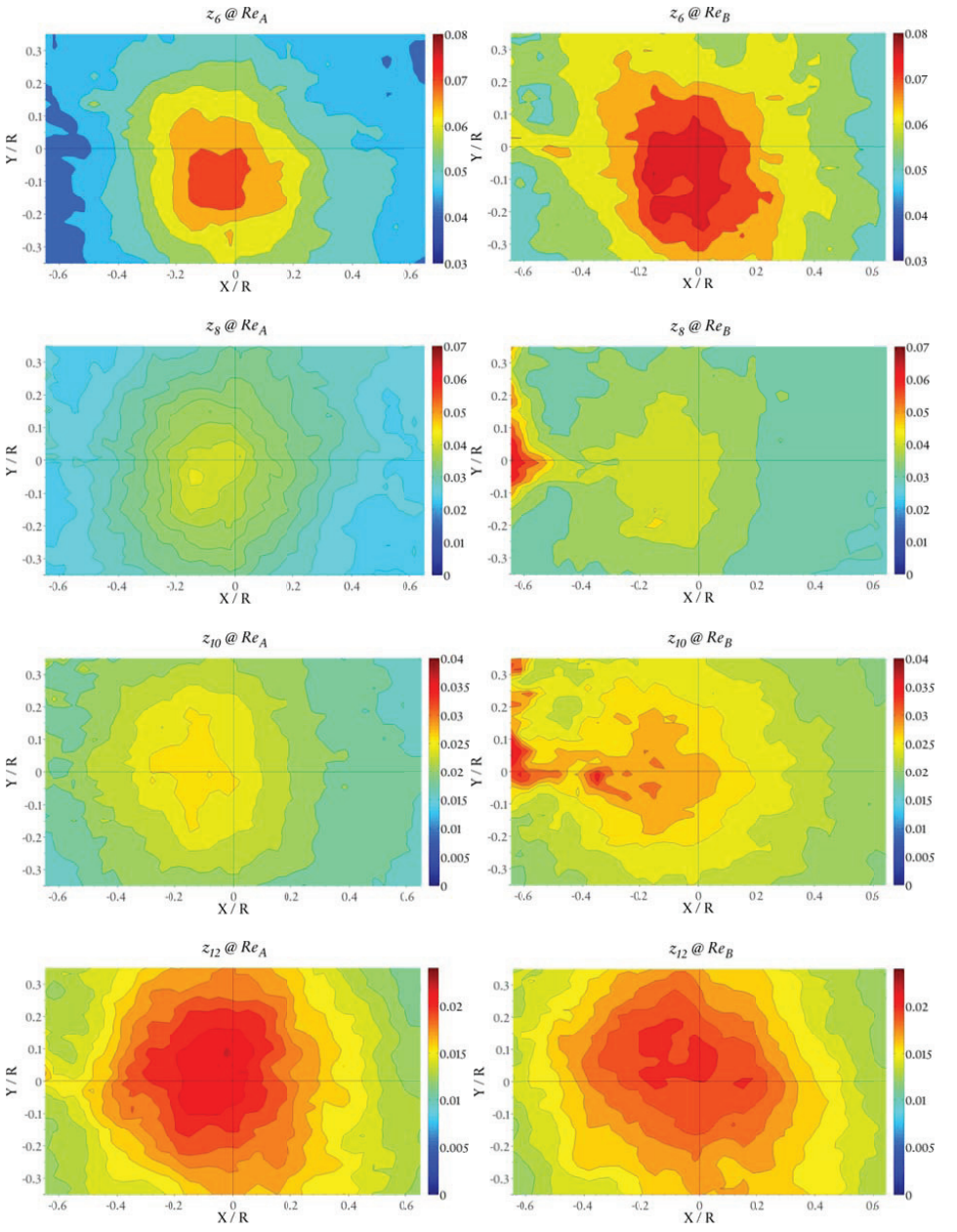

Appendix B

B.1 PIV Experimental Results (Port Closure 25%)

B.1.1 *Mean Velocity Field*

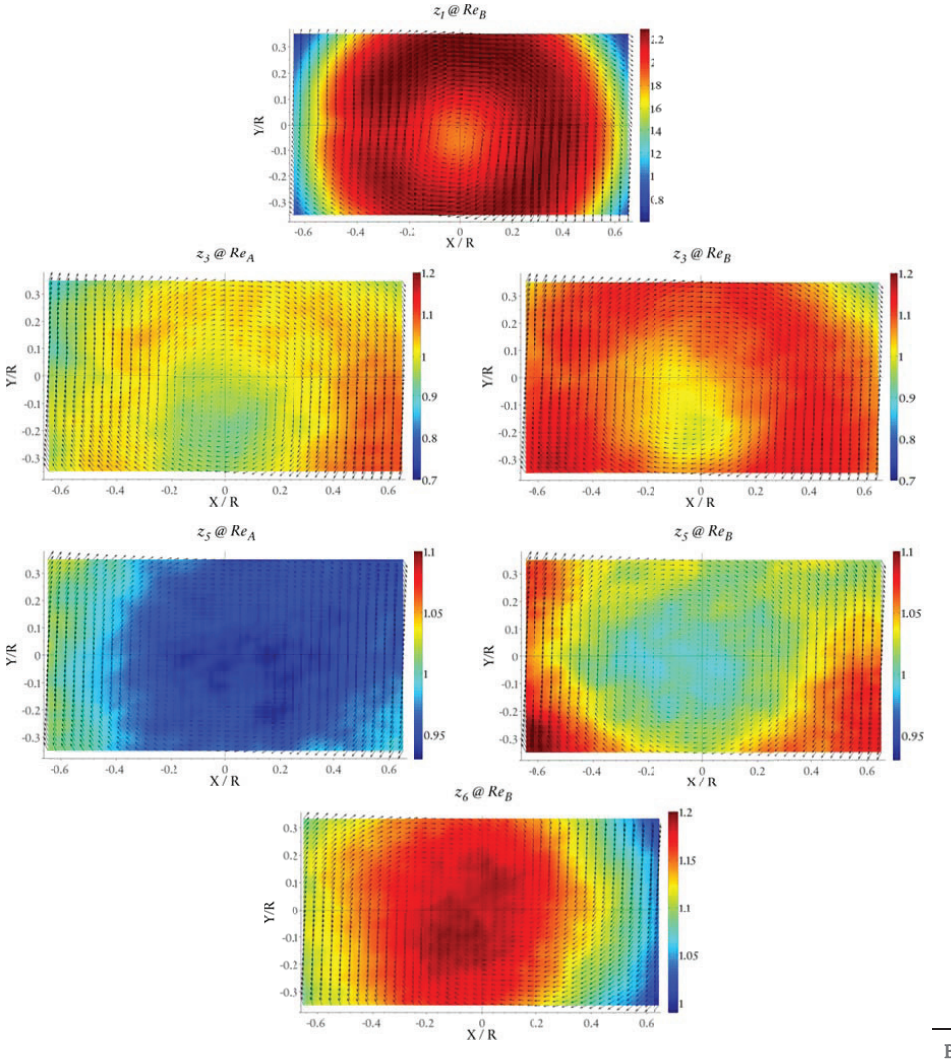

B.1.2 *Mean Axial Vorticity*

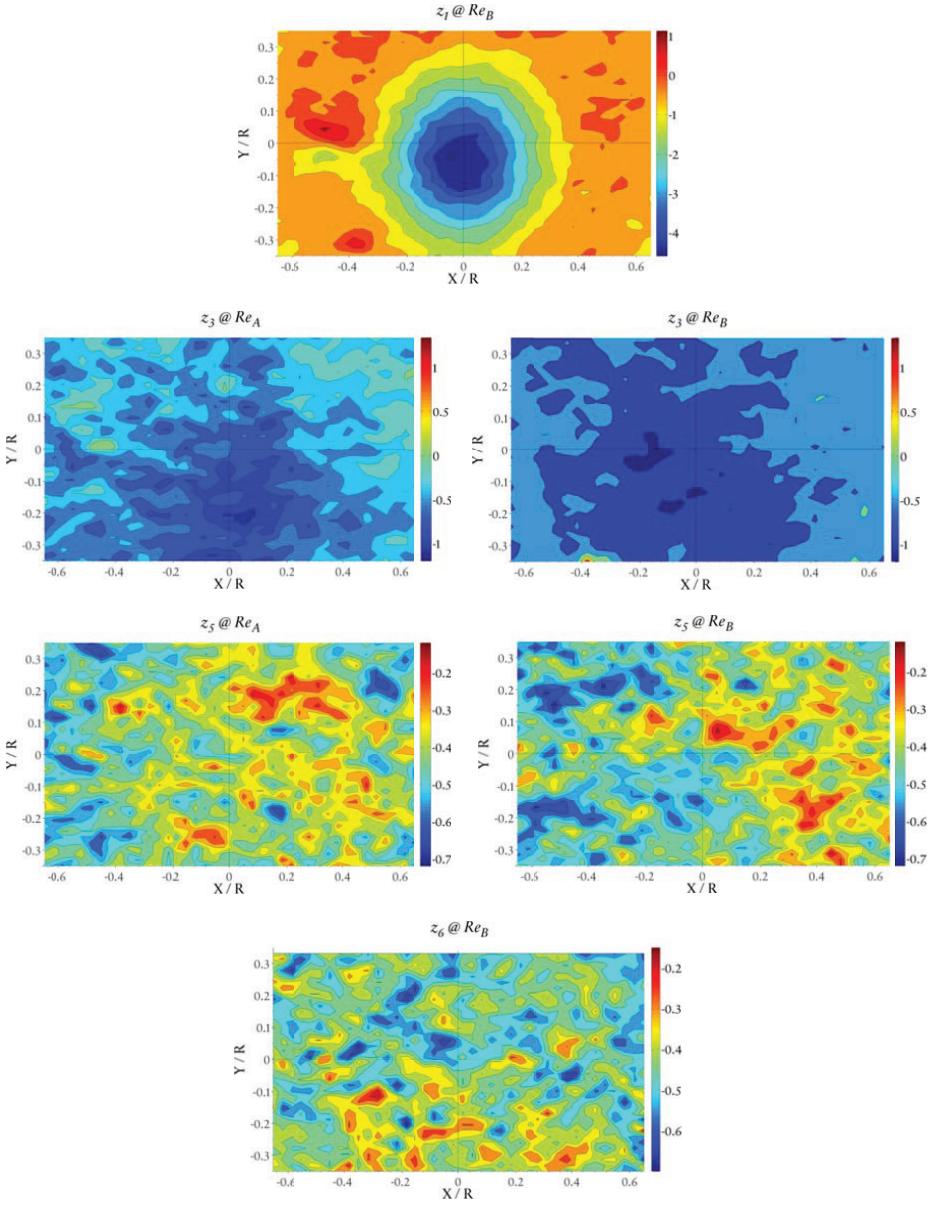

B.1.3 *Reynolds Normal Stress* $\overline{u'u'}$

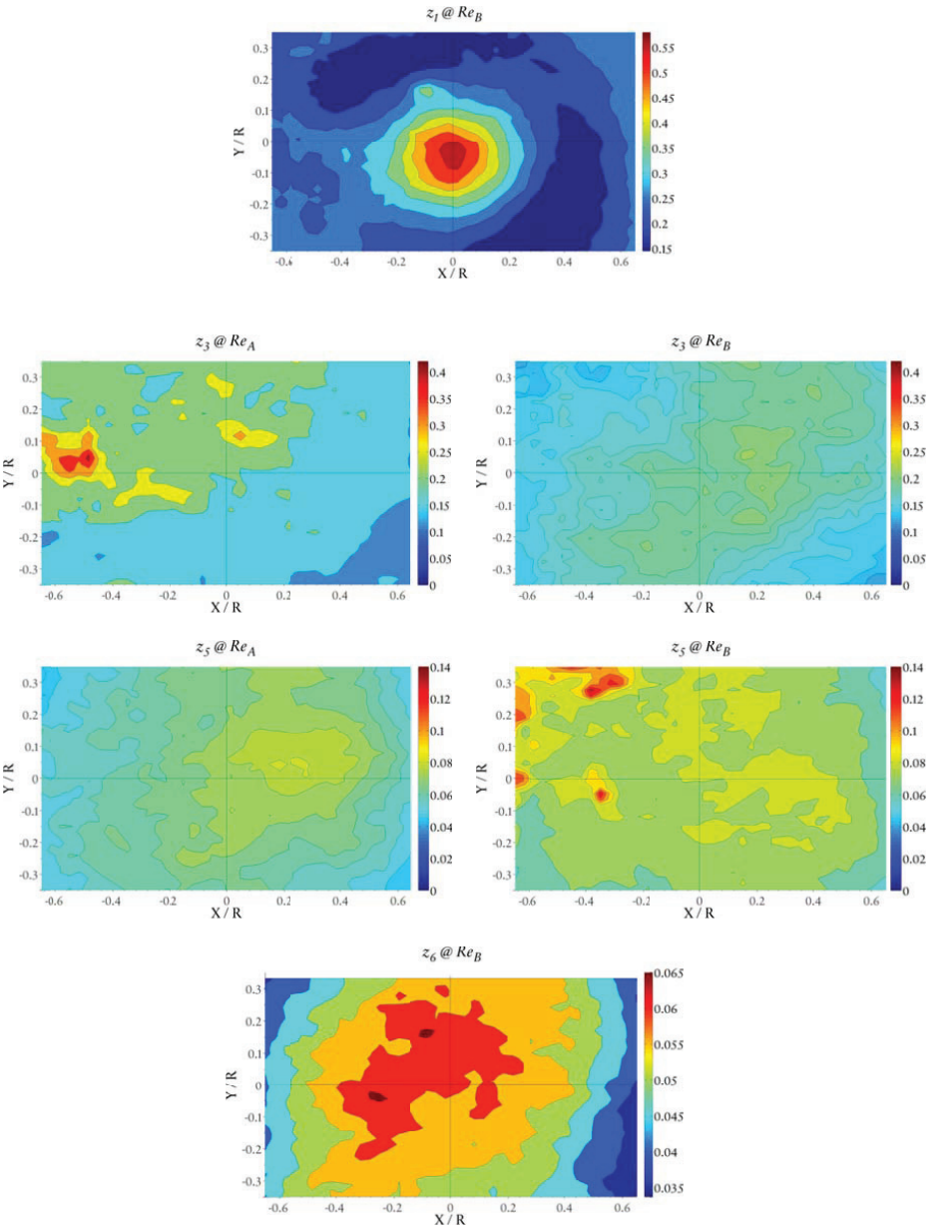

B.1.4 *Reynolds Normal Stress* $\overline{v'v'}$

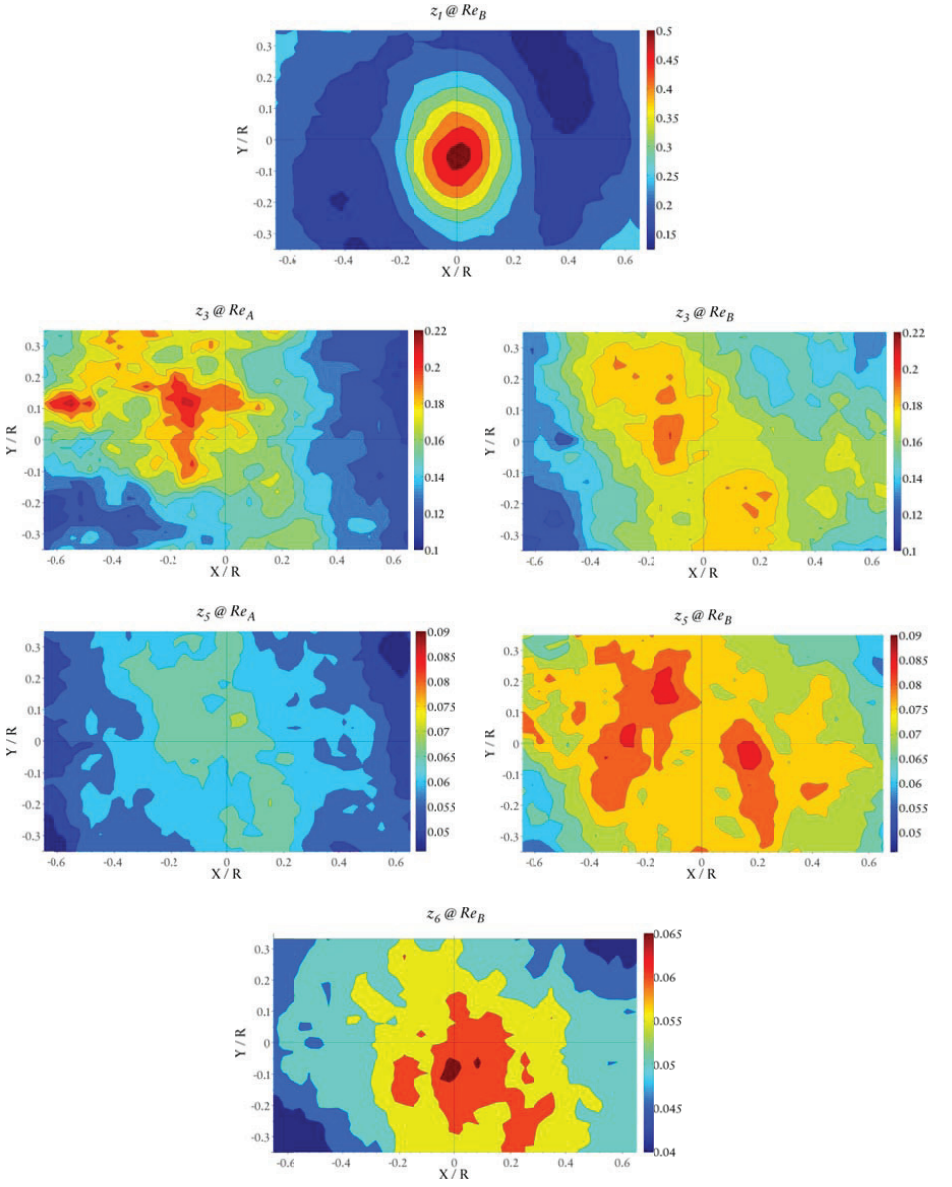

B.1.5 *Reynolds Normal Stress* $\overline{w'w'}$

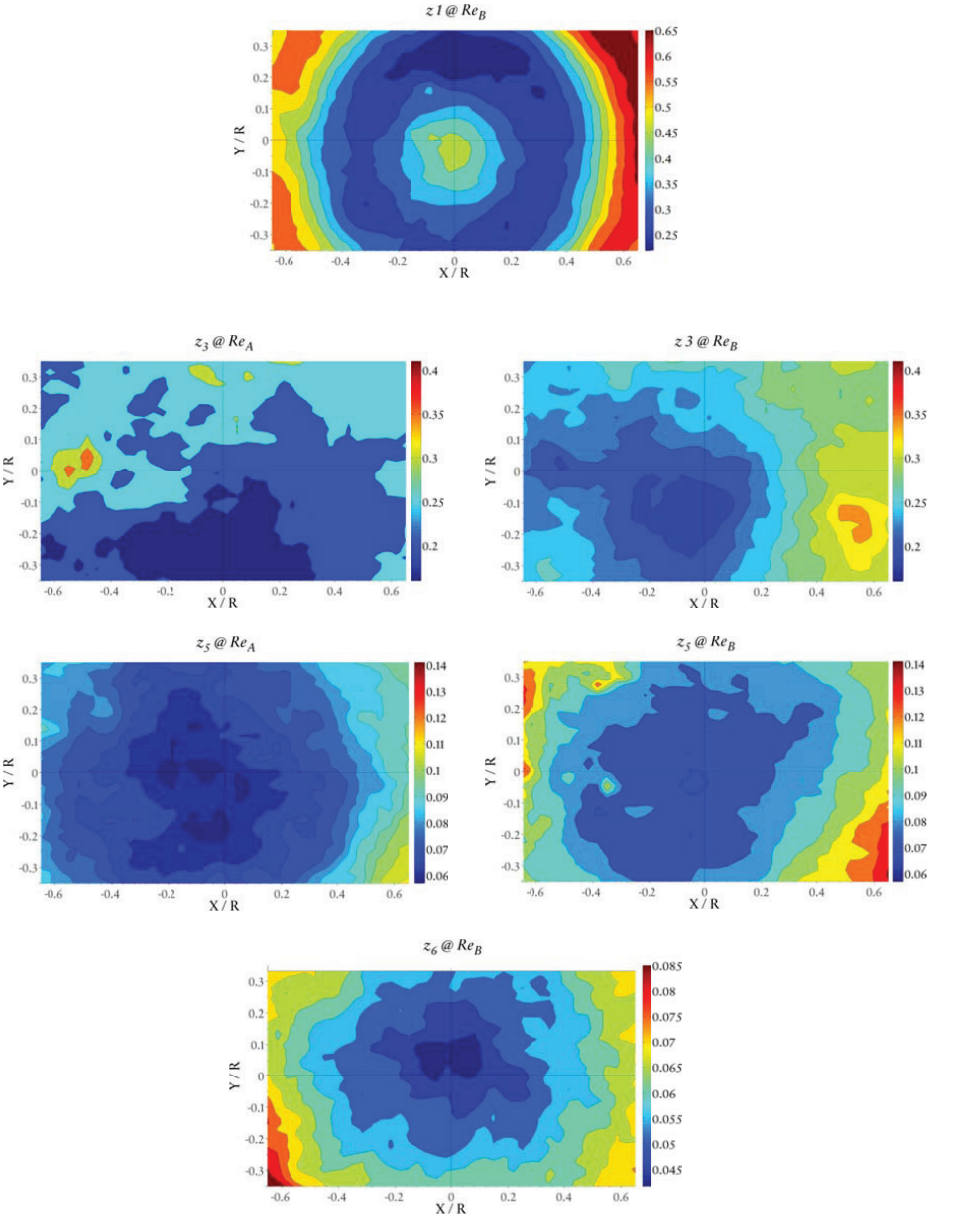

B.1.6 *Reynolds Shear Stress* $\overline{u'v'}$

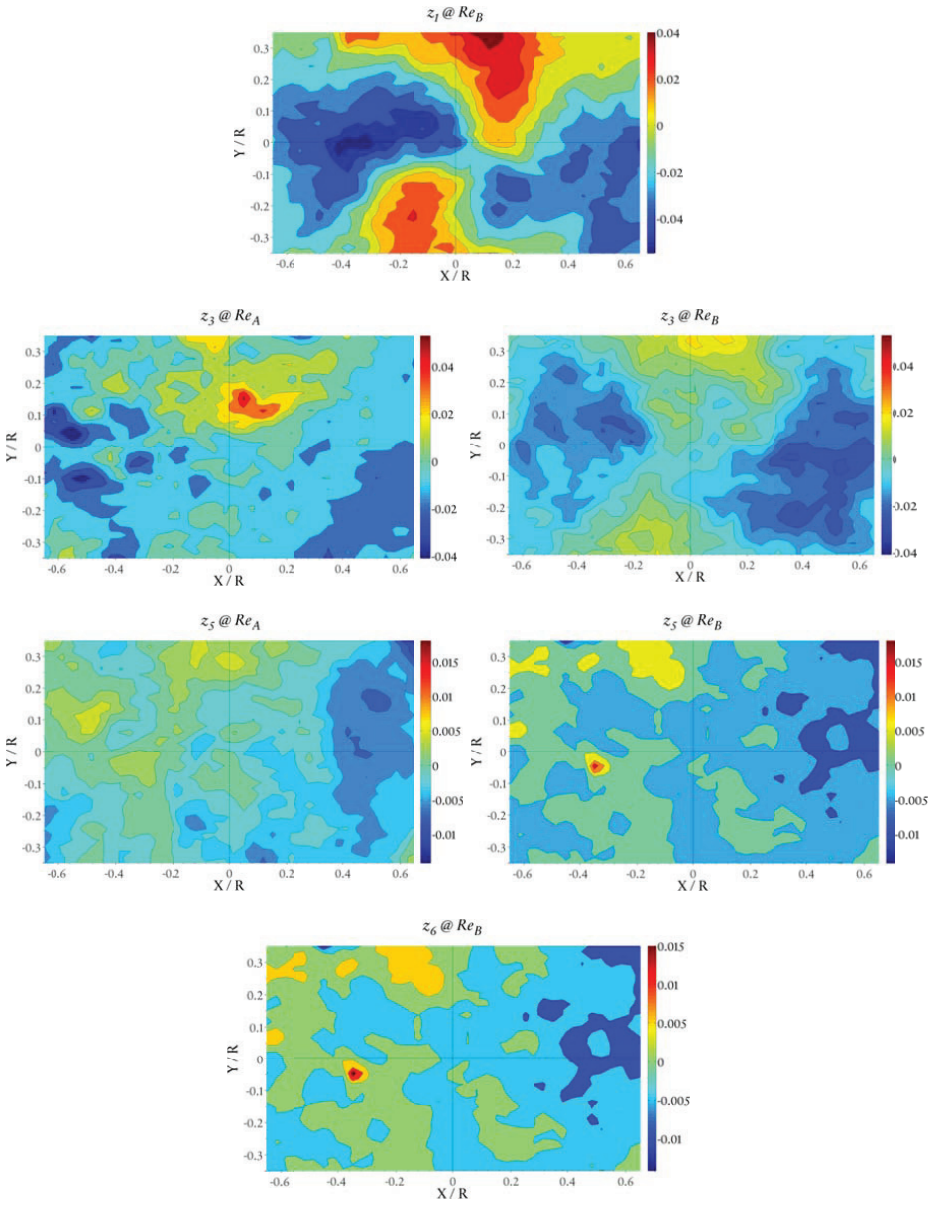

B.1.7 *Reynolds Shear Stress* $\overline{u'w'}$

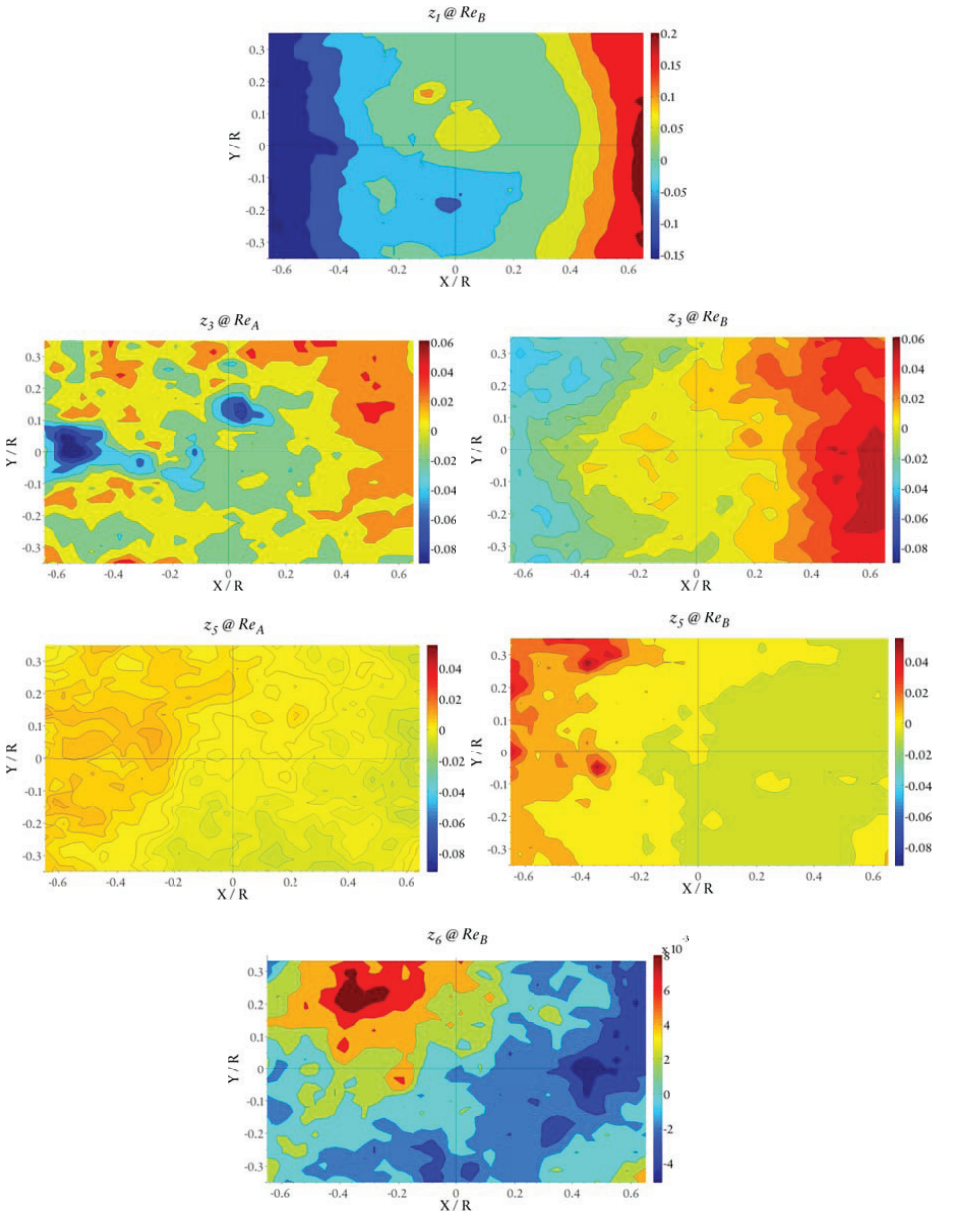

B.1.8 *Reynolds Shear Stress* $\overline{v'w'}$

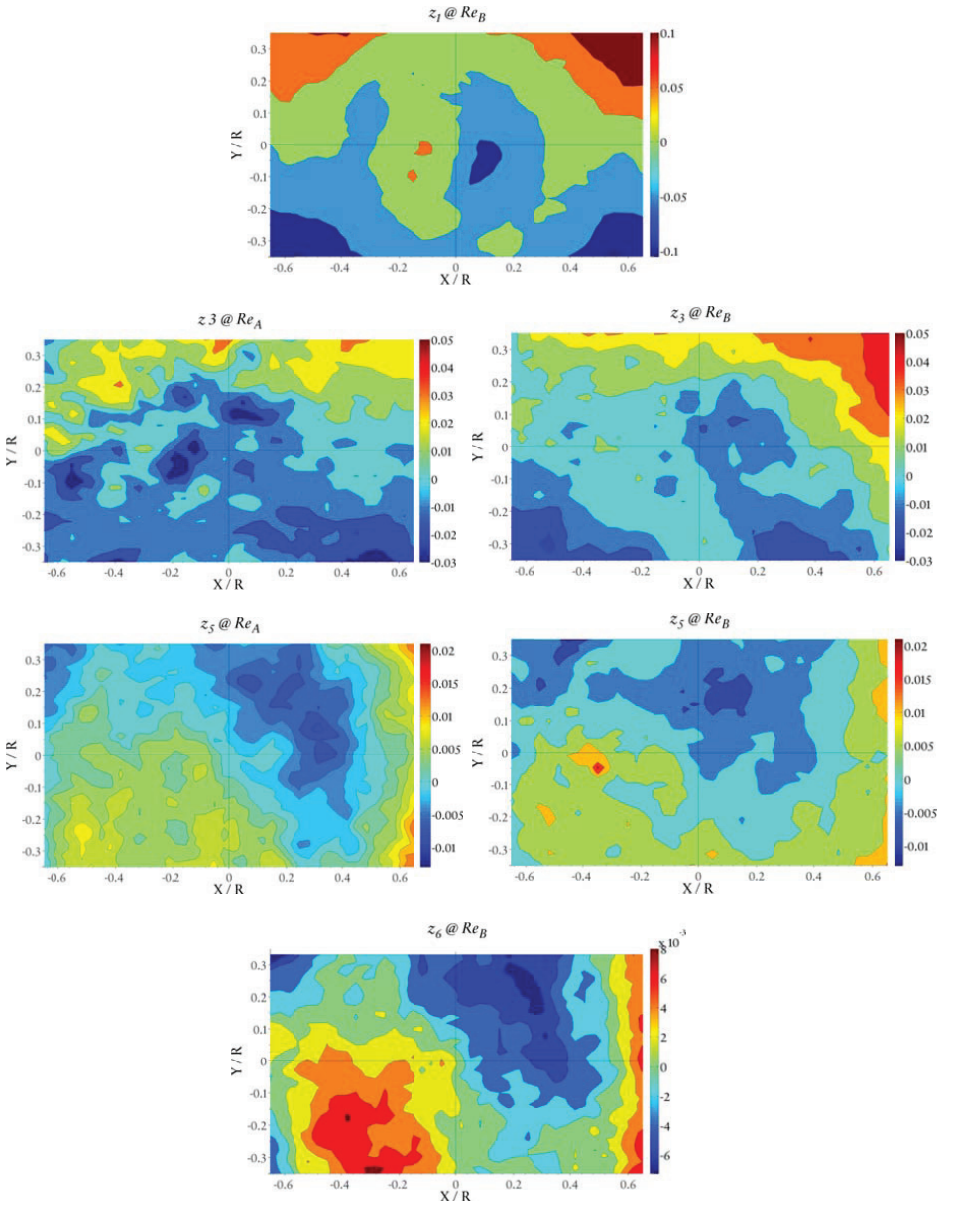

B.1.9 *Average Turbulent Kinetic Energy*

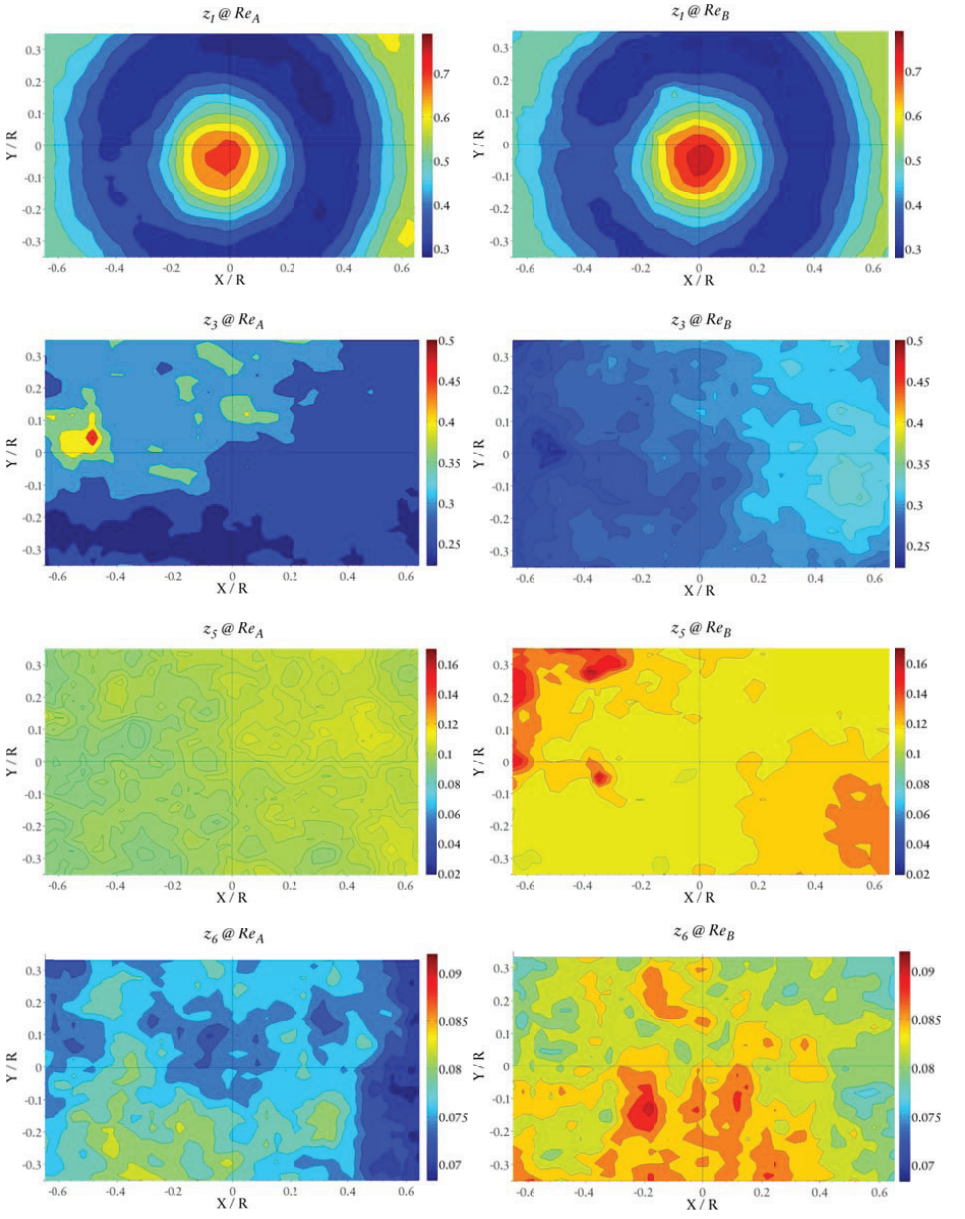

B.2 PIV Experimental Results (Port Closure 50%)

B.2.1 *Mean Velocity Field*

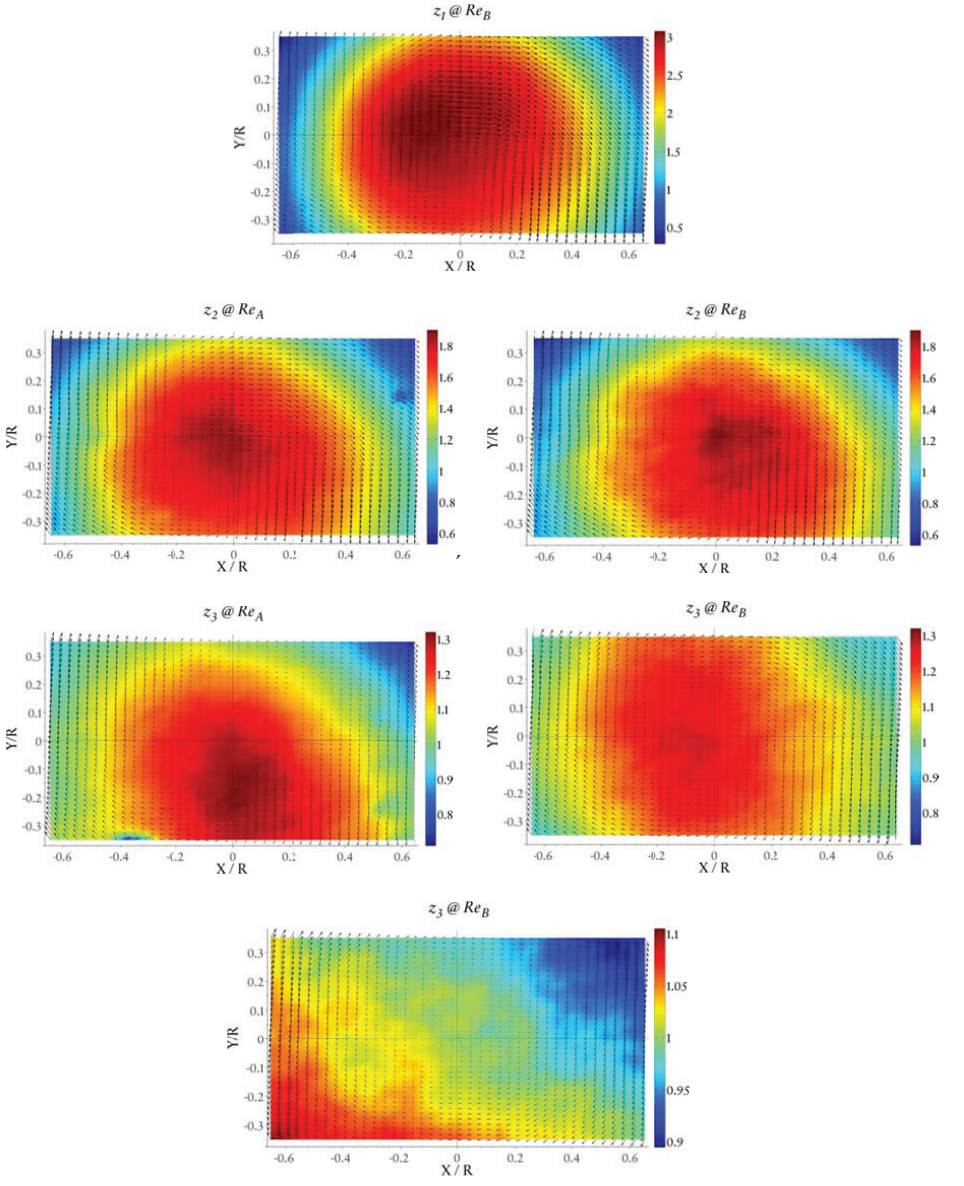

B.2.2 *Mean Axial Vorticity*

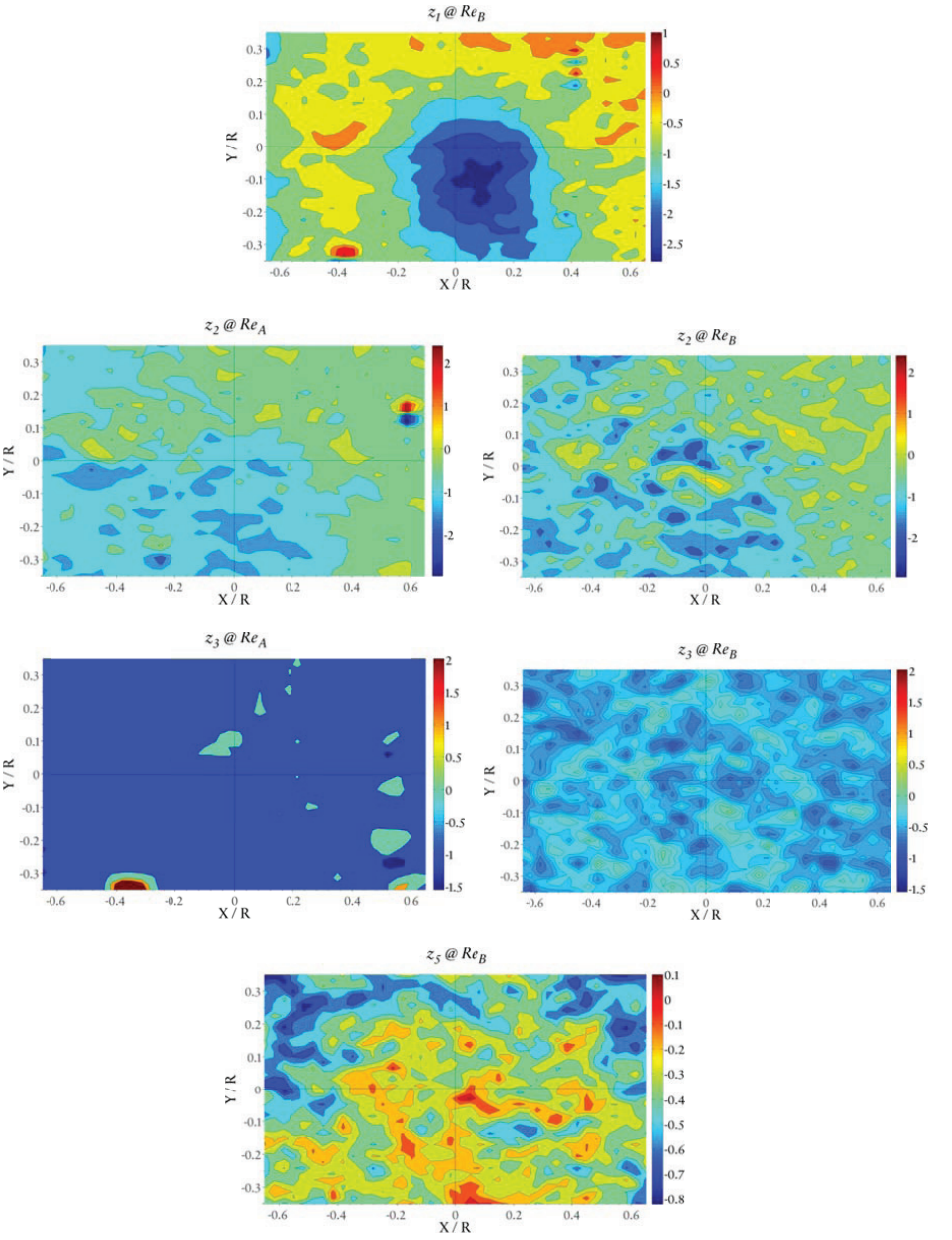

B.2.3 *Reynolds Normal Stress* $\overline{u'u'}$

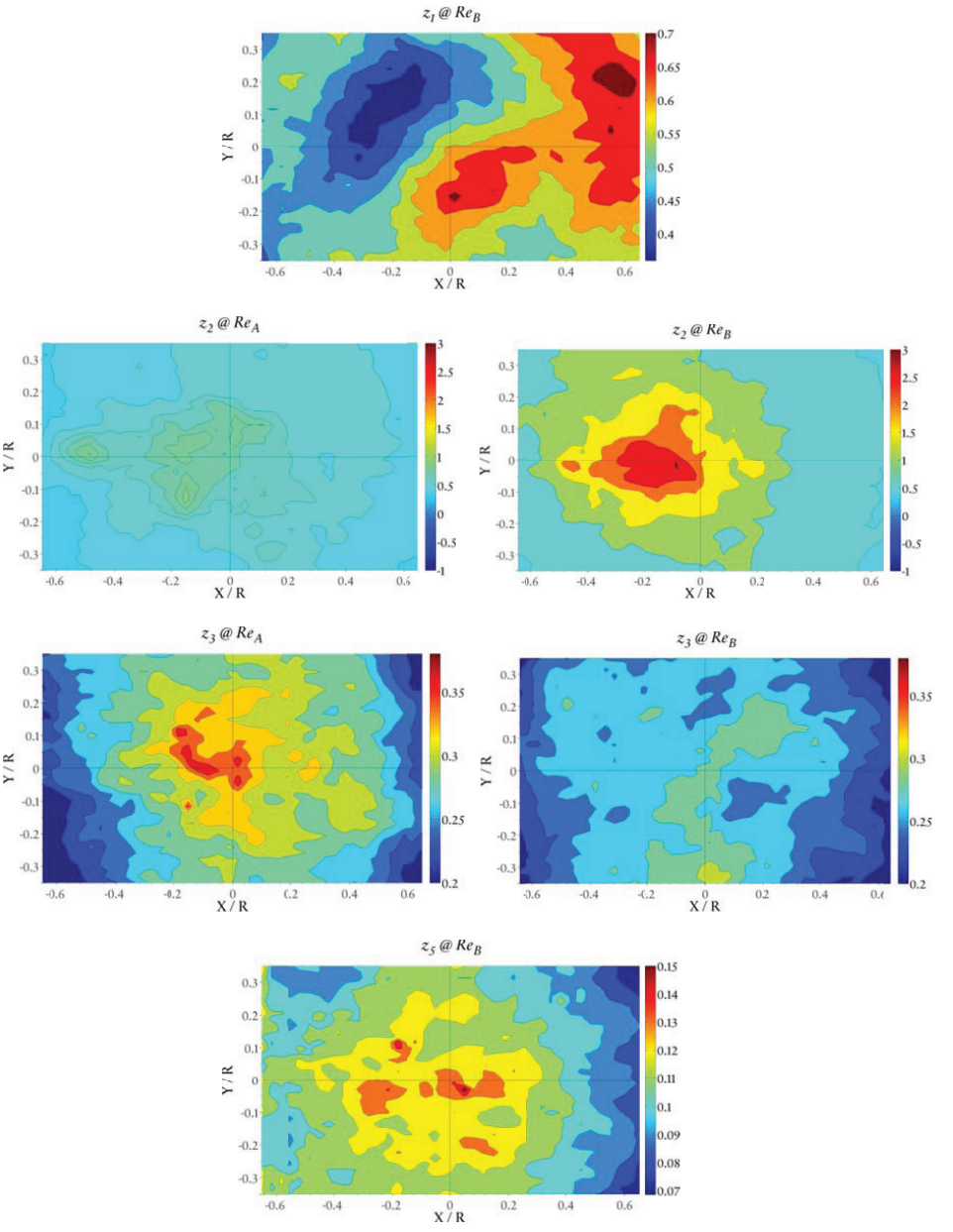

B.2.4 *Reynolds Normal Stress* $\overline{v'v'}$

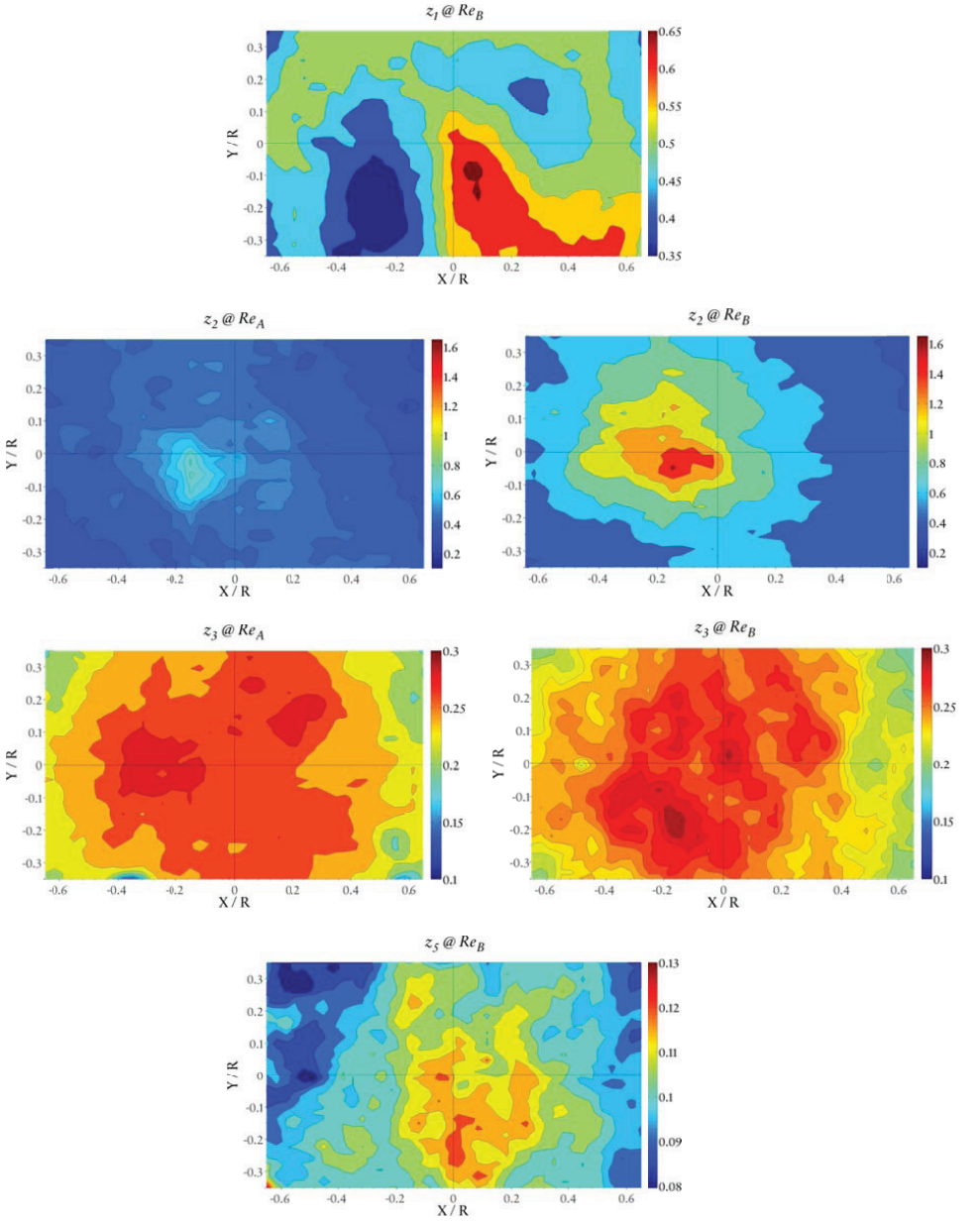

B.2.5 *Reynolds Normal Stress* $\overline{w'w'}$

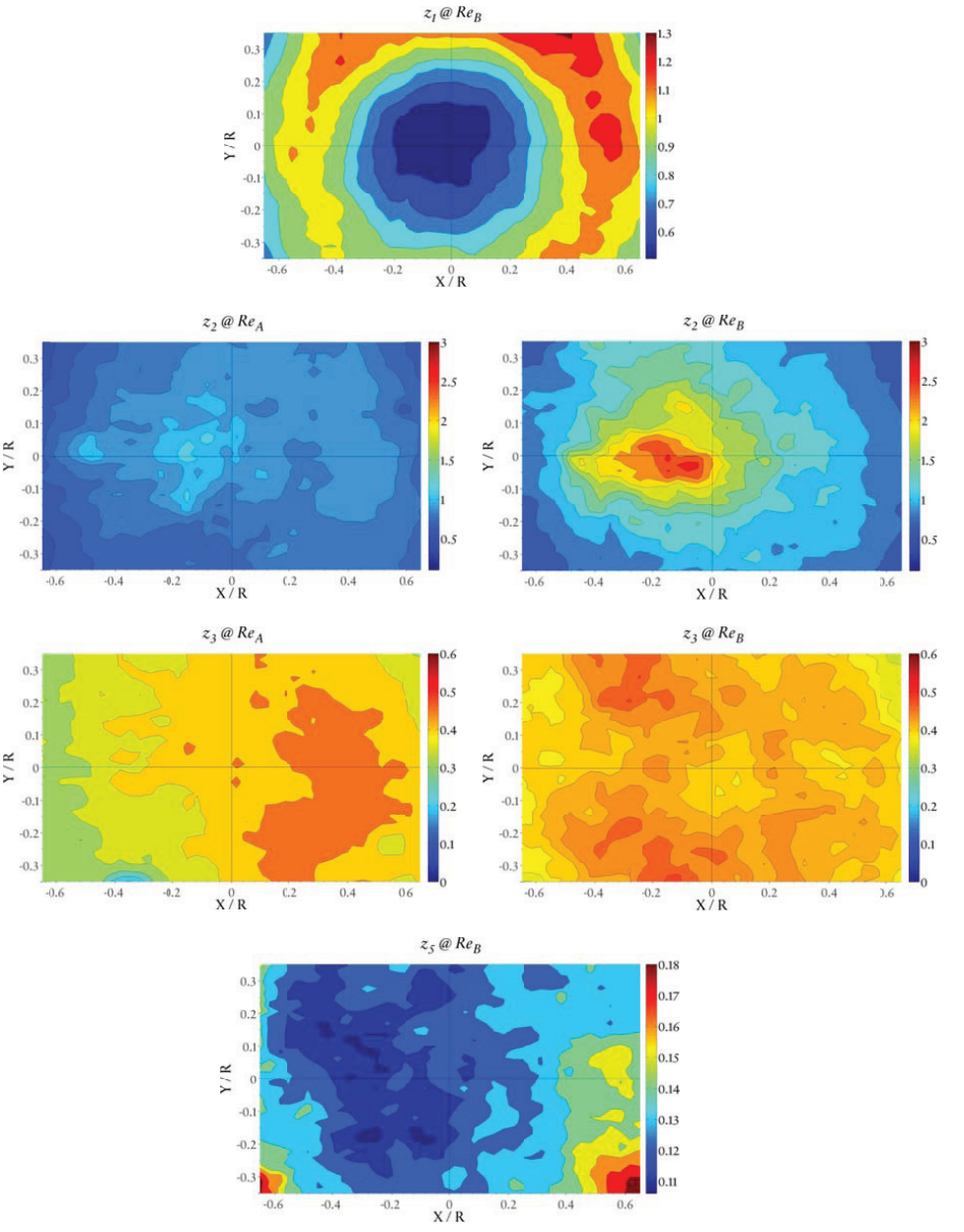

B.2.6 *Reynolds Shear Stress* $\overline{u'v'}$

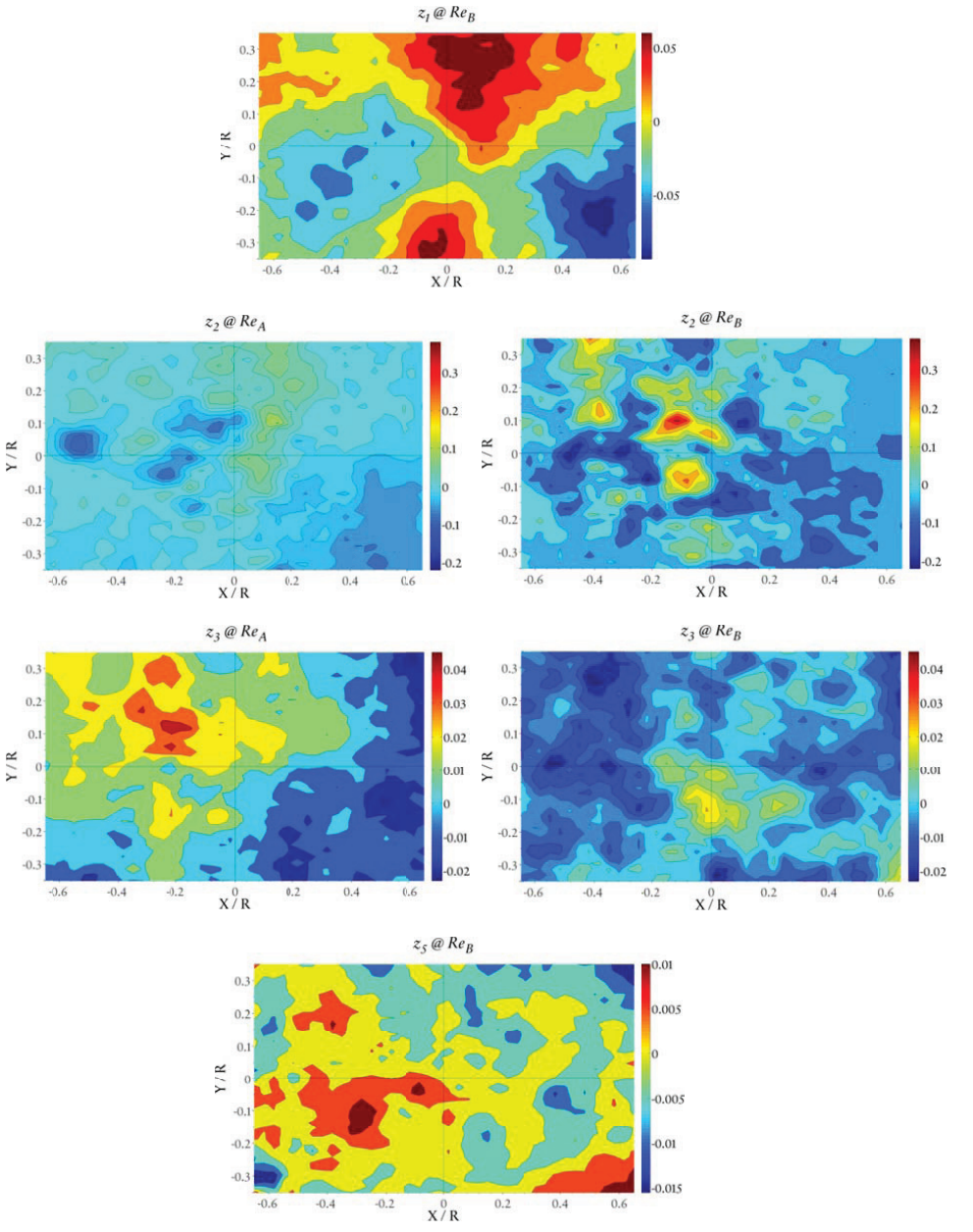

B.2.7 *Reynolds Shear Stress* $\overline{u'w'}$

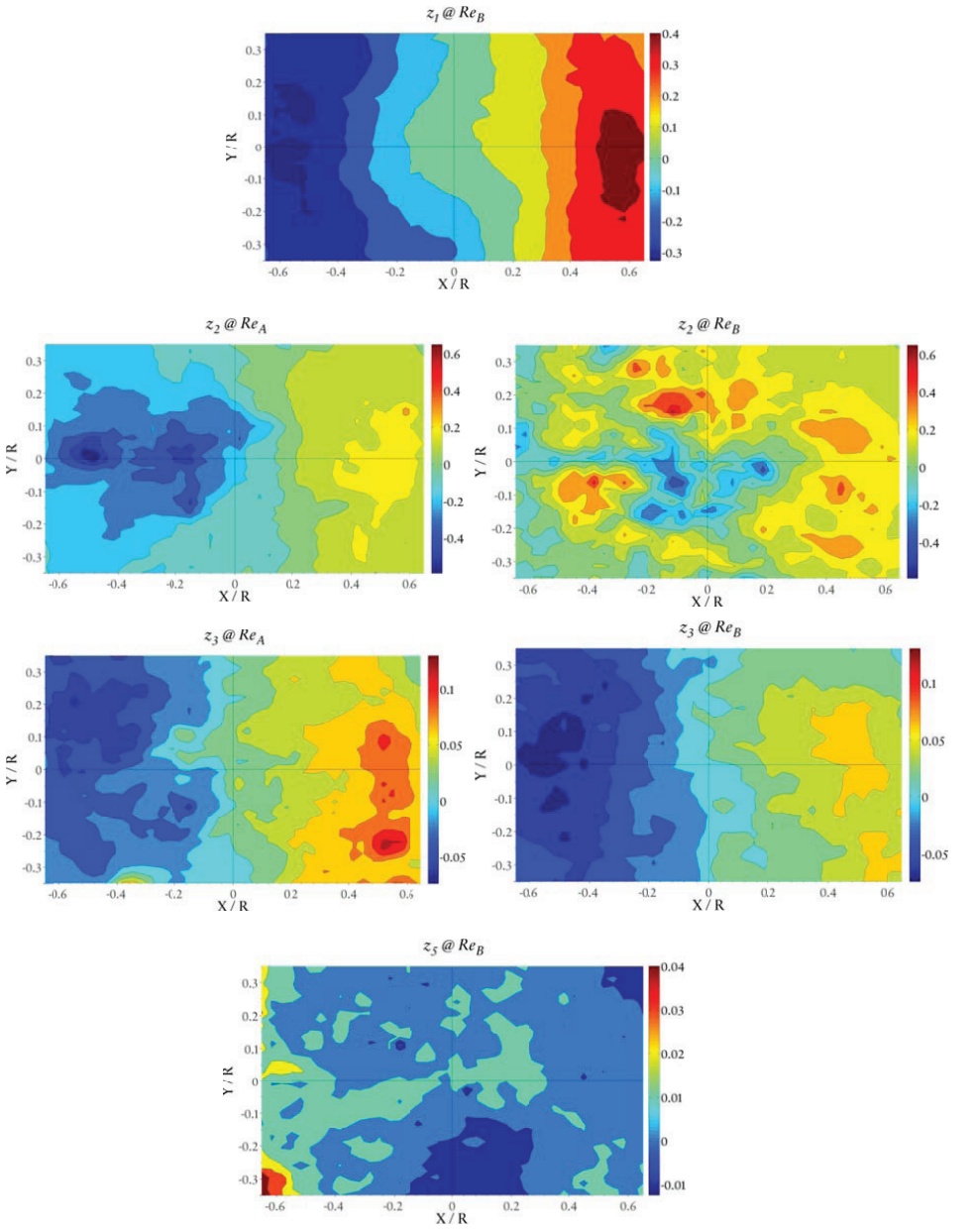

B.2.8 *Reynolds Shear Stress* $\overline{v'w'}$

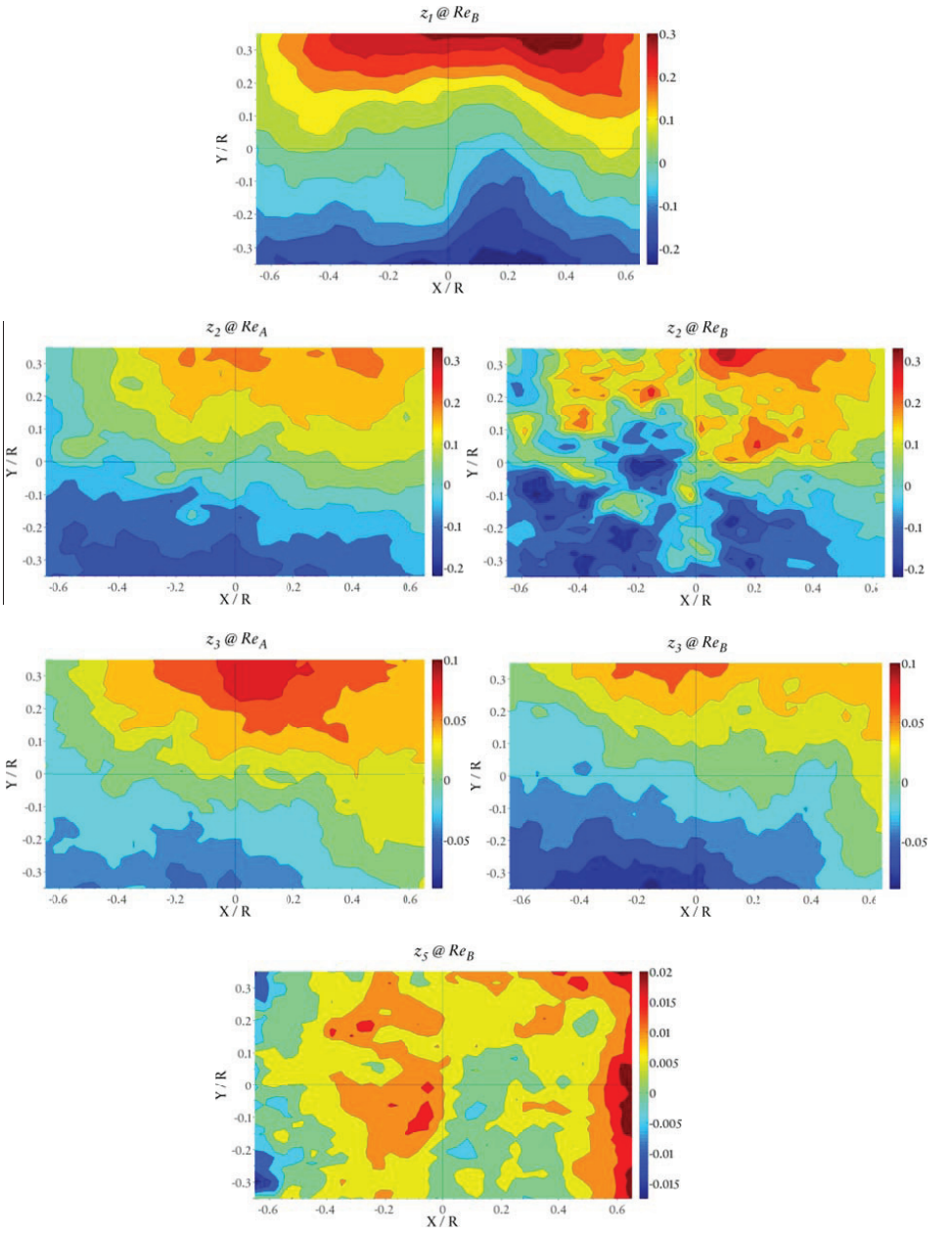

B.2.9 *Average Turbulent Kinetic Energy*

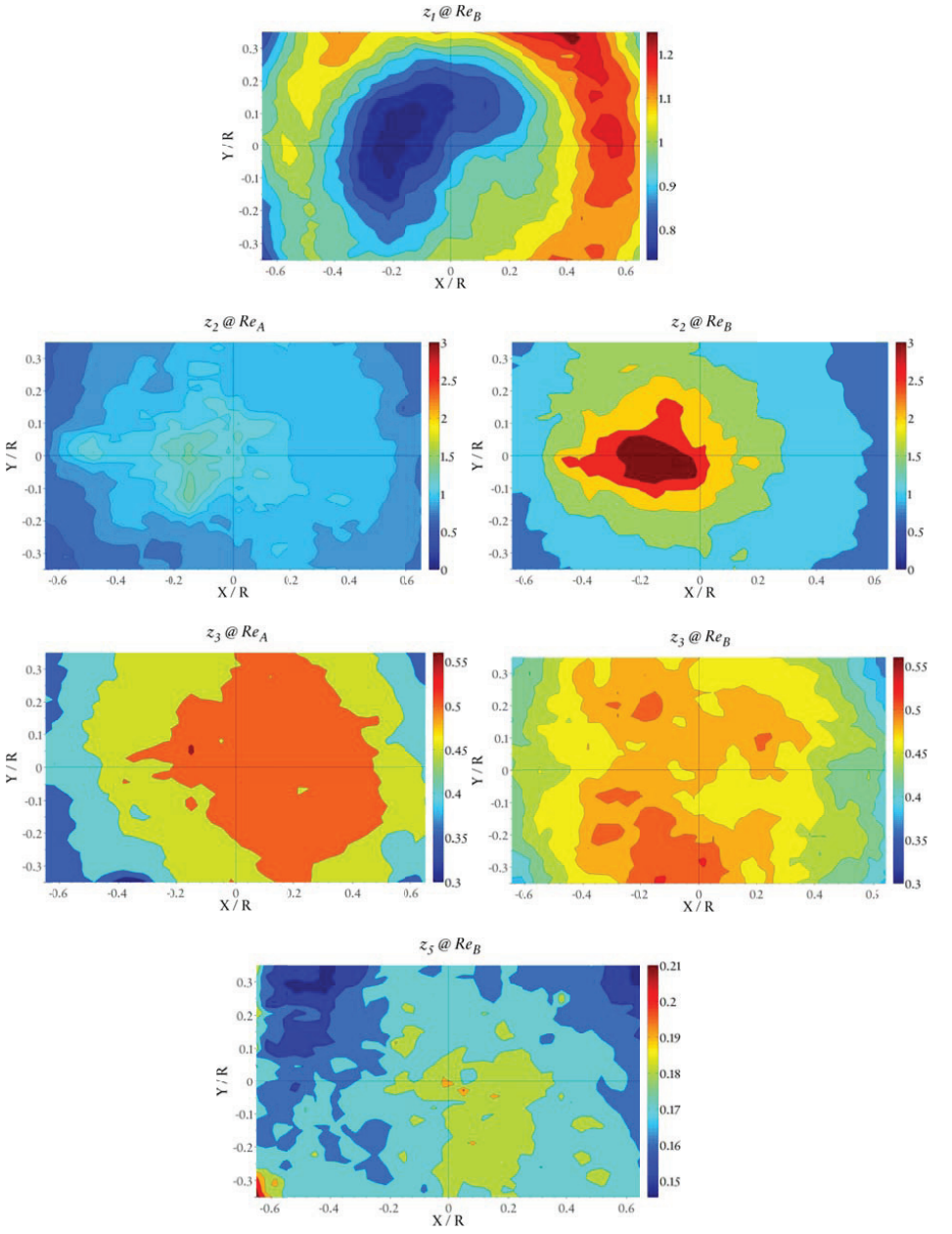

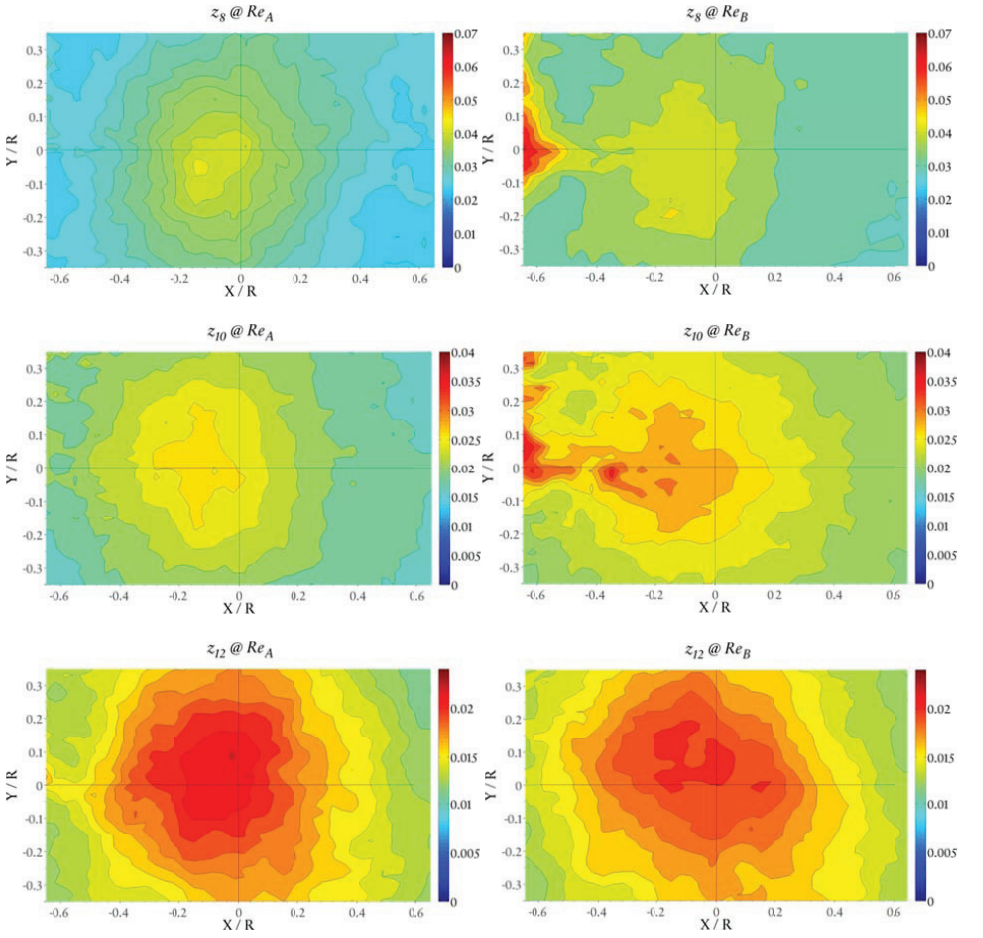
z_8 @ Re_A
z_8 @ Re_B
z_{10} @ Re_A
z_{10} @ Re_B
z_{12} @ Re_A
z_{12} @ Re_B
Y / R
X / R

B.3 PIV Experimental Results (Port Closure 75%)

B.3.1 *Mean Velocity Field*

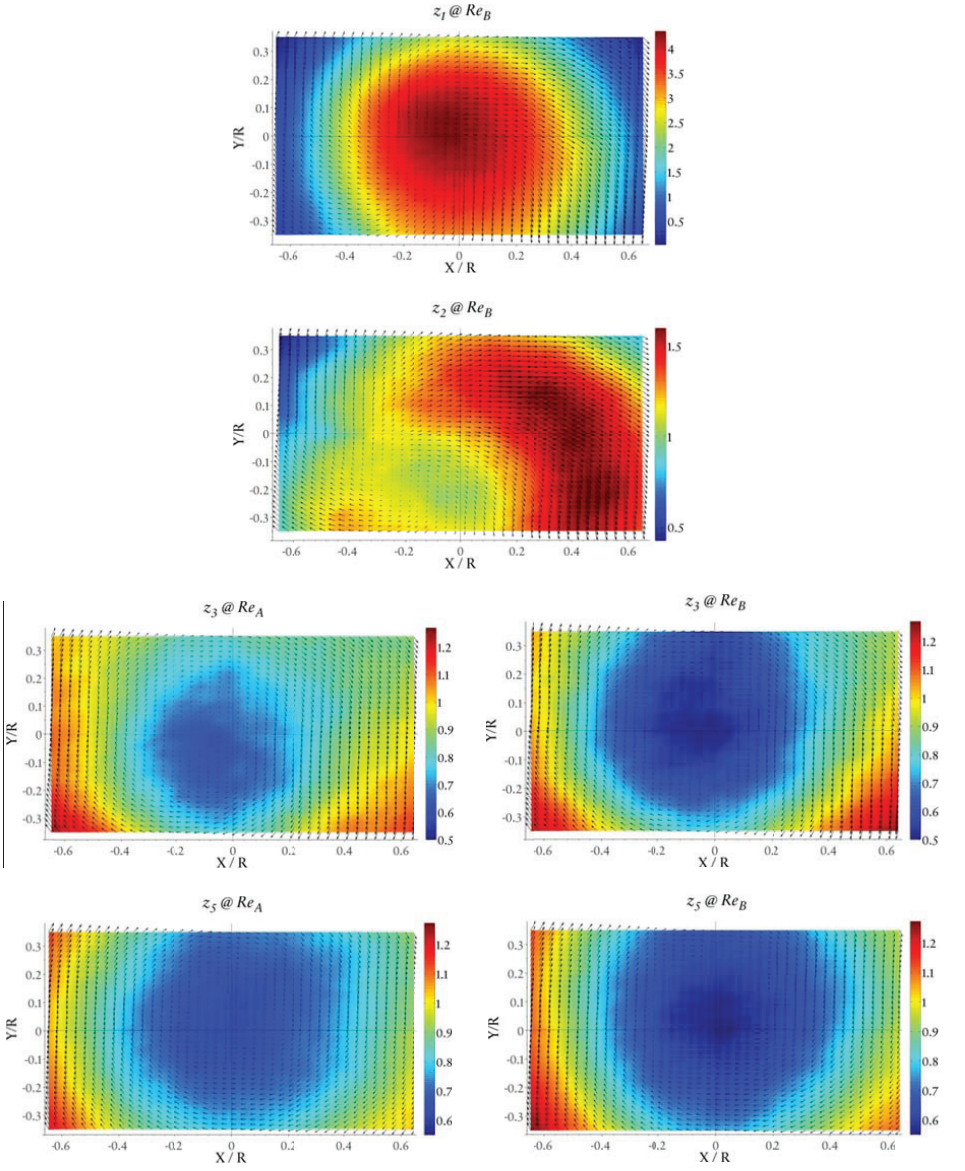

B.3.2 *Mean Axial Vorticity*

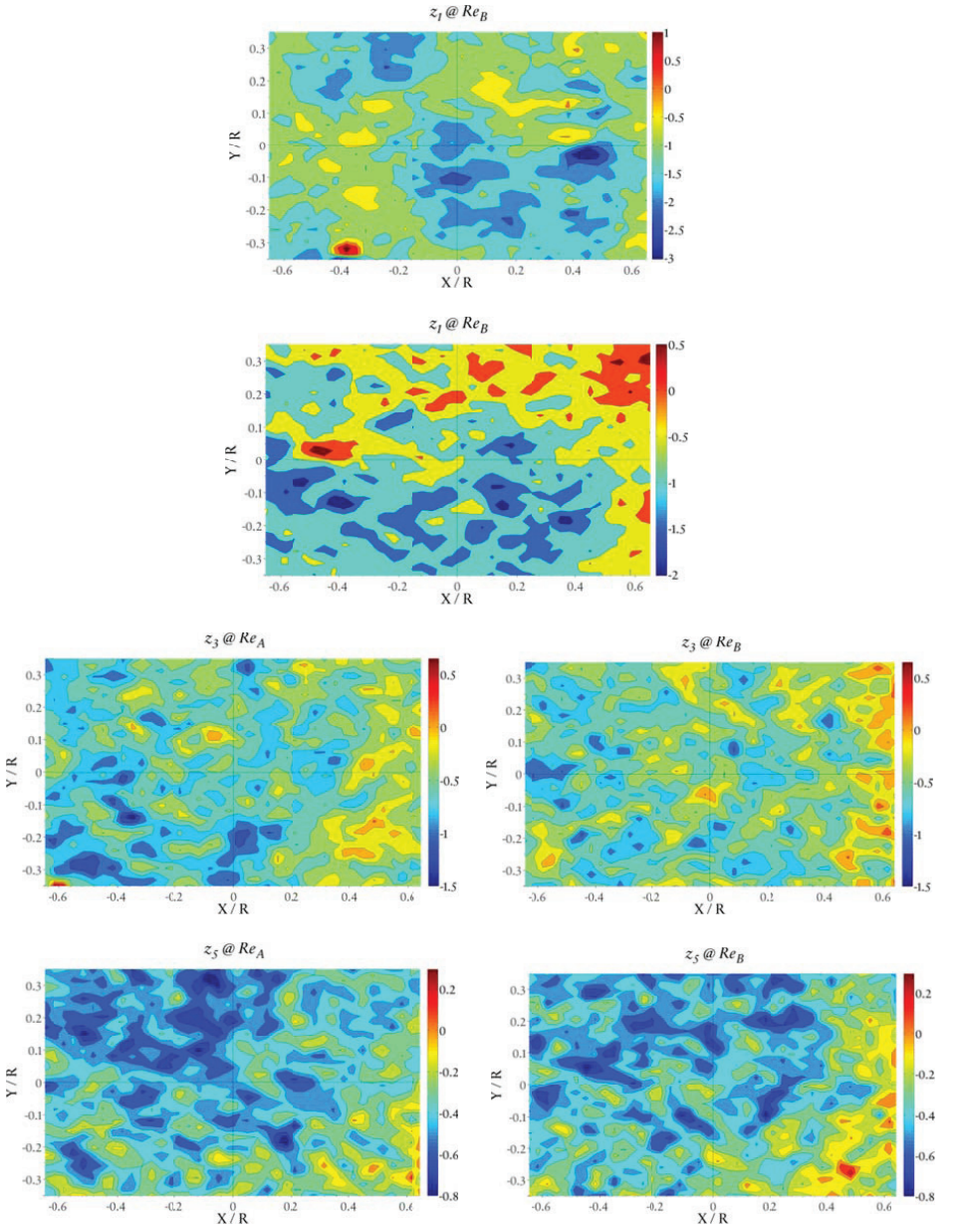

B.3.3 *Reynolds Normal Stress* $\overline{u'u'}$

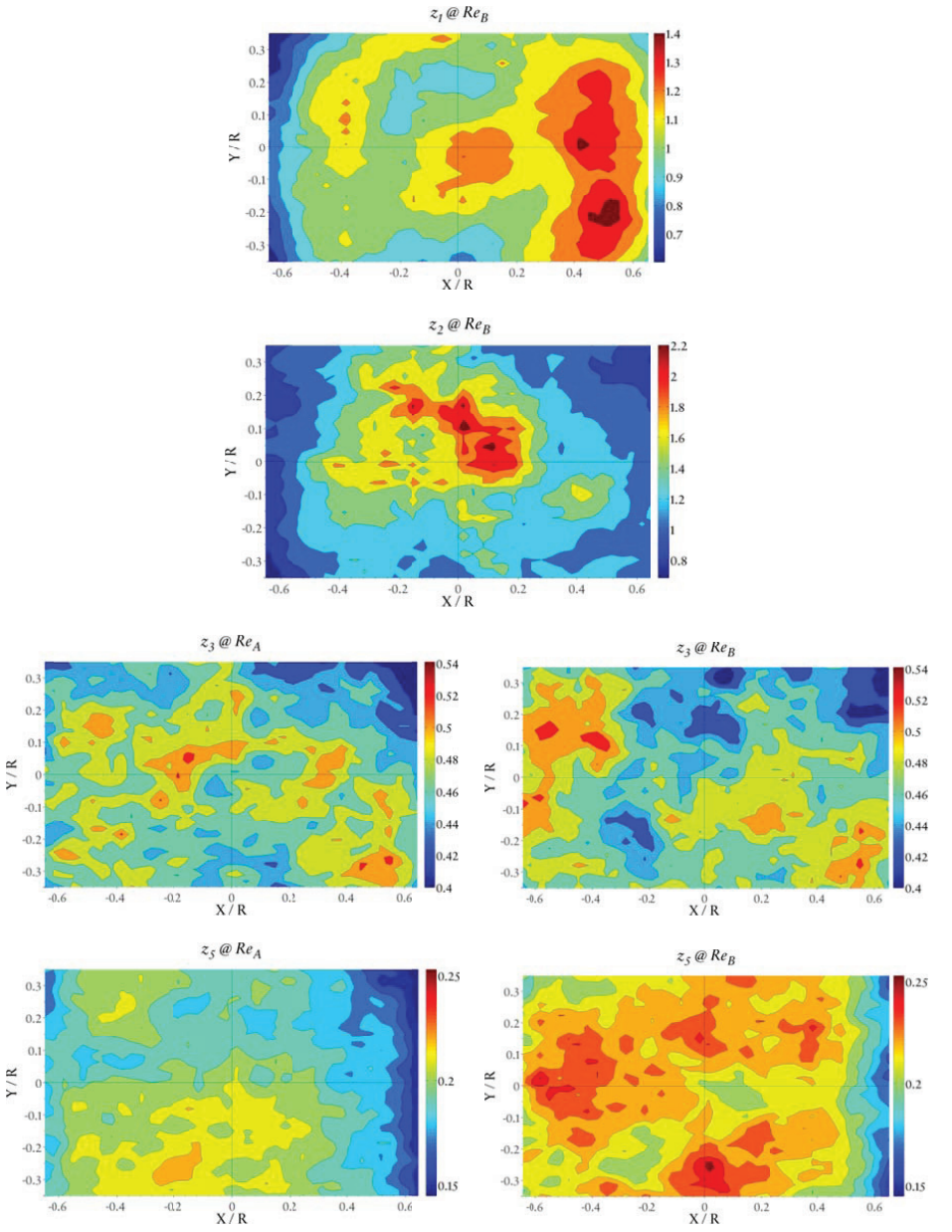

B.3.4 *Reynolds Normal Stress* $\overline{v'v'}$

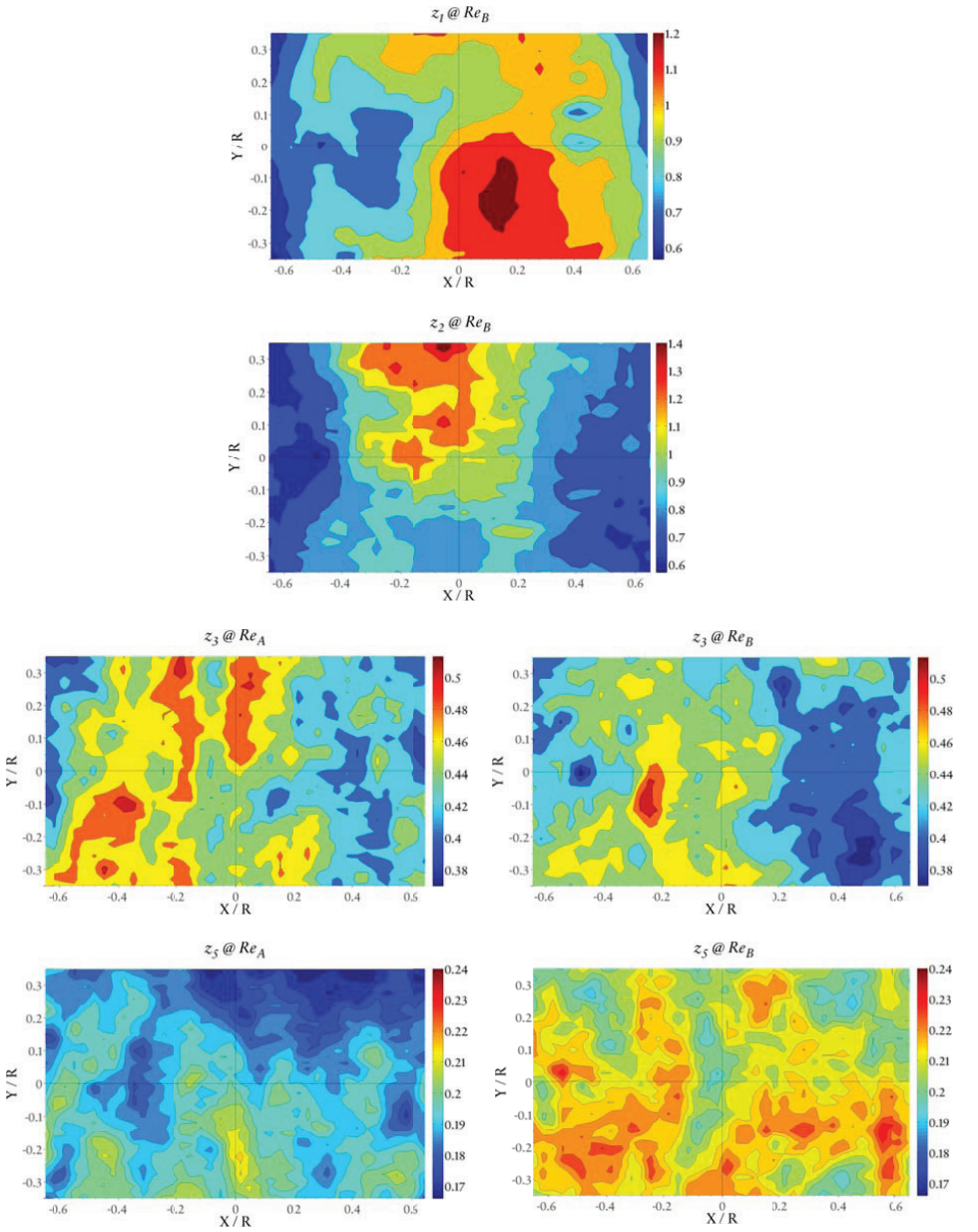

B.3.5 *Reynolds Normal Stress* $\overline{w'w'}$

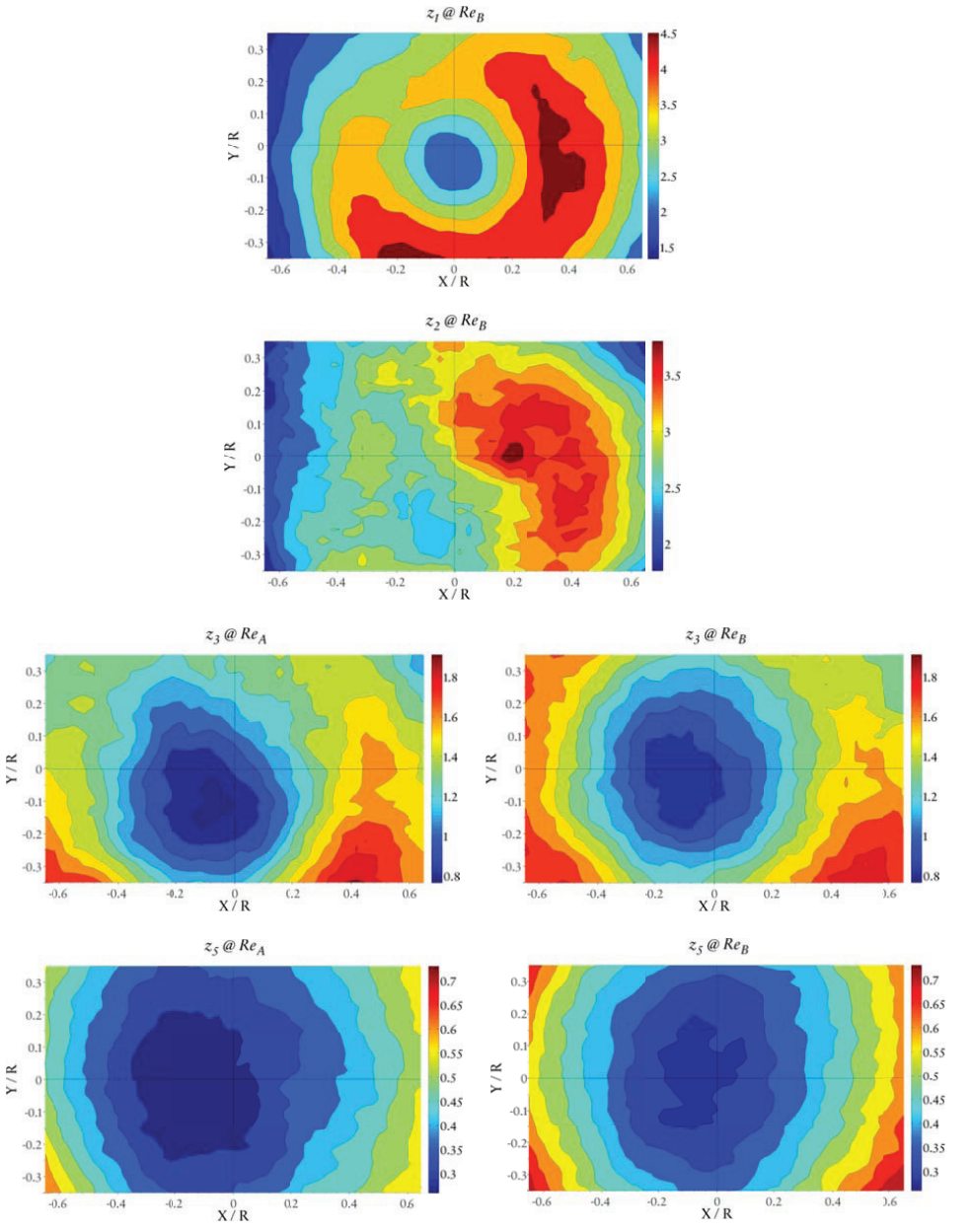

B.3.6 *Reynolds Shear Stress* $\overline{u'v'}$

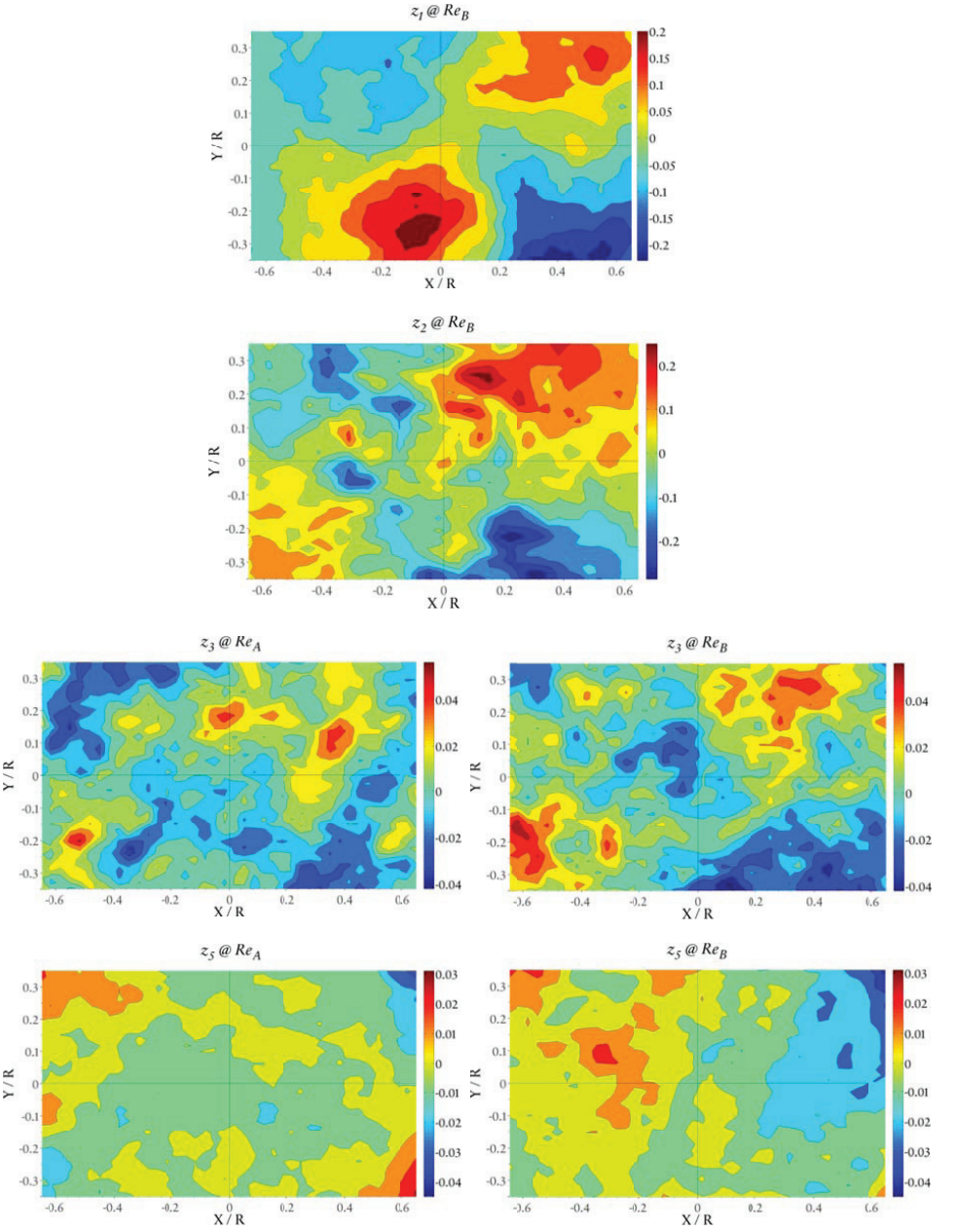

B.3.7 *Reynolds Shear Stress* $\overline{u'w'}$

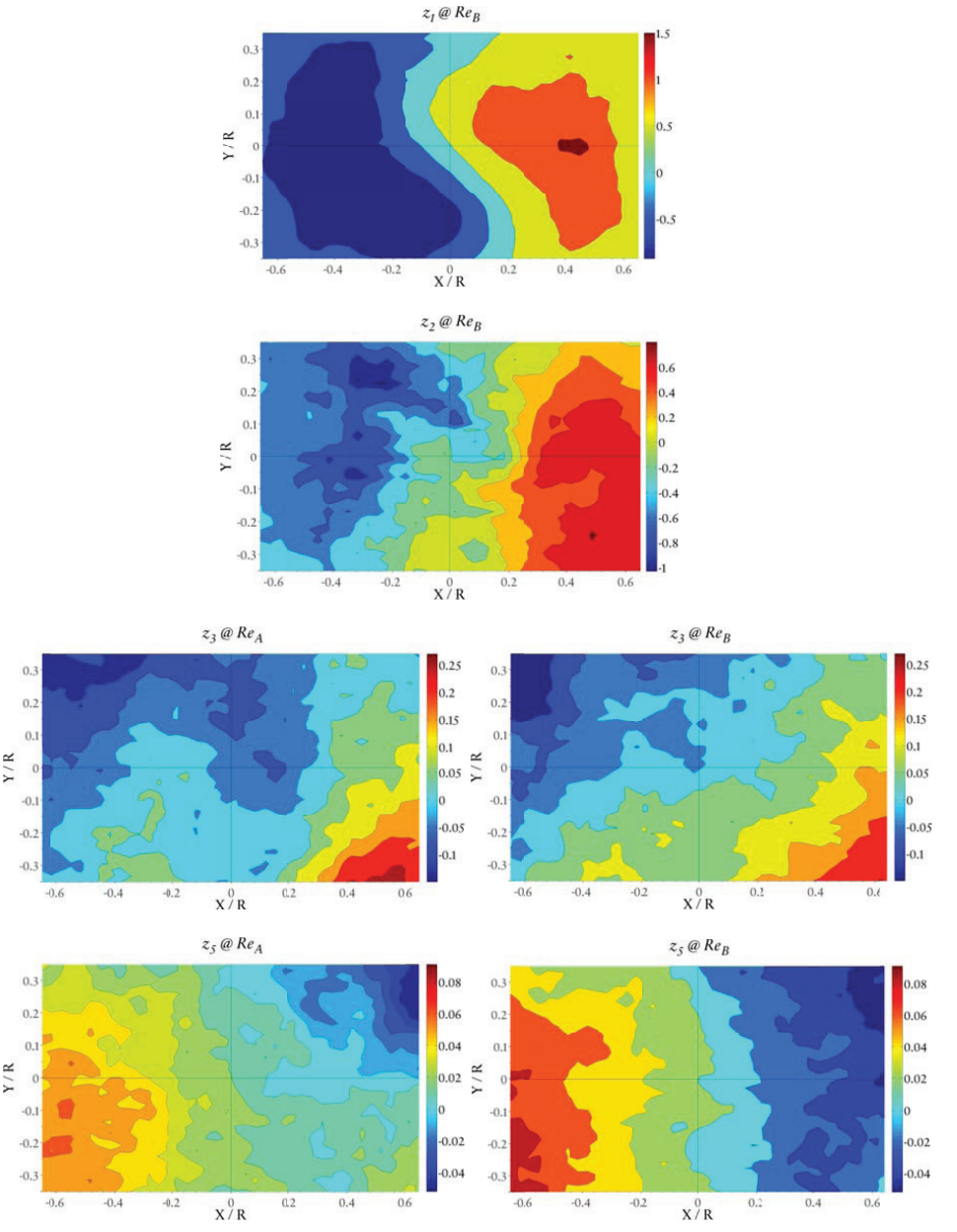

B.3.8 *Reynolds Shear Stress* $\overline{v'w'}$

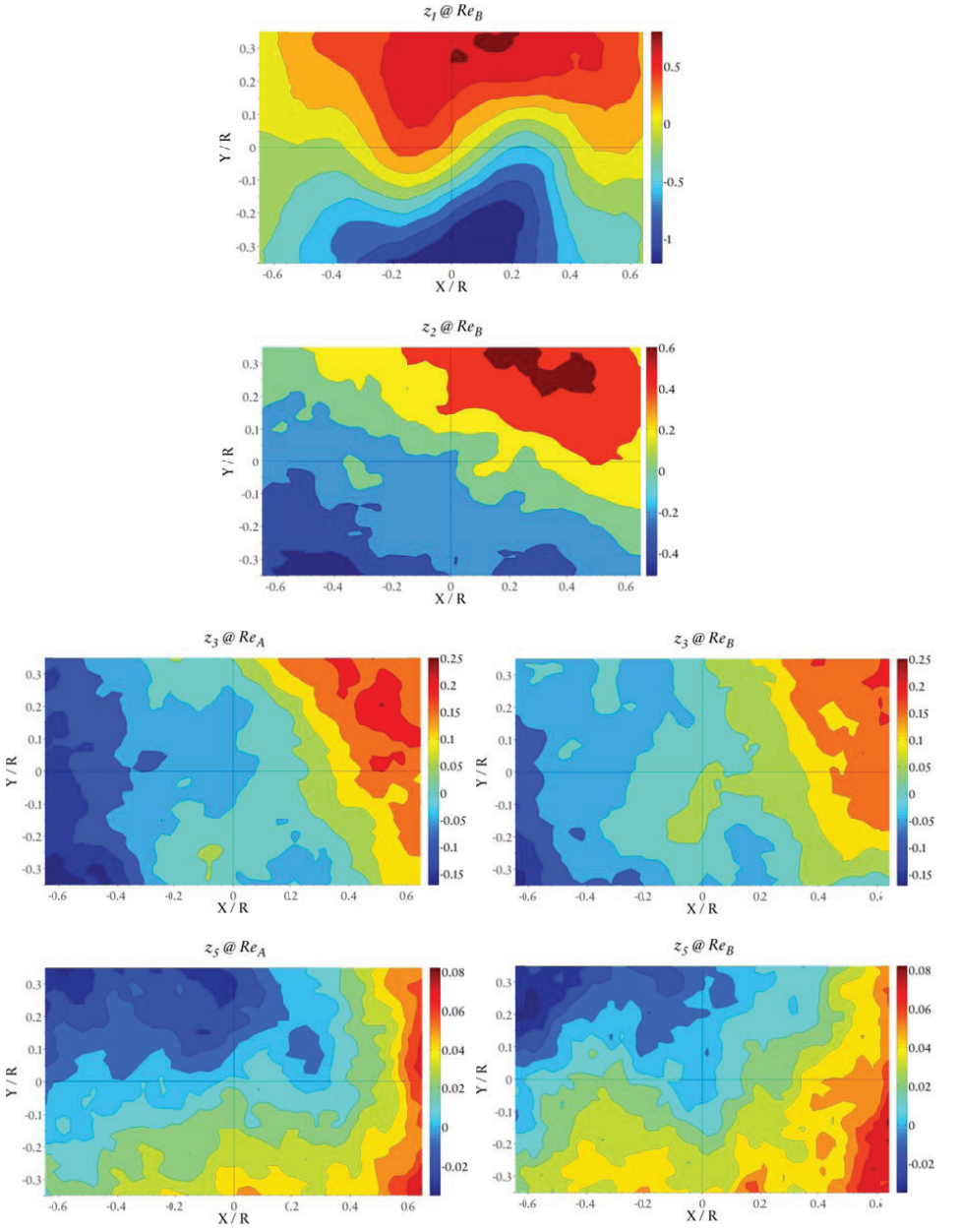

B.3.9 *Average Turbulent Kinetic Energy*

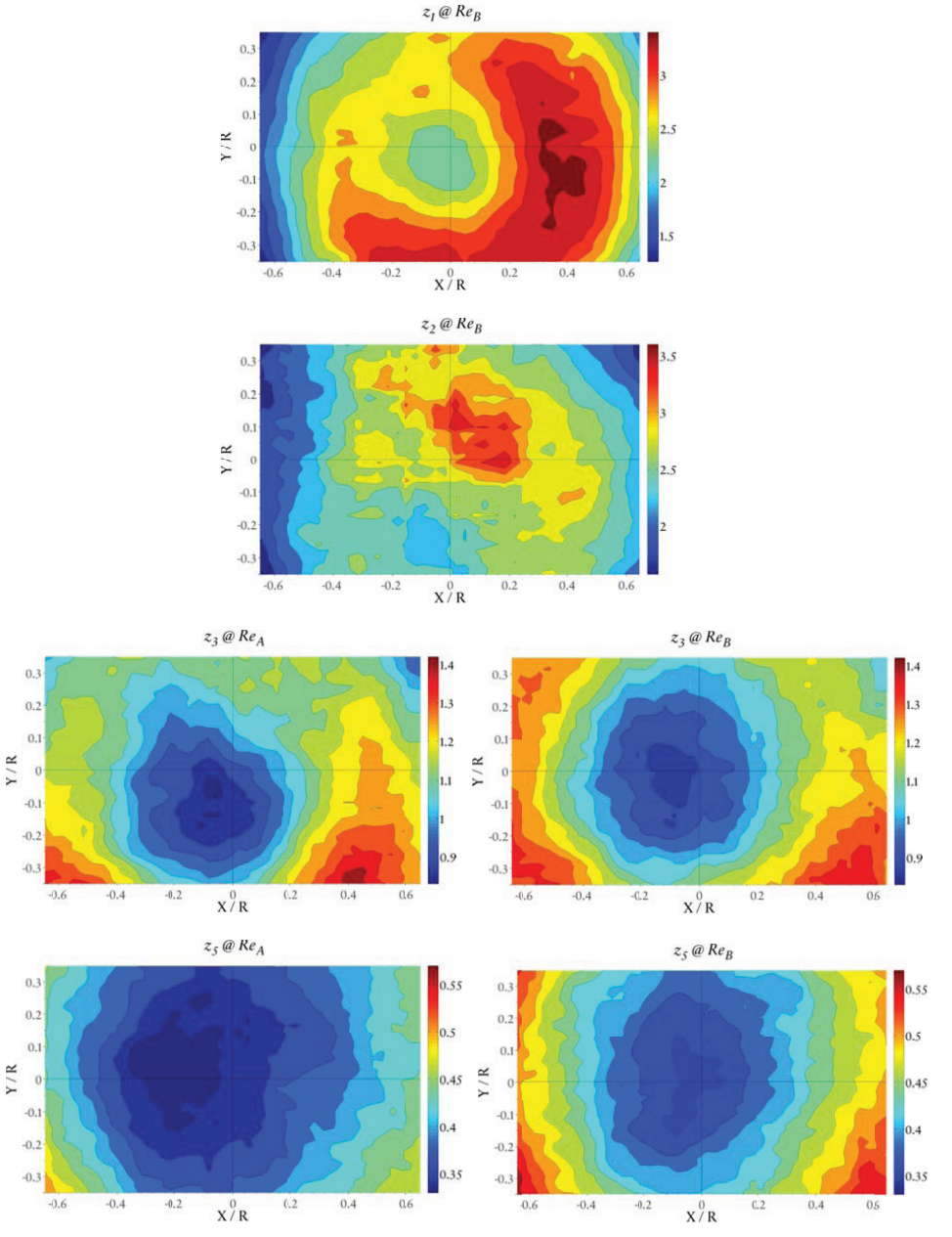

Appendix C

C.1 Article Manuscript

J Mar Sci Technol manuscript No.
(will be inserted by the editor)

PIV Study of the Effect of Piston Position on the In-Cylinder Swirling Flow During the Scavenging Process in Large Two-Stroke Marine Diesel Engines

S. Haider[1] · **T. Schnipper**[1] · **A. Obeidat**[1] · **K. E. Meyer**[1] · **V. L. Okulov**[1] · **S. Mayer**[2] · **J. H Walther**[1,3]
[1] **Department of Mechanical Engineering, Technical University of Denmark, DK-2800 Kgs. Lyngby, Denmark**
[2] **MAN Diesel & Turbo, Teglholmsgade 41, DK-2450 Copenhagen SV, Denmark**
[3] **Chair of Computational Science, ETH Zürich, CH-8092 Zürich, Switzerland**

Received: date / Accepted: date

Abstract A simplified model of a low speed large two-stroke marine diesel engine cylinder is developed. The effect of piston position on the in-cylinder swirling flow during the scavenging process is studied using the stereoscopic particle image velocimetry technique. The measurements are conducted at different cross-sectional planes along the cylinder length and at piston positions covering the air intake port by 0 %, 25 %, 50 % and 75 %. When the intake port is fully open, the tangential velocity profile is similar to a Burgers vortex whereas the axial velocity has a wake-like profile. Due to internal wall friction, the swirl decays downstream and the size of the vortex core increases. For increasing port closures the tangential velocity profile changes from a Burgers vortex to a forced vortex, and the axial velocity changes correspondingly from a wake-like profile to a jet-like profile. For piston position with 75 % intake port closure, the jet-like axial velocity profile at a cross-sectional plane close to the intake port changes back to a wake-like profile at the adjacent downstream cross-sectional plane. This is characteristic of a vortex breakdown. The non-dimensional velocity profiles show no significant variation with the variation in Reynolds number.

Keywords swirl · scavenging · two-stroke engine · PIV

1 Introduction

Low Speed Engine (LSE) are large two-stroke marine diesel engines that use air swirling inside the engine cylinder for scavenging process. The air intake ports are located near the bottom-dead-center (BDC). The exhaust port is located in the cylinder head. An exhaust valve is used to open and close the exhaust port whereas the intake ports are controlled by piston motion. The fresh air enters the cylinder near the bottom-dead-center and flows upward and removes the exhaust gases though the exhaust port at the cylinder head. Since the scavenging air flows from the bottom to the top of the cylinder, this type of scavenging is called uniflow scavenging. Uniflow scavenging accounts for higher engine thermal efficiency due to better air/gas exchange (Pevzner, 1998). Efficient scavenging improves the combustion efficiency of the two-stroke diesel engines (Nakagawa et al, 1990). The scavenging ports, depending on different designs, are at an angle of 15°–25° with the cylinder radius to impart tangential velocity producing a swirling air column (Litke, 1999). The resulting in-cylinder confined swirling flow removes the exhaust gases from the cylinder, provides fresh air charge for the next cycle and introduces swirl to enhance mixing of injected fuel and its consequent combustion. Moreover, it also increases cooling of the cylinder liner and in case of a non-axis symmetric swirl, can result in an uneven temperature distribution at the walls. Thus investigation and optimization of the scavenging process is key parameter for the performance and development of fuel efficient and low emission marine engines.

Experimental results available in scientific literature, focused on studying the uniflow scavenging process in large low speed marine diesel engines, are very few compared to scavenging in other (smaller and high speed) two stroke diesel engines. Previous studies include the experiments by Nishimoto and Takeyuki (1984), who obtained the shape of the front surface of the scavenging air using thermocouple in a uniflow model engine. The model engine used hot air for scavenging the cylinder filled with air at room temperature. It was observed that with the increase in the engine RPM (rotations per minute) and port angle, the scavenging air front surface profile changes from jet like to a wake like profile analogous to vortex breakdown in an axial flow vor-

J. H. Walther. E-mail: jhw@mek.dtu.dk

tex chamber. A method was also proposed to obtain a flat profile front surface at an arbitrary Reynolds number for maximum scavenging efficiency. Laser Doppler Velocimetry (LDV) experiment was conducted on a model test engine by Dedeoglu (1988). The experiments used a single liquid and cylinder liner with different intake port configurations. Result show that the in-cylinder flow consists of a rotational flow in the cylinder axis region and a potential flow in the near wall region. Nakagawa et al (1990) used two-component LDV measurements on a model of large, low speed engine with large bore acrylic cylinder and air as the working fluid. The tangential velocity profile for the piston at TDC was found to depend on the scavenging port angle. Larger port angles resulted in a larger axial velocity drop in the central region of the cylinder thus occasionally resulting in a reverse flow. Litke (1999) studied the influence of the scavenging port angles on the scavenging efficiency by using liquids in a 1:4 scaled engine model. It was observed that the highest scavenging efficiency is obtained with an inlet scavenging port angle of approximately 20°. The results also indicated a better performance of using scavenging ports with combination of different angles compared to the ports with uniform angle.

The large physical size and high in-cylinder pressure for LSE makes experimental investigations in the engine very expensive to conduct and with difficult optical access. The scavenging process is unsteady and complex in nature thus making statistics difficult. In terms of variation in geometry of the flow domain, piston is in continuous motion during the scavenging process thus changing the cylinder length and also the effective shape of air intake ports. Such complex inlet flow conditions make it difficult to distinguish between inlet effects and swirling flow effects. Regarding the flow physics, mixing and stratification of exhaust gases with fresh air charge occurs while the in-cylinder mass flow rate changes between opening and closing of the scavenging ports. This simultaneous variation in flow domain and flow physics consequently affects the in-cylinder swirl characteristics and the type of the vortex generated by the swirl.

Considering the complex nature of the real engine scavenging process, a detailed understanding of the in-cylinder scavenging process requires isolation and consequent study of each flow phenomenon in a simplified form. The complex physics can then be better analyzed by gradually adding complexity. The focus in this study is to characterize the in-cylinder confined swirling flow at different piston positions during the scavenging process. In order to simplify the problem an experimental down-scale and simplified model of the engine cylinder is developed which is analogous to a straight cylinder connected to a swirl generator but having features like movable piston, cylinder head and guide vanes to divert the flow entering the cylinder at a desired angle etc. In the present study the cylinder exhaust port is fully open and the exhaust valve is removed. The experimental results will provide a detailed understanding within areas of large two stroke LSE and fundamental studies in turbulent confined swirling flows.

In the present experiment, air at atmospheric conditions is used as the working fluid and the cylinder length is fixed at $4D$ i.e. equal to stroke-to-bore ratio for LSE, and where D is the diameter of the cylinder. Stereoscopic Particle Image Velocimetry (PIV) measurements are carried out to study the in-cylinder confined swirling flow. The study does not include the effects of mixing and stratification. The measurements are conducted at four fixed piston positions in translational direction where piston partially covers intake ports by 0 % (fully open ports), 25 %, 50 % and 75 %. PIV data acquisition is performed by keeping the piston at any aforementioned fixed position and then taking measurements at different cross-sectional planes along the length of the cylinder. The piston is then moved to the next position and the procedure is repeated. Conducting measurements at fixed piston positions will give snapshots of the in-cylinder flow characteristics without transient effects induced by the continuous piston motion. This makes the results of the current study very useful for computational studies. In order to study the effect of variation in Reynolds number on the in-cylinder swirling flow, for each given piston position, the measurements are conducted at two different flow Reynolds numbers: $\mathrm{Re} = v_b D/\nu = 65000$ and 32500, where v_b denotes the bulk axial velocity in the cylinder, and ν the fluid viscosity.

2 Experimental Set-up

An overview of the experimental set-up is shown in Fig. 1. The scavenging flow test rig is connected with a fan with speed controller and an orifice meter to measure the volumetric flow rate through the set-up.

2.1 Cylinder

A transparent acrylic cylinder (produced using casting process to give good optical properties) is used. The internal diameter (D) of the cylinder is 190 mm and the total length L of the cylinder is 760 mm. JHW In one end, an inlet section is mounted, and in the other end an outlet section is mounted. JHW instead One end of the cylinder enters inside the inlet section and at the other end an outlet section is inserted.

2.2 Inlet Section

The inlet section (Fig. 1) consists of two transparent ring-shaped acrylic plates with an outer diameter of 600 mm. The

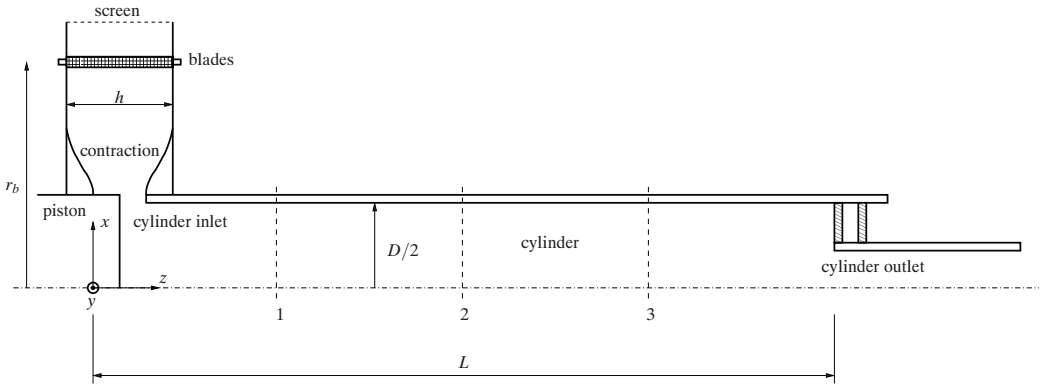

Fig. 1 Schematics of the experimental set-up. The ports are here closed 50 % by the piston. The blades are located at $r_b = 250$ mm with a length $h = 100$ mm. The cylinder has a length (L) to diameter (D) ratio of 4. The numbers 1, 2, and 3 mark the measurement positions for the PIV system.

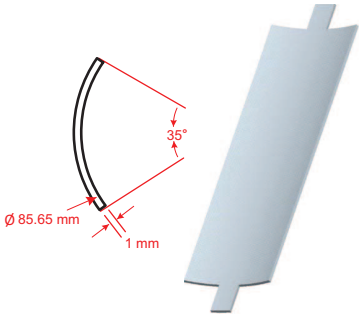

Fig. 2 Illustration of the guide vane blade geometry.

plates are fitted in parallel by mounting 60 guide vanes in between them thus serving as walls bounding the flow. The distance (h) between the internal walls of the plates/height of individual blade is $h = 100$ mm. A screen with 51 % open area ratio is glued around the outer periphery of the inlet section to obtain a uniform velocity profile at the inlet cf. Fig. 1. A bell-mouth shape contraction section (Fig. 1), is mounted internally at the inner periphery of the inlet section. The contraction reduced the width of the channel from the 100 mm at the inlet to 40 mm at the inlet of the cylinder.

An overview of the individual guide vane construction is shown in Fig. 2. Each guide vane has a thickness of 1 mm and a width of 26.16 mm (when flat). The guide vanes are then deformed into an arc shape with details given in Fig. 2. Each individual guide vane is fitted inside the inlet section in a way that one end is aligned in radial direction with the flow entering through the inlet. The other end follows the curved geometry of the guide vane. Thus the flow from inlet enters the guide vane in the radial direction and diverts at an angle of $\alpha_{\text{blade}} = 35^\circ$ with the radial direction. The guide vanes are mounted at a large radial distance ($r_b = 250$ mm) from the geometric center of the cylinder and close to the inlet (Fig. 1). This will give some time to the flow after the vanes to settle thereby minimizing the wake effects behinds the guide vanes. Further, before entering the cylinder, the flow enters the contraction section which will accelerate the flow and reduce the velocity fluctuations. The acrylic cylinder is entered into the inlet section from one side and from the other side, a transparent piston is mounted. The piston can slide inside the cylinder thus partially/fully close the cylinder inlet section, similar in a way that in real engine the reciprocating piston uncovers and covers the scavenging ports. However, the outer diameter of the piston is larger (by wall thickness) than the cylinder inner diameter. This limits the displacements of the piston to a position where it fully covers the cylinder intake port. The current work is focused on studying the in-cylinder swirling flow when the piston is at the BDC (the inlet to the cylinder is fully open) and piston positions where it covers the intake port by 25 %, 50 % and 75 %.

2.3 Outlet Section

The outlet section consists of a smaller internal diameter pipe ($d = 110$ mm) and length ($l = 1415$ mm). The large length of the pipe will minimize any effect on the nature of the swirling flow inside the cylinder due to bending in the connecting pipes to the orifice plate and fan. The shape of the outlet provides a flat-bottom head to the cylinder. The outlet section can slide inside the cylinder and facilitates experiments at a desired effective length of the cylinder which in this study is kept fixed at 4D.

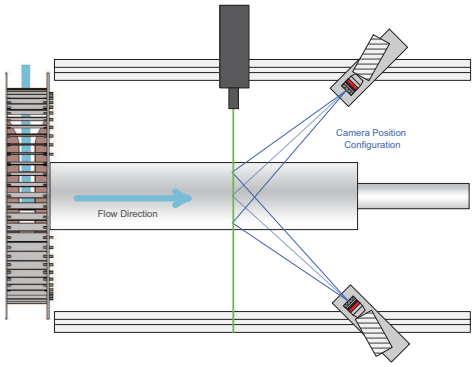

Fig. 3 Illustration of the Stereoscopic PIV set-up.

3 Stereoscopic PIV Setup

An overview of the stereoscopic particle image velocimetry set-up is given in Fig. 3. The laser optics and the two cameras are mounted on a large traverse system that moves in the axial direction i.e. along the length of the test cylinder. The traverse is carefully aligned with the cylinder and uses a stepping motor for accurate positioning. The traverse system moves independently of the test rig.

3.0.1 Alignment and Calibration

A NewWave Solo Nd:Yag pulse laser (120 mJ pulses at wavelength 532 nm) is mounted on the traverse so that the laser sheet is exactly perpendicular to the cylinder axis. The approximate laser sheet thickness is 4 mm. Two Dantec HiSense cameras with 1344×1024 pixels and pixel size of $6.45\,\mu$m are equipped with 60 mm focal length lenses and green light filters. Both cameras are in Scheimpflug condition and mounted on the same traverse as the laser source. The cameras are at one side of the laser sheet and the cylinder is placed between the two cameras (Fig. 3). The calibration target is kept on a disc of same diameter as the internal diameter of the cylinder and is slided inside the test cylinder. The calibration target is kept aligned with the laser sheet at a given measuring cross-sectional position. Both cameras are aligned in a way that their rectangular frames capture maximum area of the given cross-section within the pipe diameter. Thus avoiding measurements close to the cylinder wall due to strong reflections of the laser light. The calibration is performed at single measuring position. Dantec DynamicStudio software is used for PIV measurements and data processing. Calibration was performed using the 3rd order xyz-polynomial imaging model which is capable of handling distortion caused by the lens or curved windows (DantecDynamics, 2009). In order to account for the possible misalignment of the calibration target with the laser sheet, disparity error correction is performed. Since the relative positions of laser source and two cameras are fixed, considering the test cylinder being axially aligned, the same calibration is used for all the other measuring cross-sections.

The F-number is set to 8 for the camera receiving the forward scatter and for the camera receiving the backward scatter, the F-number is set to 4.

3.1 Seeding

The seeding generator contains 75/25 % by volume glycerol-water solution and the size distribution of seeding droplets is in range of 1-3 μm. For a uniform and adequate seeding, the particles should mix properly with the incoming air entering the inlet section. For this purpose a metal frame, with a diameter of 860 mm and width 150 mm, is mounted around the inlet section. A plastic pipe with a diameter of 40 mm is tied with the internal periphery of the metal frame in a helical shape so as to cover the whole breadth of the metal frame and consequently the inlet surface. A large number of holes (approximately $1.5\,\mathrm{cm}^{-2}$ with a diameter of 3 mm) are drilled in the pipe wall facing the inlet of the experimental set-up and the two ends of the pipe are connected to the seed generator. The radial distance of the pipe wall from the inlet surface is sufficiently large to minimize any effect to the the incoming flow and provide a uniform seeding across the inlet surface.

4 Data Acquisition

The measurements are conducted at different cross sectional planes along the length of the cylinder, with their distances measured from the piston surface as reference (Fig. 1). For every position, a minimum of 994 PIV snapshots are taken. Data processing and analysis of the PIV images is performed using multi-pass “Adaptive Correlation” algorithm in Dantec DynamicStudio software. The initial interrogation window size is 128×128 pixels with two refinement steps to a final interrogation area of size 32×32 pixels and 50 % overlap of the side of the interrogation area. The time-between-pulses (TBP) was optimized by testing several values. The largest value that gave a low amount of outlier vectors was selected. This was performed for each combination of measurement position, piston position and Reynolds number.

5 Results and Discussion

In order to present the results in a comprehensive manner, first the results for the case of fully open intake port are presented and discussed. The results for the cases with 25 %,

50 % and 75 % partially closed intake port are then discussed in a successive manner. The measurements are conducted for two flow Reynolds numbers: Re $= v_b D/\nu = 65000$ and 32500. The results are presented for Reynolds number 65000 since no significant differences are observed compared to Reynolds number 32500 for a given measuring plane and piston position.

A significant effort has been made to make the experimental set-up rotational symmetric. In order to asses the uncertainties involved in the measurement process and the repeatability of the experimental results, different measurement sessions were conducted for a given position and Reynolds number. These measurement sessions were conducted at different days, dismantling and reassembling of the PIV set-up (Fig. 3) and using different TBP. The results from different measurement sessions are labeled in each presented profile and represent repeated experiment but with different TBP for PIV and on a reassembled PIV set-up. The profiles of the tangential and axial velocity components include the error bars. The error bars are based on standard error (SE) of the mean with upper and lower 95 % confidence limits and present the uncertainty involved in a given measurement

$$SE = \frac{\sigma}{\sqrt{n}} \tag{1}$$

where σ is the standard deviation of all the observations for a given measurement and n represents the total number of observations.

The degree of swirl in a given swirling flow is quantified by the non-dimensional swirl number S. The swirl number in this experiment is measured using the relation for the design swirl parameter given by Gupta et al (1984) and Alekseenko et al (2007)

$$S \equiv \frac{2F_{\theta,z}}{F_{z,z}D} \tag{2}$$

where $F_{\theta,z}$ and $F_{z,z}$ denote the flux of angular and axial momentum in the flow direction. The angular momentum is estimated from the radial flux of angular momentum

$$F_{\theta,z} \approx F_{\theta,r} = \rho v_\theta v_r r(2\pi r h), \tag{3}$$

where h denotes the height of the channel at the radius r (Fig. 1), and

$$F_{z,z} = \rho v_b^2 \left(\frac{\pi}{4}D^2\right), \tag{4}$$

where $v_r = v_r(r)$ is related to the bulk velocity $v_b = v_r 8rhD^{-2}$. Thus, the swirl number is

$$S = \frac{v_\theta}{v_r}\frac{D}{4h}. \tag{5}$$

At the guide vanes ($r = 250$ mm) the velocity ratio $v_\theta v_r^{-1} \approx \tan(\alpha_{\text{blade}})$ and hence the design swirl number is $S = 0.33$. In addition, preliminary Laser Doppler Anemometry (LDA) experiments have been conducted to study the wake behind the blades (not shown). At $r = 200$ mm the measured flow angle is 26°, which results in an effective swirl number of $S = 0.23$.

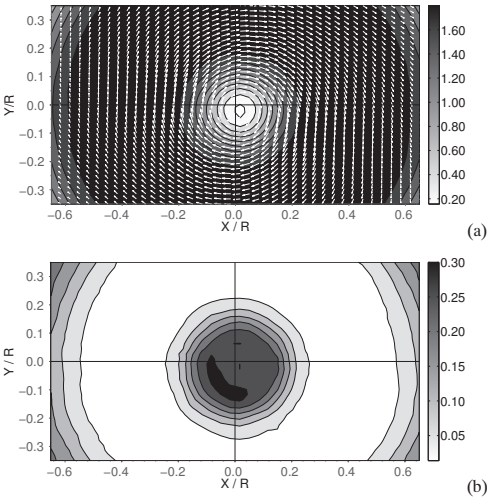

Fig. 4 Time average flow fields at z/D = 0.963 with fully open ports: (a) normalized velocity field (contour colors represent magnitude of out-of-plane velocity component); (b) normalized turbulent kinetic energy.

5.1 Fully Open Ports

When the intake port is fully open, the in-cylinder swirling flow results in a high velocity region at an intermediate radial position between the cylinder wall and geometric center cf. Fig. 4a). Here R is the radius of the cylinder. X and Y shown in Fig. 4 represent the x-axis and y-axis, respectively, when origin of the coordinate system is defined at the cylinder axis. The origin of the z axis is at the piston surface when the port is fully open. Contour color represents the axial velocity (out of the plane component) v_z normalized by bulk flow velocity v_b. It can be seen that the resulting in-cylinder swirling flow is comprised of a concentrated vortex with a core surrounded by a high velocity region. The velocity magnitude in the vortex core is very low compared to its surroundings. A low velocity region exists at a larger radial positions close to the cylinder wall (not shown). Although great care has been taken to make the experimental set-up rotational symmetric, the recirculating vortex core is asymmetric i.e. the mean vortex position is not coinciding with the geometric center of cylinder. Fig. 5a shows that when the intake port is fully open, the tangential velocity profile at $z/D = 0.963$ is comprised of a forced vortex region (solid body rotation) and an outer region with very low rotation or weak vorticity . The X_v shown in Fig. 5a represents the x-axis when the origin of the coordinate system is shifted to the mean vortex center. Higher velocities are observed in the radial position where the inner forced and outer free vortices meet. The vortex core region has low velocity magnitude

compared to other regions of the cylinder (except near cylinder wall as in the current experiment measurements near the wall have not been taken).

The axial velocity v_z has a wake-like profile cf. Fig. 5b and has overall magnitude higher than v_θ. This shows that flow has low swirl intensity. The size of vortex core increases downstream as both the tangential and axial velocities gradually decay downstream the cylinder and the velocity peaks become less distinct (Fig. 5d,e,g,h).

The flow at $z/D = 0.963$ has a large negative value of the normalized mean axial vorticity (ω_z) in the core region (calculated by first normalizing x, y with cylinder radius R and u, v with bulk flow velocity v_b) cf. Fig. 5c. The vorticity distribution appears to have a Gaussian-like profile. The vorticity is concentrated in a small tubular region near the vortex center and decays rapidly outward in the radial direction indicating a concentrated vortex profile cf. Lam (1993). Very low vorticity is observed only at large radial distances $X/R = 0.5$ from the vortex center.

With the decay of the swirl along the cylinder length, the vortex core gradually loses its vorticity. The size of the core increases and the weak-vortical region diminishes downstream the cylinder (Fig. 5f,i).

At $z/D = 0.963$, the vortex core exhibits an asymmetric distribution of the mean turbulent kinetic energy (TKE) cf. Fig. 4b indicating that the flow is three-dimensional. The largest value of TKE is observed in the vortex core region. However, the kidney shape of the region with high variance indicates the vortex precession superimposed on the three-dimensional velocity variations. The region outside the vortex core has very low turbulent kinetic energy but beyond half of cylinder radius, TKE starts increasing again towards the cylinder wall region. This is due to the 90° bend between the swirl generator outlet and the test cylinder (Fig. 1). The flow, while entering the cylinder, separates at the wall which increases the turbulence. As the swirl decays downstream (not shown), the overall magnitude of the turbulent kinetic energy also decreases but its spatial distribution increases due to enlargement of the vortex core and comparatively more uniform velocity distribution.

5.2 Ports Closed by 25 %

As the piston is translated to the positions partially covering the intake port, the in-cylinder flow becomes comparatively more chaotic. The possible reason is that the piston constitute a bluff body with a sharp edge to the flow entering the cylinder and the port area also reduces. This produces increased velocity fluctuations at the inlet compared to when the port is fully open and affects the in-cylinder velocity distribution.

At 25 % partially closed port (Fig. 6a,d,g), the maximum value of v_θ at $z/D = 0.963$ has decreased compared to fully open port. The profile shows a less distinct peak at the interface of outer region and inner enlarged forced vortex region. The size of the forced vortex region increases downstream the flow and at $z/D = 3.068$, the overall v_θ profile changes to a forced vortex i.e. the high v_θ region shifts to near wall position and eliminating the outer free vortex region. The overall v_θ magnitude decreases at all measuring positions compared to fully open port. The v_z at the near outlet positions changes from wake-like profile to a more uniform distribution cf. Fig. 6b,e,h. At position $z/D = 0.963$ near the inlet, the peak values of v_z magnitude is higher than its value at the open port position of the piston.

Fig. 6c,f,i shows the mean axial vorticity for the positions $z/D = 0.963$, $z/D = 2.016$, and $z/D = 3.068$, respectively. Compared to the fully open port case, the overall vorticity magnitude is reduced. At $z/D = 0.963$, similar to the fully open port, the vortex core region has the strongest vorticity. However, the maximum vorticity magnitude in the vortex core region is less than half the value observed in case of fully open intake port. Due to increase in the size of the vortex core region, the spatial distribution of the vorticity around the vortex center has also increased. This indicates that the Burgers vortex profile is dimished in a way that the vorticity from strong vortical region (vortex core) is transferred to the surrounding weak vortical regions and thus the vorticity of the outer (free vortex) region increases. With the flow downstream, the vorticity distribution tends to become more uniform at $z/D = 2.016$ and at $z/D = 3.068$ a uniform vorticity distribution is observed cf. Fig. 6f,i. The fluctuations in the vorticity profile plots are due to measurement noise.

At $z/D = 0.963$ the maximum value of the turbulent kinetic energy seems to have increased when the the piston partially closes the intake port by 25 %. The maximum value of TKE is still observed in the vortex core region however the region with low value of TKE, observed in case of fully open port has shrunk thus indicating an increase in the value of TKE from the half cylinder radius to the regions close to the wall (Fig. 9a).

5.3 Ports Closed by 50 %

With the piston covering 50 % of the intake port, the asymmetry in the distribution of v_θ at $z/D = 0.963$ increases cf. Fig. 7a. At $z/D = 2.016$ cf. Fig. 7d the tangential velocity profile becomes more symmetric and attains a forced vortex like profile. However, the v_θ profile seems to have a small curvature from thee mean vortex center to large radial positions indicating rather a tangential wall-jet like profile as observed by Steenbergen and Voskamp (1998). In case of plane jets, a wall-jet is defined as a fluid jet that is issued tangentially to and grows on a wall (Pani and Rajaratnam,

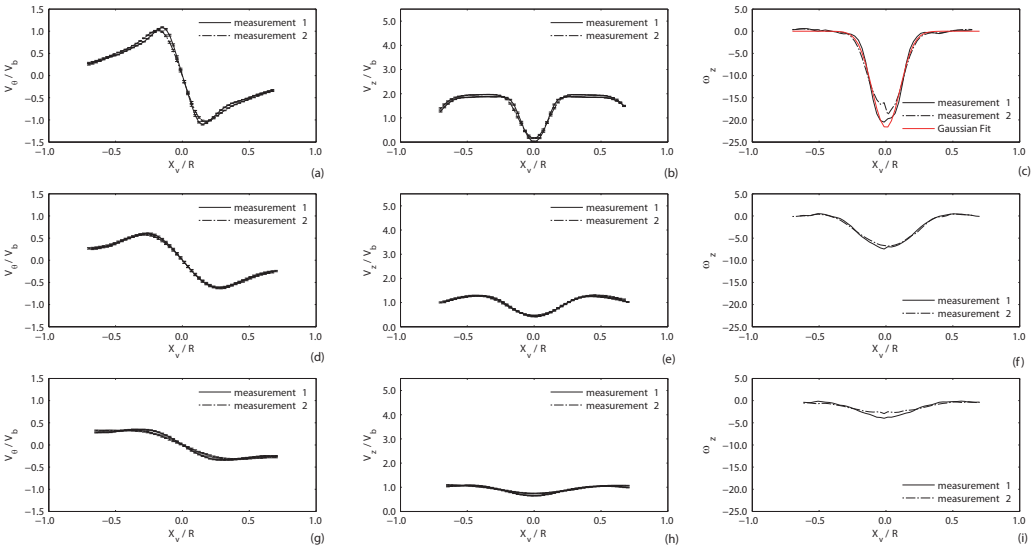

Fig. 5 Normalized time averaged profiles with fully open ports: (a) tangential velocity profile at $z/D = 0.963$; (b) axial velocity profile at $z/D = 0.963$; (c) axial vorticity profile at $z/D = 0.963$; (d) tangential velocity profile at $z/D = 2.016$; (e) axial velocity profile at $z/D = 2.016$; (f) axial vorticity profile at $z/D = 2.016$; (g) tangential velocity profile at $z/D = 3.068$; (h) axial velocity profile at $z/D = 3.068$; (i) axial vorticity profile at $z/D = 3.068$.

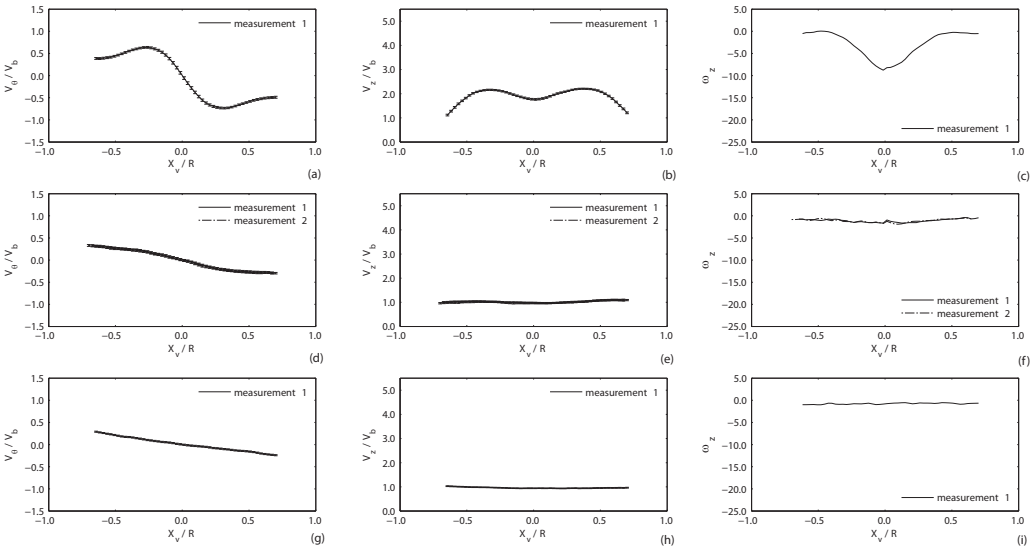

Fig. 6 Normalized time averaged profiles with 25 % closed ports: (a) tangential velocity profile at $z/D = 0.963$; (b) axial velocity profile at $z/D = 0.963$; (c) axial vorticity profile at $z/D = 0.963$; (d) tangential velocity profile at $z/D = 2.016$; (e) axial velocity profile at $z/D = 2.016$; (f) axial vorticity profile at $z/D = 2.016$; (g) tangential velocity profile at $z/D = 3.068$; (h) axial velocity profile at $z/D = 3.068$; (i) axial vorticity profile at $z/D = 3.068$.

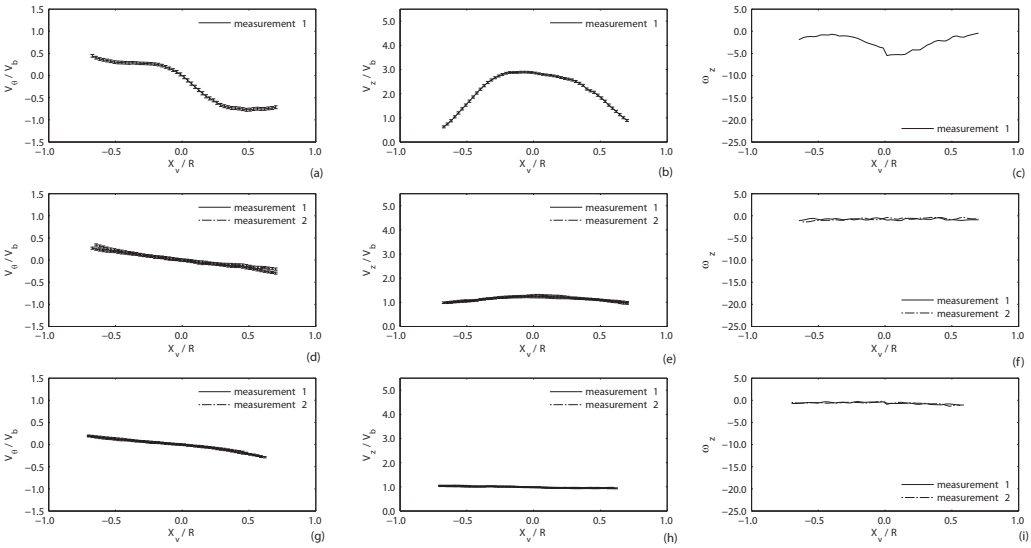

Fig. 7 Normalized time averaged profiles with 50 % closed ports: (a) tangential velocity profile at $z/D = 0.963$; (b) axial velocity profile at $z/D = 0.963$; (c) axial vorticity Profile at $z/D = 0.963$; (d) tangential velocity profile at $z/D = 2.016$; (e) axial velocity profile at $z/D = 2.016$; (f) axial vorticity Profile at $z/D = 2.016$; (g) tangential velocity profile at $z/D = 3.068$; (h) axial velocity profile at $z/D = 3.068$; (i) axial vorticity Profile at $z/D = 3.068$.

1976). Due to a velocity discontinuity, a shear layer develops on the fluid side and on the wall side a boundary layer is developed (Rajaratnam, 1976). For confined swirling flows with a tangential wall-jet like profile, analogous to plane wall jets, a tangential velocity jet is issued to the cylinder walls. The maximum tangential velocity is observed at a radial distance from the curved wall where the shear layer meets the wall boundary layer and minimum tangential velocity is observed in the vortex center. A similar v_θ profile is observed for $z/D = 3.068$ but with a smaller magnitude thus indicating decay in the swirl (Fig. 7g).

A significant change in the axial velocity profile is observed at the positions close to the cylinder inlet where, compared to fully open and 25 % port closure, it has changed to jet-like profile i.e. the peak velocity magnitude is at the center of the cylinder and decreases radially towards the wall (Fig. 7b). However, there is a rapid decay in the velocity peaks from position $z/D = 0.963$ to $z/D = 2.016$ and again at $z/D = 3.068$ where a uniform distribution of v_z is observed cf. Fig. 7e,h.

For 50 % intake port closure, the mean axial vorticity at $z/D = 0.963$ is shown in Fig. 7c. The ripples in the axial vorticity profile is due to the measurement noise. The vorticity of the vortex core region is still stronger than other radial positions at that cross-sectional plane but less pronounced compared to the vorticity at $z/D = 0.963$ and with 25 % port closure. The maximum value of the axial vorticity has reduced to nearly half of the maximum value at $z/D = 0.963$ for 25 % intake port closure.

The mean axial vorticity distribution at $z/D = 2.016$ and $z/D = 3.068$ (Fig. 7f,i) respectively, the vorticity is more uniformly distributed. This indicates that the initial strength of the vortex core decreases along the flow downstream by transferring vorticity to other weak vortical regions.

The turbulent kinetic energy increases further with the increase in the partial closure of the intake port from 25 % to 50 % cf. Fig. 9b. The vortex core region now has a very low TKE value. The maximum value of TKE is observed in the region $X/R = 0.4$ to 0.6. This indicates that the overall velocity variance in the center of the jet-like axial velocity is very low. The asymmetric distribution of TKE in the vortex core region can be understood from an asymmetric jet-like profile of mean axial velocity component.

5.4 Ports Closed by 75 %

The tangential velocity exhibits a solid body rotation throughout the cylinder i.e. peak v_θ in the entire cylinder is shifted to the near wall positions cf. Fig. 8a,d,g.The overall tangent velocity magnitude decays downstream the flow.

At $z/D = 0.963$ the axial velocity component v_z still has a jet-like profile (Fig. 8b). However, the profile has a sharp peak compared to the 50 % intake port closure (Fig. 7b).

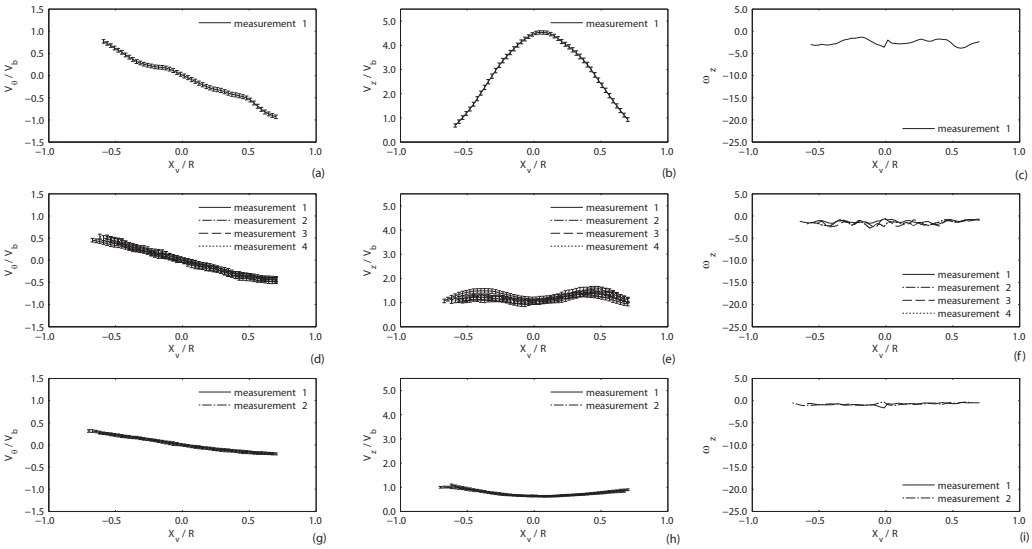

Fig. 8 Normalized time averaged profiles with 75 % closed ports: (a) tangential velocity profile at $z/D = 0.963$; (b) axial velocity profile at $z/D = 0.963$; (c) axial vorticity Profile at $z/D = 0.963$; (d) tangential velocity profile at $z/D = 1.489$; (e) axial velocity profile at $z/D = 1.489$; (f) axial vorticity Profile at $z/D = 1.489$; (g) tangential velocity profile at $z/D = 3.068$; (h) axial velocity profile at $z/D = 3.068$; (i) axial vorticity Profile at $z/D = 3.068$.

A significant change in the v_z profile is observed at $z/D = 1.489$ where v_z changes back from jet-like to wake-like profile (Fig. 8e) which is characteristic of a vortex breakdown (Escudier et al, 1982). The profile for v_z remains the same i.e. wake-like at all downstream positions (Fig. 8h), however, the peak value v_z is observed at large radial distance from the vortex center indicating an increase in the vortex core size downstream the flow.

When the intake port is closed by 75 % (Fig. 8c), compared to the other positions of the piston, at $z/D = 0.963$ the strong vorticity of the vortex core region no longer exists. Instead the mean velocity field has nearly uniform ω_z-distribution throughout the cylinder.

The increase in the value of the turbulent kinetic energy continues with the partial closure of the intake port. For 75 %, similar to 50 %, the vortex core region has a low value of TKE at $z/D = 0.963$ (Fig. 9c). The distribution of TKE in the core region is comparatively more symmetric than at 50 %. This can be observed from the v_z profile (Fig. 8b) which is more symmetric than v_z profile at 50 % port closure (Fig. 7b).

6 Conclusion

The magnitudes of the tangential and axial velocities decay downstream due to friction with the internal cylinder wall. The tangential velocity profile, at fully open port, is similar to a Burgers vortex i.e. an inner forced vortex core and free vortex outer region. The higher velocities are observed at some intermediate radial position between the cylinder wall and the geometric center where force and free vortex regions meet. With the downstream decay in swirl the size of the forced vortex region increases. At piston positions partially closing the port, the tangential velocity profile starts changing to a forced vortex i.e. higher velocities are observed near the cylinder walls. This change in velocity profile begins from cross-sectional positions near the cylinder outlet and moves to upstream positions as the piston gradually closes the port. However, in case of piston position with 50 % port closure, the tangential velocity profiles resembled a wall-jet like profile rather than the forced vortex. For the cross-sectional positions close to the intake port, the partial closure of the intake port introduces asymmetry and variation in the mean tangential velocity profile.

Fully open ports result in an axial velocity with wake-like profile at all measuring planes. However, no reverse flow at the vortex core has been observed. The downstream decay in swirl is decreasing the wake effect by transferring more mass into the wake region. As the piston starts closing the ports the axial velocity profile changes from wake-like to jet-like at 50 % port closure. However, at 75 % port closure the jet-like mean axial velocity profile at the cross-sectional position close to intake port changes back to wake-like at the

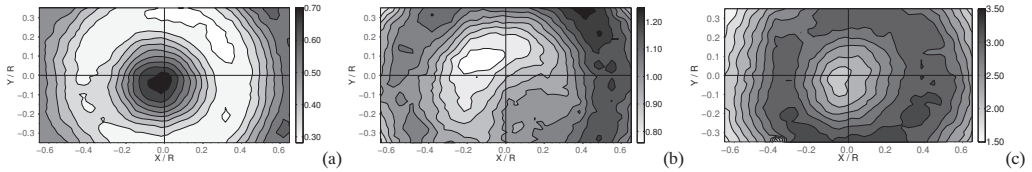

Fig. 9 Time average turbulent kinetic energy at $z/D = 0.963$ for the (a) 25 %, (b) 50 % and (c) 75 % closed ports.

adjacent downstream cross-sectional position. This is characteristic of a vortex breakdown. The mean axial velocity profile then continues to have the wake-like profile at the remaining downstream positions.

The mean axial vorticity of the mean velocity field has a Gaussian-like profile when the intake port is fully open. However, with the downstream decay of swirl as well as the partial closure of the intake port, the vorticity confined in the vortex core region is transmitted to the outer regions. This results in a comparatively uniform mean axial vorticity distribution throughout the cylinder for the 75 % port closure. The turbulent kinetic energy increases with the partial closure of the intake port. For a given cross-sectional plane, the distribution of TKE seems to be understood from the mean axial velocity distribution. For a wake-like v_z profile, the maximum value of TKE is observed in the vortex core region and the minimum value is observed in the high v_z region. Similarly, for a jet-like v_z profile, the minimum value is observed in the center of the jet and maximum value is observed in the jet skirt region.

The experimental results presented in this paper provide insight into the nature of the in-cylinder confined swirling flow during the scavenging process. With the piston motion the change in the tangential and axial velocity profiles, both at different piston position and at different cross-sectional planes represent a specific type of vortex. Studying the characteristics of the different types of vortex structures is a key to the understanding of the real engine scavenging process including critical issues such as the mixing of fresh charge with exhaust gases. Moreover, the modelling of swirling flow is a challenge to standard computational fluid dynamics (CFD) tools and the present, fixed piston experiment provides an essential benchmark for the validation of CFD tools for engine simulations.

Acknowledgements The authors acknowledge support from MAN Diesel & Turbo, the Danish Centre for Maritime Technology (DCMT), and the Danish Research Council of Independent Research (grant 09-070608). The authors futhermore acknowledge CIMAC for granting permission to publish some of the results presented by the authors at the CIMAC 2010 Congress.

References

Alekseenko SV, Kuibin PA, Okulov VL (2007) Theory of Concentrated Vortices: An Introduction. Springer-Verlag

DantecDynamics (2009) Dantec dynamicstudio v 2.3 user manual. Tech. rep.

Dedeoglu N (1988) Improvement of mixture formation in a uniflow-scavenged two-stroke engine. SAE Tech Paper Ser 901536

egon, friends (????) some title. J Fluid Mech pp –

Escudier MP, Bornstein J, Maxworthy T (1982) The dynamics of confined vortices. Proc R Soc Lond A 382:335–350

Gupta AK, Lilley DG, Syred N (1984) Swirl Flows. Abacus Press

Lam H (1993) An experimental investigation and dimensional analysis of confined vortex flows. PhD thesis, Concordia University, Quebec, Canada, unpublished

Litke B (1999) The influence of inlet angles in inlet ports on the scavenving process in two-stroke uniflow-scavenged engine. Mar Tech III 45:247–252

Nakagawa H, Kato S, Tateishi M, Adachi T, Tsujimura H, Nakashima M (1990) Airflow in the cylinder of a 2-stoke cycle uniform scavenging diesel engine during compreession stroke. Jpn Soc Mech Eng 33(3):591–598

Nishimoto K, Takeyuki K (1984) A study on the influnce of inlel angel and Reynolds number on the flow-pattern of uniflow scavenging air. SAE Tech Paper Ser 93

Pani BS, Rajaratnam N (1976) Swirling circular turbulent wall jets. J Hydralic Res 14(2):145–154

Pevzner LA (1998) Aspects of marine low-speed, crosshead diesel engine lubrication. Lubri Engng 54(6):16–21

Rajaratnam N (1976) Turbulent Jets. Elsevier

Steenbergen W, Voskamp J (1998) The rate of decay of swirl in turbulent pipe flow. Flow Mea Instru 9(2):67–78